BEILSTEIN JOURNAL OF NANOTECHNOLOGY

Noncontact atomic force microscopy II

Edited by Mehmet Z. Baykara and Udo D. Schwarz

Imprint

Beilstein Journal of Nanotechnology
www.bjnano.org
ISSN 2190-4286
Email: journals-support@beilstein-institut.de

The *Beilstein Journal of Nanotechnology* is published by the Beilstein-Institut zur Förderung der Chemischen Wissenschaften.

Beilstein-Institut zur Förderung der
Chemischen Wissenschaften
Trakehner Straße 7–9
60487 Frankfurt am Main
Germany
www.beilstein-institut.de

Beilstein Journal
of Nanotechnology

Noncontact atomic force microscopy II

Mehmet Z. Baykara[*1] and Udo D. Schwarz[*2]

Editorial

Open Access

Address:
[1]Department of Mechanical Engineering and UNAM-Institute of Materials Science and Nanotechnology, Bilkent University, Ankara 06800, Turkey and [2]Departments of Mechanical Engineering & Materials Science and Chemical & Environmental Engineering and Center for Research on Interface Structures and Phenomena (CRISP), Yale University, P.O. Box 208284, New Haven, CT 06520-8284, USA

Email:
Mehmet Z. Baykara[*] - mehmet.baykara@bilkent.edu.tr;
Udo D. Schwarz[*] - udo.schwarz@yale.edu

[*] Corresponding author

Keywords:
atomic force microscopy, scanning force microscopy

Beilstein J. Nanotechnol. **2014,** *5,* 289–290.
doi:10.3762/bjnano.5.31

Received: 03 February 2014
Accepted: 06 February 2014
Published: 12 March 2014

This article is part of the Thematic Series "Noncontact atomic force microscopy II".

Editor-in-Chief: T. Schimmel

In order to visualize the atomic structure of materials in real space, a microscope with sub-nanometer resolution is needed. As such, breaking the resolution limit associated with the wavelength of visible light employed in traditional optical microscopy has been a long-standing dream of scientists around the world. This goal was finally reached in the early 1980s with the invention of the scanning tunneling microscope (STM). While it is possible to obtain atomic-resolution images of material surfaces by using STM with relative ease, its basic operational principle depends on the phenomenon of *quantum tunneling*, rendering the technique applicable only to conductive and semi-conductive samples. The atomic force microscope (AFM), which was invented only a few years after the introduction of the STM, overcame this fundamental limitation and was used with great success to image a number of sample surfaces with nanometer resolution without limitations associated with electrical conductivity. However, unlike the STM, the operation of the AFM in its traditional form requires the establishment of a permanent – albeit *light* – contact between the probe tip and the sample surface, leading to a finite contact area, which prevents true atomic-resolution imaging.

True atomic resolution imaging through AFM was finally achieved in 1994 with the invention of *noncontact atomic force microscopy* (NC-AFM). The basic idea behind NC-AFM is based on the detection of minor changes in the resonance frequency of a micro-machined cantilever carrying a sharp probe tip due to attractive force interactions while it is oscillated above the sample surface to be investigated. Since actual contact with the sample is avoided, the probe tip retains its sharpness and atomic-resolution images may be obtained. Since its introduction two decades ago, NC-AFM has indeed been used to image a large number of conducting, semi-conducting, and insulating material surfaces of technological and scientific importance with atomic resolution, thus contributing to nanoscale science in a major way with each passing year. The capabilities of NC-AFM are not only limited to atomic-resolution imaging: Force spectroscopy allows characterization of interatomic forces with unprecedented resolution in three spatial dimensions, while manipulation experiments at both low temperatures and room temperature have demonstrated the capability of the technique to controllably construct atomic-scale structures on surfaces.

While initially small, the NC-AFM community gradually grew with each passing year. To provide a forum for exchange between researchers, progress in the field has been discussed since 1998 at annual conferences held in various cities around the world. The latest meeting in that series, the *16th International Conference on Non-Contact Atomic Force Microscopy* hosted by the University of Maryland in August 2013, demonstrated once again rapid progress in the field. For this Thematic Series, many of the leading groups have provided contributions with the goal of assembling a collection of papers that provide an overview of the current state-of-the-art in NC-AFM research, thereby delivering a snapshot of the newest trends in the field. For example, the realization that experimental results in NC-AFM are often strongly influenced by the mechanical and chemical properties of probe tips have sparked an increase in simulation work aimed at uncovering the associated principles, which is reflected in a number of contributions. Additionally, three-dimensional force spectroscopy on adsorbed molecules as well as challenges associated with the correct incorporation of long-range forces in such experiments are emphasized. Finally, it becomes apparent how new experimental methods that are based on the working principle of NC-AFM are continuously being developed, which is documented by a number of papers dealing with multi-frequency AFM as well as Kelvin probe force microscopy (KPFM).

We thank all the scientists who have submitted their outstanding work to the second edition of this Thematic Series, the referees for their careful reviews, and the *Beilstein Journal of Nanotechnology* for providing a truly open-access forum for publication and dissemination of research results. We hope that the papers presented here will contribute their share to stimulate new ideas and inspire new directions for future research.

Mehmet Z. Baykara and Udo D. Schwarz

Ankara, New Haven, February 2014

License and Terms

The definitive version of this article is the electronic one which can be found at:
doi:10.3762/bjnano.5.31

Beilstein Journal
of Nanotechnology

Structural development and energy dissipation in simulated silicon apices

Samuel Paul Jarvis*[1], Lev Kantorovich[2] and Philip Moriarty[1]

Full Research Paper

Open Access

Address:
[1]School of Physics and Astronomy, University of Nottingham, Nottingham NG7 2RD, United Kingdom and [2]Department of Physics, King's College London, The Strand, London WC2R 2LS, United Kingdom

Email:
Samuel Paul Jarvis* - samuel.jarvis@nottingham.ac.uk

* Corresponding author

Keywords:
apex structure; atomic force microscopy; DFT; dissipation; hysteresis; NC-AFM; silicon; spectroscopy; tip structure

Beilstein J. Nanotechnol. **2013,** *4,* 941–948.
doi:10.3762/bjnano.4.106

Received: 17 October 2013
Accepted: 04 December 2013
Published: 20 December 2013

This article is part of the Thematic Series "Noncontact atomic force microscopy II".

Guest Editors: U. D. Schwarz and M. Z. Baykara

Abstract

In this paper we examine the stability of silicon tip apices by using density functional theory (DFT) calculations. We find that some tip structures - modelled as small, simple clusters - show variations in stability during manipulation dependent on their orientation with respect to the sample surface. Moreover, we observe that unstable structures can be revealed by a characteristic hysteretic behaviour present in the $F(z)$ curves that were calculated with DFT, which corresponds to a tip-induced dissipation of hundreds of millielectronvolts resulting from reversible structural deformations. Additionally, in order to model the structural evolution of the tip apex within a low temperature NC-AFM experiment, we simulated a repeated tip–surface indentation until the tip structure converged to a stable termination and the characteristic hysteretic behaviour was no longer observed. Our calculations suggest that varying just a single rotational degree of freedom can have as measurable an impact on the tip–surface interaction as a completely different tip structure.

Introduction

The theoretical treatment of chemical interactions at the single atom level has driven considerable progress in NC-AFM over the past decade. Through understanding the interactions between the AFM tip and sample surface, the chemical interactions present in AFM images [1-5], manipulation experiments [6-10], and, more recently, submolecular investigations of planar molecules [11,12], have been revealed. In covalent systems in particular, density functional theory (DFT) calculations have been extremely successful in explaining the fundamental interactions that underpin NC-AFM experiments [2,3,13-16]. Moreover, atomistic simulations remain essential to many current studies in covalent [17-19] and ionic [20,21] systems because of the inherent difficulties in determining the tip apex structure from purely experimental evidence. In contrast, on metal surfaces the requirement to use atomistic simulations for tip identification is not always as critical. For instance, there has been significant recent progress in developing experimentally driven methods to determine or engineer the tip structure with the use of CO molecules either adsorbed to the scanning probe tip [11], or used to reverse image a metallic tip apex by using the so-called carbon oxide front atom identification method (COFI) [22]. Such techniques provide an intuitive way in which to analyse and prepare the scanning probe tip. Similarly, reverse imaging can be employed on semiconductor surfaces, such as Si(111)-7×7 [23,24]. A comparison with either the COFI method or DFT calculations, however, is usually required to obtain the same level of confidence.

Semiconductors with covalent bonds remain one of the most promising systems for the advancement of atom-by-atom manipulation strategies in multiple dimensions and at room temperature. This is evidenced by numerous studies, which have shown the manipulation of single atoms in both lateral and vertical directions, which was made possible by the strong covalent nature of the bonding [25]. As such, understanding the AFM tip structure and successfully modelling experimental observations remains critical to furthering this goal. Several methods have been used to successfully model complicated tip structures such as variations in tip structure [16,26], chemical species [17,27] and, more recently, the directional dependence of reactive tips [18,28].

The orientation of the tip is rarely considered in theoretical work because of the high computational cost of running multiple simulations, although some do exist [29,30]. Therefore results are generally only presented for tip structures at a single orientation, even though modifying the tip–surface alignment can also strongly affect calculated tip-force $F(z)$ curves and the hysteresis pathways followed by the tip and surface structures [28]. For instance, the bulk-like rear structure of tip apices is almost always aligned parallel to the surface for convenience when designing the tip. There is no reason to expect, however, that the experimental tip apex will follow the same rules. Therefore there is a clear constraint on current theoretical simulations due to the huge number of possible orientations that *a single* tip apex can adopt relative to *any* surface, even surfaces with perfectly symmetric dangling bond protrusions, let alone due to variations in tip apices.

Energy dissipation in NC-AFM measurements has most effectively been explained by adhesion hysteresis due to deformations in the tip–sample junction originating from bistable defects [31-33] or by structural relaxations within the larger structure of the AFM tip [34,35]. Dissipation is measured if the positions of some of the atoms (either in the surface, tip, or both) on approach and retraction are different, with the same atoms returning to their original positions at the end of the oscillation cycle. Observations of large dissipation signals of the order of electronvolts have been attributed to chain formation on insulating surfaces [36] and significant structural rearrangements of *both* the tip and sample over each oscillation of the AFM tip [16,37]. It has also been shown that in some cases the dissipation may be apparent – an instrumental artefact caused by mechanical coupling between the sensor and the piezo actuator [38].

In the current study we use the Si(100)-c(4×2) surface as a prototypical system, chosen because of its known dissipative behaviour in NCAFM experiments [8,13,37,39]. In particular, we have previously shown that a large variety of tip types are possible on the Si(100) surface, each demonstrating a different tip–sample interaction, and importantly, each exhibiting markedly different levels of measured dissipation [40]. Here we examine the effect that simple rotations of the simulated cluster can have on the tip–sample forces and the long-term stability of the tip apex. We observe that the rotation of the simulated tip cluster around the surface normal axis can have a dramatic effect on the stability of the tip apex such that at particular alignments permanent structural deformations occur which lead to new, stabilised tip geometries. We find that a tip prone to this behaviour demonstrates enhanced hysteresis in calculated $F(z)$ data, dependent *only* on deformations within the tip apex, until complex structural rearrangements move the geometry into a more stable state. This suggests that even when varying just a single rotational degree of freedom, the difference in tip–surface interactions can be as significant as for a completely different tip structure.

Simulation details

Our investigation is performed with ab initio density functional theory (DFT) simulations carried out by using the SIESTA code [41], which uses a double-zeta polarized basis set in the generalized gradient approximation with a Perdew–Burke–Ernzerhof density functional and norm-conserving pseudopotentials. Due to the relatively large size of the unit cell only a single $|\mathbf{k}| = 0$ point was used for sampling the Brillouin zone. The atomic structure was considered relaxed when forces on atoms fell below 0.01 eV/Å. To obtain calculated $F(z)$ curves the silicon tip clusters were placed at an initial vertical position of 8 Å above the Si(100) surface upper dimer atom. The vertical distance, z, is defined as the distance between the surface upper dimer atom and the lowest atom of the tip structure *prior* to relaxation. To ensure a smooth evolution of the tip structure and to avoid missing any of the hysteresis pathways, the tip was moved in quasi-static steps of 0.1 Å towards the surface and then retracted in the same way. At each point the vertical forces acting on the fixed tip atoms were summed up to give the total force that acts on the tip.

Results and Discussion

The structures considered in this study, and the characterisation process, are illustrated in Figure 1. The three tip structures considered, and a ball-and-stick model of the Si(100)-(c4×2) surface are shown in Figure 1a and Figure 1c. We consider three tip clusters that are commonly used to describe silicon tip apices, the so called "H3" structure and two dimerised silicon tip clusters. The dimerised tip in particular can be modified through inclusion of an atom on one side of the cluster which, as will be described below, has a stabilising effect on the tip. We are therefore able to model a high and low stability dimerised tip, which we label D_1 and D_2 respectively (see Figure 1a). It has previously been shown [28] that $F(z)$ measurements can be used to characterise the tip structure through the examination of the energy dissipation during the dimer manipulation. A similar method is implemented in this work to assess the evolving structure of a silicon tip. In the current instance the tips are rotated through angles up to 360° around the surface normal axis, either positioned above the down, or up atom of a surface dimer. The angled nature of the Si(100) surface dangling bonds, particularly on the structurally rigid "up" dimer atom, allows us to easily investigate the effect of the tip-cluster alignment by rotations around a single axis, without having to consider the many other degrees of freedom available that would become more important on symmetric surfaces. The $F(z)$ curves are calculated at four tip-surface alignments (see Figure 1b). This procedure is used not only as a theoretical assessment of tip stability, but also highlights that the rotational alignment of the tip relative to the surface, in some cases, can dramatically affect the chances of a major structural rearrangement.

Energy dissipation in small apex clusters

Presented in Figure 2 are simulated $F(z)$ curves taken with the H3 (a) and D_1 (b) tips positioned above the up (green and black triangles) and down (red and blue circles) atoms of a surface Si(100) dimer. An in-depth description of the origins of the calculated force profile have been given elsewhere [8,13,42]. The key points, however, are summarised below. For tip apices positioned above the up dimer atom, a typical $F(z)$ curve is observed with indistinguishable approach and retraction profiles (see, for example, 2a). When positioned above the down atom of the surface dimer, however, at a certain tip–sample distance a threshold force is met and a sharp jump is observed in the $F(z)$ curve, which corresponds to a switching of the surface Si(100) dimer from a bond angle of approximately +19° to about −19°. For the remainder of the approach, and the subsequent retraction, the force profile follows that of the stable up dimer atom, a

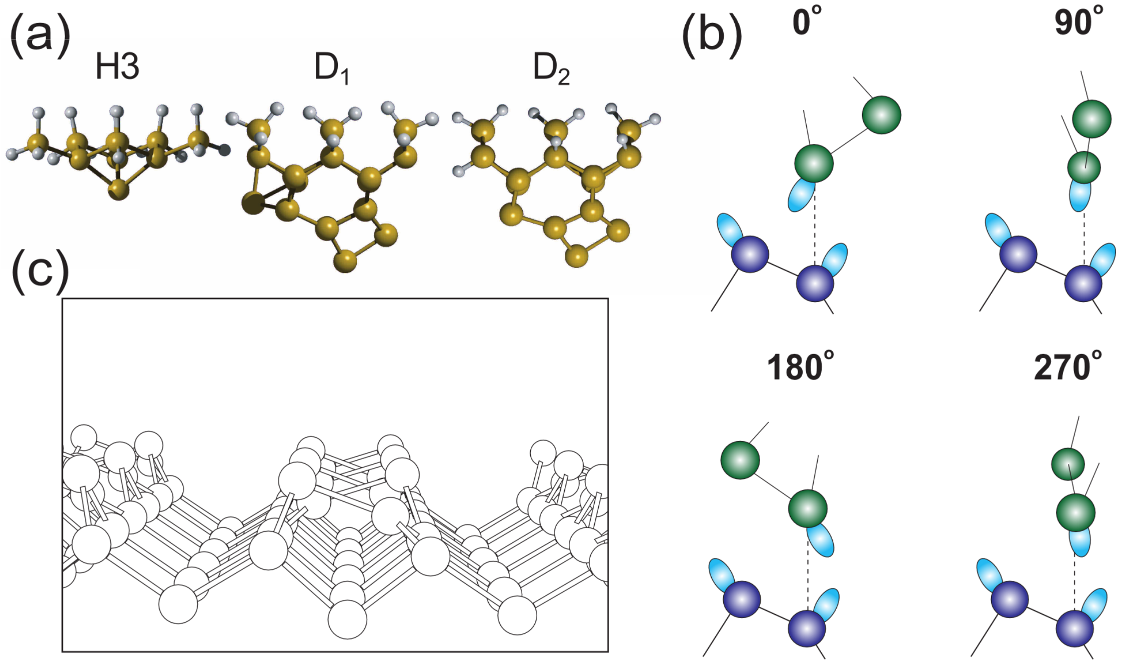

Figure 1: The three tip structures considered, a structurally rigid 'H3' termination, and two dimer-terminated tips, are shown in (a). D_1 is relaxed with an additional stabilising atom as compared to D_2. (b) $F(z)$ was calculated for four rotations of the dimer tips with respect to the surface dimers. Note that due to the symmetry of the surface 90° and 270° are equivalent, but are still calculated independently for control. (c) A ball-and-stick model of the upper layers of the Si(100)-c(4×2) surface.

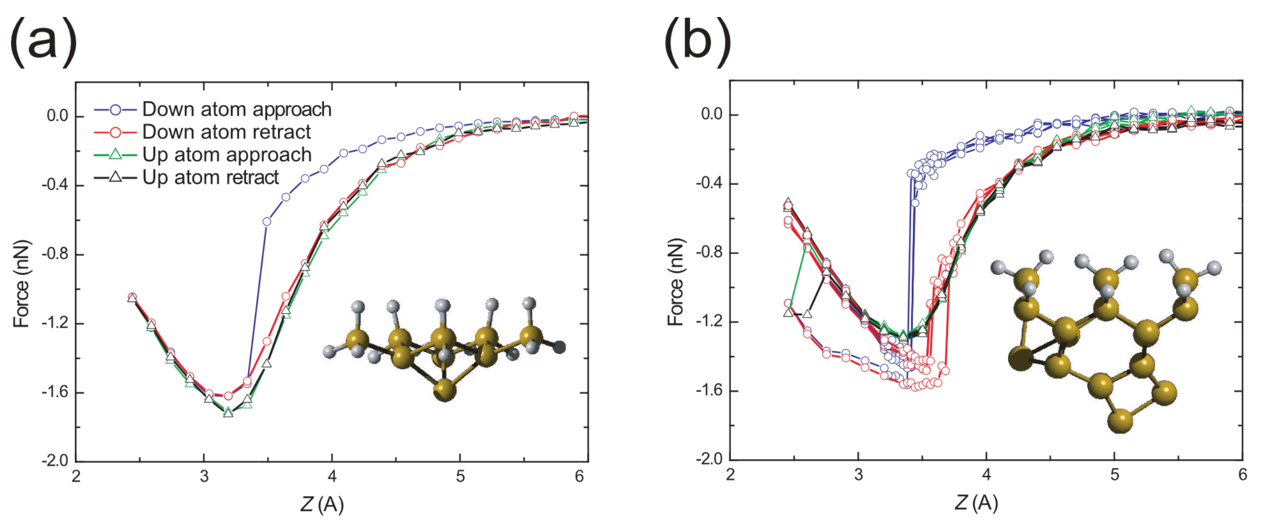

Figure 2: Simulated $F(z)$ curves for the (a) H3 and (b) D_1 tip structures taken above the up (green and black triangles) and down (red and blue circles) atoms of a surface Si(100) dimer. Curves in (b) of the same colour correspond to the different orientations of the tip with respect to the surface dimer as described in Figure 1b. It can be seen that the D_1 tip shows little variation upon rotation around the surface normal axis. The H3 tip contains a symmetric apex and does not produce variation when rotated, therefore only a single rotation is shown.

clear indicator of the successful switching event. Figure 2a depicts spectra that were taken with the high-stability H3 structure, which is used as our reference for a structurally rigid tip, which shows no variation upon rotation.

For the asymmetric D_1 tip, even though the tip–surface alignment varies upon rotation around the surface normal axis, its structure is very stable and we observe minimal variation in the simulated $F(z)$ curves. A small deviation is calculated only when the tip is rotated to the position we define as 180° (see Figure 1b), in which *both* of the atoms within the tip and surface dimers are able to interact with each other at very close approach. More interesting behaviour arises when we carry out the same simulations with the D_2 apex as is shown in Figure 3. In this case a significant increase in energy dissipation (over a single cycle) is calculated for the down atom position of the tip (red and blue circles) amounting to an average 74% increase, from 0.39 eV to 0.68 eV relative to the more stable D_1 cluster. The increase in hysteresis corresponds to hysteretic tip-deformations throughout the simulated $F(z)$ curve. For the D_2 tip, even though a significant level of dissipation is observed in the down atom position (a typical indicator of dimer manipulation [8,13]), the dimer, part way through the flipping process, in fact returns to its original state. This is noticeable as a sharp decrease in force during the retract curve. For successful manipulation, the target down atom of the dimer must be “pulled” high enough such that the up and down atoms trade places, switching the dimer buckling angle. The tip–dimer interaction for the D_2 tip, therefore, is not sufficient to pull the down atom high enough to instigate manipulation [39,42,43].

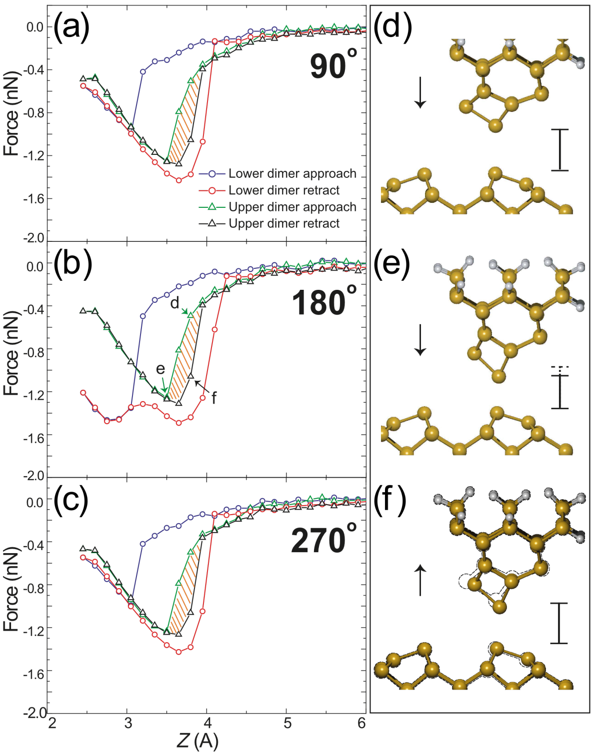

Figure 3: Simulated $F(z)$ curves for the D_2 tip at rotations (a) 90°, (b) 180°, and (c) 270°. The energy dissipation is significantly increased, and is critically also observed for the up atom site. Ball-and-stick snap shots are shown (d) within and (e) after the region of hysteresis as indicated in (b) during tip approach. (f) Ball-and-stick snap shot during retraction at the same position as (d), which is shown as a dashed outline, illustrating the alternative structural pathway taken by the tip, thus causing the observed hysteresis.

Particularly interesting observations are made when the D_2 tip is positioned above the structurally rigid up atom of the Si(100) dimer. Even though the surface atom remains mostly stationary throughout the approach–retraction calculation, a significant level of energy dissipation is calculated that amounts to 0.17 eV over a single cycle. The calculated $F(z)$ curves taken above the up Si(100) dimer atom are shown in Figure 3 (approach: green triangles, retraction: black triangles). Ball-and-stick snap shots, at the positions marked in Figure 3b, are shown in (d–f) within and after the region of hysteresis. Although the surface dimer remains in the same position, it is clear that the D_2 tip experiences significant deformation, which pulls the apex downwards into a narrower shape. The geometry shown in Figure 3f is taken at the same z position as (d), during retraction from the surface. From the calculated geometries we can see that the tip structures in (d) and (f) differ, thus modifying the tip–surface interaction, which in turn leads to the observed hysteresis. This theoretical result is very similar to experimental observations on the Si(100) surface that recorded a dissipation of up to 0.5 eV/cycle [40] for a tip that demonstrated a “dimer-tip”-type atomic resolution [44]. It has also been shown [34] that very large simulated tip clusters demonstrate the same behaviour, which is attributed to more permanent structural changes that are likely to occur within the much larger experimental tip. The difference we observe, therefore, is that no permanent structural change is required to observe a significant dissipation, even in much smaller silicon clusters.

This result has significant implications for understanding the origin of experimental observations of dissipation. Unlike the hysteresis observed for the down atom position (occurring over the single oscillation cycle when dimer manipulation takes place), *all* oscillation cycles, in which the point of closest approach falls below 3.5 Å will demonstrate hysteresis. Thus tip-dependent dissipation, even with very simple, small tip clusters such as the D_2 tip, should be noticeable on *any* surface, which further confirms the assumption that the tip structure plays the dominant role in many experimental dissipation observations.

Enhancing tip stability via surface indentation

Examination of the tip geometries in our simulations suggest that the increase in $F(z)$ hysteresis is driven by significant structural rearrangements. Our calculations suggest that the D_2 tip potential energy surface (PES) contains a number of shallow minima, which are separated by small barriers. Upon interaction with the surface the PES distorts in such a way that some of the barriers collapse, which opens a path for the tip to transform from one configuration to another. As a result the D_2 tip provides alternative structural pathways during approach and retraction. Clusters that demonstrate a greater stability do not allow for the atomic rearrangements that are required for the additional hysteresis, because the barriers that separate the different minima on the PES of these clusters are not reduced sufficiently upon interaction with the surface. Therefore, in some instances, the presence of a tip-hysteresis may act as an identifier for a potentially unstable tip configurations.

Tip indentation is a commonly applied technique to improve the quality of tips in NC-AFM, and in turn to modify the quality of the image. The process typically involves gentle indentations of the tip by 1–2 Å into the surface relative to the Δf feedback z position. As the tip is indented into the surface either material transfer, or atomic rearrangement can improve or worsen the quality of the AFM image. Thus far very few simulated studies have looked at the influence of surface indentation on the structure of the tip. Existing studies have either concentrated on coating the AFM tip with sample material [36] or sharpening very small and unstable silicon clusters [45]. Experiments that are carried out at room temperature are likely to have a sufficient energy available to heal any metastable tip states that might arise from such indentations. In this case simulated annealing [26] is usually sufficient for an accurate description. At low temperatures, however, where many exotic tip states have been observed [40], the available thermal energy becomes insufficient for restructuring the tip. Metastable tips are therefore far more likely to remain stable after a reconstruction of the tip.

In Figure 4 we show one such instance of tip development, in which the D_2 tip, although stable for the simulations in Figure 3, undergoes major structural rearrangement when aligned at “0°”. The calculated $F(z)$ curve at this position is shown in Figure 4a, in which two sharp jumps in force are present during retraction of the tip. Shown in (b–e) are geometries illustrating the major stages of tip rearrangement. Initially the tip configuration is as shown in (b), then the D_2 tip forms a strong bond with the Si(100) surface dimer in (c), which results in similar deformations to those already shown in Figure 3. Upon retraction of the tip, however, the strong tip–surface bond (due to the favourable alignment with the surface [28]) introduces a significant strain to the tip structure, which develops it into a much sharper configuration relative to the initial D_2 apex. Partial electron density maps, highlighting the dangling bond orbitals, are shown for the original D_2 tip (f) and the sharpened structure (g) which we term D_{2a}. A simple examination of the electron density plot reveals that the tip structure maintains a single prominent dangling bond orbital at its apex, which in principle should produce atomic resolution that is not significantly different from that to be expected from the initial tip structure. This may implicate that structural rearrangements of the tip may occur during the scan, which do not significantly affect the contrast and possibly remain largely unnoticed. We note that in previous studies the D_2 tip remained stable during simulated spectroscopy [16,26], and in our own simulations, when positioned above the surface Si(100) up dimer atom, no structural changes are observed regardless of orientation. As such we believe that the D_2 tip represents a plausible tip structure and a good candidate to test the orientation-dependent stability of the AFM tip cluster.

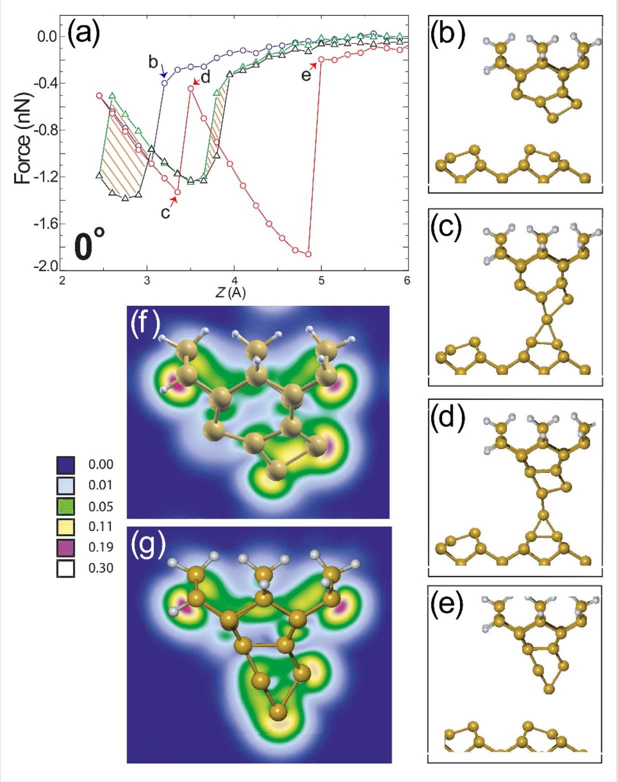

Figure 4: Structural development during tip indentation. (a) Calculated $F(z)$ approach and retraction curves for the D_2 tip at “0°” positioned above down (red and blue circles) and up (green and black triangles) surface dimer atoms. Calculation with the tip positioned above the down atom leads to structural rearrangement of the tip, noticed as discontinuities in the retract curve at ≈3.5 Å and ≈5 Å. The ball-and-stick model in (b) depicts the starting configuration of the tip during the approach, which is followed by the major stages in tip rearrangement during retraction (c–e). Partial electron density plots (calculated within the range 0–1 eV below the Fermi energy and plotted on a square root scale of electrons/Bohr^3) of (f) initial and (g) final tip (D_{2a}) configurations. Plots were made using the XCrySDen software [46].

Experimentally, during $\Delta f(z)$ measurements or tip indentations carried out specifically to modify the apex, the scanning tip is constantly oscillating at a rate of a few kilohertz, often with an amplitude that is larger than the silicon interaction potential. Therefore, as the average z position is ramped towards the sample, the tip will undergo multiple cycles of approach and retraction. As a result, any structural development of the tip apex must occur over multiple approach–retraction cycles, until a stable configuration is obtained that no longer reconstructs. To properly reflect this process, DFT $F(z)$ calculations were continued by using the D_{2a} tip without any modification of the system. Upon continuation we observe two further stages of structural development until a final stable configuration is reached. We term these two tips D_{2b} and D_{2c} and show the respective $F(z)$ curves leading to their development in Figure 5.

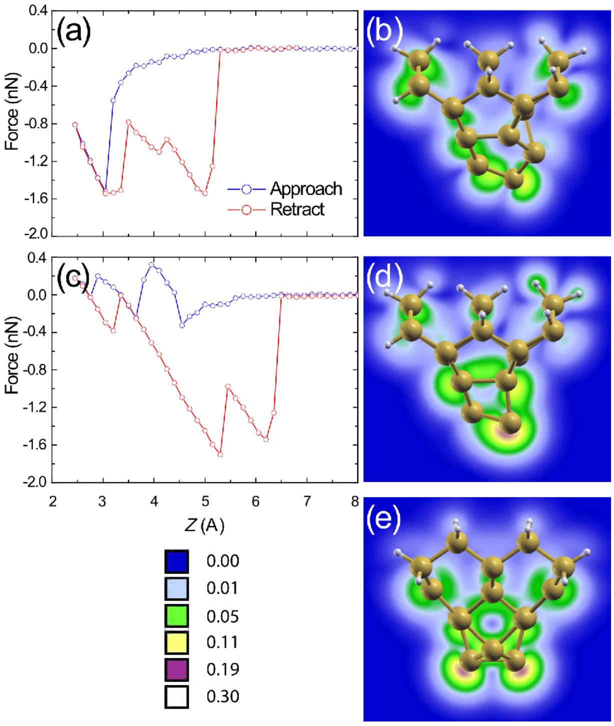

Figure 5: Continued development of tip D_{2a} via repeated tip indentations. (a) Calculated $F(z)$ curve and (b) final tip configuration following indentation of the tip structure shown in Figure 4(g) leading to tip D_{2b}. (c) Indentation of tip D_{2b} results in further modification noticeable as a series of sharp discontinuities in calculated $F(z)$ prior to reaching a final, stable double tip shown from two perspectives in (d–e). Partial electron density plots shown with square root scale in units of electrons/Bohr^3.

For the transition from D_{2a} to D_{2b} shown in Figure 5a, a significant number of atomic rearrangements occur, visible as rapid variations in the retraction curve. In fact, the tip not only undergoes significant rearrangement, but actually deposits an atom onto the Si(100) surface. Material deposition is commonly observed during experimental imaging and spectroscopy, sometimes leading to improvements in image resolution, or often leading to instabilities and deterioration of image quality. The partial electron density plot in (b) illustrates the apex dangling bond structure of tip D_{2b}, which appears to protrude at a large angle relative to the surface normal. This structure would likely lead to a complicated tip-surface interaction [40].

To test the stability of the D_{2b} tip a further calculation was carried out, just as for the D_{2a} structure, over the same deposited silicon atom. In this case the tip remained in the D_{2b} configuration without any further reordering. Assuming that this tip must now be stable when imaging the clean Si(100) surface, a final indentation was calculated above a clean Si(100) dimer. In this new position a further rearrangement of the tip was observed into a final, stable, configuration resulting in the $F(z)$ curve that is shown in Figure 5c. For the D_{2b} to D_{2c} transition, extreme features are observed both in the approach and retraction sections of the calculated $F(z)$ because of the complicated interaction between the tip and the surface Si(100) dimers. These features originate from the blunt structure of the tip interacting with two dimers on the surface during rearrangement. The D_{2c} tip structure is shown in Figure 5d and Figure 5e displayed from two perpendicular perspectives. This final tip configuration is found to be stable upon continued spectroscopy, which suggests that the tip apex is fully structurally developed. Interestingly, we find that the stable tip terminates in a dimer like structure, with each terminating atom located at very similar z positions. Each “dimer” atom is associated with a dangling bond protruding in the $-z$ direction, angled away from one another as shown in Figure 5e. The cluster appears to be more crystalline than its predecessors, which may perhaps explain the dimer termination because of the (100) orientation of the base structure. It is interesting to note that a dimer-terminated tip such as this might be able to produce double-lobed surface features, doubling effects, or even fail to produce a well separated, understandable signal altogether. Such observations would depend on the surface under study, and on the separation of the surface atoms, which can be a particularly challenging problem when obtaining atomic resolution.

The simulated results in this paper provide interesting insights into the atomic rearrangements that take place during well known, and commonly observed, experimental processes. We examine the role that alternative structural pathways play during spectroscopy measurements, which might lead to tip-dominated dissipation observations, similar to previous suggestions [34]. Critically, however, our observations are made by using the small, simple tip clusters that are tractable using a DFT treatment of the system, rather than the larger, more complicated, structures that must exist experimentally. Therefore, if dissipation can be observed for clusters of this size, it is very reasonable to expect that the same processes can occur in much larger, and hence more realistic systems. This suggests that the tip structure could play a dominant role in many experimental observations of dissipation.

We also show that tip apices that demonstrate hysteretic behaviour may be inherently unstable during $F(z)$ measurements, or soft tip indentations that lead to a major structural redevelopment of the tip apex. In our specific example, we show that a tip that may appear to be structurally stable at certain orientations with respect to the surface, might interact completely differently at another position. We suggest, therefore, that the examination of the tip orientation may be just as valuable as testing entirely new structures when making experimental comparisons. We expect that these results might apply not only for a rotation around the z axis (as studied here) but also around the x and y axes, which are not considered in this study. We also propose a method for developing tip structures, similar to experimental approaches, through repeated soft indentation into the surface until alternative stable structures are obtained. Such an approach might be particularly useful to build up a library of theoretical tip structures, which could assist the interpretation of experimental observations [40].

Acknowledgements

SJ and PJM would like to thank the Engineering and Physical Sciences Research Council (EPSRC) for the award of fellowships (EP/J500483/1) and (EP/G007837/1) respectively. We also acknowledge funding from the European Commission’s ICT-FET programme via the *Atomic Scale and Single Molecule Logic gate Technologies* (AtMol) project, Contract No. 270028 and for access to the University of Nottingham High Performance Computing Facility.

References

1. Giessibl, F. J. *Science* **1995,** *267,* 68–71. doi:10.1126/science.267.5194.68
2. Pérez, R.; Payne, M. C.; Štich, I.; Terakura, K. *Phys. Rev. Lett.* **1997,** *78,* 678–681. doi:10.1103/PhysRevLett.78.678
3. Pérez, R.; Štich, I.; Payne, M. C.; Terakura, K. *Phys. Rev. B* **1998,** *58,* 10835–10849. doi:10.1103/PhysRevB.58.10835
4. Foster, A. S.; Barth, C.; Shluger, A. L.; Reichling, M. *Phys. Rev. Lett.* **2001,** *86,* 2373–2376. doi:10.1103/PhysRevLett.86.2373
5. Such, B.; Glatzel, T.; Kawai, S.; Meyer, E.; Turanský, R.; Brndiar, J.; Štich, I. *Nanotechnology* **2012,** *23,* 045705. doi:10.1088/0957-4484/23/4/045705
6. Sugimoto, Y.; Jelinek, P.; Pou, P.; Abe, M.; Morita, S.; Perez, R.; Custance, O. *Phys. Rev. Lett.* **2007,** *98,* 106104. doi:10.1103/PhysRevLett.98.106104
7. Sugimoto, Y.; Pou, P.; Custance, O.; Jelinek, P.; Abe, M.; Perez, R.; Morita, S. *Science* **2008,** *322,* 413–417. doi:10.1126/science.1160601
8. Sweetman, A.; Jarvis, S.; Danza, R.; Bamidele, J.; Gangopadhyay, S.; Shaw, G. A.; Kantorovich, L.; Moriarty, P. *Phys. Rev. Lett.* **2011,** *106,* 136101. doi:10.1103/PhysRevLett.106.136101
9. Martsinovich, N.; Kantorovich, L. *Nanotechnology* **2009,** *20,* 135706. doi:10.1088/0957-4484/20/13/135706
10. Trevethan, T.; Watkins, M.; Kantorovich, L. N.; Shluger, A. L.; Polesel-Maris, J.; Gauthier, S. *Nanotechnology* **2006,** *17,* 5866–5874. doi:10.1088/0957-4484/17/23/026
11. Gross, L.; Mohn, F.; Moll, N.; Liljeroth, P.; Meyer, G. *Science* **2009,** *325,* 1110–1114. doi:10.1126/science.1176210
12. Moll, N.; Gross, L.; Mohn, F.; Curioni, A.; Meyer, G. *New J. Phys.* **2010,** *12,* 125020. doi:10.1088/1367-2630/12/12/125020

13. Sweetman, A.; Jarvis, S.; Danza, R.; Bamidele, J.; Kantorovich, L.; Moriarty, P. *Phys. Rev. B* **2011,** *84,* 085426. doi:10.1103/PhysRevB.84.085426
14. Sharp, P.; Jarvis, S.; Woolley, R.; Sweetman, A.; Kantorovich, L.; Pakes, C.; Moriarty, P. *Appl. Phys. Lett.* **2012,** *100,* 233120. doi:10.1063/1.4726086
15. Sugimoto, Y.; Pou, P.; Abe, M.; Jelinek, P.; Pérez, R.; Morita, S.; Custance, O. *Nature* **2007,** *446,* 64–67. doi:10.1038/nature05530
16. Oyabu, N.; Pou, P.; Sugimoto, Y.; Jelinek, P.; Abe, M.; Morita, S.; Pérez, R.; Custance, O. *Phys. Rev. Lett.* **2006,** *96,* 106101. doi:10.1103/PhysRevLett.96.106101
17. Yurtsever, A.; Sugimoto, Y.; Tanaka, H.; Abe, M.; Morita, S.; Ondráček, M.; Pou, P.; Pérez, R.; Jelínek, P. *Phys. Rev. B* **2013,** *87,* 155403. doi:10.1103/PhysRevB.87.155403
18. Sugimoto, Y.; Yurtsever, A.; Abe, M.; Morita, S.; Ondráček, M.; Pou, P.; Pérez, R.; Jelínek, P. *ACS Nano* **2013,** *7,* 7370–7376. doi:10.1021/nn403097p
19. Weymouth, A. J.; Meuer, D.; Mutombo, P.; Wutscher, T.; Ondracek, M.; Jelinek, P.; Giessibl, F. J. *Phys. Rev. Lett.* **2013,** *111,* 126103. doi:10.1103/PhysRevLett.111.126103
20. Federici Canova, F.; Kawai, S.; de Capitani, C.; Kan’no, K.-i.; Glatzel, T.; Such, B.; Foster, A. S.; Meyer, E. *Phys. Rev. Lett.* **2013,** *110,* 203203. doi:10.1103/PhysRevLett.110.203203
21. Yurtsever, A.; Fernández-Torre, D.; González, C.; Jelínek, P.; Pou, P.; Sugimoto, Y.; Abe, M.; Pérez, R.; Morita, S. *Phys. Rev. B* **2012,** *85,* 125416. doi:10.1103/PhysRevB.85.125416
22. Welker, J.; Giessibl, F. J. *Science* **2012,** *336,* 444–449. doi:10.1126/science.1219850
23. Welker, J.; Weymouth, A. J.; Giessibl, F. J. *ACS Nano* **2013,** *7,* 7377–7382. doi:10.1021/nn403106v
24. Chiutu, C.; Sweetman, A. M.; Lakin, A. J.; Stannard, A.; Jarvis, S.; Kantorovich, L.; Dunn, J. L.; Moriarty, P. *Phys. Rev. Lett.* **2012,** *108,* 268302. doi:10.1103/PhysRevLett.108.268302
25. Custance, O.; Perez, R.; Morita, S. *Nat. Nanotechnol.* **2009,** *4,* 803–810. doi:10.1038/nnano.2009.347
26. Pou, P.; Ghasemi, S. A.; Jelinek, P.; Lenosky, T.; Goedecker, S.; Perez, R. *Nanotechnology* **2009,** *20,* 264015. doi:10.1088/0957-4484/20/26/264015
27. Campbellová, A.; Ondráček, M.; Pou, P.; Pérez, R.; Klapetek, P.; Jelínek, P. *Nanotechnology* **2011,** *22,* 295710. doi:10.1088/0957-4484/22/29/295710
28. Jarvis, S.; Sweetman, A.; Bamidele, J.; Kantorovich, L.; Moriarty, P. *Phys. Rev. B* **2012,** *85,* 235305. doi:10.1103/PhysRevB.85.235305
29. Hoffmann, R.; Weiner, D.; Schirmeisen, A.; Foster, A. S. *Phys. Rev. B* **2009,** *80,* 115426. doi:10.1103/PhysRevB.80.115426
30. Foster, A.; Shluger, A.; Barth, C.; Reichling, M. Contrast Mechanisms on Insulating Surfaces. In *Noncontact Atomic Force Microscopy;* Morita, S.; Mayer, E.; Wiesendanger, R., Eds.; Springer: Berlin, Heidelberg, 2002; pp 305–348.
31. Kantorovich, L. N.; Trevethan, T. *Phys. Rev. Lett.* **2004,** *93,* 236102. doi:10.1103/PhysRevLett.93.236102
32. Hoffmann, P. M.; Jeffery, S.; Pethica, J.; Özgür Özer, H.; Oral, A. *Phys. Rev. Lett.* **2001,** *87,* 265502. doi:10.1103/PhysRevLett.87.265502
33. Hoffmann, R.; Baratoff, A.; Hug, H. J.; Hidber, H. R.; Löhneysen, H. V.; Güntherodt, H.-J. *Nanotechnology* **2007,** *18,* 395503. doi:10.1088/0957-4484/18/39/395503
34. Ghasemi, S. A.; Goedecker, S.; Baratoff, A.; Lenosky, T.; Meyer, E.; Hug, H. J. *Phys. Rev. Lett.* **2008,** *100,* 236106. doi:10.1103/PhysRevLett.100.236106
35. Kawai, S.; Glatzel, T.; Such, B.; Koch, S.; Baratoff, A.; Meyer, E. *Phys. Rev. B* **2012,** *86,* 245419. doi:10.1103/PhysRevB.86.245419
36. Kawai, S.; Canova, F. F.; Glatzel, T.; Foster, A. S.; Meyer, E. *Phys. Rev. B* **2011,** *84,* 115415. doi:10.1103/PhysRevB.84.115415
37. Bamidele, J.; Li, Y. J.; Jarvis, S.; Naitoh, Y.; Sugawara, Y.; Kantorovich, L. *Phys. Chem. Chem. Phys.* **2012,** *14,* 16250–16257. doi:10.1039/c2cp43121a
38. Labuda, A.; Miyahara, Y.; Cockins, L.; Grütter, P. H. *Phys. Rev. B* **2011,** *84,* 125433. doi:10.1103/PhysRevB.84.125433
39. Li, Y. J.; Nomura, H.; Ozaki, N.; Naitoh, Y.; Kageshima, M.; Sugawara, Y.; Hobbs, C.; Kantorovich, L. *Phys. Rev. Lett.* **2006,** *96,* 106104. doi:10.1103/PhysRevLett.96.106104
40. Sweetman, A.; Jarvis, S.; Danza, R.; Moriarty, P. *Beilstein J. Nanotechnol.* **2012,** *3,* 25–32. doi:10.3762/bjnano.3.3
41. Soler, J. M.; Artacho, E.; Gale, J. D.; Garcia, A.; Junquera, J.; Ordejón, P.; Sánchez-Portal, D. *J. Phys.: Condens. Matter* **2002,** *14,* 2745–2779. doi:10.1088/0953-8984/14/11/302
42. Kantorovich, L.; Hobbs, C. *Phys. Rev. B* **2006,** *73,* 245420. doi:10.1103/PhysRevB.73.245420
43. Sweetman, A.; Danza, R.; Gangopadhyay, S.; Moriarty, P. *J. Phys.: Condens. Matter* **2012,** *24,* 084009. doi:10.1088/0953-8984/24/8/084009
44. Naitoh, Y.; Kinoshita, Y.; Li, Y. J.; Kageshima, M.; Sugawara, Y. *Nanotechnology* **2009,** *20,* 264011. doi:10.1088/0957-4484/20/26/264011
45. Caciuc, V.; Hölscher, H.; Blügel, S.; Fuchs, H. *Phys. Rev. Lett.* **2006,** *96,* 016101. doi:10.1103/PhysRevLett.96.016101
46. Kokalj, A. *Comput. Mater. Sci.* **2003,** *28,* 155–168. doi:10.1016/S0927-0256(03)00104-6

License and Terms

Beilstein Journal
of Nanotechnology

Noise performance of frequency modulation Kelvin force microscopy

Heinrich Diesinger*, Dominique Deresmes and Thierry Mélin

Full Research Paper

Address:
Institut d'Electronique, Microélectronique et Nanotechnologie (IEMN), CNRS UMR 8520, CS 60069, Avenue Poincaré, 59652 Villeneuve d'Ascq, France

Email:
Heinrich Diesinger* - heinrich.diesinger@isen.iemn.univ-lille1.fr

* Corresponding author

Keywords:
dynamic; frequency noise; Kelvin force microscopy; noise performance; phase noise; thermal excitation

Beilstein J. Nanotechnol. **2014,** *5,* 1–18.
doi:10.3762/bjnano.5.1

Received: 29 August 2013
Accepted: 04 December 2013
Published: 02 January 2014

This article is part of the Thematic Series "Noncontact atomic force microscopy II".

Guest Editors: U. D. Schwarz and M. Z. Baykara

Abstract

Noise performance of a phase-locked loop (PLL) based frequency modulation Kelvin force microscope (FM-KFM) is assessed. Noise propagation is modeled step by step throughout the setup using both exact closed loop noise gains and an approximation known as "noise gain" from operational amplifier (OpAmp) design that offers the advantage of decoupling the noise performance study from considerations of stability and ideal loop response. The bandwidth can be chosen depending on how much noise is acceptable and it is shown that stability is not an issue up to a limit that will be discussed. With thermal and detector noise as the only sources, both approaches yield PLL frequency noise expressions equal to the theoretical value for self-oscillating circuits and in agreement with measurement, demonstrating that the PLL components neither modify nor contribute noise. Kelvin output noise is then investigated by modeling the surrounding bias feedback loop. A design rule is proposed that allows choosing the AC modulation frequency for optimized sharing of the PLL bandwidth between Kelvin and topography loops. A crossover criterion determines as a function of bandwidth, temperature and probe parameters whether thermal or detector noise is the dominating noise source. Probe merit factors for both cases are then established, suggesting how to tackle noise performance by probe design. Typical merit factors of common probe types are compared. This comprehensive study is an encouraging step toward a more integral performance assessment and a remedy against focusing on single aspects and optimizing around randomly chosen key values.

Introduction

Surface potential imaging in combination with atomic force microscopy in ultrahigh vacuum is based on the measurement of electrostatic forces in amplitude modulation Kelvin force microscopy (AM-KFM) [1] or the measurement of the electrostatic force gradient in FM-KFM [2], in analogy with the FM mode used in noncontact atomic force microscopy (nc-AFM) [3]. The FM-KFM mode is often favored either because when a higher derivative of the probe–sample capacity is used, it is expected to be more sensitive to the very extremity of the tip [4], or because the use of probes with an increased fundamental resonance frequency makes the use of higher harmonics for simultaneous surface potential imaging inaccessible to the bandwidth of the deflection detector.

Previous studies of noise propagation often retrieve the general expression of frequency noise of a thermally excited harmonic oscillator and are not specific to a PLL based setup, and furthermore, do not extend to the noise in the KFM signal. The pioneer work on nc-AFM, [3] already mentions frequency noise for the first time in the context of nc-AFM, but takes into account only thermal probe excitation noise. Fukuma et al. [5] performed a detailed study on optimizing the probe deflection sensor and compare the measured noise power spectral density (PSD) at the PLL frequency output to the theoretical values derived from both thermal probe excitation and deflection sensor noise. Kobayashi et al. [6] focus on noise propagation in low quality factor (low-Q) environments for the application in liquids. Polesel-Maris et al. [7] studied the noise propagation in both amplitude and phase feedback loops of a nc-AFM as a function of the feedback controller settings, and showed that at a weak probe–surface interaction, the feedback loops can be considered independently whereas at a strong interaction, they become coupled. In our work on the dynamic behavior of AM-KFM [8], we studied the noise propagation from sensor displacement noise to the Kelvin voltage output. Giessibl et al. [9] compared qPlus and length-extension resonator (LER) sensors with respect to four noise sources: thermal excitation, sensor displacement noise, oscillator noise and thermal drift noise. The impact of all noise sources on frequency noise was discussed. Finally, Lubbe et al [10] numerically modeled noise propagation from sensor displacement noise to frequency noise of a PLL based nc-AFM depending on filter settings.

In this work, the noise propagation of a PLL based FM-KFM is studied by measuring and analytically modeling noise at different stages of the setup starting from the beam deflection signal, via the phase detector and the PLL outputs up to the Kelvin output voltage. The concept of noise gain allows for decoupling noise performance from the optimization of bandwidth and stability. It is commonly used in designing operational amplifier circuits. The noise PSD is modeled as if the bandwidth was unlimited and later, the bandwidth is chosen as a function of the acceptable signal fluctuation. This approach is appropriate because (1) increasing the closed loop bandwidth of a stable feedback loop above a certain frequency does not alter the noise PSD shape at the onset up to that frequency, and (2) stability and bandwidth are in many cases, including the described setup, not the bottleneck, i.e., constant gain can easily be achieved up to a frequency above the one at which the total output noise exceeds an acceptable value. The modeled noise PSD is in agreement with the measured one, showing that no significant noise contribution is added by the PLL. Since in FM-KFM the frequency shift signal is shared by both distance and potential control loops, a design rule for choosing the AC modulation frequency is proposed that ensures making best use of the available PLL bandwidth with negligible crosstalk between the loops and that yields equal bandwidth for both loops. The Kelvin output noise reduces to a compact analytic expression in terms of probe merit factors and a criterion for the transition between dominating detector and thermal excitation noise is derived. Noise optimization can then be approached via probe design after identifying the bottlenecks and addressing the respective parameters. The work is an approach toward a more integral view of KFM performance. A limit to optimization is the complicated interdependence of probe and detector parameters that for a practical implementation prevent reaching the ultimate theoretical limit imposed by the uncertainty principle.

Gain and noise gain

For studying the noise propagation across the control loops, the concept of noise gain from OpAmp circuits is adopted. Figure 1

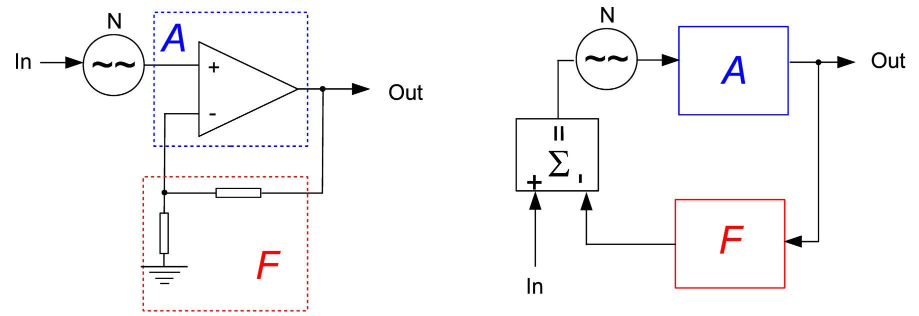

Figure 1: An OpAmp circuit and its equivalent circuit of forward gain *A* and feedback gain *F*.

shows an OpAmp in a typical configuration and its decomposition into forward and feedback gain, adder and noise source. Later on, each of the KFM control loops will be represented by a similar equivalent circuit. Generally, the feedback gain F corresponds to a PI (proportional, integral) controller.

The output signal Out is written as function of the input signal In, the noise A_n and the gains:

$$\mathrm{Out} = \left(\mathrm{In} + A_\mathrm{n}\right)\frac{A}{1+AF} \tag{1}$$

In this case the signal gain is equivalent to the noise gain

$$H_\mathrm{sig} = H_\mathrm{noise} = \frac{A}{1+AF} \approx \frac{1}{F} \tag{2}$$

Depending on where the noise generator is inserted in the loop, the gains for signal and noise can be different as will be shown later. The approximation, although valid only in the operating bandwidth below the closed loop cutoff frequency, is widely accepted as the noise gain. The reason will be explained later.

The PLL controller

Figure 2 shows the setup of the PLL and the attribution of its components to the blocks A and F similar to Figure 1. The input is the resonance frequency variation Δf of the tip, which is subject to external influence (van-der-Waals or electrostatic tip–sample interaction), and which is to be tracked by a numerically controlled oscillator (NCO) that drives the piezo dither. To match the oscillator to the resonance frequency of the tip, the deflection of the tip is detected, and the phase shift with respect to the drive signal is determined by a lock-in amplifier. The phase shift is compared to a setpoint, and the error signal is amplified by a PI controller that controls the NCO with the objective of keeping the drive frequency matched to the resonance frequency. A perturbation can be injected to an input of a signal adder (as indicated) to study the loop response, or by modulating the resonance frequency of the probe, e.g., by exposing it to an electric field, which shall both yield the same closed loop response.

Phase detector gain - phase as function of frequency shift

We shall study the phase difference between a passive oscillator and a frequency modulated drive signal. If a resonator described by a quality factor Q and a resonance frequency f_0 is excited by a frequency modulated drive force with an excursion f_exc and a modulation frequency f_pert:

$$F = F_0 \exp\left\{2\pi i\left[f_0 + f_\mathrm{exc}\exp\left(2\pi i f_\mathrm{pert} t\right)\right]t\right\} \tag{3}$$

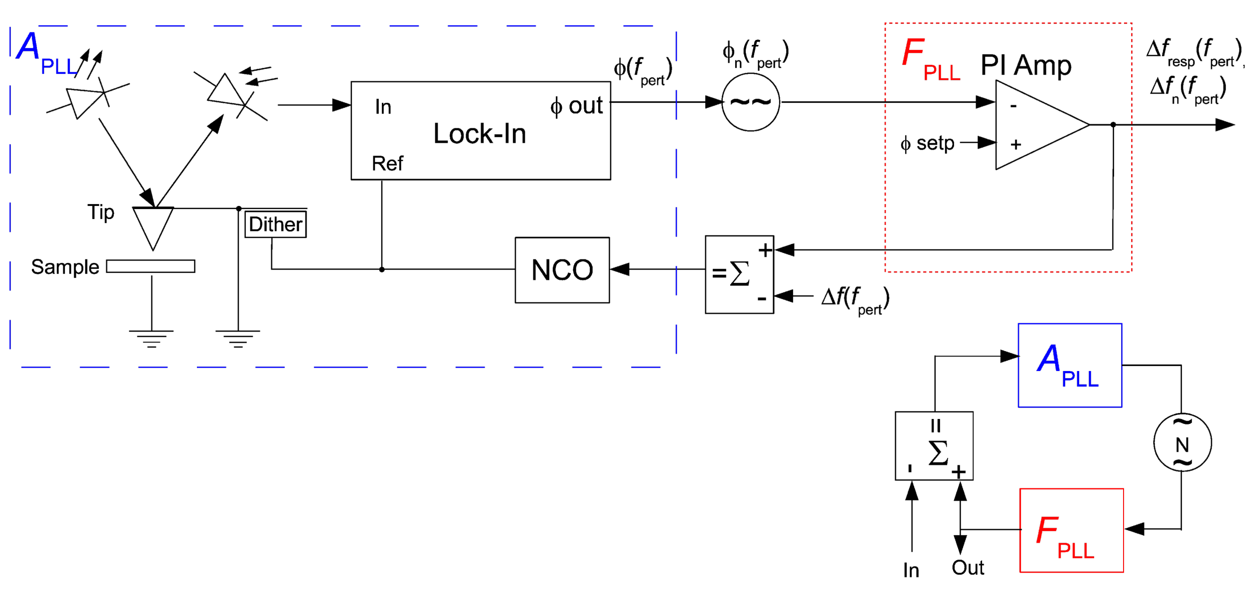

Figure 2: PLL: in the blue box, the components belonging to the forward gain A_PLL, i.e., NCO, probe, optical beam detection, and lock-in amplifier used as phase detector, and in the red box, the PI controller representing the feedback gain F_PLL, comparable to Figure 1. At the lower right, the equivalent circuit similar to Figure 1.

The phase shift is, without any assumptions about frequency excursion, width of the resonance peak, or modulation frequency exactly:

$$\phi = \arctan\left[\frac{2Qf_{\text{exc}}/f_0}{\sqrt{1+\left(2Qf_{\text{exc}}/f_0\right)^2}}\right]\cdot\frac{1-i2Qf_{\text{pert}}/f_0}{\sqrt{1+\left(2Qf_{\text{pert}}/f_0\right)^2}} \quad (4)$$

This can be derived heuristically by knowing that the phase is the integral over frequency difference in the regime of high modulation frequency f_{pert}, but that the phase shift is capped by the extrema of the arctan function in the regime of steady excitation since one oscillator is passive. The same result had been found by Portes et al. [11] by solving the differential oscillation equation. This general equation yields the approximations for particular cases below that are so frequently found in the literature. It is noteworthy that the phase is generally complex, i.e., the phase difference is itself dephased with respect to the frequency modulation at f_{pert}.

For this result, it is irrelevant whether the frequency difference is the result of applying a perturbation at the entrance of the NCO or of detuning the cantilever frequency. Since our digital AFM controller does not provide the option of modulating the excitation frequency, we will study the PLL response by perturbing the resonance frequency of the tip by applying a voltage between tip and sample. The first task is to determine the frequency shift induced as a function of the voltage and the fixed tip–sample distance of some tens of nanometers for the static case $f_{\text{pert}} = 0$.

Figure 3 shows the frequency shift Δf as a function of the voltage, measured by acquiring a resonance curve per voltage value (black squares and black solid line parabola fit). It also shows the static phase shift under excitation at constant frequency f_0 (red squares), which is then shifted from the actual resonance by Δf due to the influence of the electric field. Then, Equation 4 reduces to

$$\phi = \arctan\left(\frac{2Q\Delta f}{f_0}\right) \quad (5)$$

The red solid line is an arctan fit according to Equation 5. Note that the two branches of arctan functions do not intersect exactly at zero phase. This occurs if the resonance frequency of the tip drifts above the excitation frequency during the measurement. Consequently, the possible phase excursion may be higher than 90°.

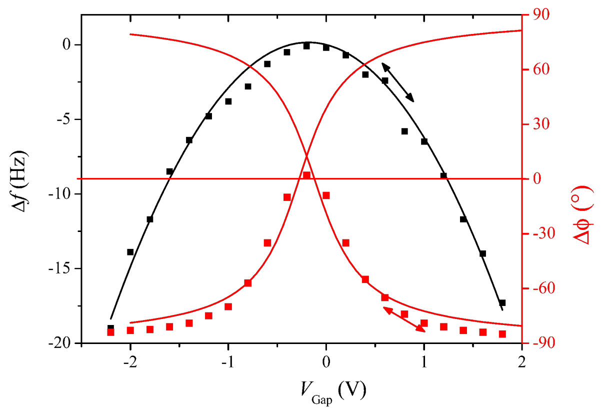

Figure 3: Resonance frequency shift resulting from applying a voltage between a retracted tip and sample (black, left scale) and phase shift resulting of exciting at constant frequency (red, right scale). The arrows indicate AC and DC bias applied in the dynamic study of the phase modulation, leading to Figure 4.

Next, the forward response of the PLL, A_{PLL}, is studied dynamically. This experiment has to be performed by applying a frequency modulation indirectly since the integrated lock-in module does not allow transfer function measurements by introducing a Δf perturbation. For doing so, the tip is excited at constant frequency f_0 = 61.835 kHz. Then, the resonance frequency is modulated by applying a bias containing both a DC and a smaller AC component of 0.8 V and 0.2 V respectively, and the phase detector output is recorded as function of modulation frequency of a small AC bias. We set the DC and the AC voltage components to aim at a frequency excursion of around $f_{\text{exc}} \approx 2$ Hz as indicated by the arrow in Figure 3. The result is the spectrum shown in Figure 4 by black squares, giving the phase shift as a function of the modulation frequency.

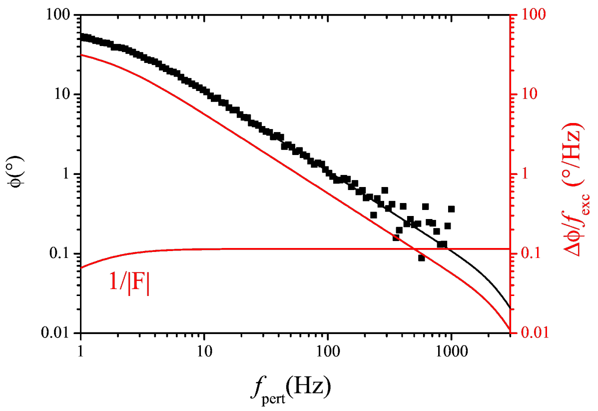

Figure 4: Phase detector output as function of modulation frequency (black squares), fitted with Equation 4, using f_{exc} = 1.9 Hz, multiplied by a Butterworth lowpass function with cutoff at 2.5 kHz. Also shown (red line), the gain A_{PLL} according to Equation 7, and the reciprocal feedback gain $1/F_{\text{PLL}}$ according to Equation 8.

It is fitted with Equation 4 multiplied by a lowpass function of the phase detector output filtering, a 2nd order Butterworth with $f_{\mathrm{c,LP}} = 2500$ Hz cutoff frequency.

$$H_{\mathrm{LP}}\left(f_{\mathrm{pert}}\right) = \frac{1}{1+\frac{\sqrt{2}if_{\mathrm{pert}}}{f_{\mathrm{c,LP}}} - \frac{f_{\mathrm{pert}}^{2}}{f_{\mathrm{c,LP}}^{2}}} \qquad (6)$$

The best fit is obtained for an excursion of $f_{\mathrm{exc}} = 1.9$ Hz and the previously found values for $f_0 = 61.835$ kHz and $Q = 22800$ (see Experimental section).

For the following, a linear conversion gain of the phase detector must be defined in terms of phase divided by frequency excursion, as function of modulation frequency. Before we can divide Equation 4 by f_{exc}, it is compulsory to approach the arctan function by its argument for small excursion, $f_{\mathrm{exc}} < f_0/(2Q)$, since the definition of a gain implies a linear dependence. Then, Equation 4 simplifies and dividing by the excursion yields:

$$\begin{aligned} A_{\mathrm{PLL}}\left(f_{\mathrm{pert}}\right) &= \frac{\phi}{f_{\mathrm{pert}}}\left(f_{\mathrm{pert}}\right)\left[\frac{\circ}{\mathrm{Hz}}\right] \\ &= \frac{180}{\pi}\cdot\frac{2Q/f_0}{1+i2Qf_{\mathrm{pert}}/f_0}\cdot H_{\mathrm{LP}} \end{aligned} \qquad (7)$$

The approximation of the arctan function by its argument for small excursion is at the very limit of validity here because $f_0/(2Q) = 1.35$ Hz and $f_{\mathrm{exc}} = 1.9$ Hz. However when the phase detector is ulteriorly used in the closed PLL loop within its tracking bandwidth, the error is negligible: The closed loop gain is near unity in this range, meaning that the oscillator follows the (detuned) resonance frequency, and the frequency error remains at a fraction of the frequency excursion. The forward gain Equation 7 will be used to model both the closed loop PLL response and the shape of frequency noise PSD. It is also shown on Figure 4 as red curve. At the same time, the reciprocal value of the feedback gain F_{PLL} is displayed. The feedback circuit is a PI (proportional, integral) amplifier with the following response F_{PLL}:

$$\begin{aligned} F_{\mathrm{PLL}}\left(f_{\mathrm{pert}}\right) &= \frac{f_{\mathrm{exp}}}{\phi}\left(f_{\mathrm{pert}}\right) \\ &= P_{\mathrm{PLL}}\left(1+\frac{1}{i2\pi f_{\mathrm{pert}}\tau_{\mathrm{PLL}}}\right) \end{aligned} \qquad (8)$$

The controller software automatically sets the time constant of the phase locked loop PI amplifier equal to the time constant of the phase detector lowpass function, $\tau_{\mathrm{PLL}} = 2Q/2\pi f_0$, and the P gain such that the crossing with the forward gain occurs at the chosen PLL bandwidth of 1 kHz.

The 2.5 kHz lowpass H_{LP} of the phase detector output is also a consequence of the choice of 1 kHz PLL bandwidth and automatically set by the controller. In this case, the feedback parameters were $P_{\mathrm{PLL}} = 8.73$ Hz/° and $\tau_{\mathrm{PLL}} = 112$ ms.

PLL noise

First, a noise spectrum is measured at the output of the photodetector, without probe excitation. It is shown in Figure 5.

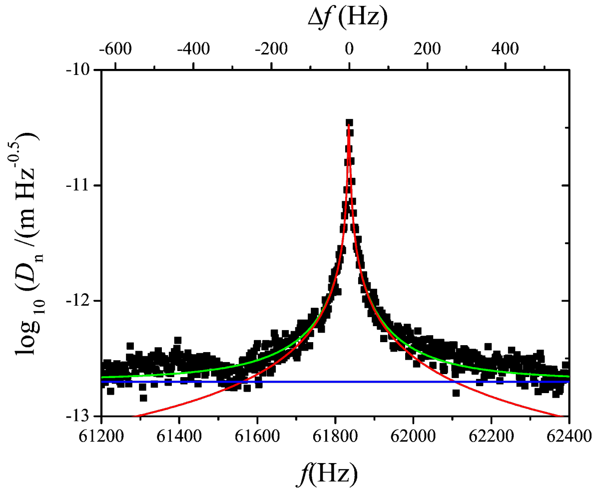

Figure 5: Noise PSD at the photodetector output. Fiteed with Equation 9 (green) and decomposition into thermal excitation noise (red) and constant detector noise $z_{\mathrm{n,S}}$ (blue).

The deflection noise spectrum $D_{\mathrm{n}}(f)$ contains a component due to thermal probe excitation plus a component due to detector output noise. The latter can be assumed to be constant over the relatively small frequency interval of the spectrum. The respective power spectral densities (PSD) in units of $\mathrm{m}/\sqrt{\mathrm{Hz}}$ are uncorrelated and hence add in quadrature. The noise PSD $D_{\mathrm{n}}(f)$ is therefore described by a quadrature sum of detector noise $z_{\mathrm{n,S}}$ and a Lorentzian component of the same Q and f_0 as the resonance curve previously determined by the microscope controller:

$$D_{\mathrm{n}}\left(f\right)\left[\frac{\mathrm{m}}{\sqrt{\mathrm{Hz}}}\right] = \sqrt{z_{\mathrm{n,S}}^{2} + \frac{4k_{\mathrm{B}}T}{\pi f_0 Qk\left[\left(1-\frac{f^2}{f_0^2}\right)+\frac{f^2}{Q^2 f_0^2}\right]}} \qquad (9)$$

A curve fit with Equation 9 yields $k = 1.2$ N/m, $Q = 22800$, $f_0 = 61835$ Hz and $z_{\mathrm{n,S}} = 2\cdot 10^{-13}\ \mathrm{m}/\sqrt{\mathrm{Hz}}$.

The decomposition is also indicated in Figure 5. The optical beam deflection conversion gain leading to the scale was calibrated by using the method of reduced frequency shift [12] and was 0.15 nm/mV. The principle of this method is to maintain a constant reduced frequency shift by varying simultaneously the excitation amplitude and the frequency shift setpoint of the noncontact mode following a certain algorithm. Then, the lower turning point of the tip remains equidistant from the sample surface, and the motion of the z-piezo represents the shift of oscillation amplitude as response to varying excitation amplitude.

Next, the noise propagation throughout PLL and Kelvin loop are studied. In order to be able to model the noise by the approach of noise gains as in Figure 1, it is necessary to present it by a noise source inserted between blocks A_{PLL} and F_{PLL}. We shall now calculate how the displacement noise at the photodetector output transforms into phase noise at the phase detector output, which is represented by the phase noise generator of Figure 2. Figure 6 shows the vector diagram in the complex plane of a signal $D_0\cos(2\pi f_0 t)$, representing the tip deflection, plus a spurious small signal $a\cos(2\pi f_1 t)$ as a representation of the deflection detector noise. If demodulated by a lock-in amplifier at f_0, in the reference system rotating at f_0, the D_0 vector is stationary and a is rotating around the end of D_0 at $f_1 - f_0$.

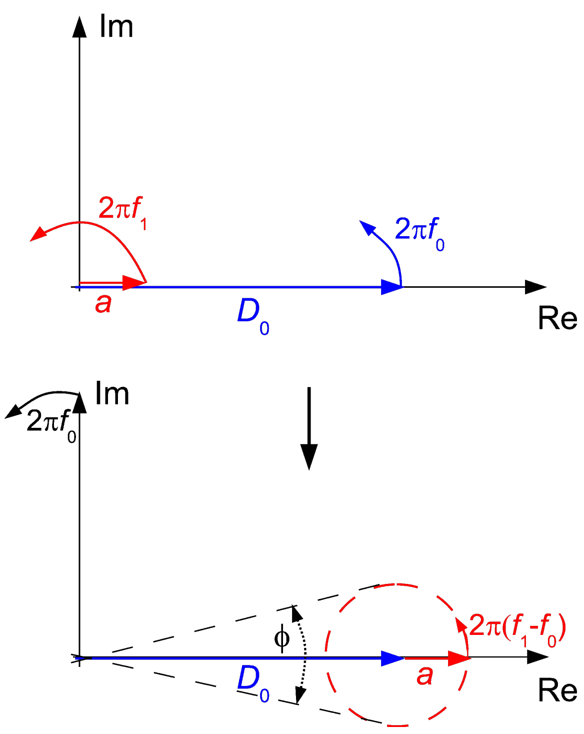

Figure 6: Vector diagram showing the impact of amplitude noise on phase noise in the complex plain: main vector and a small perturbation of amplitudes D_0 and a and at frequencies f_0 and f_1 respectively (upper drawing) and their resulting sum in the reference plane rotating at f_0 (lower drawing).

The imaginary projection is then

$$Y(t) = a\sin\left(2\pi\left[f_1 - f_0\right]t\right) \tag{10}$$

The phase is for $a \ll D_0$

$$\phi(t)[\mathrm{rad}] = \frac{a}{D_0}\sin\left(2\pi\left[f_1 - f_0\right]t\right) \tag{11}$$

A small signal vector a at $f_1 = f_0 + f_{\mathrm{pert}}$ causes a phase oscillation at f_{pert}. If a was rotating at $f_1 = f_0 - f_{\mathrm{pert}}$, it would also cause a phase oscillation at f but with opposite sign, and hence two vectors a at opposite difference frequencies would add arithmetically and cancel. Regarding the phase noise at a frequency f_{pert}, the spurious superimposed oscillations are replaced by the respective noise densities at frequencies $D_{\mathrm{n}}(f_0 \pm f_{\mathrm{pert}})[\mathrm{V}/\sqrt{\mathrm{Hz}}]$. Since the two noise components are uncorrelated, the densities add in quadrature:

$$\begin{aligned} X_{\mathrm{n}}^2\left(f_{\mathrm{pert}}\right) &= Y_{\mathrm{n}}^2\left(f_{\mathrm{pert}}\right) \\ &= \frac{1}{2}\left[D_{\mathrm{n}}^2\left(f_0 + f_{\mathrm{pert}}\right) + D_{\mathrm{n}}^2\left(f_0 - f_{\mathrm{pert}}\right)\right] \end{aligned} \tag{12}$$

The factor 1/2 applies because half of the power spectral density (PSD) is projected onto each real and imaginary axis in the complex plane. In analogy with Equation 11, the phase noise PSD ϕ_{n}, becomes:

$$\phi_{\mathrm{n}}^2\left(f_{\mathrm{pert}}\right)\left[\mathrm{rad}^2/\mathrm{Hz}\right] = \frac{1}{2D_0^2}\left[D_{\mathrm{n}}^2\left(f_0 + f_{\mathrm{pert}}\right) + D_{\mathrm{n}}^2\left(f_0 - f_{\mathrm{pert}}\right)\right] \tag{13}$$

Due to the symmetry of the Lorentzian with its high quality factor, it is sufficient to use one branch of the Lorentzian, and expressed in degrees we obtain:

$$\phi_{\mathrm{n}}\left(f_{\mathrm{pert}}\right)\left[\frac{\circ}{\sqrt{\mathrm{Hz}}}\right] = \frac{180}{\pi}\frac{D_{\mathrm{n}}\left(f_0 + f_{\mathrm{pert}}\right)}{D_0} \tag{14}$$

This expression gives the phase noise with the use of a lock-in amplifier. It had been derived in a similar way by Rast et al. [13]. It may not be valid for other phase comparators, e.g., edge triggered ones. It is basically a translation by f_0 of the deflection noise PSD. The translation of the Lorentzian component of the deflection noise yields a first order lowpass with respect to f_{pert} with a cutoff frequency $f_0/(2Q)$, whereas the constant detector shot noise $z_{\mathrm{n,S}}$ is invariant under translation, yielding for the total phase noise the quadrature sum:

$$\phi_{\mathrm{n}}\left(f_{\mathrm{pert}}\right)\left[\frac{^\circ}{\sqrt{\mathrm{Hz}}}\right]=\frac{180}{\pi D_0}\sqrt{z_{\mathrm{n,S}}^2+\frac{4k_{\mathrm{B}}TQ}{\pi f_0 k\left[1+\left(\frac{2Qf_{\mathrm{pert}}}{f_0}\right)^2\right]}} \quad (15)$$

Figure 7 shows the measured phase noise at the phase detector output in open PLL, and in green the fit according to Equation 15. The parameters $z_{\mathrm{n,S}}$, f_0, Q and k were kept identical to the ones of the curve fit of Figure 5, whereas the oscillation amplitude had to be adjusted to $D_0 = 0.85$ nm. The red and blue lines show the fit decomposed into thermal excitation and detector noise components, respectively.

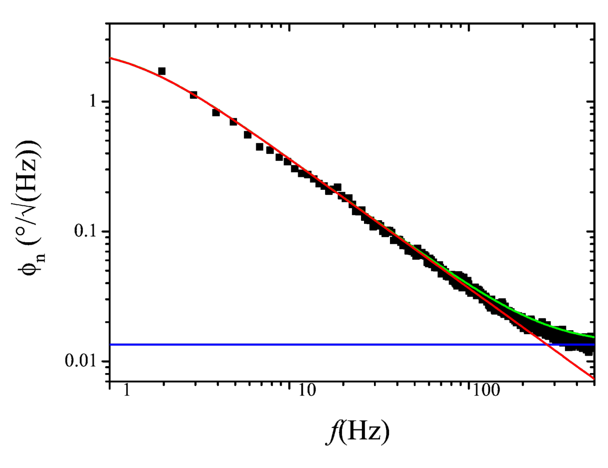

Figure 7: Phase noise PSD at the lock-in phase detector output in open PLL loop and under probe excitation at D_0 = 0.75 nm: measured (black squares), fitted according to Equation 15 (green), and decomposed into detector noise (blue, constant) and thermal excitation contribution (red, lowpass) according to the two terms of Equation 15.

PLL closed loop gain

With the known transfer functions A_{PLL} from Equation 7 and F from Equation 8, the closed loop response of the PLL can be computed. For the equivalent circuit of Figure 2, we find a signal gain

$$H_{\mathrm{PLL,sig}}=\frac{A_{\mathrm{PLL}}F_{\mathrm{PLL}}}{1+A_{\mathrm{PLL}}F_{\mathrm{PLL}}} \quad (16)$$

which is plotted along with the measured response in Figure 8. The computation is performed on complex transfer functions and the plot only shows the modulus of the result. Note that in Equation 16, A_{PLL} and F_{PLL} are complex and only in the end of the computation, the module is calculated.

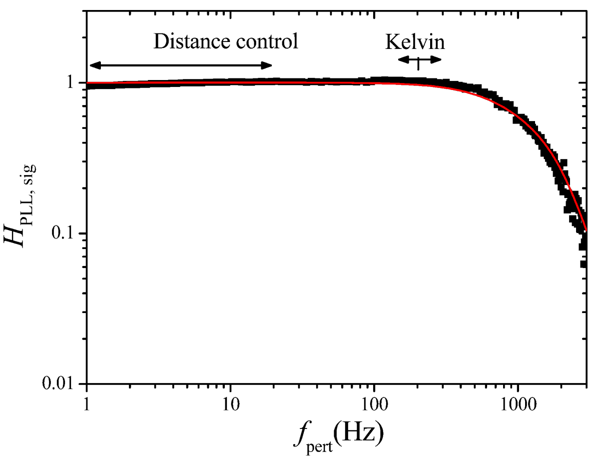

Figure 8: Closed loop PLL response: measured (black squares) and computed (red line) according to Equation 16.

PLL closed loop noise

With the known forward and feedback gains of the PLL loop, the closed loop noise output spectrum f_{n} of the PLL is modeled. Since the noise source of Figure 2 is located differently between blocks A and F than that of Figure 1, the noise gain is different from the signal gain in contrast to the operational amplifier example, and writes

$$H_{\mathrm{PLL,noise}}=\frac{F_{\mathrm{PLL}}}{1+A_{\mathrm{PLL}}F_{\mathrm{PLL}}}\approx\frac{1}{A_{\mathrm{PLL}}} \quad (17)$$

The frequency noise PSD f_{n} at the output of the PLL is

$$f_{\mathrm{n}}\left(f_{\mathrm{pert}}\right)=\phi_{\mathrm{n}}\left(f_{\mathrm{pert}}\right)H_{\mathrm{PLL,noise}}\left(f_{\mathrm{pert}}\right) \quad (18)$$

The PLL phase detector output noise PSD modeled by Equation 15 is used as ϕ_{n} input. The calculation of the noise gain is also performed on complex gains.

Figure 9 shows the PLL closed loop PSD of noise f_{n}, (black), up to 500 Hz, the limit of the integrated spectral analyzer, and the numerically computed noise PSD (green) obtained from phase noise and gains A_{PLL} and F_{PLL}. Furthermore, the noise PSD decomposed into thermal noise (red) and sensor noise (blue) is computed according to the approximation of Equation 17 (see Equation 20 below).

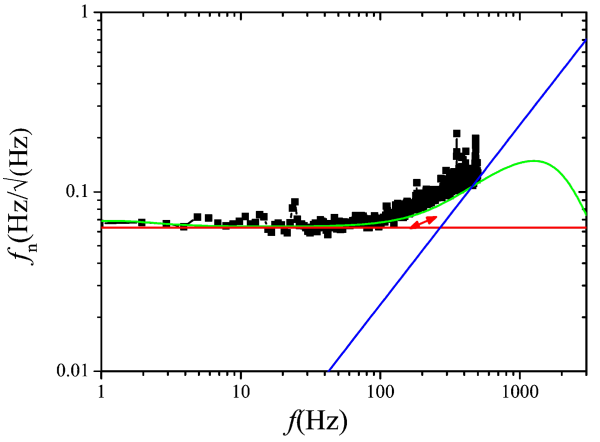

Figure 9: Output noise PSD of the PLL in closed loop configuration: measured (black squares) and modeled according to Equation 18 (green) from the previously determined gains and phase noise spectrum. The decomposition into thermal excitation contribution (red, constant) and detector noise (blue, rising) are also shown; the decomposed spectra were modeled with simplified noise gains $H_{\text{noise,PLL}} \approx 1/|A_{\text{PLL}}|$.

Regarding the approximation of Equation 17, we note that it is valid in the range in which the closed loop gain is unity and $|A_{\text{PLL}}F_{\text{PLL}}| >> 1$. Hence, the approximation does not predict the roll-off of the noise PSD beyond the closed loop bandwidth. Instead, it predicts infinite rise of the noise following the blue line of Figure 9. To use the approximation $1/A_{\text{PLL}}$, denoted "noise gain", rather than the exact computation is the idea of the noise gain formalism and is justified by the following arguments:

- The roll-off of the noise PSD cannot be exploited anyway: if the loop is used beyond its cutoff frequency, it attenuates the signal as much as the noise. The image acquisition circuitry that samples data into pixels has an anti-aliasing low-pass filter with a cut-off frequency of half the sampling rate. There is no interest of using a loop bandwidth below that cut-off frequency since the response of the loop would then smooth the image at the same rate as it would smooth out noise.
- If the loop is inserted into a surrounding loop, then the closed loop gain of the former becomes the forward gain of the latter; consequently, the roll-off has two effects that compensate each other: first, it cuts off the noise PSD, but second, since the reciprocal of the inner loop closed loop gain becomes itself the (approximate) noise gain of the surrounding loop, it would amplify the noise PSD by as much as it had been attenuated before. Therefore, it is convenient to neglect the cutoff in noise propagation.
- Last, it is noteworthy that the closed loop cutoff frequency has no influence on the noise PSD at the onset below that cutoff frequency, e.g., the noise PSD from zero to 300 Hz is the same irrespective of whether the closed loop cutoff frequency is 500 Hz or 1 kHz. Therefore, it is convenient to first calculate the noise PSD as if the closed loop bandwidth was infinite, to determine over which frequency range the noise PSD can be integrated without exceeding an acceptable total signal fluctuation, and to limit bandwidth and sampling rate a posteriori. It will be discussed later to what extent the approach is feasible and whether stability issues can become the bottleneck.

Therefore among engineers the noise gain formalism is widely used but to our knowledge has not yet been applied to noise propagation in scanning probe microscopy. The PLL output noise PSD is now obtained using the noise gain formalism:

$$f_n\left(f_{\text{pert}}\right) = \frac{\phi_n}{A_{\text{PLL}}} \qquad (19)$$

Regarding the PLL forward gain A_{PLL}, Equation 7, it is noteworthy that the open loop gain of the phase as function of frequency excursion has the same frequency dependence as the thermal contribution of the phase noise, second term of Equation 15, i.e., a first order lowpass with cutoff frequency $f_0/(2Q)$. The quotient Equation 19 yields, when inserting the phase noise PSD from Equation 15 and PLL forward gain A_{PLL} from Equation 7:

$$f_n\left(f_{\text{pert}}\right) = \sqrt{\frac{z_{n,S}^2}{D_0^2}\frac{1+4Q^2 f_{\text{pert}}^2/f_0^2}{4Q^2/f_0^2} + \frac{k_B T f_0}{\pi k D_0^2 Q}} \qquad (20)$$

Hence, the thermal part of the frequency noise, is exactly constant over a range from zero to infinite frequency, which is the third term. It was derived by theorists and resumed by Giessibl and Kobayashi that a thermally excited harmonic oscillator is expected to have constant frequency noise PSD [5,14]. Here, we have provided the comprehensive step-by-step evidence for an experimental PLL setup with a driven passive resonator, yielding the same result. Controversial debate about the frequency noise of comparable PLL setups is still ongoing [15,16].

The sensor noise contribution is split into two contributions, the first term without frequency dependence, the second rising with f_{pert} above $f_0/(2Q)$, meaning above 1.35 Hz in our case, below which it has a plateau. We state that Equation 20 is identical to

Equation 18 of reference [6], up to a factor of 2 in front of the sensor noise contributions. The first frequency independent term of our sensor noise has been referred to as "oscillator noise" by Kobayashi which was later also adopted by Giessibl [9]. Following our approach, it is arising merely from propagation of sensor noise throughout the PLL. This frequency-independent component of sensor noise is only found in modeling if the PLL forward gain, Equation 7, is derived exactly with the $f_0/(2Q)$ corner frequency, rather than an approximate $1/f_{\mathrm{pert}}$ behavior. It is generally negligible in high-Q environments as in our setup. The good agreement between computed noise and experiment shows that here the frequency noise can be attributed solely to thermal excitation and sensor noise.

The Kelvin loop

Figure 10 shows the setup of the Kelvin loop. The closed PLL loop of the previous section now presents a small part of the forward gain. The A_{K} block further contains a lock-in amplifier working at a frequency lower than the bandwidth of the PLL that modulates the gap voltage. It superposes an AC signal V_{mod} at a frequency within the operating range of the PLL and detects the resonance frequency modulation of the tip at this frequency. The output of block A_{K} is the demodulated frequency shift $\Delta f_{\mathrm{demod}}$, while the input is the V_{K} component of the tip bias. The tip voltage superposition has two purposes: first to extract the polarity information of the gap voltage mismatch, and second to share the PLL bandwidth between Kelvin and distance controller: van-der-Waals and electrostatic interaction both shift the resonance frequency. A modulation of Δf at a frequency within the bandwidth of the distance controller would cause the distance controller to retract the tip periodically. Therefore, by modulation and demodulation, the electrostatically induced tip frequency modulation is translated in a range above the cutoff frequency of the distance controller, but below the cutoff frequency of the PLL.

The contact potential difference (CPD) between tip and sample is indicated by a voltage applied to the sample. It may be due to a work function difference between the sample and the tip or due to a sample to which a bias is applied. The objective is to cancel the CPD by applying a Kelvin voltage to the tip such that CPD − V_{K} = 0.

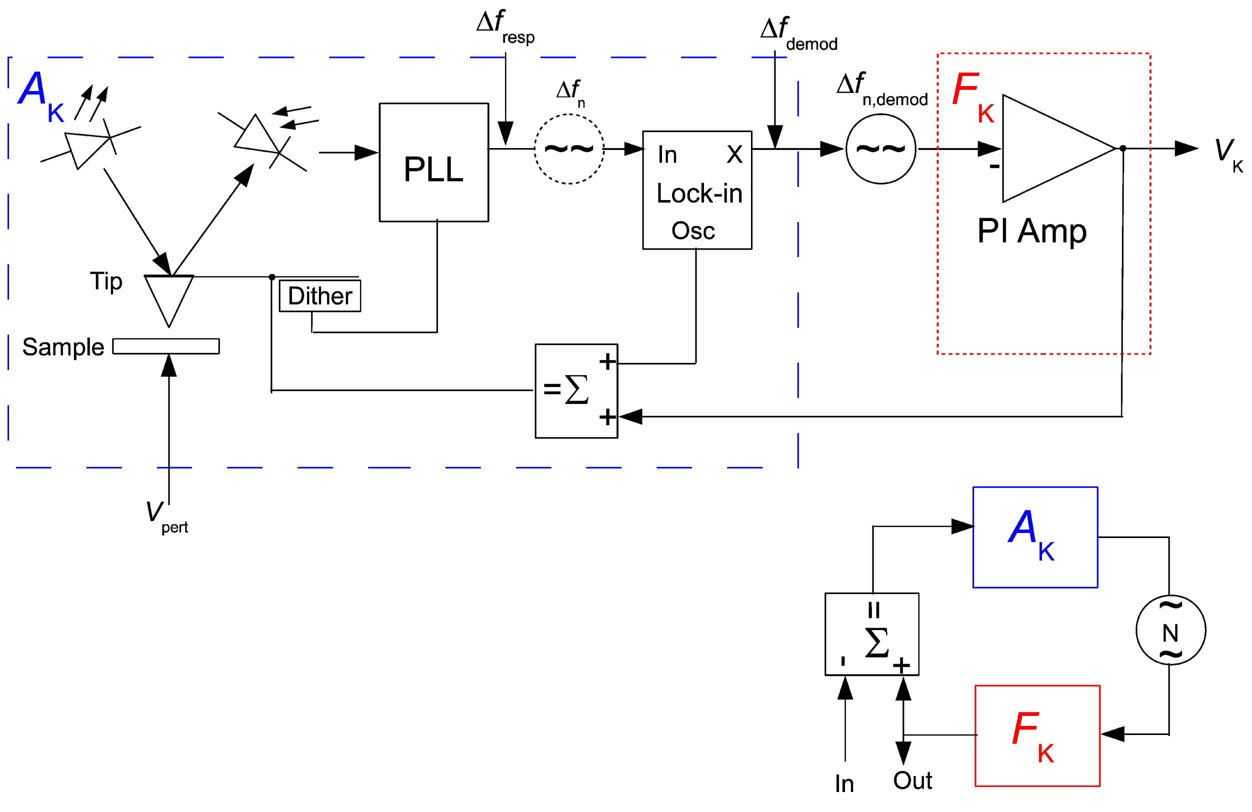

Figure 10: Kelvin loop and its equivalent circuit: the forward gain A_{K} is the transfer function between V_{pert} and $(\Delta f)_{\mathrm{demod}}$ and contains the previously studied closed loop PLL, a Kelvin lock-in amplifier, and a signal adder (components in the blue box). The feedback gain F_{K} is a PI amplifier (red) that adjusts the tip voltage V_{K} to compensate the CPD. The output noise of the PLL controller is projected onto the *X* output of the Kelvin lock-in amplifier to facilitate the representation in an equivalent feedback circuit (lower right) for the calculation of noise in the Kelvin signal.

Open loop forward gain

The CPD, the Kelvin voltage, V_K, and the AC voltage, V_mod, cause an electrostatic field gradient that alters the resonance frequency:

$$\Delta f_\mathrm{resp}(t)=\frac{f_0}{2k}\frac{d^2C}{dz^2}\left[\mathrm{CPD}-V_\mathrm{K}-V_\mathrm{mod}\cos\left(2\pi f_\mathrm{mod}t\right)\right]^2 \quad (21)$$

The assumption of a constant d^2C/dz^2 is an approximation for oscillation amplitudes smaller than the mean tip–sample distance. However, the voltage dependence is valid even if this condition is not exactly met. By expanding the square bracket of Equation 21, one gets

$$\begin{aligned}\Delta f_\mathrm{resp}(t)=\frac{f_0}{2k}\frac{d^2C}{dz^2}&[\left(\mathrm{CPD}-V_\mathrm{K}\right)^2\\ &-2\left(\mathrm{CPD}-V_\mathrm{K}\right)V_\mathrm{mod}\cos\left(2\pi f_\mathrm{mod}t\right)\\ &+\frac{1}{2}V_\mathrm{mod}^2\left(1+\cos\left(4\pi f_\mathrm{mod}t\right)\right)]\end{aligned} \quad (22)$$

The term of interest is the mixed term at f_mod since it contains amplitude and sign of the CPD. It is detected by demodulating at f_mod. The PLL response $H_\mathrm{PLL}(f_\mathrm{mod})$ applies before the demodulation. The static forward gain $A_\mathrm{K,DC}$ is:

$$A_\mathrm{K,DC}=\frac{\Delta f_\mathrm{demod}}{\Delta V_\mathrm{K}}=-\frac{f_0}{k}\frac{d^2C}{dz^2}V_\mathrm{mod}H_\mathrm{PLL}\left(f_\mathrm{mod}\right) \quad (23)$$

The static forward gain is determined with engaged distance control loop while using a setpoint of $\Delta f = -5$ Hz with V_mod = 300 mV, and f_mod = 200 Hz. The demodulated error signal is then measured as a function of ΔV_K, shown in Figure 11. The gain is 25 Hz/V.

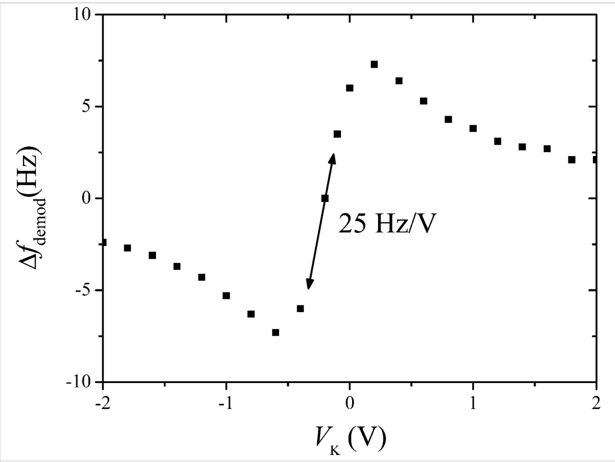

Figure 11: Measurement of static forward gain of the open Kelvin loop.

Next, the forward gain is studied dynamically. Therefore, the DC voltage mismatch CPD − V_K is replaced by an AC voltage $V_\mathrm{pert}\cos(2\pi f_\mathrm{pert}t)$ and Equation 22 becomes

$$\begin{aligned}\Delta f_\mathrm{resp}(t)=-\frac{f_0}{2k}\frac{d^2C}{dz^2}&[\frac{1}{2}\left(V_\mathrm{pert}\right)^2\left(1+\cos\left(4\pi f_\mathrm{pert}t\right)\right)\\ &-2V_\mathrm{pert}V_\mathrm{mod}\cos\left(2\pi f_\mathrm{mod}t\right)\cos\left(2\pi f_\mathrm{pert}t\right)\\ &+\frac{1}{2}V_\mathrm{mod}^2\left(1+\cos\left(4\pi f_\mathrm{mod}t\right)\right)]\end{aligned} \quad (24)$$

The mixed term will transform into two satellites at $f_\mathrm{mod} \pm f_\mathrm{pert}$ and Equation 23 becomes

$$\begin{aligned}A_\mathrm{K}\left(f_\mathrm{pert}\right)&=\frac{\Delta f_\mathrm{demod}}{\Delta V_\mathrm{pert}}\left(f_\mathrm{pert}\right)\\ &=-\frac{f_0}{k}\frac{d^2C}{dz^2}V_\mathrm{mod}H_\mathrm{lockin}\left(f_\mathrm{pert}\right)\\ &\cdot\frac{1}{2}[H_\mathrm{PLL}\left(f_\mathrm{mod}+f_\mathrm{pert}\right)+H_\mathrm{PLL}\left(f_\mathrm{mod}-f_\mathrm{pert}\right)]\end{aligned} \quad (25)$$

If the PLL response is flat and unity around $f_\mathrm{mod} \pm f_\mathrm{pert}$, above expression is equal to the static gain, multiplied by the output filtering of the Kelvin lock-in amplifier H_lockin. The validity of Equation 25 requires that the distance control loop does not interfere with the Kelvin control loop. First, it must not modify, by tip–surface interaction, the PLL response, e.g., by modifying Q via dissipation; second, it must not respond periodically to the frequency modulations caused by the Kelvin loop. This means that $f_\mathrm{mod} - f_\mathrm{pert}$ must be above the cutoff frequency of the distance control loop. The ranges of PLL bandwidth occupied by distance and Kelvin loop are indicated by the arrows in Figure 8. In a range of f_pert where the PLL closed loop has unity gain for $f_\mathrm{mod} \pm f_\mathrm{pert}$, Equation 25 can be approximated as

$$\begin{aligned}A_\mathrm{K}\left(f_\mathrm{pert}\right)&=\frac{\Delta f_\mathrm{demod}}{\Delta V_\mathrm{pert}}\\ &=-\frac{f_0}{k}\frac{d^2C}{dz^2}V_\mathrm{mod}H_\mathrm{lockin}\left(f_\mathrm{pert}\right)\end{aligned} \quad (26)$$

Noise projection behind the Kelvin lock-in amplifier

Concerning the noise, if an equivalent control loop circuit in the sense of Figure 1 is to be applied, it is required to express the noise PSD at the interface of block A of Figure 10, meaning in the X output of the Kelvin lock-in amplifier. Hence the propagation of the noise PSD of the PLL output to the output of the Kelvin lock-in is now calculated. The projection of the PLL noise to the demodulated X output is the average between the satellites at $f_{\text{mod}} \pm f_{\text{pert}}$

$$f_{\text{n,demod}}\left(f_{\text{pert}}\right) = H_{\text{lockin}}\left(f_{\text{pert}}\right) \cdot \sqrt{\frac{1}{2}\left[f_{\text{n}}^{2}\left(f_{\text{mod}}+f_{\text{pert}}\right)+f_{\text{n}}^{2}\left(f_{\text{mod}}-f_{\text{pert}}\right)\right]} \quad (27)$$

where f_{n} is given by Equation 20.

Kelvin closed loop gain and noise

The loop is closed with a feedback gain $F_{\text{K}}(f_{\text{pert}})$ of a PI controller described by Equation 28:

$$\begin{aligned} F_{\text{K}}\left(f_{\text{pert}}\right) &= \frac{\Delta V_{\text{K}}}{\Delta f_{\text{demod}}}\left(f_{\text{pert}}\right) \\ &= P_{\text{K}}\left(1+\frac{1}{i2\pi f_{\text{pert}}\tau_{\text{K}}}\right) \end{aligned} \quad (28)$$

The feedback parameters are set to P_{K} = 1 mV/Hz and τ_{K} = 200 µs. To understand the choice of the parameters and their effect on the closed loop response, a schematics depicting both forward response $|A_{\text{K}}|$ and reciprocal of the feedback response, $1/|F_{\text{K}}|$, is shown in Figure 12.

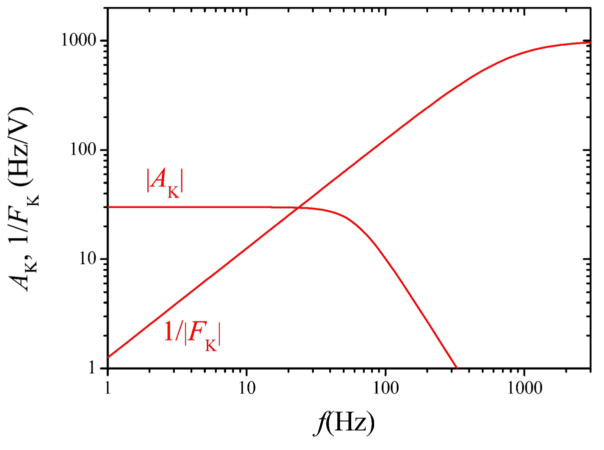

Figure 12: Schematic forward and reciprocal feedback response, for illustrating the choice of the Kelvin feedback parameters.

The main point is that the $1/F_{\text{K}}$ responsecurve crosses, with its slope, the A_{K} responsecurve at a frequency where it is essentially constant. Many combinations of P_{K} and τ_{K} are possible that yield the same closed loop cut-off frequency because only the frequency of crossing matters, but not the height of the plateau of the $|1/F_{\text{K}}|$ function. In the P–I representation, the I_{K} component would need to be set to a specific value while the P_{K} could be varied in a wide range. With the known open loop forward gain and output noise PSD $(\Delta f)_{\text{n}}$ of the PLL, it is possible to calculate the closed Kelvin loop signal and noise gain according to Figure 10 to compare them to the measured spectra:

$$H_{\text{K,sig}} = \frac{A_{\text{K}} F_{\text{K}}}{1+A_{\text{K}} F_{\text{K}}} \quad (29)$$

$$H_{\text{K,n}} = \frac{F_{\text{K}}}{1+A_{\text{K}} F_{\text{K}}} \approx \frac{1}{A_{\text{K}}} \quad (30)$$

$$V_{\text{K,n}} = H_{\text{K,n}}\left(f_{\text{pert}}\right) f_{\text{n,demod}}\left(f_{\text{pert}}\right) \quad (31)$$

The results are shown in Figure 13 and Figure 14 respectively. The fits have been obtained by using as output filtering of the Kelvin lock-in, $H_{\text{lockin}}(f_{\text{pert}})$, a second order function with cutoff at 60 Hz. This cannot be set manually in our case and is thought to be directly coupled to f_{mod} = 200 Hz.

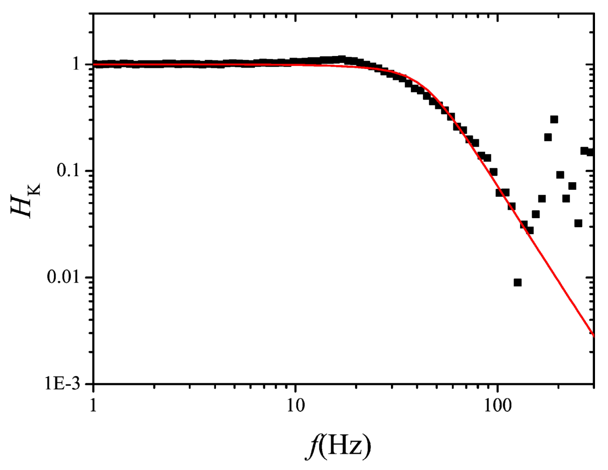

Figure 13: Measured (black squares) and calculated (red line) Kelvin closed loop gain of the setup of Figure 10.

The observation that the closed loop Kelvin response measured with engaged distance control is in agreement with the modeling based on the PLL response determined with retracted tip, supports the assumption that the gain and distance control loops with a setpoint of $\Delta f = -5$ Hz do not interfere with the Kelvin control loop by modifying the forward gain of the PLL. This situation corresponds to a weak surface interaction in the sense of [7].

The green curve of Figure 14 shows the numerically computed noise according to the exact expression of Equation 30 and

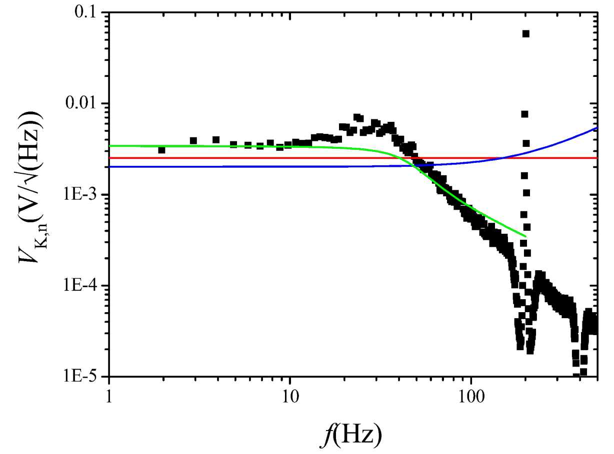

Figure 14: Measured (black squares) and computed (green line) Kelvin closed loop noise PSD of the setup of Figure 10. Also shown is the decomposition into thermal (red, constant) and sensor (blue, rising above 200 Hz) noise, calculated by using the approximate noise gain.

Equation 31 and the demodulated noise of Equation 27. The red and the blue curves are the decomposed thermal and sensor noise calculated from the approximate noise gain of Equation 31 and the demodulated noise of Equation 27. Both computations do not reflect the little harmonic overshoot of the spectrum at around 25 Hz. Again, the approximation by using noise gain is accurate only up to the roll-off of the closed loop response. The sensor noise component of $V_{\text{K,n}}$ is relatively constant in contrast to the rising sensor noise at the PLL output because it is the average between the satellites at $f_{\text{mod}} \pm f_{\text{pert}}$.

Discussion

Up to here, a typical laboratory setup has been treated in order to validate numerical and analytical treatment of noise propagation. Here, the cutoff frequency of the Kelvin loop had been set to 30 Hz by the choice of the feedback parameters as shown in Figure 12. With a Kelvin noise PSD of around 4 $\text{mV}/\sqrt{\text{Hz}}$, the total noise is expected to be around 22 mV. The bandwidth is an arbitrary choice and is limited by the acceptable noise level. The PLL bandwidth could indeed be set to a value in the kHz range, allowing to increase the AC modulation frequency and bandwidth of both distance and Kelvin control loops. In the following, the constraints with respect to a maximum bandwidth to noise performance shall be addressed.

Choice of f_{mod} with respect to bandwidth BW

A design rule for the choice of the different frequencies is given in Figure 15: the black (solid) curve schematically represents the gain of the PLL controller. The red (dashed) curve is the gain of the distance controller. The green (dotted) curve is the range in terms of PLL frequency occupied by the Kelvin loop, consisting of two satellites of the Kelvin response around the AC modulation frequency. It is reasonable to plan the bandwidth of the distance control loop to be equal to the one of the Kelvin controller, $f_{\text{c,AFM}} = f_{\text{c,KFM}}$ = BW, since usually both images are sampled at the same rate because it is a one pass technique and the Kelvin image is typically acquired with the same resolution as the topography image. If the modulation frequency is chosen to be $f_{\text{mod}} \approx 4f_{\text{c,AFM}}$, then the Kelvin loop is using the PLL in a frequency range up to $f_{\text{mod}} + f_{\text{c,KFM}}$ = 5 BW, which should be at a value such that the total noise remains acceptable (see section “Kelvin voltage noise PSD”), and on the other hand, the overlap and hence crosstalk between topography and KFM image is small since the roll-off of the distance controller at 1 BW and of the lower PLL frequency satellite of the Kelvin controller at $f_{\text{mod}} - f_{\text{c,KFM}}$ = 3 BW are 2 BW apart. The cutoff frequency of the PLL, the AC frequency and the bandwidth of the Kelvin loop can be set to much higher values as discussed in the section “Absolute frequency limits irrespective of noise”. However the effective noise PSD of the PLL is composed of thermal and detector noise, shown in Figure 5, Figure 7 and Figure 9 and by Equation 15 and Equation 20. Care has to be taken that total noise, i.e., the integral of the noise PSD over the operating range, remains acceptable.

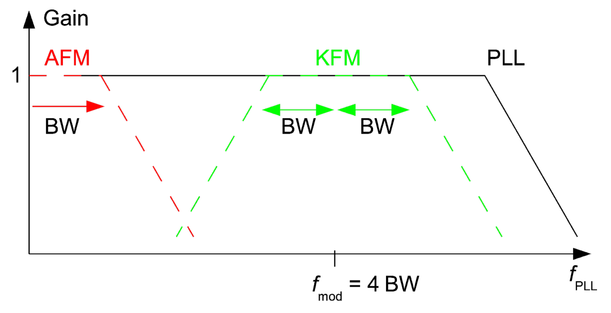

Figure 15: Design rule for cutoff and modulation frequencies in FM-KFM: gain of the PLL controller (continuous black), gain of the distance controller (red dashed), and operating range of the Kelvin loop in terms of PLL frequency (green dashed).

The 2 BW gap between the roll-off frequencies, together with the finding that both closed loop responses are second order systems, ensures that a CPD represented by V_{pert} varying at f_{c} = BW causes a response of the distance controller at $3f_{\text{c}}$ at −24 dB below its response to a static CPD. According to Equation 24, an AC CPD represented by V_{pert}, as well as the AC voltage V_{mod}, also both introduce a static term. The crosstalk onto the distance controller of V_{pert} oscillating at f_{c} introduces an oscillation of z at $3f_{\text{c}}$:

$$\Delta z_{\text{xtalk}} = \left(\frac{df}{dz}\right)^{-1} \frac{df}{dV^2} V_{\text{mod}} V_{\text{pert}} \cdot \left(-24\ \text{dB}\right) \tag{32}$$

The first two factors are

$$\frac{df}{dV^2} = \frac{f_0}{2k} \frac{d^2C}{dz^2} \tag{33}$$

and

$$\left(\frac{df}{dz}\right)^{-1} \tag{34}$$

which is highly non-linear and dependent on the Δf setpoint. It is sufficient to know the product. This can be determined from the static term:

$$\Delta z_{\mathrm{stat}} = \left(\frac{df}{dz}\right)^{-1} \frac{df}{dV^2} \frac{1}{2}\left(V_{\mathrm{mod}}^2 + V_{\mathrm{pert}}^2\right) \tag{35}$$

It is appropriate to choose a Δf setpoint such that the tip does not retract considerably in response to the applied value of V_{mod}. Equation 24 contains terms that cause a static tip retraction, and a dynamic tip movement at $3f_{\mathrm{c}}$ and $5f_{\mathrm{c}}$ due to mixed terms, and at $2f_{\mathrm{c}}$ and $8f_{\mathrm{c}}$ due to squared terms. If amplitudes are equal, $V_{\mathrm{mod}}V_{\mathrm{pert}} = V_{\mathrm{mod}}^2 = V_{\mathrm{pert}}^2$, then the dynamic tip retraction at $3f_{\mathrm{c}}$ is −24 dB below the sum of the constant terms, or 6%. The constant tip retraction can be thought to be less troublesome because it introduces only an offset in the topography image while the retraction from varying surface potential introduces a real artifact. Nevertheless, it is favorable to minimize the tip–sample distance since it deteriorates the lateral resolution. Setpoint Δf and V_{mod} should be chosen such that the topography feedback is still dominated by van-der-Waals interaction. However, the tip–sample separation cannot be made infinitely small by hardening the topography feedback because of the snap-to-contact phenomenon. The ultimate limit is discussed below, and constraints between tip–sample separation, oscillation amplitude, and V_{mod} enter into a probe merit factor.

The electrostatic force terms of Equation 24 at $5f_{\mathrm{c}}$ and at $8f_{\mathrm{c}}$ are even further apart from the distance controller cutoff frequency. The term at $2f_{\mathrm{c}}$ does introduce some response of the distance controller, but this has a negligible effect on the Kelvin controller that demodulates at $4f_{\mathrm{c}}$. Vice versa, the crosstalk of a topography varying at f_{c} onto the V_K voltage is a variation at $3f_{\mathrm{c}}$ damped by 24 dB:

$$\Delta V_{\mathrm{K,xtalk}} = \frac{df}{dz}\left(\frac{df}{dV^2}\right)^{-1} V_{\mathrm{mod}}^{-1} \Delta z \cdot (-24\ \mathrm{dB}) \tag{36}$$

Kelvin voltage noise PSD

The thermal noise PSD of the PLL frequency noise Equation 20 is constant and hence invariant under the frequency translation, yielding as Kelvin noise PSD, by dividing through the Kelvin gain Equation 26,

$$V_{\mathrm{K,n,th}}\left[\frac{\mathrm{V}}{\sqrt{\mathrm{Hz}}}\right] = \frac{1}{|A_{\mathrm{K}}|}\sqrt{\frac{k_{\mathrm{B}}Tf_0}{\pi k D_0^2 Q}} \tag{37}$$

indicated as red curve in Figure 14. The integrated noise is

$$\Delta V_{\mathrm{K,th}}(\mathrm{BW})[\mathrm{V}] = \frac{1}{|A_{\mathrm{K}}|}\sqrt{\frac{k_{\mathrm{B}}Tf_0}{\pi k D_0^2 Q}}\sqrt{\mathrm{BW}} \tag{38}$$

while the sensor noise of Equation 20 contributes to the Kelvin noise PSD

$$V_{\mathrm{K,n,S}}(f_{\mathrm{pert}})\left[\frac{\mathrm{V}}{\sqrt{\mathrm{Hz}}}\right] = \frac{z_{\mathrm{n,S}}}{|A_{\mathrm{K}}|D_0}\sqrt{f_{\mathrm{mod}}^2 + f_{\mathrm{pert}}^2} \tag{39}$$

(blue curve of Figure 14). The integrated noise due to sensor noise, still with the condition that f_{mod} = 4 BW, is

$$\Delta V_{\mathrm{K,S}}(\mathrm{BW})[\mathrm{V}] = \frac{z_{\mathrm{n,S}}}{|A_{\mathrm{K}}|D_0}\frac{7}{\sqrt{3}}\mathrm{BW}^{1.5} \tag{40}$$

The following treatment supposes that one of the noise sources is dominant and hence the total integrated noise ΔV_{K} is either equal to $\Delta V_{\mathrm{K,th}}$ or to $\Delta V_{\mathrm{K,S}}$.

Merit factor and design optimization

We define the merit factor as

$$M = \frac{1}{\Delta V_{\mathrm{K}}\sqrt{S_{\mathrm{eff}}}V_{\mathrm{mod}}} \tag{41}$$

To obtain a merit factor, it is necessary to divide the reciprocal of the integrated noise ΔV_{K} by the root of the effective probed surface S_{eff}. It is obvious and a basic rule of statistics that a potential measurement on a *n* times bigger surface made in the same time with the same state of the art of measurement apparatus has a fluctuation of $1/\sqrt{\mathrm{n}}$ times the one on a simple surface.

We also divide by the AC voltage V_{mod} since for otherwise identical conditions, the Kelvin forward gain A_{K} given by Equation 26 is proportional to it but at the same time this voltage has the effect of introducing an error on semiconductors by asymmetric band bending. The subject has been addressed by several authors [17-20]. If KFM is performed on a semiconductor, the AC bias applied to the tip causes a response of the underlying semiconductor that alternates between majority-carrier depletion and accumulation. The tip–substrate junction can be thought of as a capacitive voltage divider formed by the tip–substrate capacitance and the Mott–Schottky capacitance. We expect this description to be valid over a wide frequency. The competing process of inversion-layer buildup has a time constant that is typically on the order of seconds to minutes for industrial grade semiconductor and hence negligible even in FM-KFM. If charge capture and emission by defect states is involved, it is imaginable that time constants are such that frequency dependence or non-linearity can play a role. Due to the lack of detailed knowledge, we justify dividing the merit factor by V_{mod}.

The integrated noise ΔV_{K} is dominated by thermal or detector noise depending on bandwidth and temperature. We define as crossover temperature T_{cross} the temperature above which at a given bandwidth, the integrated thermal noise of Equation 38 exceeds the integrated sensor noise Equation 40, while the design rule is respected:

$$T_{\mathrm{cross}} = \frac{49\,\mathrm{BW}^2 \pi k Q z_{\mathrm{n,S}}^2}{3 k_{\mathrm{B}} f_0} \tag{42}$$

Regarding the effective probed surface S_{eff}, its absolute value is not known, but the relation between tip–sample distance and probed surface, as illustrated in Figure 16, is described by a power law derived from the second derivative of the capacitance [21]. Here we make the approximation that the probe oscillates with a small amplitude D_0 around a larger average probe distance z.

$$\frac{d^2C}{dz^2} \propto \frac{d^2}{dz^2}\left(\frac{S_{\mathrm{eff}}(z)}{z}\right) \propto z^{-1.5} \tag{43}$$

Hence

$$S_{\mathrm{eff}}(z) \propto z^{1.5} \tag{44}$$

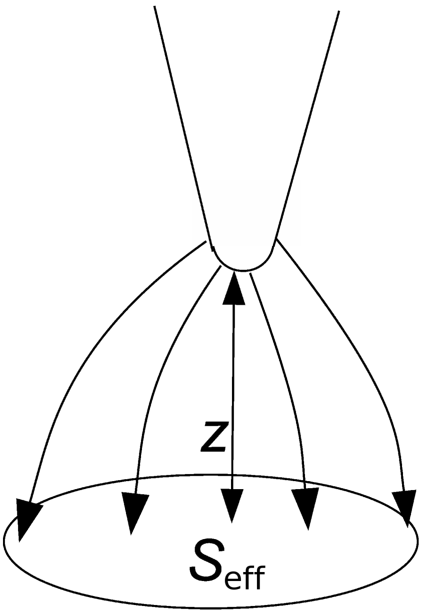

Figure 16: Effective probed surface S_{eff} depending on tip–sample separation z.

For thermal noise domination, Equation 38, the merit factor is

$$M_{\mathrm{th}} = \sqrt{\frac{\pi f_0 D_0^2 Q}{k k_{\mathrm{B}} \mathrm{BW} T z^{4.5}}} \tag{45}$$

If it is assumed that the maximum oscillation amplitude D_0 cannot exceed a certain fraction of z and hence is proportional to it, it reduces to

$$M_{\mathrm{th}} \approx \sqrt{\frac{\pi f_0 Q}{k k_{\mathrm{B}} \mathrm{BW} T z^{2.5}}} \tag{46}$$

Furthermore, a relation has to be respected between minimum tip–sample distance z and spring constant k to avoid snap to contact.

Figure 17 shows the tip in the attractive part of the van-der-Waals interaction. The force gradient in this field must not exceed the spring constant to avoid snap to contact. We take the attractive range of a Lennard-Jones type of potential

$$V \propto z^{-6} \tag{47}$$

The force gradient is proportional to the second derivative:

$$\frac{dF}{dz} \propto z^{-8} \tag{48}$$

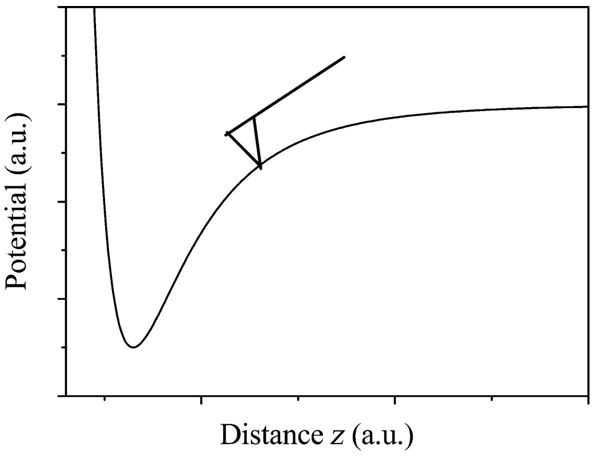

Figure 17: Probe in the attractive part of the Van-der-Waals interaction.

To avoid snap to contact, the force gradient must be smaller than the cantilever stiffness

$$z > \text{const}\; k^{-\frac{1}{8}} \tag{49}$$

And hence Equation 46 reduces to

$$M_{\text{th}} < \sqrt{\frac{\pi f_0 Q}{k_{\text{B}} \text{BW}\, T k^{0.69}}} \tag{50}$$

For comparison, a widely used merit factor for MEMS resonators is

$$M_{\text{MEMS}} = f_0 Q \tag{51}$$

and the one of minimum force detection is

$$M_{\text{NCAFM}} = \frac{f_0 Q}{k} \tag{52}$$

This result, i.e., the maximization of $f_0Q/k^{0.69}$ is positioned between the usual MEMS benchmark f_0Q and a merit factor f_0Q/k found by Albrecht [3] for the minimum detectable force by noncontact AFM.

If the noise PSD is dominated by detector noise, Equation 40, then we obtain a merit factor M_{S} instead of Equation 45:

$$M_{\text{S}} = \frac{\sqrt{3} f_0 D_0 z^{-2.25}}{7 z_{\text{n,S}} k\, \text{BW}^{1.5}} \tag{53}$$

similarly as above, D_0 is a fraction of z and hence

$$M_{\text{S}} = \frac{\sqrt{3} f_0}{7 z_{\text{n,S}} k z^{1.25}\, \text{BW}^{1.5}} \tag{54}$$

Using Equation 49 for the relation between z and k yields

$$M_{\text{S}} < \frac{\sqrt{3} f_0}{7 z_{\text{n,S}} k^{0.85}\, \text{BW}^{1.5}} \tag{55}$$

Unsurprisingly, for the case of dominating sensor noise, maximization of the merit factor requires minimizing the sensor noise. Both merit factors, Equation 50 and Equation 55, suggest downsizing both the probe spring constant and mass. If one considers $f_0 = \sqrt{k/m}$, the exponents of k higher than 1/2 in the denominator yield increasing merit factors for decreasing stiffness. Both merit factors cannot be increased infinitely because downsizing the probe beyond a certain limit will decrease the Q-factor and increase sensor noise.

A table of merit factors for thermally dominated noise, sensor dominated noise and crossover criteria is given in Table 1. The table lists probe parameters, followed by a crossover criterion, Equation 42, the crossover temperature for a bandwidth of 50 Hz, the merit factor for dominant thermal noise according to Equation 50, and the merit factor for dominant detector noise according to Equation 55. For the stiffness of the Kolibri sensor, we use 1 MN/m, about the double of what is given in the documents from Specs [22]. The 540 kN/m is the spring constant of the entire needle which is suspended in the middle. In SPM operation, the two prongs are moving oppositely and the suspension remains stationary. Therefore, for comparison with the other probes, the effective stiffness of twice the given value has to be used. The use of the table for comparison of probe performance consists in first determining the crossover temperature as function of the desired bandwidth by multiplying the value $T_{\text{cross}}/\text{BW}^2$ with BW^2. If the working temperature is below the obtained crossover temperature, the merit factor M_{S} applies and is obtained by dividing the value $M_{\text{S}}{\cdot}\text{BW}^{3/2}$ through $\text{BW}^{3/2}$. If the working temperature is above the crossover temperature, the merit factor M_{th} applies and is obtained by dividing $M_{\text{th}}{\cdot}\sqrt{\text{BW}T}$ by $\sqrt{\text{BW}T}$. The dominating merit factor among M_{S} and M_{th} is the one with the lowest value, due to its definition containing the reciprocal of $V_{\text{K,n}}$, according to Equation 41. The performance of probes with thermally dominated noise can be compared directly to others with dominating sensor noise.

Table 1: Key values, crossover criteria, and merit factors for different probes.

	Cantilever (Nanosensors)	qPlus Sensor (Giessibl, 2011 [9])	Kolibri Length Extension Resonator (Specs [22])	IEMN Disk Resonator (Algre 2012 [23])
	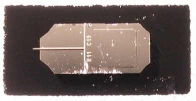	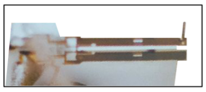	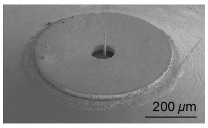	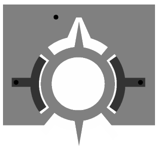
f_0 (Hz)	61836	30k	1M	1.45M
Q	22k8	200k	14k	1k6
k (N/m)	1.2	1k8	1M	135k
$Z_{n,S}$ (m/$\sqrt{\mathrm{Hz}}$)	2e-13	6.2e-14	1e-15	1e-12
T_{cross}/BW^2 (K/Hz^2)	6.81e-2	177.5	5.38e-2	594
Crossover Temp (K) at BW = 50 Hz	170	444k	135	1.48M
$M_{th}\cdot\sqrt{\mathrm{BW}T}$	1.71e16	2.83e15	4.89e14	3.97e14
$M_S\cdot\mathrm{BW}^{3/2}$	6.75e16	2.05e14	1.97e15	1.56e13

The table shows that cryogenic cooling is useful only for reducing the thermal excitation of the Kolibri sensor and to some extent of cantilevers, whereas the qPlus and disk resonator have dominant detector noise at all achievable temperatures, recognizable by crossover temperatures in the kilo- or Mega-Kelvin range. (Detector noise was assumed temperature independent). The best FM-KFM performance is expected from standard cantilevers. It can be expected that these probes in combination with interferometric detection might benefit from cooling to temperatures even below liquid helium. Despite significant performance differences, the existence of all compared probe types seems to be justified. For instance, some environments require a need for electrical rather than optical deflection detection, and the performance criteria for topography imaging differ largely from the FM-KFM merit factor, due to the highly non-linear probe sample interaction that motivates a wide range of cantilever stiffness and oscillation amplitudes.

Absolute frequency limits irrespective of noise

The example treated here seems to have rather low performance compared to, e.g., video-rate SPM setups that claim to image biological processes in real-time (however in topography mode only). We emphasize that the choice of our bandwidth is our personal preference of making the compromise between bandwidth and noise. As stated above, the 30 Hz bandwidth leads to 22 mV signal fluctuation. Since the sampling circuitry has an anti-aliasing filter that cuts above half the sampling rate and it is not justified to smooth the image by slow response of the Kelvin and topography loop responses, we can acquire at 50 pixel per second, meaning that a line with 256 pixels is scanned back and forth in 10 seconds and an image at 256 × 256 resolution takes 45 minutes. We are used to acquire images with higher resolution over night. Since the output noise has been tracked down to thermal excitation and displacement detector noise, said compromise has universal validity. We also mention here that the exchange of the light source in the optical beam deflection sensor has already decreased the detector noise by an order of magnitude with respect to the original value, and that otherwise for the same choice of bandwidth, the detector noise would be dominating and the Kelvin signal fluctuation would be a multiple. In this short paragraph we address the question to what extent speed can be increased at the expense of noise and when other limitations apply.

- PLL bandwidth: for phase locked loops, the terms capture range and lock range denominate the frequency range in which the PLL can lock on to an incoming signal and maintain the phase lock. It is given as percentage of center frequency, depends on the degree of sophistication of the circuit (phase detection, filters) and is above 10 percent even for primitive monolithic circuits that use edge detection and simple filters such as the NE567 PLL tone decoder. The capture range is always below the lock range. The given percentage is the frequency shift of the frequency modulated signal, which is a function of both the excursion frequency and the modulation frequency. Without entering PLL theory in detail, we can say that a PLL bandwidth of 10 percent of the center frequency is realistic and it has been experimentally confirmed that our PLL bandwidth can be set to 5 kHz.

- AC frequency f_{mod} and PLL bandwidth $\mathrm{BW}_{\mathrm{PLL}}$: these frequencies have to be chosen such that $f_{\mathrm{mod}} + \mathrm{BW} \leq \mathrm{BW}_{\mathrm{PLL}}$. Together with the design rule, for our example, we would obtain $f_{\mathrm{mod}} = 4$ kHz and BW = 1 kHz.
- Distance control: this component is probably the most limiting. In our setup where the sample is mounted on a 3 axis piezo scanner, the bandwidth is limited to a value between 100 and 200 Hz.

Consequently, if we had set the PLL bandwidth $\mathrm{BW}_{\mathrm{PLL}} = 5$ kHz, the AC frequency $f_{\mathrm{mod}} = 4$ kHz and the bandwidth of the Kelvin controller BW = 1 kHz, according to Figure 9 the detector noise would be dominating and due to the power law with exponent 3/2 of Equation 40, we would expect Kelvin voltage fluctuation in the volt range. Furthermore, the distance control would not be able to keep up with the Kelvin loop.

Perspective on the ultimate probe and detector

It is obvious from the two merit factors that a reduction of both thermal and detector noise at the same time is difficult. If thermal excitation is dominant and the effort aims at reducing it, the frequency range where it dominates becomes smaller, as can be seen in Figure 9. Mass and spring constant cannot be reduced infinitely without reducing the *Q*-factor. Furthermore, increasing the merit factor in the thermally dominated case is a simple downsizing of the detector, and with the same type of sensor, would increase the sensor noise or decrease the *Q*-factor of the oscillator by sensor back-action (e.g., radiation pressure). Similarly, all attempts of improving the detector have a trend to increase invasiveness and to reduce the *Q*-factor. As long as one type of noise is clearly dominant, the remedy is to maximize the respective merit factor, keeping in mind the above dependencies. Present state of the art for measuring the excursion of harmonic oscillators consists in optical interferometry [24] or single electron transistors [25] used as position probe coupled to oscillators, combined with cooling of the resonator to cryogenic temperatures, possibly using laser cooling. These works aim at the Heisenberg limit and are not specific to scanning probe microscopy. Practical SPM systems seem to be still further away from the ultimate limit.

Conclusion

The dynamic behavior of an FM-KFM has been measured and modeled for a system with characteristics typically obtained in ultrahigh vacuum implementations. It has been shown that in a PLL based setup, the two main noise sources, thermal excitation and detector noise, transform into frequency noise exactly the same way as in a free-running oscillator, and that the PLL components do not contribute considerable noise, meaning that the main noise sources are sufficient to derive Kelvin voltage noise. Feedback parameters for PLL and Kelvin loop have been set for a stable behavior and been used for the numerical modeling of the noise propagation, yielding output noise spectra in agreement with the measurements. The choice of the AC modulation frequency to be four times the intended bandwidth has been proposed and justified as design rule. Based on the acquired knowledge, the KFM performance has been modeled for three other well-known AFM probes. A crossover criteria allows one to determine for each probe, depending on temperature, detector noise PSD, bandwidth and probe parameters, whether Kelvin output noise is dominated by thermal probe excitation or by detector noise. Depending on the regime, one of two merit factors apply to obtain the overall noise performance from instrument parameters, to suggest improvements and to allow for a comparison of different probes. Limitations to the optimization remain due to unresolved interdependent parameters, the trend of entering a thermally limited regime when improvement is made to detector noise and vice versa, and deteriorating one noise source when improving the other, ultimately merging into the uncertainty relation governing that a system cannot be measured without changing it by whatever kind of sensor back-action.

Experimental

The KFM is based on an Omicron ultrahigh vacuum variable temperature atomic force microscope (UHV-VT-AFM). It is operated by a Nanonis scanning probe microscopy (SPM) controller entirely based on digital signal processing (DSP). The probe that was used in these experiments is a platinum-iridium coated Nanosensors Point Probe Plus EFM tip with a spring constant between 1 and 3 N/m. Its resonance frequency f_0 = 61.835 kHz and the *Q*-factor Q = 22800 were determined in vacuum by recording a resonance curve with the built in function of the Nanonis controller. The optical beam deflection detection uses a 20 mW Superluminescent (TM) light emitting diode that was operated at an intensity of 7 mW. About 0.5 mW intensity is received by the photodiode, which was estimated from its known current–intensity characteristics. To compensate the increased intensity of the light source, the gain of the transimpedance amplifier was reduced accordingly to avoid output voltage saturation. The sample is a gold coated silicon substrate (Omicron test sample). KFM measurements are performed while distance control is enabled.

Acknowledgements

This work was achieved with the financial support of the European Union, the French Government and the Regional Council, using the facilities of the EXCELSIOR Nanoscience Characterization Center. Further financial aid from the French Agence Nationale de Recherche (ANR-11-BS10-004 NANOKAN) and from a Merlion program of the French Embassy in Singapore (grant 8.11.08) is gratefully acknowledged. We thank Benjamin Walter for fruitful discussions and David Troadec for technical help.

References

1. Kikukawa, A.; Hosaka, S.; Imura, R. *Appl. Phys. Lett.* **1995,** *66,* 3510. doi:10.1063/1.113780
2. Kitamura, S.; Iwatsuki, M. *Appl. Phys. Lett.* **1998,** *72,* 3154. doi:10.1063/1.121577
3. Albrecht, T. R.; Grütter, P.; Horne, D.; Rugar, D. *J. Appl. Phys.* **1991,** *69,* 668. doi:10.1063/1.347347
4. Glatzel, T.; Sadewasser, S.; Lux-Steiner, M. C. *Appl. Surf. Sci.* **2003,** *210,* 84. doi:10.1016/S0169-4332(02)01484-8
5. Fukuma, T.; Kimura, M.; Kobayashi, K.; Matsushige, K.; Yamada, H. *Rev. Sci. Instrum.* **2005,** *76,* 53704. doi:10.1063/1.1896938
6. Kobayashi, K.; Yamada, H.; Matsushige, K. *Rev. Sci. Instrum.* **2009,** *80,* 043708. doi:10.1063/1.3120913
7. Polesel-Maris, J.; Venegas de la Cerda, M. A.; Martrou, D.; Gauthier, S. *Phys. Rev. B* **2009,** *79,* 235401. doi:10.1103/PhysRevB.79.235401
8. Diesinger, H.; Deresmes, D.; Nys, J.-P.; Mélin, T. *Ultramicroscopy* **2010,** *110,* 162. doi:10.1016/j.ultramic.2009.10.016
9. Giessibl, F.-J.; Pielmeier, F.; Eguchi, T.; An, T.; Hasegawa, Y. *Phys. Rev. B* **2011,** *84,* 125409. doi:10.1103/PhysRevB.84.125409
10. Lübbe, J.; Temmen, M.; Rode, S.; Rahe, P.; Kühnle, A.; Reichling, M. *Beilstein J. Nanotechnol.* **2013,** *4,* 32. doi:10.3762/bjnano.4.4
11. Portes, L.; Ramonda, M.; Arinero, R.; Girard, P. *Ultramicroscopy* **2007,** *107,* 1027. doi:10.1016/j.ultramic.2007.03.012
12. Giessibl, F.-J. *Phys. Rev. B* **1997,** *56,* 16010. doi:10.1103/PhysRevB.56.16010
13. Rast, S.; Gysin, U.; Meyer, E. *Phys. Rev. B* **2009,** *79,* 054106. doi:10.1103/PhysRevB.79.054106
14. Giessibl, F.-J. *Rev. Mod. Phys.* **2003,** *75,* 949. doi:10.1103/RevModPhys.75.949
15. Colchero, J.; Cuenca, M.; Martínez, J.-F. G.; Abad, J.; García, B. P.; Palacios-Lidón, E.; Abellán, J. *J. Appl. Phys.* **2011,** *109,* 024310. doi:10.1063/1.3533769
16. Gauthier, S. *J. Appl. Phys.* **2011,** *110,* 036107. doi:10.1063/1.3619776
17. Leng, Y.; Williams, C. C.; Su, L. C.; Stringfellow, G. B. *Appl. Phys. Lett.* **1995,** *66,* 1264. doi:10.1063/1.113257
18. Henning, A.-K.; Hochwitz, T. *Mater. Sci. Eng. B* **1996,** *42,* 88. doi:10.1016/S0921-5107(96)01688-1
19. Sommerhalter, C.; Matthes, T. W.; Glatzel, T.; Jäger-Waldau, A.; Lux-Steiner, M. C. *Appl. Phys. Lett.* **1999,** *75,* 286. doi:10.1063/1.124357
20. Sommerhalter, C.; Glatzel, T.; Matthes, T.; Jager-Waldau, A.; Lux-Steiner, M. *Appl. Surf. Sci.* **2000,** *157,* 263. doi:10.1016/S0169-4332(99)00537-1
21. Mélin, T.; Diesinger, H.; Deresmes, D.; Stiévenard, D. *Phys. Rev. B* **2004,** *69,* 35321. doi:10.1103/PhysRevB.69.035321
22. Specs, Kolibri Sensor, Advanced Quartz Sensor Technology for NC-AFM. http://www.specs.de/cms/front_content.php?idcat=246.
23. Algre, E.; Xiong, Z.; Faucher, M.; Walter, B.; Buchaillot, L.; Legrand, B. *J. Microelectromech. Syst.* **2012,** *21,* 385. doi:10.1109/JMEMS.2011.2179012
24. Schliesser, A.; Arcizet, O.; Rivière, R.; Anetsberger, G.; Kippenberg, T.-J. *Nat. Phys.* **2009,** *5,* 509. doi:10.1038/nphys1304
25. LaHaye, M.-D.; Buu, O.; Camarota, B.; Schwab, K.-C. *Science* **2004,** *304,* 74. doi:10.1126/science.1094419

License and Terms

Beilstein Journal
of Nanotechnology

Influence of the adsorption geometry of PTCDA on Ag(111) on the tip–molecule forces in non-contact atomic force microscopy

Gernot Langewisch[1,2], Jens Falter[1,2,3], André Schirmeisen*[3]
and Harald Fuchs[1,2]

Full Research Paper

Open Access

Address:
[1]Physikalisches Institut, Westfälische Wilhelms-Universität Münster, Wilhelm-Klemm-Straße 10, 48149 Münster, Germany, [2]Center for Nanotechnology (CeNTech), Westfälische Wilhelms-Universität Münster, Heisenbergstraße 11, 48149 Münster, Germany and [3]Institut für Angewandte Physik, Justus-Liebig-Universität Gießen, Heinrich-Buff-Ring 16, 35392 Gießen, Germany

Email:
André Schirmeisen* - Andre.Schirmeisen@ap.physik.uni-giessen.de

* Corresponding author

Keywords:
atomic force microscopy; organic molecules; three-dimensional (3D) force spectroscopy

Beilstein J. Nanotechnol. **2014,** *5,* 98–104.
doi:10.3762/bjnano.5.9

Received: 30 October 2013
Accepted: 06 January 2014
Published: 27 January 2014

This article is part of the Thematic Series "Noncontact atomic force microscopy II".

Guest Editors: U. D. Schwarz and M. Z. Baykara

Abstract

Perylene-3,4,9,10-tetracarboxylic dianhydride (PTCDA) adsorbed on a metal surface is a prototypical organic–anorganic interface. In the past, scanning tunneling microscopy and scanning tunneling spectroscopy studies of PTCDA adsorbed on Ag(111) have revealed differences in the electronic structure of the molecules depending on their adsorption geometry. In the work presented here, high-resolution 3D force spectroscopy measurements at cryogenic temperatures were performed on a surface area that contained a complete PTCDA unit cell with the two possible geometries. At small tip-molecule separations, deviations in the tip-sample forces were found between the two molecule orientations. These deviations can be explained by a different electron density in both cases. This result demonstrates the capability of 3D force spectroscopy to detect even small effects in the electronic properties of organic adsorbates.

Introduction

Perylene-3,4,9,10-tetracarboxylic dianhydride (PTCDA) adsorbed on the Ag(111) surface is a prototypical organic–anorganic interface that has been investigated by a large variety of different methods in the past [1]. Based on scanning tunneling microscopy (STM) and scanning tunneling spectroscopy (STS) experiments as well as theoretical simulations, it was found that the differences between the two possible adsorption geometries of PTCDA on the Ag(111) substrate affect the electronic structure of the molecules [2-5]. The chemical nature of the molecule–substrate bond leads to a charge transfer from the metal surface into the former LUMO of the molecules, however to a different extend for the two cases. As a result, the energetic centers of the now partially occupied LUMO levels are located at energies below the Fermi level with a shift of about 160 meV between the two adsorption geometries [4]. These deviations in the spectral weight below the Fermi level correspond to different electron densities.

Atomic force microscopy (AFM) investigations indicate that electronic properties such as the electron density distribution or partial charges within organic adsorbates are reflected by the tip–molecule force interactions [6-9]. However, a correlation between the electronic differences of the two PTCDA molecules of the unit cell and a force contrast in AFM experiments has not been reported yet. A possible reason might be the fact that the tip–sample forces are a complex superposition of several contributions of different physical effects and therefore of different range. AFM topography scans provide only a cut through the three-dimensional force field at a certain tip–sample separation. If the relevant interactions happen at a different distance, such an effect would not be detected. Therefore, we used the method of high-resolution three-dimensional (3D) force spectroscopy [10] to investigate the complete force field quantitatively, while starting at large tip–sample distances with no force interactions down to the regime of repulsive forces.

Experimental

The experiments have been performed with a commercial low-temperature atomic force microscope (Omicron LT-SPM) that was operated in frequency-modulation mode [11] under ultra-high vacuum conditions and at a temperature of ≈5 K using a tuning fork sensor (resonance frequency f_0 = 24640 Hz, spring constant $k \approx 2000$ N/m) in the qPlus design [12]. The amplitude of the sensor oscillation was held constant at A = 0.40 nm. To avoid crosstalk between tunneling current and deflection signal, no voltage was applied to the tip during NC-AFM operation. The tip was prepared by voltage pulses and soft indentation into the Ag sample most likely resulting in a Ag-terminated apex. However, it can not be excluded that a PTCDA molecule was picked-up afterwards during the scans. The PTCDA molecules were evaporated from a Knudsen cell up to a submonolayer coverage onto a clean Ag(111) surface, which was kept at room temperature during the deposition. More experimental details and previous measurements on the same system have been published before [3,13].

Figure 1a shows an STM topography image of a PTCDA monolayer on Ag(111). The molecules are arranged in a characteristic herring bone structure where the unit cell contains two molecules with different orientation and adsorption geometry. Here, a significant difference in the intensity of the two adsorption geometries can be observed, which is caused by the different electronic structure as described above. In contrast, this effect is not detectable in the AFM topography image in Figure 1b. However, as discussed above, the reason might be that the interactions correlated to this effect are not present at the tip–sample distance at which this scan was recorded (at a relatively large distance). Thus, 3D force field spectroscopy as described by Hölscher et al. [14] was utilized for a detailed investigation of the tip–molecule interactions. Above the surface area shown in Figure 1b, the frequency shift $\Delta f(x,y,z)$ was measured with 40 by 30 by 200 data points within a volume of 3.2 by 2.4 by 1.0 nm. In order to account for interactions that are not site-specific and beyond the z range, which was covered by this measurement, a separate $\Delta f(z)$ curve was recorded and added to the $\Delta f(x,y,z)$ matrix, by this expanding the z range to 10.2 nm in total. The resulting dataset was then converted into a three-dimensional landscape of vertical tip–sample forces BY using the Sader–Jarvis-algorithm [15]. As the duration of the 3D force spectroscopy measurement was about 5 3/4 h, the

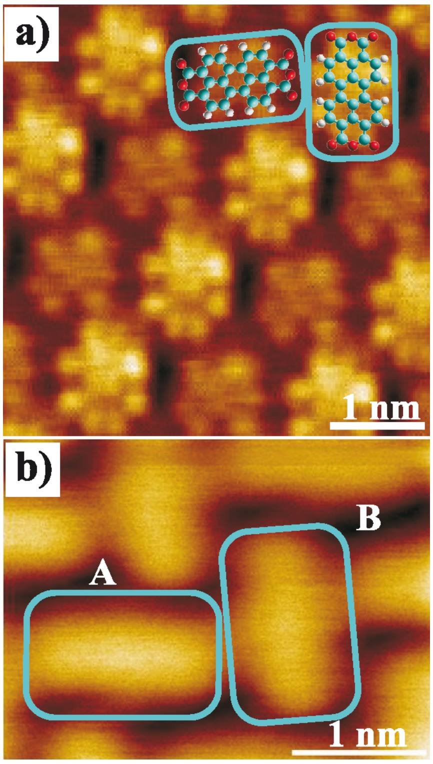

Figure 1: (a) STM topography scan (V = 0.2 V, I = 0.3 nA) of PTCDA on Ag(111). The two molecule orientations (turquois rectangles) of the unit cell correspond to different adsorption geometries and are imaged with a different intensity. (b) NC-AFM topography scan (Δf = −0.6 Hz) of the surface area where the 3D force spectroscopy measurement was performed. No difference between the two orientations is detectable.

lateral drift of ≈40 pm/h led to a distortion of the originally rectangular surface area. In addition, a continuous drift of the frequency shift reference point of the order of 0.1 Hz/h was observed. The precise drift as a function of time was determined by a comparison of the $\Delta f(z)$ curves in the distance regime, in which no site-specific variations appeared (at large z distances) and used for a correction of the $\Delta f(x,y,z)$ matrix.

Results and Discussion

Figure 2 shows a horizontal cut through the 3D landscape of the vertical tip–sample forces at a distance of $z = 0.60$ nm. Please note that the origin of the z axis was defined arbitrarily as the absolute distance was unknown in the experiment. In this cut, intramolecular structures can be observed that can unambiguously be assigned to specific parts of the molecules. In particular, the characteristic structure of the five carbon rings in the perylene core can be identified. As already described by Moll et al. for PTCDA on Cu(111) [16], the contrast in AFM images recorded at tip–sample distances that correspond to the regime of repulsive forces reflects the electron density distribution of the molecules. This effect allows for a precise localization of the molecules and molecule moieties.

To analyze the general evolution of the tip–sample forces as a function of the z distance as well as site-specific effects, $F_{\mathrm{TS}}(z)$ curves were averaged for the different molecule moieties (see sketch in Figure 3a: colored rectangular areas; number of curves used for the averaging was 5 × 8 per small rectangle and 8 × 8 per large rectangle). The resulting curves are shown exemplarily for the orientation A in Figure 3a. In this graph, the minimum of the z axis is the lower limit of the z range covered by the 3D force spectroscopy measurement. The evolution of the forces up to this point is typical and basically reflects a superposition of attractive long range (and additional attractive short range) forces with repulsive short range forces. When extrapolating this progression toward smaller distances, it can be assumed that the minimum of the $F_{\mathrm{TS}}(z)$ curves is reached at $z \approx 0.60$ nm. The net force is attractive at this point and about -0.32 ± 0.06 nN on average. As this distance is below the turning point of the curve, which is at $z \approx 0.67$ nm, the absolute value of the force gradient is declining with decreasing z. This means that repulsive forces are acting and are partially compensating the attractive forces in this distance regime.

When comparing the interactions at the different molecule moieties, a general trend can be observed, which is similar for both orientations of the unit cell. While at large distances only small deviations between the end groups and the center are detectable, the differences are significant at distances of 0.65 nm and below. Here, the interactions at the end groups are more attractive. This trend is also obvious in horizontal cuts through the 3D force field at different distances (Figure 3b). At $z = 0.75$ nm, the molecules appear as featureless ovals. With decreasing distance, intramolecular structures arise that are clearly visible at distances of $z \leq 0.65$ nm with areas of enhanced attractive forces (depicted in red) at the end groups.

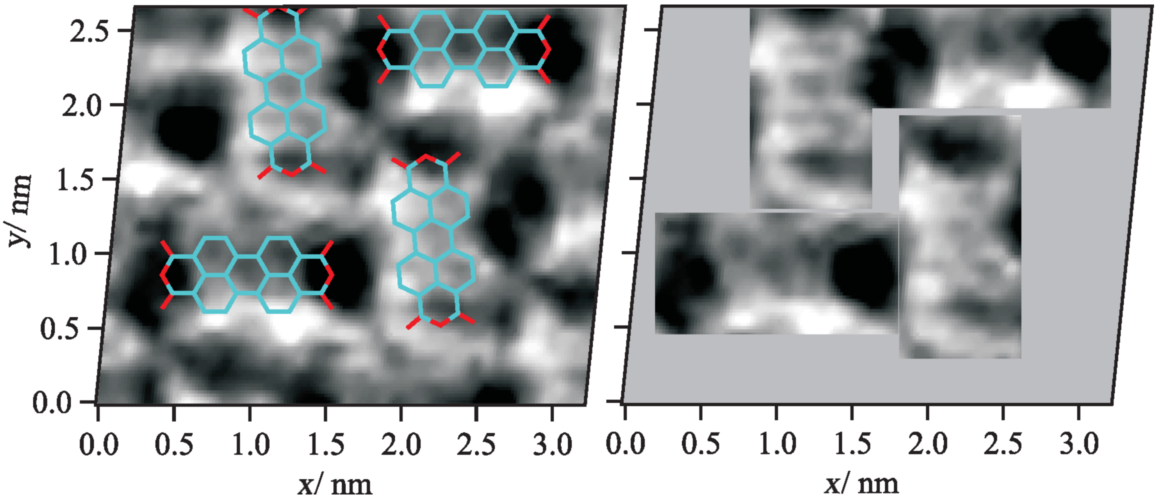

Figure 2: Horizontal cut through the 3D field of the vertical tip–sample forces at a distance of $z = 0.60$ nm (left). Dark features correspond to areas of enhanced attractive forces (for a quantitative analysis: see below in Figure 3 and Figure 4). The lateral drift was corrected in the images resulting in a distortion of the originally rectangular surface area. The images were linearly interpolated with a factor of 4 to enhance the visibility. Intramolecular structures can be seen in both the raw data images and the interpolated images. The characteristic shape of the perylene core consisting of five carbon rings can be identified, which allows an exact determination of the molecule positions in the 3D force spectroscopy measurement. The areas that can be assigned to PTCDA molecules are shown separately (right).

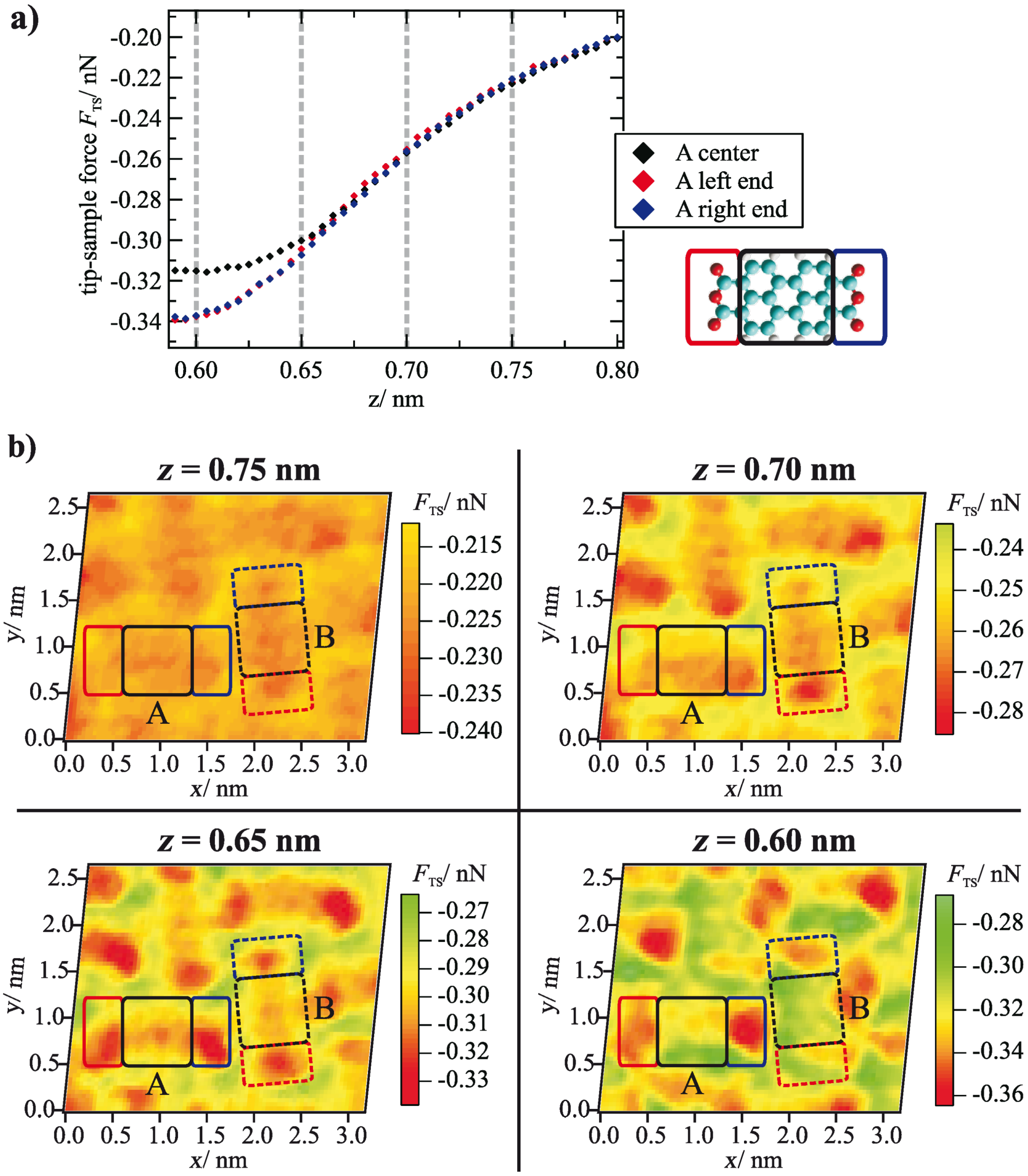

Figure 3: (a) Tip–sample forces as a function of *z* distance averaged for the area above the end groups and the center of a molecule (here: orientation A) as indicated by colored rectangles in the sketch on the right side. (b) Horizontal cuts through the 3D force field at different *z* distances that are marked by gray dashed lines in the $F_{TS}(z)$ curves in (a). In the cuts at *z* = 0.65 nm and *z* = 0.60 nm, a clear intramolecular contrast can be observed. In addition, at *z* = 0.60 nm, differences between the two molecule orientations appear. For all cuts, the color-force gradient is the same. However, the minimum of the color scale was adjusted to match the minimum force value within the cut. Furthermore, a slight linear interpolation with a factor of 2 was applied.

However, more interesting than this common trend are the differences between the two molecular orientations A and B. While in the horizontal cuts at *z* = 0.75 nm, 0.70 nm and 0.65 nm the two molecules of the unit cell appear nearly the same, at small distances of *z* = 0.60 nm, higher attractive tip–sample forces are acting on molecules with orientation A. To illustrate this effect in more detail, vertical cuts through the 3D force field are shown in Figure 4b and Figure 4c. These cuts run along the long axis of both molecule orientations as indicated by the dashed lines in Figure 4a. Here, the behavior observed in the horizontal cut at *z* = 0.60 nm can be found again: All partial groups of molecule A exert higher forces on the tip than the corresponding groups of molecule B. The onset of this trend is in the distance range between 0.65 and 0.60 nm. Additionally we find an asymmetry of the forces above the two ends on the molecules, for molecule A as well as for molecule

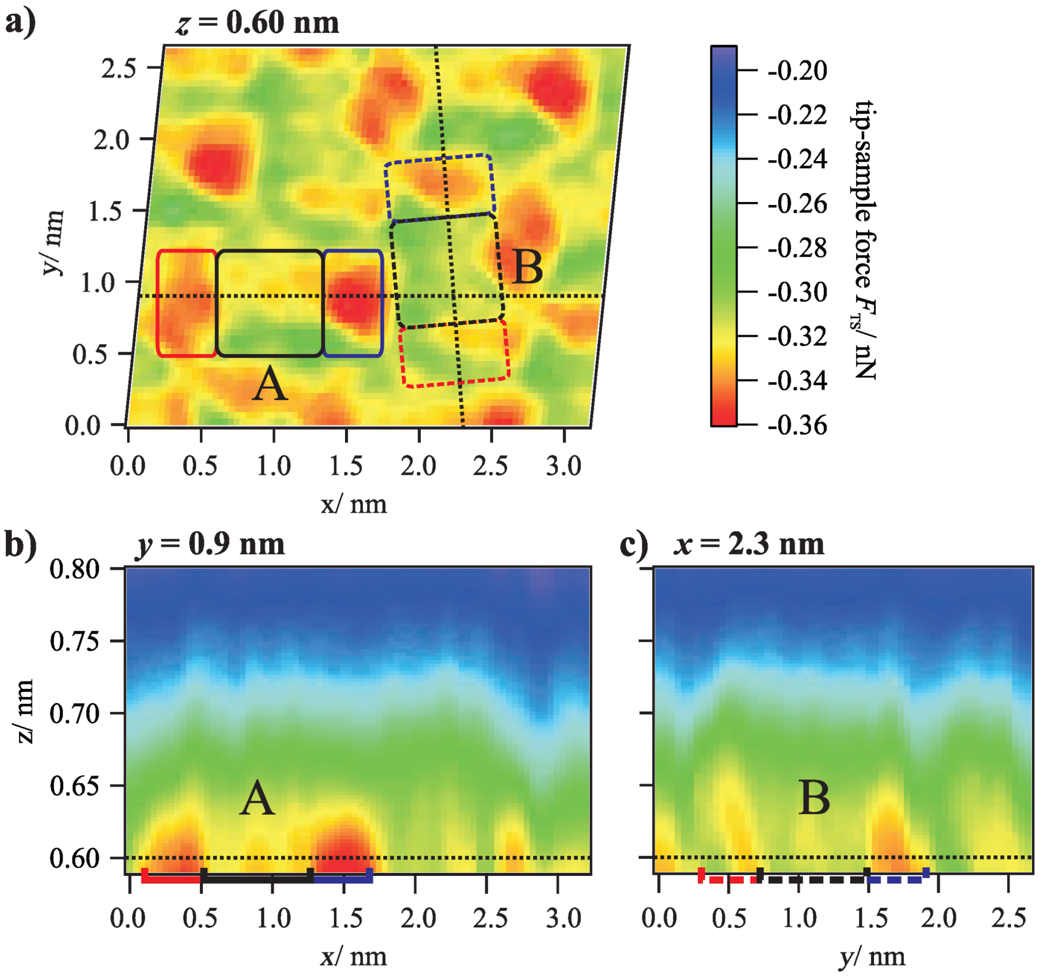

Figure 4: (a) Horizontal cut through the 3D force field at $z = 0.60$ nm and (b) vertical cuts at $y = 0.9$ nm and $x \approx 2.3$ nm (diagonal progression) along the long axis of two different molecule orientations of the unit cell (the images are linearly interpolated with a factor of 2). For $z < 0.65$ nm, higher attractive forces are acting on molecule A in comparison to molecule B.

B. Previous ab-initio simulations of PTCDA on Ag(111) predict a slight asymmetry of the end groups in the dissipation channel at small distances [17], but only for one molecular orientation. Therefore we speculate that this effect is related to an asymmetry of the tip apex in this experiment [18].

This onset can be determined more accurately based on a comparison of the $F_{TS}(z)$ curves for both molecule orientations. The corresponding curves, which are averaged for the perylene cores (left) and the complete molecules (right), are shown in Figure 5. The deviations between the two orientations start obviously at $z = 0.65$ nm. At $z = 0.60$ nm, the difference, which is slightly lower at the perylene core in comparison to the complete molecule, is about 0.01 nN.

When analyzing the qualitative behavior of the tip–sample forces for the two molecule orientations individually, the evolution of the intramolecular contrast as a function of the distance z is as expected. At larger distances, in the regime of attractive long-range interactions such as van-der-Waals forces, no internal structures can be observed in the horizontal cuts through the 3D force field. The molecules appear as featureless ovals, which results in a corresponding contrast in the topography images recorded at small frequency shift values and, thus, large tip–sample distances (compare Figure 1b). Below a certain distance, the regime of short-range forces such as chemical interactions, short-range electrostatic forces or Pauli repulsion is reached. These forces most likely lead to the barbell-like structure as shown in Figure 3b at $z = 0.65$ nm with higher attractive forces at the end groups. While the physical origin of this contrast is not clear, a likely explanation for the structure that illustrated in Figure 2, in which the five carbon rings of the perylene core are visible, is provided by Gross and Moll et al. [8,16]. As was found for the first time for pentacene molecules and later also for PTCDA adsorbed on Cu(111), the atomic contrast revealing the carbon rings of organic molecules can be

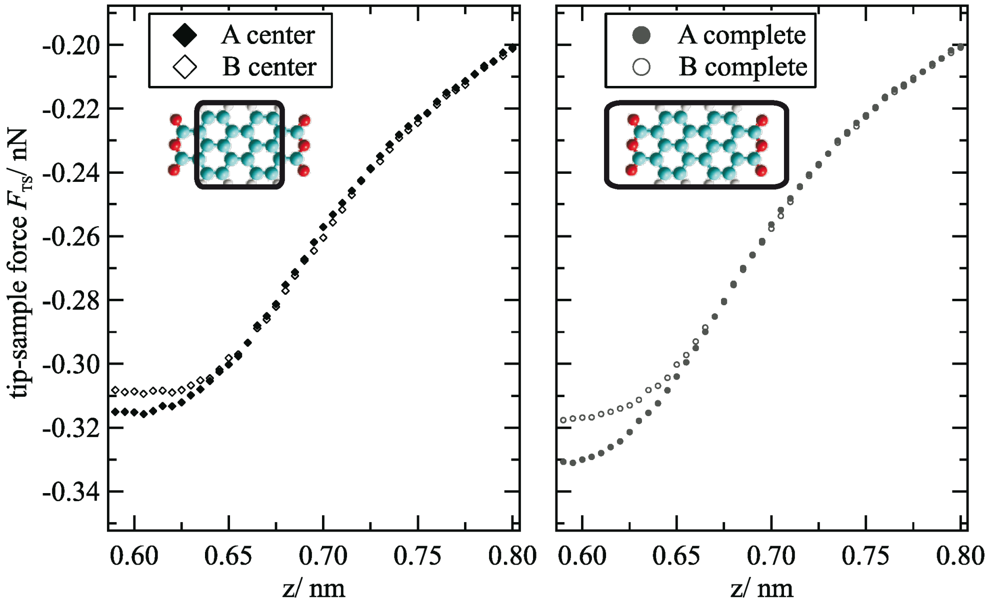

Figure 5: Comparison of force versus distance curves for molecule sites A and B. The forces are averaged for the perylene core (left) and the complete molecule (right) as indicated in the sketches of the molecules. At *z* distances below 0.65 nm, higher attractive forces are acting at molecule A.

assigned to Pauli repulsion and reflects the electron density distribution of the molecules. Therefore, it can be assumed that Pauli repulsion also represents a significant contribution to the force interactions at small tip–sample distances in our measurements. Here, the characteristic contrast appears at distances below $z \approx 0.65$ nm, at first only weakly and then increasing. As one would expect, this distance regime starts near the turning point of the $F_{TS}(z)$ curves, the point at which repulsive forces begin to compensate the attractive interactions.

Interestingly, this distance of about 0.65 nm is also the point at which the differences between the two molecule orientations arise. Thus, one can suspect that both effects have a common origin, i.e., that the different tip–sample forces are also related to Pauli repulsion. Deviations of this force interaction, which is sensitive to the electron density, could in this case be explained by the different spectral weight of the energetically shifted LUMO state (the hybrid state resulting from the chemisorption) below the Fermi level and corresponding differences in the electron density of the two orientations. A higher electron density would lead to a stronger repulsion and, thus, less attractive net forces near the minimum of the $F_{TS}(z)$ curves. Please note that no STM measurements were performed on the surface area investigated by the 3D force spectroscopy. Therefore, it is not possible to unambiguously verify this proposed relationship between electronic properties and forces in this case. However, the fact that the deviations in the tip–sample forces for the two orientations can be observed at the perylene core as well as at the end groups is in agreement with this interpretation because the LUMO state extends over the entire molecule.

As this effect can only be observed in the regime of repulsive forces near the minimum of the $F_{TS}(z)$ curves, it is not surprising that it was not observed in NC-AFM topography scans, yet. Such scans are in most cases recorded at a constant frequency shift. In the repulsive force regime (in which the repulsive forces start to partially compensate the attractive forces), the non-monotonic behavior of the frequency shift as a function of the tip–sample distance makes a stable operation of the distance feedback loop impossible. Furthermore, a stable and inert tip is required to avoid that the tip deforms or picks up the molecule. This is an additional factor that complicates AFM measurements at small tip–sample separations.

Conclusion

Our 3D force spectroscopy measurements allow for a quantitative determination of the forces between an AFM tip and a PTCDA molecule on a Ag(111) surface as well as a detailed analysis of the qualitative evolution of the forces in three dimensions with submolecular resolution. In the regime of repulsive forces, a clear difference in the tip–sample forces was found between the two molecule orientations of the unit cell. For one orientation, the net force is higher than for the other one, an effect that extends over the complete molecule. This observation can be explained by the different electronic structure of the two orientations and demonstrates the capability of high-resolution 3D force spectroscopy to detect even minor deviations in the electronic properties of organic adsorbates.

Acknowledgements

Financial support by the Deutsche Forschungsgemeinschaft (DFG) through the Transregional Collaborative Research Center TRR 61 (project B7) is gratefully acknowledged.

References

1. Tautz, F. S. *Prog. Surf. Sci.* **2007,** *82,* 479–520. doi:10.1016/j.progsurf.2007.09.001
2. Umbach, E.; Glöckler, K.; Sokolowski, M. *Surf. Sci.* **1998,** *402–404,* 20–31. doi:10.1016/S0039-6028(98)00014-4
3. Braun, D.-A.; Schirmeisen, A.; Fuchs, H. *Surf. Sci.* **2005,** *575,* 3–11. doi:10.1016/j.susc.2004.10.032
4. Kraft, A.; Temirov, R.; Henze, S. K. M.; Soubatch, S.; Rohlfing, M.; Tautz, F. S. *Phys. Rev. B: Condens. Matter Mater. Phys.* **2006,** *74,* 041402. doi:10.1103/PhysRevB.74.041402
5. Rohlfing, M.; Temirov, R.; Tautz, F. S. *Phys. Rev. B: Condens. Matter Mater. Phys.* **2007,** *76,* 115421. doi:10.1103/PhysRevB.76.115421
6. Such, B.; Weiner, D.; Schirmeisen, A.; Fuchs, H. *Appl. Phys. Lett.* **2006,** *89,* 093104. doi:10.1063/1.2345235
7. Braun, D.-A.; Weiner, D.; Such, B.; Fuchs, H.; Schirmeisen, A. *Nanotechnology* **2009,** *20,* 264004. doi:10.1088/0957-4484/20/26/264004
8. Gross, L.; Mohn, F.; Moll, N.; Liljeroth, P.; Meyer, G. *Science* **2009,** *325,* 1110–1114. doi:10.1126/science.1176210
9. Mohn, F.; Gross, L.; Moll, N.; Meyer, G. *Nat. Nanotechnol.* **2012,** *7,* 227–231. doi:10.1038/nnano.2012.20
10. Baykara, M. Z.; Schwendemann, T. C.; Altman, E. I.; Schwarz, U. D. *Adv. Mater.* **2010,** *22,* 2838–2853. doi:10.1002/adma.200903909
11. Albrecht, T. R.; Grütter, P.; Horne, D.; Rugar, D. *J. Appl. Phys.* **1991,** *69,* 668–673. doi:10.1063/1.347347
12. Giessibl, F. J. *Appl. Phys. Lett.* **2000,** *76,* 1470–1472. doi:10.1063/1.126067
13. Langewisch, G.; Falter, J.; Fuchs, H.; Schirmeisen, A. *Phys. Rev. Lett.* **2013,** *110,* 036101. doi:10.1103/PhysRevLett.110.036101
14. Hölscher, H.; Langkat, S. M.; Schwarz, A.; Wiesendanger, R. *Appl. Phys. Lett.* **2002,** *81,* 4428–4430. doi:10.1063/1.1525056
15. Sader, J. E.; Jarvis, S. P. *Appl. Phys. Lett.* **2004,** *84,* 1801–1803. doi:10.1063/1.1667267
16. Moll, N.; Gross, L.; Mohn, F.; Curioni, A.; Meyer, G. *New J. Phys.* **2012,** *14,* 083023. doi:10.1088/1367-2630/14/8/083023
17. Langewisch, G.; Kamiński, W.; Braun, D.-A.; Möller, R.; Fuchs, H.; Schirmeisen, A.; Pérez, R. *Small* **2012,** *8,* 602–611. doi:10.1002/smll.201101919
18. Baykara, M. Z.; Dagdeviren, O.; Schwendemann, T. C.; Mönig, H.; Altman, E. I.; Schwarz, U. D. *Beilstein J. Nanotechnol.* **2012,** *3,* 637–650. doi:10.3762/bjnano.3.73

License and Terms

The definitive version of this article is the electronic one which can be found at:
doi:10.3762/bjnano.5.9

Beilstein Journal
of Nanotechnology

The role of surface corrugation and tip oscillation in single-molecule manipulation with a non-contact atomic force microscope

Christian Wagner*[1,2,3], Norman Fournier[2,3], F. Stefan Tautz[2,3] and Ruslan Temirov[2,3]

Full Research Paper

Address:
[1]Leiden Institute of Physics, Universiteit Leiden, Niels Bohrweg 2, 2333 CA Leiden, The Netherlands, [2]Peter Grünberg Institut (PGI-3), Forschungszentrum Jülich, 52425 Jülich, Germany and [3]Jülich Aachen Research Alliance (JARA)-Fundamentals of Future Information Technology, 52425 Jülich, Germany

Email:
Christian Wagner* - c.wagner@fz-juelich.de

* Corresponding author

Keywords:
atomic force microscopy (AFM); force-field model; 3,4,9,10-perylene-tetracarboxylic-dianhydride (PTCDA); qPlus; single-molecule manipulation

Beilstein J. Nanotechnol. **2014,** *5,* 202–209.
doi:10.3762/bjnano.5.22

Received: 28 October 2013
Accepted: 31 January 2014
Published: 26 February 2014

This article is part of the Thematic Series "Noncontact atomic force microscopy II".

Guest Editors: U. D. Schwarz and M. Z. Baykara

Abstract

Scanning probe microscopy (SPM) plays an important role in the investigation of molecular adsorption. The possibility to probe the molecule–surface interaction while tuning its strength through SPM tip-induced single-molecule manipulation has particularly promising potential to yield new insights. We recently reported experiments, in which 3,4,9,10-perylene-tetracarboxylic-dianhydride (PTCDA) molecules were lifted with a qPlus-sensor and analyzed these experiments by using force-field simulations. Irrespective of the good agreement between the experiment and those simulations, systematic inconsistencies remained that we attribute to effects omitted from the initial model. Here we develop a more realistic simulation of single-molecule manipulation by non-contact AFM that includes the atomic surface corrugation, the tip elasticity, and the tip oscillation amplitude. In short, we simulate a full tip oscillation cycle at each step of the manipulation process and calculate the frequency shift by solving the equation of motion of the tip. The new model correctly reproduces previously unexplained key features of the experiment, and facilitates a better understanding of the mechanics of single-molecular junctions. Our simulations reveal that the surface corrugation adds a positive frequency shift to the measurement that generates an apparent repulsive force. Furthermore, we demonstrate that the scatter observed in the experimental data points is related to the sliding of the molecule across the surface.

Introduction

The problem of the adsorption of organic molecules presents many fundamental challenges that stem mostly from the chemical complexity of organic compounds. A complex chemical structure often leads to a wide variety of different types of interactions, the interplay of which defines the behavior of such adsorption systems [1]. With the advent and consequent rapid development of scanning probe microscopy (SPM) techniques, investigations of adsorbate–surface interactions on a single-molecule level have become possible [2-18]. Especially interesting is the possibility of probing the molecule–surface interaction while tuning its strength through a well-controlled single-molecule manipulation induced by the SPM tip [6,11,19-22]. Such experiments demand special instrumentation. It has been demonstrated that the recently developed experimental setups that combine low-temperature scanning tunneling, and qPlus-based non-contact atomic force (NC-AFM) microscopes can be a potent tool when applied to studies of single-molecule manipulation [6,11,15]. The STM function facilitates the effective preparation of the experiment while the NC-AFM, operated simultaneously with the STM, is used to control the structure and to measure the forces that act in the junction during the manipulation. Although, in principle, the conductance measured with the STM could also be used to control the structure during the manipulation of a molecule, the relation between the conductance and the structure of single-molecule junctions is still not generally understood and therefore the forces that act in the junction during the manipulation provide more direct information about the conformation of the molecule.

One of the first attempts to manipulate large organic adsorbates with the tip of the LT-STM/NC-AFM has been made on 3,4,9,10-perylene-tetracarboxylic-dianhydride (PTCDA) molecules [6] (cf. inset of Figure 1a). This system is considered to be an archetypal case of a functional organic adsorbate [1]. PTCDA interacts with surfaces via two distinct functionalities: the π-conjugated perylene core and the carboxylic oxygen atoms attached at the four corners of the rectangular aromatic backbone. Approaching the metal tip to one of the carboxylic oxygen atoms, it is possible to form a local chemical bond between the oxygen and the outermost atom of the tip apex [23]. This bond is of sufficient mechanical strength to allow the lifting of the molecule from the surface up to the point of its complete removal. Recording the frequency shift $\Delta f(z)$ of the qPlus tuning fork during the removal of the molecule, we have previously succeeded in reconstructing the junction structure throughout the manipulation process. This has been achieved by simulating the experimental curves

$$\Delta f\left(z\right)\approx -\frac{f_{\mathrm{qPlus}}}{2k_{\mathrm{qPlus}}}\frac{\partial F_z}{\partial z}\left(z\right),$$

in which f_{qPlus} = 30.311 kHz and k_{qPlus} = 1800 N/m, with a custom-developed force-field model [11].

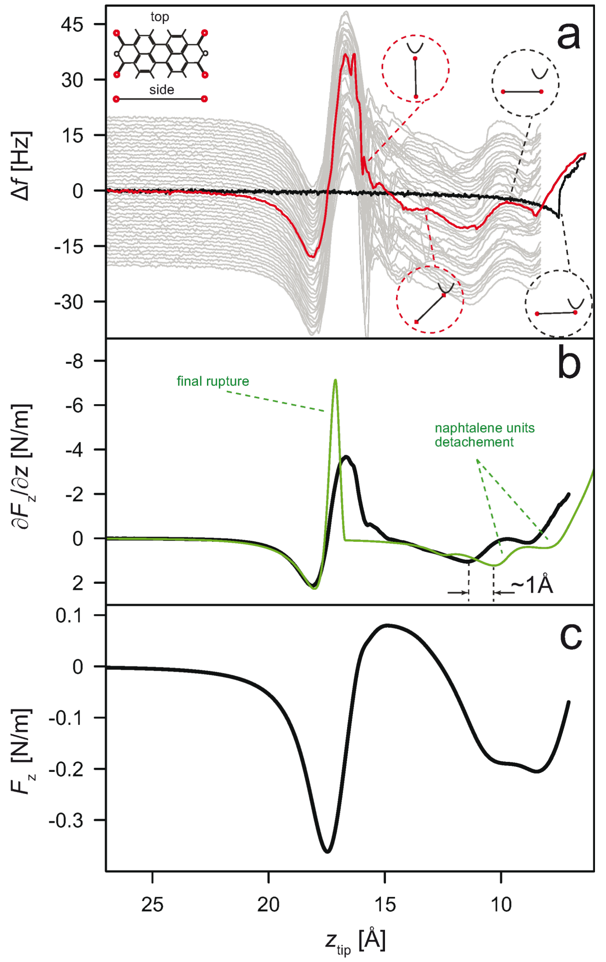

Figure 1: (a) Exemplary data from an experiment in which a single PTCDA molecule on the Au(111) surface was contacted, lifted up and put down again. The number of executed “lift–put” cycles is 40. The surface is located on the right. The black curve shows the initial approach and the contacting event. The first lift curve is shown in red. The consequent “lift–put” curves are shown in grey. The “lift” (“put”) curves are shifted up (down) for clarity. The inset in the upper left corner shows the chemical structure of PTCDA. (b) Generic $\partial F_z/\partial z(z)$ curve (black) for the lifting of PTCDA from Au(111) as obtained by averaging over seven individual contacting experiments. The green curve shows the result of simulations reported in [11]. (c) $F_z(z)$ force curve as obtained by direct integration of the experimental $\partial F_z/\partial z(z)$ shown in panel (b) in black.

A detailed comparison between the simulation and the experiment, however, reveals systematic inconsistencies that can be attributed to three main factors that have been omitted from the initial model: i) the atomic corrugation of the surface, ii) the elasticity of the tip material, and iii) the finite amplitude of the qPlus tuning fork oscillation. Here we take a step towards more realistic force-field simulations of single-molecule manipulation by including the three factors mentioned above into the simulation model and by demonstrating that even their qualitative consideration improves the correspondence between simulations and experiment, and therefore facilitates an improved understanding of the mechanics of single-molecular junctions.

Experimental

The details of PTCDA lifting experiments have been described previously [3,6,11]. Here we briefly repeat the essential features of the experimental procedure. We lift single PTCDA molecules (cf. inset of Figure 1a) from a Au(111) single crystal surface by using an LT-STM/NC-AFM from CREATEC [3,6,11,24] at $T = 5$ K in ultra-high vacuum. When preparing the manipulation we detach one PTCDA molecule from the edge of a molecular island with the tip and move it to a clean spot on the bare metal surface. For establishing the contact to the molecule, the tip is placed over one of its carboxylic oxygen atoms and is moved further towards the surface until a sudden increase in junction conductance and change in Δf occurs (cf. Figure 1a). The conductance increases due to the snap-up of the oxygen atom to the tip, which marks the formation of a chemical tip–molecule bond [23]. Once the contact to the carboxylic oxygen atom has been formed, the tip is retracted away from the surface until the smallest distance between the surface and the atoms of the molecule suspended vertically from the tip is approximately 2 nm. After it has been removed from the surface the molecule is put back again by moving the tip towards the position at which the contact to the molecule has been initially established. In our experiments at least 30% of all tips enabled us to execute series of tens of such “lift–put” cycles without loosing the contact between tip and molecule while simultaneously recording $\Delta f(z)$ of the qPlus sensor [6,11,24].

Figure 1a, which exhibits an example of such a measurement, reveals that the qPlus sensor oscillating with the amplitude of $A_{\mathrm{qPlus}} = 0.2$–0.3 Å can indeed measure the stiffness $\partial F_z/\partial z(z)$ of the junction continuously through all stages of the manipulation experiment. Since the intrinsic stiffness of the qPlus tuning fork (k_{qPlus}) is much higher than the typical strengths of single atomic bonds, it can be used to test processes of single-bond ruptures reliably (in practice the overall success of such tests is limited by the stiffness of the metallic tip that is employed in the manipulation experiment). In particular, the superior stiffness of the qPlus sensor results in the absence of any systematic hysteresis between the stiffness curves measured in the “lift” and “put” parts of the manipulation cycle. As a result, the measurement of Δf shown in Figure 1a exhibits a remarkable degree of overall reproducibility.

A closer inspection, however, reveals that in the intermediate range of tip–surface distances, 13 Å $\le z \le$ 17 Å the recorded Δf traces show higher scattering. Previously we avoided analyzing the detailed junction behavior in this region and concentrated exclusively on the generic features that can be clearly isolated by averaging over many individual manipulation curves (cf. Figure 1b). Averaging out the observed experimental scattering, however, does not resolve the underlying issue, as the presence of the problem becomes apparent again when we try to reconstruct the force acting in the junction by integrating the averaged $\partial F_z/\partial z(z)$ curve displayed in Figure 1b: In the same range, in which $\partial F_z/\partial z(z)$ shows higher scatter, $F_z(z)$ apparently becomes positive, which suggests that the molecule–surface interaction there is repulsive (cf. Figure 1c). It will be shown below that this repulsion is spurious and stems from the combined effects of surface corrugation and the finite amplitude of the qPlus oscillation. In addition, it will be demonstrated that the increased scattering of the experimental data observed in the range 13 Å $\le z \le$ 17 Å can be explained by the sliding of the molecule across the corrugated surface potential. On the methodological side, the important message of this work is to demonstrate that the force-field modeling of single-molecule manipulation can be successful in explaining precise details of the NC-AFM junction mechanics. However, to do so the simulation must account for the oscillatory dynamics of the qPlus sensor.

Simulations

We start building the force-field model of the tip–PTCDA–surface junction according to the principles that have been developed in our earlier work [11]. First we use the standard force-field approach to simulate the intramolecular mechanics of PTCDA, fitting it explicitly to DFT calculations of the mechanical properties of a gas phase molecule. The intramolecular force-field parameters are kept fixed through the rest of the simulation. The molecule–tip bond is described by a spherical Morse potential ($D = 1.3$ eV, $r_0 = 2.2$ Å, $a = 2.0$ Å^{-1}) binding one of the carboxylic oxygens to the outermost tip apex atom. The parameters of this potential have been determined with the help of DFT simulations presented in [23]. The molecule–surface interaction is described as a set of individual atom–surface potentials summed over the atoms constituting PTCDA. The surface is represented by a continuous plane that interacts with the individual atoms of PTCDA via the Pauli repulsion parameterized by an exponential potential that is proprotional to $\exp(-A_{\mathrm{p}}z)$ and the van der Waals interaction expressed as a potential proportional to z^{-3}. We note here that the correct asymptotic behavior of the van der Waals interaction is $(z - z_0)^{-3}$, where z_0 is the location of the van der Waals plane, usually $z_0 = (1/2)\ d_{\mathrm{lattice}}$. However, as discussed in [24,25], this form is only valid for $z > 5$ Å while for $z < 5$ Å the van der Waals interaction is damped. We achieve this damping by letting $z_0 \to 0$. More details can be found in [24]. For simplicity it is assumed that PTCDA consists of only two types of atoms: the 26 backbone (all carbon plus the two anhydride oxygen atoms; hydrogen atom interaction is scaled by 0.25) and the four carboxylic oxygen atoms. The interaction potentials of the carboxylic oxygen and the backbone atoms are described via two separate parameter sets that amount to a total of five free parameters (if additional chemical molecule–surface interactions are absent). These five parameters, which describe the interaction of PTCDA with the surface, have been previously determined by fitting simulated $\partial F_z/\partial z(z)$ curves to the experiment [11] (Figure 1).

In [11] the simulation of the lifting process was carried out in the following way: The model tip was lifted perpendicular to the surface such that the z-coordinate of the tip z_{tip} increased after each step by 1 pm. At each step the molecular geometry and the lateral tip position were relaxed, the former by minimizing the net force that acts on each atom in the molecule, the latter by zeroing the lateral forces on the tip. The thus obtained $F_z(z_{\text{tip}})$ was numerically differentiated to obtain $\partial F_z/\partial z(z_{\text{tip}})$. Finally, the experimental z-scale was aligned to z_{tip} by a rigid translation of the data.

Figure 1b displays a force-gradient curve simulated as described in the previous paragraph. The comparison in Figure 1b reveals a few systematic differences between the experimental (black) and the simulated (green) curves. They, in fact, occur in the same z_{tip} range where Δf shows higher scatter and the reconstructed experimental F_z becomes repulsive. The character of the observed differences can be described as follows: First, the simulation predicts the peak in $\partial F_z/\partial z(z_{\text{tip}})$ that precedes the final rupture of the molecule–surface bond to be considerably sharper than the one seen in the experiment (cf. Figure 1b). Secondly, the distance between the features corresponding to the detachment of the naphthalene units of PTCDA and the final rupture of the molecule–surface bond is larger by about 1 Å in the simulation (note that in our previous analysis we had to cut the experimental curve into two pieces and align them separately with respect to the simulation because of the same problem [11]). As was mentioned above, at least some of the observed inconsistencies occur because our initial force-field model [6,11] does not reflect the actual measurement as performed with the NC-AFM. To account for this, one has to go beyond the calculation of a sequence of relaxed geometries at increasing z_{tip} and zeroed lateral forces. In reality lateral forces are present. This should result in the lower end of the molecule sliding through a corrugated surface potential during the lifting of the tip. The lateral displacement of the molecule over the corrugated surface will be induced by the retraction of the tip as well as by the vibration of the qPlus sensor. As a result, the amplitude of the qPlus oscillation, although small, cannot be neglected any more.

To adapt the model accordingly, we change it in several steps. First we introduce the corrugation of the surface, parameterized with a simple 2D cosine potential

$$V_{\text{corr}}(x,y,z)=\frac{V_c(z)}{4}\left[-\cos\left(\frac{4\pi}{\sqrt{3}c}y\right)-\cos\left(\frac{2\pi}{c}x+\frac{2\pi}{\sqrt{3}c}y\right)-\cos\left(-\frac{2\pi}{c}x+\frac{2\pi}{\sqrt{3}c}y\right)+3\right] \quad (1)$$

with the in-plane nearest neighbor distance $c = 2.884$ Å corresponding to the Au(111) surface structure and a corrugation amplitude $V_c(z) \approx (2.6/z)^7$ that decays rapidly with increasing distance to the surface. Since here we aim at a qualitative description, the precise functional form of the corrugation potential is not relevant and we also can assume that the surface corrugation is only felt by the carboxylic oxygen atoms of PTCDA (which have the strongest tendency to form local bonds) [1]. This simplification enables a much clearer interpretation of the simulation results, in particular a direct link to an analytical model that we discuss later. Extending the model further, we allow for a finite stiffness of the tip that is simulated by introducing an additional atom situated above the tip apex atom and connected to it via a harmonic 1D potential (cf. inset Figure 2a). The stiffness k_{tip} of this harmonic bond is fixed, but the bond itself is allowed to relax during the simulation. In the simulation we find a maximal tip-extension of 1 Å. Assuming that a mesoscopic part of the tip relaxes, this elongation brakes up into relative atomic displacements of small fractions of an angstrom, justifying the use of an harmonic potential. Finally, the new model also accounts for the oscillation of the qPlus sensor. To do so, the complete lifting process is simulated in two stages. As before, z_{tip} is increased in steps of 1 pm and the structure (including the position of the lower end of the molecule as well as the extension of the tip) is relaxed. The relaxation is done by *either* allowing the lateral coordinate of the tip to change (no lateral forces in the junction are allowed, hence the lower end of the molecule does not slide over the surface) *or* fixing the lateral coordinate of the tip, thus enforcing molecular sliding if necessary. After each retraction–relaxation step the tip is moved *vertically* around z_{tip} in $N = 150$ steps of $\Delta z = 0.4$ pm each, so that the maximum deviation $(N\Delta z)/4$ totals to $A_{\text{qPlus}} = 0.15$ Å. At each deflection step i ($i \in \mathbb{Z}, -75 \le i \le 75$) the molecule is allowed to relax and the force $F_z(z_{\text{tip}} + i\Delta z)$ acting on the tip from the molecule is calculated. Numerically solving the equation of motion for the qPlus sensor with the effective mass ($m_{\text{eff}} = k_{\text{qPlus}}/2\pi f_{\text{qPlus}} = 49.62$ µg) under the influence of the total force $F_{z,\text{Total}}(z_{\text{tip}} + i\Delta z) = k_{\text{qPlus}}\, i\Delta z + F_z(z_{\text{tip}} + i\Delta z)$, we obtain the frequency of its oscillation. The time step used in the simulation of the tip oscillation is 200 ps, which corresponds to a frequency resolution of about 0.2 Hz. Note that the motion of the tip during one oscillation cycle is strictly vertical, whereas the overall motion of the tip during the retraction–relaxation steps might also involve a lateral displacement of the tip.

Results and Discussion

To understand how the refinement of the mechanical model of the junction influences the outcome of the simulations we perform several different simulation runs with tip oscillation and surface corrugation. In the first run we make the tip infinitely stiff ($k_{\text{tip}} = \infty$) and additionally relax the lateral position of the tip after each lifting step, such that no lateral forces are present and therefore the lower end of the molecule does not slide along the surface during lifting. The resulting $\partial F_z/\partial z(z_{\text{tip}})$ curve is shown in red in Figure 2a. Taking the difference between the red curve and the green curve obtained in [11] with the original model, i.e., without tip oscillation and surface corrugation, we discover that the inclusion of the qPlus oscillation and the surface corrugation in the model changes $\partial F_z/\partial z(z_{\text{tip}})$ by adding an additional negative correction term Δ_{corr} that increases its absolute value towards the end of the manipulation (cf. Figure 2b). Note that by definition of our positive z-direction the force gradient $\partial F_z/\partial z$ has the opposite sign of the frequency shift. Hence, the correction term means a positive contribution to Δf. If integrated, Δ_{corr} will produce an additional repulsive contribution to the force measured during the lifting, just as observed in experiment (Figure 1b and c). An understanding of the physical mechanism behind Δ_{corr} could then also clarify the unexpected appearance of the repulsive force in our measurements.

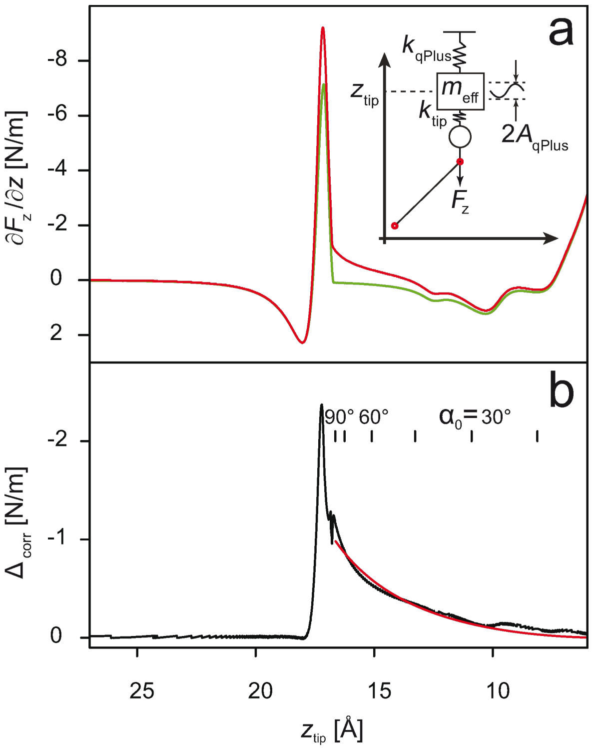

Figure 2: (a) Comparison between the $\partial F_z/\partial z(z)$ curves obtained from the initial ([11]) and the extended (this work) force-field model. The green curve is the same as the one shown in Figure 1b and was obtained with the model that accounts neither for oscillation of the qPlus sensor nor for the corrugation of the surface. The red curve is produced with the model taking both of the above effects into account (cf. text). The inset in the upper right corner clarifies the schematics of the single-molecule junction used in the extended simulation model. (b) Correction term Δ_{corr} calculated as the difference between the two curves from panel (a). The red curve was obtained from the analytic expression (Equation 2) and fitted to the simulated Δ_{corr}. Additional tick-marks show the correspondence between the α_0 and z_{tip} scales (cf. text).

The way in which the surface corrugation affects $\partial F_z/\partial z(z)$ curves measured with NC-AFM can be understood by considering the model of an elastically stretchable (and compressible) rod lifted from a corrugated surface. The model consists of two connected springs, one of which mimics the elasticity of the rod, while the other accounts for the surface corrugation potential felt by the lower end of the rod (cf. Figure 3, left). In the model the motion of the lower end of the rod is confined to the surface. Since the sole purpose of this one-dimensional spring model is the analysis of the influence of surface corrugation on dynamic force measurements with the qPlus sensor, we assume that at each tilt angle α_0 of the rod with respect to the surface plane both springs are fully relaxed (zero forces). This in fact corresponds to the situation of the molecule in the simulated junction when we allow lateral relaxation of the tip position at each step in z_{tip} (the vertical attractive forces in the simulated junction are of course non-zero, but since they do not play any role for understanding the influence of the surface corrugation on dynamic force measurements with the qPlus sensor, they are not included in the spring model of Figure 3, left).

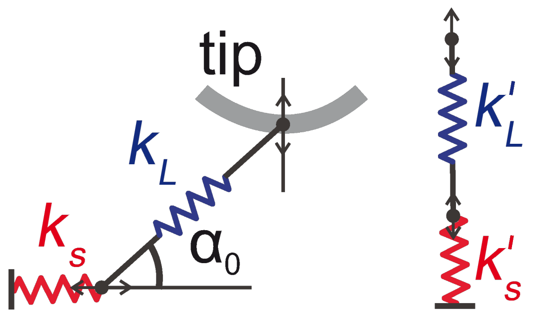

Figure 3: One-dimensional spring model of the manipulation process. Left: The molecule is represented by a spring with stiffness k_L, the surface corrugation by a spring with stiffness k_S. The molecule is tilted by an angle α_0 with respect to the surface. Right: For simplification, the two springs are replaced by vertical effective springs with constants k'_L and k'_S. For more details, refer to the main text.

The relevant quantity that we seek an expression for is the gradient of the force needed to move the upper end of the rod along the vertical, corresponding to the direction of oscillation of the qPlus sensor, evaluated at the relaxed position of the springs (equivalent to zero deflection $i\Delta z$ of the qPlus sensor). Initially assuming spring S to be infinitely stiff ($k_S \to \infty$), we find $\partial F_z^{k_S \to \infty} / \partial z = -k_L \sin^2 \alpha_0 = -k'_L$ for spring L, and vice versa for an infinitely stiff spring L ($k_L \to \infty$) we find $\partial F_z^{k_L \to \infty} / \partial z = -k_S \tan^2 \alpha_0 = -k'_S$ for spring S. A detailed derivation of these expressions can be found in Supporting Information File 1. We simplify the model by replacing S and L by two effective vertical springs, adding the spring constants derived in the two opposite limits, k'_S and k'_L, in series (Figure 3 right). In the present case this is a realistic approximation, because for most angles α_0 the behavior of the model will be determined by the softer spring S (surface corrugation) and L can be considered as rigid, except for α_0 close to 90°, where k'_S diverges while k'_L remains finite. The total spring constant of the system becomes

$$\begin{aligned}\Delta_{\mathrm{corr}}\left(\alpha_0\right) &\propto \frac{\partial F_z}{\partial z}\left(\alpha_0\right)\\ &= -\frac{k'_L k'_S}{k'_L + k'_S}\\ &= -\frac{k_L \sin^2 \alpha_0 \cdot k_S \tan^2 \alpha_0}{k_L \sin^2 \alpha_0 + k_S \tan^2 \alpha_0}.\end{aligned} \tag{2}$$

This expression reflects the basic properties of the correction term $\Delta_{\mathrm{corr}}(\alpha_0)$. Firstly, we find that $\Delta_{\mathrm{corr}}(\alpha_0)$ must always be negative (Δf positive), and hence produce an additional repulsion after integration. Furthermore, $\Delta_{\mathrm{corr}}(\alpha_0)$ is zero for a molecule that is lying flat on the surface ($\alpha_0 = 0$) and it approaches the intrinsic stiffness of the molecule $-k_L$ for an upright standing orientation ($\alpha_0 = 90°$) where k'_S diverges. As the fit of $\Delta_{\mathrm{corr}}(\alpha_0)$ from the force field simulation in Figure 2b shows, the above analytic expression fully explains its qualitative behavior.

Having studied the influence of the tip oscillation and the surface corrugation potential, we turn to the next simulation run. This time we additionally allow the tip to deform (in the vertical direction only) in the course of the lifting process. In Figure 4a we compare simulations performed for two different k_{tip} values that were chosen according to typical values reported for atomic nano-contacts [26]. Apparently, the softening of the tip has a strong influence on the shapes of the calculated $\partial F_z/\partial z(z_{\mathrm{tip}})$ curves. This influence is strongest when the force pulling the tip towards the surface is large. The first of such instances can be observed in the z_{tip} range in which the naphthalene units of PTCDA are detached from the surface (8 Å $\le z_{\mathrm{tip}} \le$ 12 Å, cf. Figure 1b), while the second occurs during the final detachment of the molecule (17 Å $\le z_{\mathrm{tip}} \le$ 20 Å). In both cases the effect of the soft tip manifests itself as a partial decoupling between the position z of the tip (i.e., the read-out in the experiment of the position of the piezo-actuator to which the tip is attached) and the position z_{tip} of the microscopic tip apex, the latter determining the actual junction structure. As a result, each time the attractive force acting on the tip apex rises, the microscopic tip apex gets elongated and thus the features of the $\partial F_z/\partial z(z_{\mathrm{tip}})$ curve are shifted to higher z_{tip} values. As soon as the attractive force decreases, the tip apex shrinks back, thus synchronizing the microscopic and the macroscopic z-scales again. Overall, allowing elastic tip deformations improves the agreement of the simulated curve with the experimental one, mostly by smearing out the sharp $\partial F_z/\partial z(z_{\mathrm{tip}})$ peak.

Finally, we combine our findings regarding surface corrugation and tip stiffness to perform the most realistic simulation of our single-molecule manipulation experiments yet. As in the experiment, we use a strictly vertical tip trajectory that leads to a sliding motion of the lower end of the molecule across the surface prior to its detachment from the surface. The sliding motion manifests itself in the simulations as a series of spikes in $\partial F_z/\partial z(z_{\mathrm{tip}})$ (cf. Figure 4b). Qualitatively, the spikes produced in the simulation look similar to the features observed in the individual $\partial F_z/\partial z(z)$ curves recorded in the experiment. Furthermore, both in the simulated and experimental curves the spike density on the z-axis increases as the molecule approaches the upright configuration. This is fully consistent with the assumption that the spikes are due to the lower end of the molecule sliding across the corrugation potential of the surface: Indeed, as the molecule stands-up the frequency of the sliding events per unit distance of the vertical tip retraction must increase. By the same token, it is very unlikely that the spikes result from structural changes in the tip. Such changes would be expected to occur mostly where the vertical force on the tip is strong (for $z_{\mathrm{tip}} <$ 12 Å and 16.5 Å $< z_{\mathrm{tip}} <$ 18 Å; see Figure 1c). However, this is not the region in which spikes are observed in the experiment. Lateral forces are not expected to play a role in deforming the tip. The simulation shows that due to the weak surface corrugation they are approximately ten times smaller than the vertical force.

Comparing the result of the final simulation run to the experiment, we note further that the overall fit quality is not perfect. In particular, the detachment of the naphthalene units in the simulation still happens 1 Å closer to the surface (compare Figure 1b to Figure 4b). To address the remaining discrepancies, it would be necessary to refine the parameter set describing the interaction of PTCDA with the Au(111) surface.

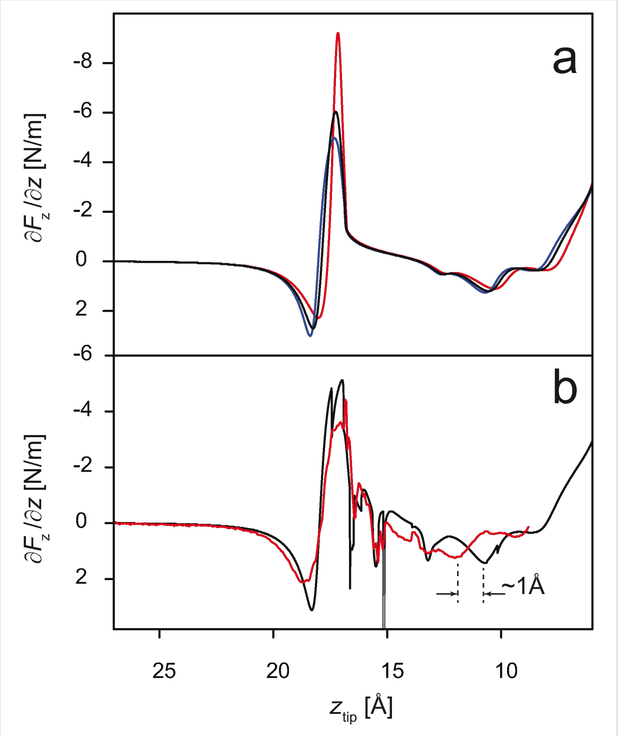

Figure 4: (a) Comparison between the $\partial F_z/\partial z(z)$ curves of PTCDA lifted from Au(111), obtained for different tip elastic constants. Simulations take oscillations of the qPlus sensor and the surface corrugation into account. Lateral forces are zeroed out (cf. text). Red corresponds to $k_{tip} = \infty$, blue to k_{tip} = 9 N/m, black to k_{tip} = 14 N/m. (b) Comparison between an individual experimental curve (red) taken from the series shown in Figure 1a and the simulation (black) obtained with oscillations of the qPlus sensor, tip flexibility, surface corrugation, and non-zero lateral forces acting during lifting. Sharp spikes in the black curve indicate sliding of the lower end of PTCDA across the corrugated potential of the surface.

Conclusion

In summary, we have simulated the lifting of a single PTCDA molecule from the surface using an extended force-field model that accounts for both surface corrugation and tip elasticity. Most importantly, the model also explicitly includes the finite oscillation amplitude of the qPlus tuning fork sensor. This has been achieved by the direct calculation of the qPlus oscillation frequency, solving the equation of motion of the tip within a full oscillation cycle. We have shown that the oscillation of the sensor together with the corrugation of the surface adds a positive frequency shift to the measurement that generates an apparent repulsive force. This contribution that we refer to as the correction term Δ_{corr} should get stronger with increasing corrugation. Therefore, we suggest that for strongly interacting surfaces its influence may dominate the measurement, in which case the measured force might seem repulsive during the whole molecular lifting process.

Finally, we have demonstrated that the scattering observed in the experiments is related to the sliding of the molecule across the surface that occurs in a certain z-range. Control over the sliding motion could be very difficult to achieve, since it requires control of the initial adsorption site and, in the best case, vanishing oscillation amplitude of the qPlus sensor. We thus conclude that for a fully controlled molecular lifting experiment it is desirable to lift molecules along trajectories that minimize the lateral forces in the junction.

Supporting Information

Supporting Information File 1

Derivation of the two-spring model
[http://www.beilstein-journals.org/bjnano/content/supplementary/2190-4286-5-22-S1.pdf]

Acknowledgements

RT acknowledges support from the Helmholtz Gemeinschaft. CW acknowledges support from the European Union by a Marie-Curie Fellowship. FST acknowledges support from the Deutsche Forschungsgemeinschaft through the priority program SPP 1243 “Quantum Transport Through Molecules” (DFG TA 244/5). The authors thank R. Merkel (Forschungszentrum Jülich) for helpful discussions.

References

1. Tautz, F. S. *Prog. Surf. Sci.* **2007,** *82,* 479. doi:10.1016/j.progsurf.2007.09.001
2. Otero, R.; Rosei, F.; Besenbacher, F. *Annu. Rev. Phys. Chem.* **2006,** *57,* 497. doi:10.1146/annurev.physchem.57.032905.104634
3. Temirov, R.; Lassise, A.; Anders, F. B.; Tautz, F. S. *Nanotechnology* **2008,** *19,* 065401. doi:10.1088/0957-4484/19/6/065401
4. Lafferentz, L.; Ample, F.; Yu, H.; Hecht, S.; Joachim, C.; Grill, L. *Science* **2009,** *323,* 1193. doi:10.1126/science.1168255
5. Schull, G.; Frederiksen, T.; Arnau, A.; Sánchez-Portal, D.; Berndt, R. *Nat. Nanotechnol.* **2010,** *6,* 23. doi:10.1038/nnano.2010.215
6. Fournier, N.; Wagner, C.; Weiss, C.; Temirov, R.; Tautz, F. S. *Phys. Rev. B* **2011,** *84,* 035435. doi:10.1103/PhysRevB.84.035435
7. Fu, Y.-S.; Schwöbel, J.; Hla, S.-W.; Dilullo, A.; Hoffmann, G.; Klyatskaya, S.; Ruben, M.; Wiesendanger, R. *Nano Lett.* **2012,** *12,* 3931. doi:10.1021/nl302166z
8. Schulze, G.; Franke, K. J.; Pascual, J. I. *Phys. Rev. Lett.* **2012,** *109,* 026102. doi:10.1103/PhysRevLett.109.026102
9. Hauptmann, N.; Mohn, F.; Gross, L.; Meyer, G.; Frederiksen, T.; Berndt, R. *New J. Phys.* **2012,** *14,* 073032. doi:10.1088/1367-2630/14/7/073032
10. Chiutu, C.; Sweetman, A. M.; Lakin, A. J.; Stannard, A.; Jarvis, S.; Kantorovich, L.; Dunn, J. L.; Moriarty, P. *Phys. Rev. Lett.* **2012,** *108,* 268302. doi:10.1103/PhysRevLett.108.268302
11. Wagner, C.; Fournier, N.; Tautz, F. S.; Temirov, R. *Phys. Rev. Lett.* **2012,** *109,* 076102. doi:10.1103/PhysRevLett.109.076102
12. Pawlak, R.; Fremy, S.; Kawai, S.; Glatzel, T.; Fang, H.; Fendt, L.-A.; Diederich, F.; Meyer, E. *ACS Nano* **2012,** *6,* 6318. doi:10.1021/nn301774d

13. Mohn, F.; Gross, L.; Moll, N.; Meyer, G. *Nat. Nanotechnol.* **2012,** *7,* 227. doi:10.1038/nnano.2012.20
14. Wegner, D.; Yamachika, R.; Zhang, X.; Wang, Y.; Crommie, M. F.; Lorente, N. *Nano Lett.* **2013,** *13,* 2346. doi:10.1021/nl304081q
15. Langewisch, G.; Falter, J.; Fuchs, H.; Schirmeisen, A. *Phys. Rev. Lett.* **2013,** *110,* 036101. doi:10.1103/PhysRevLett.110.036101
16. Schuler, B.; Liu, W.; Tkatchenko, A.; Moll, N.; Meyer, G.; Mistry, A.; Fox, D.; Gross, L. *Phys. Rev. Lett.* **2013,** *111,* 106103. doi:10.1103/PhysRevLett.111.106103
17. de Oteyza, D. G.; Gorman, P.; Chen, Y.-C.; Wickenburg, S.; Riss, A.; Mowbray, D. J.; Etkin, G.; Pedramrazi, Z.; Tsai, H.-Z.; Rubio, A.; Crommie, M. F.; Fischer, F. R. *Science* **2013,** *340,* 1434. doi:10.1126/science.1238187
18. Albrecht, F.; Neu, M.; Quest, C.; Swart, I.; Repp, J. *J. Am. Chem. Soc.* **2013,** *135,* 9200. doi:10.1021/ja404084p
19. Frei, M.; Aradhya, S. V.; Koentopp, M.; Hybertsen, M. S.; Venkataraman, L. *Nano Lett.* **2011,** *11,* 1518. doi:10.1021/nl1042903
20. Aradhya, S. V.; Frei, M.; Hybertsen, M. S.; Venkataraman, L. *Nat. Mater.* **2012,** *11,* 872. doi:10.1038/nmat3403
21. Hao, X.; Zhu, N.; Gschneidtner, T.; Jonsson, E. Ö.; Zhang, J.; Moth-Poulsen, K.; Wang, H.; Thygesen, K. S.; Jacobsen, K. W.; Ulstrup, J.; Chi, Q. *Nat. Commun.* **2013,** *4,* 2121. doi:10.1038/ncomms3121
22. Aradhya, S. V.; Venkataraman, L. *Nat. Nanotechnol.* **2013,** *8,* 399. doi:10.1038/nnano.2013.91
23. Toher, C.; Temirov, R.; Greuling, A.; Pump, F.; Kaczmarski, M.; Cuniberti, G.; Rohlfing, M.; Tautz, F. S. *Phys. Rev. B* **2011,** *83,* 155402. doi:10.1103/PhysRevB.83.155402
24. Wagner, C.; Fournier, N.; Ruiz, V. G.; Li, C.; Müllen, K.; Rohlfing, M.; Tkatchenko, A.; Temirov, R.; Tautz, F. S. **2014**. *To be published*.
25. Rohlfing, M.; Bredow, T. *Phys. Rev. Lett.* **2008,** *101,* 266106. doi:10.1103/PhysRevLett.101.266106
26. Rubio, G.; Agraït, N.; Vieira, S. *Phys. Rev. Lett.* **1996,** *76,* 2302. doi:10.1103/PhysRevLett.76.2302

License and Terms

The definitive version of this article is the electronic one which can be found at:
doi:10.3762/bjnano.5.22

Beilstein Journal
of Nanotechnology

Unlocking higher harmonics in atomic force microscopy with gentle interactions

Sergio Santos*,‡1, Victor Barcons‡1, Josep Font1 and Albert Verdaguer2,3

Full Research Paper

Open Access

Address:
1Departament de Disseny i Programació de Sistemes Electrònics, UPC - Universitat Politècnica de Catalunya Av. Bases, 61, 08242 Manresa (Barcelona), Spain, 2ICN2 - Institut Catala de Nanociencia i Nanotecnologia, Campus UAB, 08193 Bellaterra (Barcelona), Spain and 3CSIC - Consejo Superior de Investigaciones Cientificas, ICN2 Building ,08193 Bellaterra (Barcelona), Spain

Email:
Sergio Santos* - santos_en@yahoo.com

* Corresponding author ‡ Equal contributors

Keywords:
atomic force microscopy; chemistry; composition; heterogeneity; higher harmonics; phase

Beilstein J. Nanotechnol. **2014,** *5,* 268–277.
doi:10.3762/bjnano.5.29

Received: 09 October 2013
Accepted: 14 February 2014
Published: 11 March 2014

This article is part of the Thematic Series "Noncontact atomic force microscopy II".

Guest Editors: U. D. Schwarz and M. Z. Baykara

Abstract

In dynamic atomic force microscopy, nanoscale properties are encoded in the higher harmonics. Nevertheless, when gentle interactions and minimal invasiveness are required, these harmonics are typically undetectable. Here, we propose to externally drive an arbitrary number of exact higher harmonics above the noise level. In this way, multiple contrast channels that are sensitive to compositional variations are made accessible. Numerical integration of the equation of motion shows that the external introduction of exact harmonic frequencies does not compromise the fundamental frequency. Thermal fluctuations are also considered within the detection bandwidth of interest and discussed in terms of higher-harmonic phase contrast in the presence and absence of an external excitation of higher harmonics. Higher harmonic phase shifts further provide the means to directly decouple the true topography from that induced by compositional heterogeneity.

Introduction

It has long been recognized in the community that higher harmonics encode detailed information about the non-linearities of the tip–sample interaction in dynamic atomic force microscopy (AFM) [1-5]. Physically, non-linearities relate to the chemical and mechanical composition [6] of the tip–sample system and imply that higher harmonics can be translated into conservative and dissipative [7] nanoscale and atomic properties [8]. Furthermore, conventional dynamic AFM can already reach molecular [9,10], sub-molecular [11] and atomic [12,13] resolution in some systems. Thus, the simultaneous detection and interpretation of multiple higher harmonic signals while scanning [14] can lead to spectroscopy-like capabilities [15,16], such as chemical identification, with similar or higher resolution [5,17,18]. The higher harmonic approach however, and particularly in other than highly damped environments [19,20], requires dealing with the recurrent challenge of detecting higher harmonics [1,3,21,22]. Higher harmonics are a result of the non-linear tip–sample interaction in the sense that the interaction effectively acts as the driving force of each harmonic component [7]. Accordingly, relatively high peak forces, of the order of 1–100 nN, are required [22,23] to excite higher harmonics above the noise level. In order to address this issue, in 2004 Rodriguez and García [23] proposed to drive the second higher flexural mode of the cantilever with an external drive. In this way, and by driving with sufficiently small (sub-nanometer) second mode amplitudes, the first mode amplitude [24] or frequency [17] can be employed to track the sample in amplitude or frequency modulation (AM and FM), respectively. The second mode can then be left as an open loop for high sensitivity mapping of compositional variations [25] or as a closed loop, in which case the tip–sample stiffness k_{ts} can be computed [17,26]. More recently, the multifrequency AFM approach has been extended to employ three flexural modes [27] and/or simultaneous torsional modes [28], for which, typically, the frequency and mode under consideration are externally excited [24]. In summary, FM and/or AM feedback systems can be employed in one [29], several [27] or all of the modes under consideration in order to quantify properties on the nanoscale through observables [30] while simultaneously enhancing sensitivity and throughput [31]. The dynamics in the multifrequency approach, however, might lead to extra complexities in the analysis, acquisition and interpretation of data [31,32]. For example, recent studies [31] show that multiple regimes of operation might follow depending on the relative kinetic energy between the higher mode of choice and the fundamental eigenmode [31,33].

Here, exact multiple harmonics of the fundamental drive frequency are externally excited above the noise level to open multiple contrast channels that are sensitive to compositional variations. The focus is on amplitude modulation (AM) AFM, in which the fundamental amplitude $A_1 \equiv A$ tracks the sample as usual. For standard cantilevers the eigenmodes are nonharmonic [29]. That is, the natural resonant frequencies of the cantilevers are not integer multiples. Furthermore, these natural frequencies relate to the geometry and mechanical properties of the cantilever [34]. The practical implication is that it is only easy to induce large oscillations at the frequencies that coincide with these natural frequencies. Nevertheless the tip–sample coupling always occurs via harmonic frequencies. This is because a periodic motion always implies that there is a fundamental frequency and that all other higher frequencies are integer multiples of the fundamental [35]. The implication is that externally introducing frequencies other than harmonic frequencies could induce a fundamental sub-harmonic frequency [24,35]. In short, the incommensurability between external drives in the standard multifrequency approach implies that the cantilever motion is not exactly periodic relative to the fundamental drive and that a sub-harmonic excitation typically follows [32]. Furthermore, simplifications in eigenmode frequency shift theory [36] might lead to inconsistencies [37]. This issue becomes more prominent when dealing with third or higher eigenmodes [27,38], for which the theory is now emerging [31]. The introduction of exact harmonic external drives keeps the fundamental frequency intact and the analytical expressions are simplified by orthogonality. Furthermore $2(N-1)$ observables, i.e., higher harmonic amplitudes and phases, are made available even with peak forces no higher than 200 pN, as they are required [25,39] for high resolution and minimally invasive imaging of soft matter. Thermal fluctuations are also considered here in order to establish a possible loss of contrast due to fundamental sources of noise. It is also shown that true topography and apparent topography, which is induced by chemical heterogeneity, can be decoupled at once by monitoring the phase contrast of higher harmonics.

Results and Discussion

Consider the equation of motion of the *m*th eigenmode

$$\frac{k_{(m)}}{\omega_{(m)}^{2}}\ddot{z}_{(m)}(t)+\frac{k_{(m)}}{Q_{(m)}\omega_{(m)}}\dot{z}_{(m)}(t)+k_{(m)}z_{(m)}=F_{\mathrm{D}}+F_{\mathrm{ts}}(d,\dot{d}), \quad (1)$$

where $k_{(m)}$, $Q_{(m)}$, $\omega_{(m)}$, and $z_{(m)}$ are the spring constant, quality factor, natural frequency and position of the *m*th eigenmode. The term F_{D} stands for the external driving force

$$F_{\mathrm{D}}(t)=\sum_{n=1}^{N}F_{0n}\cos(n\omega t), \quad (2)$$

where the subscript without brackets, *n*, indicates the harmonic number. Note that here $\omega_n = n\omega$, where ω is the fundamental drive frequency set near mode $m = 1$, i.e., $\omega = \omega_1 \equiv \omega_{(1)}$. The term F_{ts} is the tip–sample force, which is a function of both the tip–sample distance, *d*, and velocity, $\dot{d}$. Here however, we focus on conservative forces since these are present even with gentle interactions. Hence we can write $F_{\mathrm{ts}}(d)$. Since the higher harmonic amplitudes here are externally excited, the number of harmonics *N* that is to be monitored can, in principle, be arbitrarily chosen up to the limits of frequency detection, i.e., of the order of MHz, without compromising detection. The main constraint is that the number of higher modes, *M*, that is to be considered needs to be consistent with the number of higher harmonics *N* that are to be analysed [22]. For simplicity, we consider $M = 2$ and $N = 10$ in the numerical analysis without loss of generality. For clarity we emphasize that *M* is the number of modes and *N* is the number of harmonics taken into consideration in the analysis in this work. A particular mode or harmonic is referred to in lower case, i.e., *m* or *n* respectively.

The *n*th harmonic velocity $\dot{z}_n$ is

$$\dot{z}_n\left(t\right) = -A_n \omega_n \sin\left(n\omega t - \phi_n\right). \tag{3}$$

Multiplying Equation 1 by Equation 3 and integrating over a cycle results in

$$\begin{aligned} &\pi k\left[n^3 A_{(m)n} A_n \mathrm{B}_{(m)n}\right] \\ &+\pi \frac{k}{Q}\left[n^2 A_{(m)n} A_n \mathrm{C}_{(m)n}\right] \\ &-\pi k_{(m)}\left[n A_{(m)n} A_n \mathrm{B}_{(m)n}\right] = \pi F_{0(n)} n A_n \sin\phi_n - E_n \ , \end{aligned} \tag{4}$$

where 1 is assumed when no subscripts are given. The relationships $(\omega/\omega_{(m)})^2 = k/k_{(m)}$ and $Q/Q_{(m)} = \omega/\omega_{(m)}$ [7] have been employed in Equation 4 and it has been assumed that the fundamental drive frequency ω is set near $\omega_{(1)}$. Furthermore, in Equation 4 $A_{(m)n}$ and A_n are the amplitudes of the *n*th harmonic that correspond to the position of mode *m*, i.e., $z_{(m)}$, and to the absolute position of the tip, i.e., *z*, respectively. Also

$$\mathrm{B}_{(m)n} = \cos\phi_n \sin\phi_{(m)n} - \sin\phi_n \cos\phi_{(m)n} \ , \tag{5}$$

$$\mathrm{C}_{(m)n} = \cos\phi_n \cos\phi_{(m)n} + \sin\phi_n \sin\phi_{(m)n} \ , \tag{6}$$

$$E_n = -\int_{u=t}^{u=t+T} F_{\mathrm{ts}}(d) z_n dt \ , \tag{7}$$

where $\phi_{(m)n}$ and ϕ_n are the phase shifts of the *n*th harmonic that correspond to the *m*th mode position and the absolute position, *z*, respectively, and E_n is the energy involved with the n_{th} harmonic tip–sample interaction. Near the modal frequency $\omega_{(m)}$ only the *m*th mode significantly contributes to the interaction and $\mathrm{B}_{(m)n} \approx 0$ and $\mathrm{C}_{(m)n} \approx 1$ in Equation 4. This approximation has been currently employed in the literature [6]. Nevertheless, far from the modes, these terms might not be zero. To allow for simple analytical formulae and ease the qualitative interpretation we consider the harmonics close to the modes only [6]. Then

$$E_n \approx \pi F_{0n} n A_n \sin\phi_n - \pi \frac{k}{Q} n^2 A_n^2 \ . \tag{8}$$

If the *n*th drive F_{0n} is zero, then

$$E_n \approx -\pi \frac{k}{Q} n^2 A_n^2 \ . \tag{9}$$

Equation 9 is the energy transferred to the *n*th harmonic of the cantilever through the tip–sample interaction. It should be noted that this is consistent with a conservative tip–sample force $F_{\mathrm{ts}}(d)$ since the energy is provided during each cycle by the external driving force(s). The quadratic dependence of the energy E_n on nA_n is of particular relevance for the detection of higher harmonics. First, Equation 9 implies that for a given amplitude A_n the transfer of energy E_n scales quadratically with the harmonic number. This explains why for sufficiently large *n*, higher harmonics are typically undetectable. Second, the proportionality between E_n and A_n^2 in Equation 9 explains why for higher harmonic amplitudes to be detected, the interaction in Equation 7 needs to be considerably large, even when *n* is not necessarily very large.

From Equation 8 it follows that A_n can be set to any arbitrary value by increasing F_{0n}, even if there is no tip–sample energy transfer, i.e., $E_n = 0$. The higher harmonics for the free cantilever are termed A_{0n}. This case corresponds to a free cantilever oscillating sufficiently high above the sample ($A/A_0 = 1$) as illustrated in Figure 1 (circles). The data has been acquired by numerically solving the simultaneous equations in Equation 1 for the first two flexural modes, i.e., $M = 2$, and for $N = 10$. Furthermore, since only long range attractive forces are of interest here, the tip–sample force is simply [23]

$$F_{\mathrm{ts}}\left(d\right) = -\frac{RH}{6d^2} \text{ with } d > a_0 \ , \tag{10}$$

where *R* is the tip radius, *H* is the Hamaker constant and a_0 is an intermolecular distance ($a_0 = 0.165$ nm throughout and in all the data here, we consider $d > a_0$ throughout). It is relevant to note that the Hamaker constant depends on the tip and sample in the sense that its value is determined by the atomic composition or chemical elements that compose the tip and the sample [40,41]. For this reason, in this work we will employ the terms chemistry, Hamaker and tip–sample composition or chemistry interchangeably. The common parameters in this work are $k = 2$ N/m, $Q = 100$, $\omega = 2\pi\cdot70$ kHz and $R = 7$ nm, i.e., they correspond to commercially available standard probes for AM AFM. Furthermore, in Figure 1, $H = 6.2 \times 10^{-19}$ J, i.e., it is close to that calculated for materials such as polystyrene or fused quartz [40]. The parameters for the second mode have been obtained with the above formulae [7]. The modal frequencies 1 and 2 are shown with dashed lines. The phase shifts ϕ_n are shown in the vertical axis in Figure 1 for each harmonic.

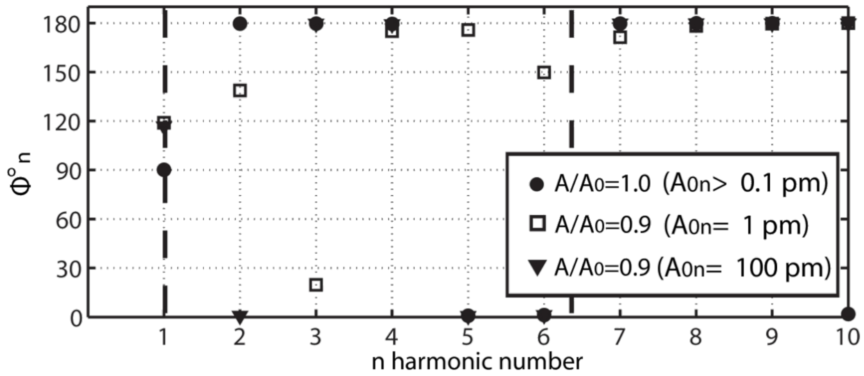

Figure 1: Phase shifts ϕ_n of higher harmonics, including the fundamental shift ϕ_1, when *N* = 10 external harmonic drives are introduced. The values ϕ_n are shown for a free oscillating cantilever (circles). For the free cantilever the separation is $z_c >> A/A_0 = 1$. Then the cantilever is gently interacting (peak forces smaller than 20 0pN) with the surface, i.e., $A/A_0 < 1$, while the free higher harmonic amplitudes A_{0n} are set to 1 (squares) and 100 (triangles) pm.

The actual harmonic amplitudes A_n that resulted when interacting are not shown, instead $A_n \approx A_{0n}$ is given throughout. The case of a free cantilever (circles) shows that the fundamental phase shift ϕ_1 is exactly 90 degrees as expected while the higher harmonic phase shifts ϕ_n ($n > 1$) lie either close to 180° or to 0°. This is in agreement with Equation 8 when $E_n \approx 0$ since then

$$\sin\phi_n \approx \frac{1}{(Q_{(m)}Q)^{1/2}}\frac{1}{n}, \qquad (11)$$

where the approximation $F_{0n} \approx k_{(\mathrm{m})}n^2A_{0n}$ (near *m*) has been employed. Also from Figure 1 (circles) it follows that for a free cantilever, and when *n* is higher than the modal frequency (close to a given mode and for $n > 1$), $\phi_n \approx 180°$. When *n* is lower than the modal frequency $\phi_n \approx 0°$. This is true irrespective of the value of A_{0n}. When the tip is allowed to interact with the sample $E_n \neq 0$ and, from Equation 8, the phase shift ϕ_n is affected by the interaction. Nevertheless, the weight of the driving force, i.e., the first term in Equation 8, increases with increasing F_{0n}, or A_{0n}, and then the sensitivity of ϕ_n to E_n might be compromised. This is confirmed in Figure 1 by allowing a gentle interaction, i.e., $A_{01} \equiv A_0 = 4$ nm and $A/A_0 \approx 0.9$ (also Figure 2 and Figure 3), and monitoring $\phi_n$when A_{0n} = 1 pm (squares) and A_{0n} = 100 pm (triangles). When A_{0n} = 100 pm (triangles) all ϕ_n remain close to 180° or 0°. A shift in phase, i.e., from 180° to 0°, is observed for $n = 2$ only. While these jumps of nearly 180° might be of interest they are ignored from now on. The reader can refer to recent works that discuss multiple regimes of operation in bimodal AFM [31,33]. It follows that variations in Hamaker are not detected by higher harmonic frequencies when A_{0n} = 100 pm. When A_{0n} = 1 pm (squares), however, the values of ϕ_n are not exactly 180° or 0° for some *n*. Thus, the values ϕ_n are now sensitive to

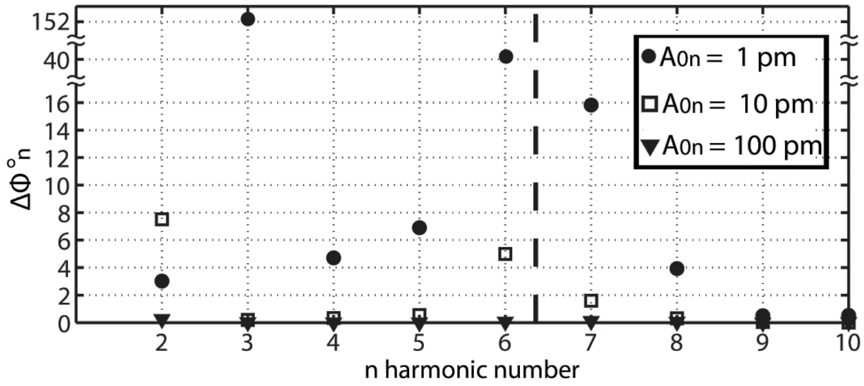

Figure 2: Phase shift analysis, in which the contrast in the higher harmonic phase shifts $\Delta\phi_n = \mathrm{abs}(\phi_n(H_2) - \phi_n(H_1))$, n = 2–10, which is induced by variations in the Hamaker constant *H* is shown. The variation in *H* is $H_2 - H_1 = 1.0 \times 10^{-19}$ J, where $H_2 = 1.2 \times 10^{-19}$ J, and effectively corresponds to variations in chemistry only. Results are shown when higher harmonic amplitudes A_{0n} of 1 (circles), 10 (squares) and 100 (triangles) pm are introduced. Peak forces are smaller than 200 pN throughout.

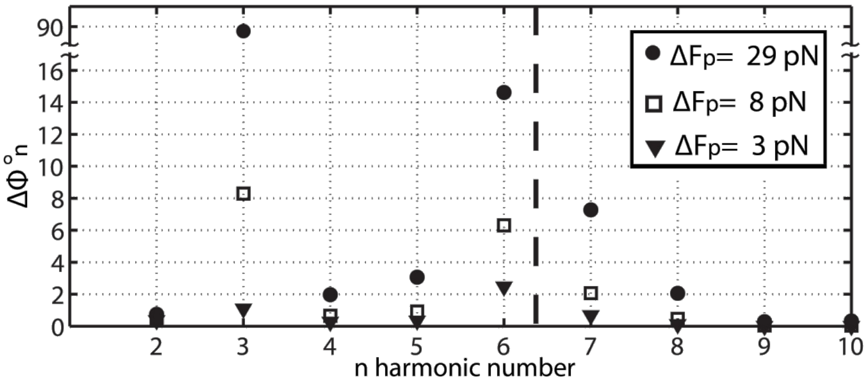

Figure 3: Phase shift analysis, in which the contrast in the higher harmonic phase shifts $\Delta\phi_n$ = abs($\phi_n(H_2) - \phi_n(H_1)$) for n = 2–10 results only from variations in the Hamaker constant, H, or in the chemistry. The variations of H are $H_2 - H_1 = 0.2 \times 10^{-19}$ J for $H_2 = 0.4 \times 10^{-19}$ J (circles), 0.8×10^{-19} J (squares) and 1.2×10^{-19} J (triangles). These variations induce variations in peak force of 29 (circles), 8 (squares) and 3 (trinagles) pN.

the Hamaker values or tip–sample forces. The peak forces were 140 pN (circles) and 160 pN (triangles) respectively.

The loss of phase sensitivity to Hamaker variations with increasing A_{0n} is further corroborated with the use of Figure 2 and by varying the Hamaker values from $H_1 = 0.2 \times 10^{-19}$ J to $H_2 = 1.4 \times 10^{-19}$ J, and setting A_{0n} = 1 pm (circles), A_{0n} =10 pm (squares) and A_{0n} = 100 pm (triangles). This range of H is characteristic of materials interacting in ambient conditions [40]. The y-axis stands for the contrast in higher harmonic phase $\Delta\phi_n$ = abs($\phi_n(H_2) - \phi_n(H_1)$). We consider that variations, for which $\Delta\phi_n > 0.2°$ lie above the noise of the instrument and can potentially be detected. The corresponding variations in peak forces were 63, 47 and 79 pN respectively. The sensitivity of $\Delta\phi_n$ is clearly controlled by the chosen values of A_{0n}. For example, if A_{0n} = 100 pm then $\Delta\phi_n < 0.2°$ throughout. If A_{0n} = 1 or 10 pm, however, then $\Delta\phi_n > 0.2°$ at least for some n. In particular, if A_{0n} = 1 pm then $\Delta\phi_n > 0.2°$ for all n. This implies that all the externally excited higher harmonics act as simultaneous contrast channels that are sensitive to Hamaker, or chemical, variations.

In Figure 3 the sensitivity of $\Delta\phi_n$ when A_{0n} = 1 pm is tested by varying H (a) from $H_1 = 0.2 \times 10^{-19}$ J to $H_2 = 0.4 \times 10^{-19}$ J (peak force variation of 29 pN, circles), (b) from $H_1 = 0.6 \times 10^{-19}$ J to $H_2 = 0.8 \times 10^{-19}$ J (peak force variation of 8 pN, squares) and (c) from $H_1 = 1.2 \times 10^{-19}$ J to $H_2 = 1.4 \times 10^{-19}$ J (peak force variation of 3 pN, triangles). The shifts $\Delta\phi_n$ are larger than 0.2° for all n provided the variations in peak force are large enough (circles). If the variations in the peak force are sufficiently small then $\Delta\phi_n > 0.2°$ for some n only. Also, it can be deduced by inspection that, in general, $\Delta\phi_n$ escalates with variations in peak force and changes non-linearly with variations in Hamaker since $H_2 - H_1 = 0.2 \times 10^{-19}$ J throughout in the figure. In fact, from Figure 3, the total contributions to the phase shift calculated as the sums $\Sigma\Delta\phi_n$ (n = 1–9) are 119.8, 19.3 and 5.4° and decrease with decreasing the variations in peak force, i.e., 29, 8 and 3 pN, respectively.

It is also interesting to note that the source of variations in peak force with variations in Hamaker H (Equation 10), i.e., van der Waals forces, relates to variations in the distance of minimum approach, d_m, with variations in H. To be more specific, d_m, increases with increasing H. For example, in the simulations, by varying H from $H_1 = 0.2 \times 10^{-19}$ J to $H_2 = 1.4 \times 10^{-19}$ J the variation is $\Delta d_\mathrm{m} \approx 0.83$ nm. This would experimentally result in a chemistry-induced apparent topography of approximately $\Delta z_\mathrm{c} \approx 0.83$ nm. In standard AM AFM, in which a single frequency is externally excited, this apparent topography cannot be distinguished from true topography in the presence of conservative forces only (Figure 4). A true topography can only be reconstructed from AM AFM results, if there is a variation in topography only (Figure 4a). This means that the composition of the sample is homogeneous throughout. In particular, the above discussion indicates that variations in H, or chemistry alone, produce variations in apparent topography in AM AFM, for which $\Delta z_\mathrm{c} > 0$ nm (Figure 4b). The excitation of higher harmonics, however, provides experimental observables to differentiate between the two cases. Namely, the true reconstructed topography results only if $\Delta\phi_n = 0°$ for all n. That is, if $\Delta\phi_n > 0°$, even for a single n, there is a contribution to apparent topography induced by chemistry or other compositional variations.

Thermal noise and higher harmonic external drives

As stated in the introduction, it has long been known that under ambient conditions higher harmonic amplitudes might be too

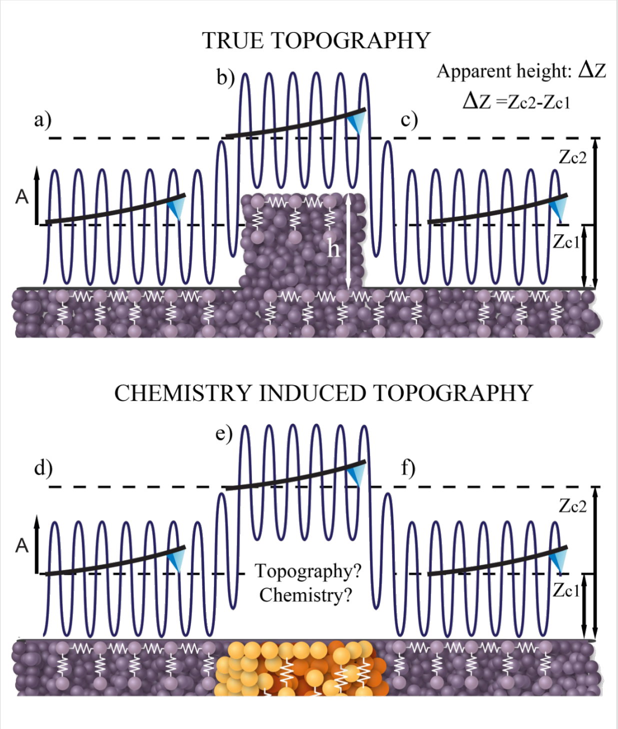

Figure 4: (a–c) Illustration of a cantilever oscillating above a surface and recovering the true height $\Delta z_c = h$ when there are no compositional heterogeneity or chemical variations. (d–f) Topographical variations $\Delta z_c > 0$ nm induced by chemical or another compositional heterogeneity. The two cases can be decoupled by noting that it is only a compositional heterogeneity, if the phase shifts of higher harmonics, $\Delta\phi_n$, are non-zero.

small to be detected [3,15,42]. This is particularly true when monitoring higher harmonics and simultaneously applying gentle tip–sample forces [23]. In liquid environments, however, the second harmonic amplitude might be large enough [43] to be recorded to map the properties even of living cells [44,45]. Still, even in highly damped environments, harmonic amplitudes rapidly decrease with increasing harmonic number particularly when imaging soft matter [6,15,46]. The main discussion above has focused on externally driving higher harmonics to amplitudes that could be experimentally detected. Then, once these amplitudes are sufficiently high, the phase shifts $\Delta\phi_n$ have been employed to map the composition through variations in the tip–sample Hamaker constant, H, in Equation 10. In this section, the presence of thermal noise is discussed with respect to the contrast in amplitude ΔA_n and phase $\Delta\phi_n$ in the presence and absence of external drive forces at the higher harmonics frequencies.

First an example of the magnitude of the harmonic amplitudes and respective phase shifts that would result when higher harmonics are not externally excited is given (Table 1). In order to sense long-range forces only, the cantilever is driven with relatively small amplitudes, i.e., A_0 = 4 nm and A/A_0 = 0.9 as in the examples above. The harmonic amplitudes A_n are given in pm. Two examples for the amplitude response are shown, one for amplitudes resulting from $H_1 = 0.2 \times 10^{-19}$ J (top row) and one for $H_2 = 1.4 \times 10^{-19}$ J (second row). For H_1, A_2 is approx. 4 pm whereas A_3 and A_6 are approx. 1 pm. All other higher harmonics lie below 1 pm. For H_2, A_2 is approx. 3 pm and all other higher harmonics have values below 1 pm. The difference in amplitudes $\Delta A_n = A_n(H_2) - A_n(H_1)$ that results from the variation in H is also given in the table. Only the second harmonic results in variations above 1 pm. Practically, these results imply that while higher harmonic amplitudes depend on the value of the Hamaker constant, or sample composition, the amplitude values are typically in the order of 1 pm or fractions of a pm. This is also true for variations in higher harmonic amplitudes ΔA_n. The corresponding phase shifts ϕ_n and varia-

Table 1: Harmonic amplitudes A_n and the corresponding phase shifts ϕ_n that result from Hamaker values of $H_1 = 0.2 \times 10^{-19}$ J and $H_2 = 1.4 \times 10^{-19}$ J. The differences in amplitudes ΔA_n and phases $\Delta\phi_n$ are also shown. A single external drive force has been employed (the fundamental frequency) and no thermal noise has been allowed.

	A_1	A_2	A_3	A_4	A_5	A_6	A_7	A_8	A_9	A_{10}
A_n [pm] for H_1	3600.00	4.38	1.03	0.21	0.16	1.11	0.39	0.12	0.06	0.03
A_n [pm] for H_2	3600.00	3.31	0.57	0.08	0.05	0.23	0.06	0.01	0.00	0.00
	ΔA_1	ΔA_2	ΔA_3	ΔA_4	ΔA_5	ΔA_6	ΔA_7	ΔA_8	ΔA_9	ΔA_{10}
ΔA_n [pm]	0.00	−1.07	−0.46	−0.12	−0.12	−0.89	−0.33	−0.11	−0.05	−0.03
	ϕ_1	ϕ_2	ϕ_3	ϕ_4	ϕ_5	ϕ_6	ϕ_7	ϕ_8	ϕ_9	ϕ_{10}
ϕ_n [°] for H_1	115.83	141.25	167.20	12.77	39.91	66.18	90.49	116.55	142.44	168.29
ϕ_n [°] for H_2	115.84	141.25	167.20	12.77	39.90	66.18	90.48	116.52	142.29	167.78
	$\Delta\ \phi_1$	$\Delta\ \phi_2$	$\Delta\ \phi_3$	$\Delta\ \phi_4$	$\Delta\ \phi_5$	$\Delta\ \phi_6$	$\Delta\ \phi_7$	$\Delta\ \phi_8$	$\Delta\ \phi_9$	$\Delta\ \phi_{10}$
$\Delta\phi_n$ [°]	0.00	0.00	0.00	0.00	−0.01	0.00	0.00	−0.03	−0.14	−0.50

tions in phase shifts $\Delta\phi_n$ are also shown in Table 1 for H_1 and H_2. These are of the order of a hundredth of a degree or less except for sufficiently high harmonic numbers, i.e., $n = 9$ and 10. The amplitudes for these higher harmonics, however, are of the order of tens of femtometers or less.

Thermal fluctuations are a fundamental source of intrinsic noise in atomic force microscopy [47]. Thus, while other sources of intrinsic and extrinsic noise should be acknowledged and might be present in a given experiment, thermal fluctuations are analyzed next in terms of their effects on amplitude and phase shifts. This should provide a measure of the impact of thermal noise on the enhanced contrast reported in this work (Figure 2 and Figure 3). Other technical issues such as tilt and probe geometry have also been ignored for simplicity since these typically involve a correction factor [48]. As in the work of Butt and Jaschke [47], the equipartition theorem is employed to estimate the thermal noise present in a given mode. However, since higher harmonics are discussed here, particular emphasis should be given to the noise at the frequencies of interest, i.e., at exact harmonic frequencies, and the noise in the detection bandwidths of interest. Then, the thermal noise power $\Delta P_{\mathrm{TN}}(\Delta f)$ in the detection bandwidth of interest, Δf, can be defined as

$$\Delta P_{\mathrm{TN}}(\Delta f) \equiv 2 \int_{f_n-\Delta f/2}^{f_n+\Delta f/2} G_{\mathrm{TN}} \left|H_{\mathrm{ZF}}\right|^2 df\,, \tag{12}$$

where TN stands for thermal noise, f_n is the frequency of interest ($\omega_n = 2\pi f_n$), that is the frequency of a particular harmonic n, G_{TN} is the power spectral density due to thermal noise, and $|H_{\mathrm{ZF}}|^2$ is the modulus of the squared transfer function of a particular mode m of position z_m relative to thermal force F_{TN}. If G_{TN} is assumed to be constant for the bandwidth of interest in AFM experiments, i.e., $f = 10^2$–10^6, it follows from Equation 1 that the thermal energy in a given mode m, by invoking the equipartition theorem, is

$$\frac{1}{2}k_{\mathrm{B}}T = \frac{1}{2}k_{(m)}G_{\mathrm{TN}} \int_{-\infty}^{+\infty} \frac{1}{k_{(m)}^2} \frac{1}{\left[1-\omega^2/\omega_{(m)}^2\right]^2 + \left[\omega/\left(\omega_{(m)}Q_{(m)}\right)\right]^2} df\,, \tag{13}$$

where here $T = 300$ K throughout, $f_{(m)}$ is the natural resonant frequency of mode m in Hz and $df = (f_{(m)}/\omega_{(m)})d\omega$. Then

$$G_{\mathrm{TN}} = k_{\mathrm{B}}T \frac{k_{(m)}}{\pi Q_{(m)}}\,. \tag{14}$$

From Equation 13 and Equation 14, the thermal noise power in the detection bandwidth of interest, $\Delta P_{\mathrm{TN}}(\Delta f)$, is found to be

$$\begin{aligned}\Delta P_{\mathrm{TN}}(\Delta f) &= 2k_{\mathrm{B}}T \frac{k_{(m)}}{\pi f_{(m)}Q_{(m)}} \\ &\times \int_{f_n-\Delta f/2}^{f_n+\Delta f/2} \frac{1}{k_{(m)}^2} \frac{1}{\left[1-\omega^2/\omega_{(m)}^2\right]^2 + \left[\omega/\left(\omega_{(m)}Q_{(m)}\right)\right]^2} df\,.\end{aligned} \tag{15}$$

Finally, the associated amplitude due to thermal noise A_{TN} in the detection bandwidth Δf is

$$A_{\mathrm{TN}}(\Delta f) = \sqrt{2\Delta P_{\mathrm{TN}}(\Delta f)}\,. \tag{16}$$

It should be noted that A_{TN} gives the contribution of thermal noise to the amplitude of a given mode m only. Each modal contribution of thermal noise to the amplitude should be calculated separately for each frequency in the formalism developed here. A driving force, F_{TN}, can also be associated to thermal noise and the respective amplitude, A_{TN}, (Equation 16) through a standard expression [49]

$$F_{\mathrm{TN}}\left(\Delta f\right) = k_{(m)}A_{\mathrm{TN}}\sqrt{\left(1-\frac{\omega^2}{\omega_{(m)}^2}\right)^2 + \left(\frac{\omega}{\omega_{(m)}Q_{(m)}}\right)^2}\,. \tag{17}$$

Equation 17 gives the effective drive force F_{TN} due to thermal fluctuations that should be expected for a given detection bandwidth Δf and a given mode m. Since the upper boundaries for noise will be considered here, the phase of the thermal noise signal has been set to be in quadrature with respect to the external drive, i.e., either the fundamental external drive or the higher harmonic external drives when these are present. Focus is now placed on the harmonics $n = 1, 2, 3$ (close to the fundamental frequency of mode 1) and 6 (close to the fundamental frequency of mode 2), since these are sufficiently close to a given mode that only the contribution of thermal noise to the amplitude from a single mode needs to be considered. This simplifies the following discussion.

In Table 2 the amplitudes $A_{\mathrm{TN}n}$ and forces $F_{\mathrm{TN}n}$ calculated for three different values of detection bandwidth Δf (5 kHz, 2 kHz and 0.2 kHz) are shown for $n = 1, 2, 3$ and 6. The values have been computed with the use of Equation 16 and Equation 17, with frequencies centered at the harmonic frequencies f_n, for a given detection bandwidth Δf. It is interesting to note that $A_{\mathrm{TN}1}$ lies between 44 and 19 pm for the three choices of detection bandwidth. These values are in agreement with those expected from an analysis that implies that all the thermal noise is centered exactly at resonance [47]. This is because the Q factors are relatively high ($Q_1 = 100$ and $Q_2 = 600$). The values of the thermal-noise amplitude expected at harmonics 2, 3 and 6 however are of the order of 0.1–1.0 pm.

Table 2: Amplitudes $A_{\mathrm{TN}n}$ resulting from thermal noise for n = 1, 2, 3 and 6 and respective drive forces $F_{\mathrm{TN}n}$ for detection bandwidths Δ*f* of 5, 2 and 0.2 kHz.

Δ*f* [kHz]	A_{TN1} [pm]	F_{TN1} [pN]	A_{TN2} [pm]	F_{TN2} [pN]	A_{TN3} [pm]	F_{TN3} [pN]	A_{TN6} [pm]	F_{TN6} [pN]
5	62.23	1.27	0.42	2.83	0.17	2.83	0.42	2.83
2	56.57	1.13	0.28	1.70	0.14	1.70	0.28	1.70
0.2	26.87	0.57	0.08	0.57	0.04	0.57	0.07	0.57

The effects that the thermal noise amplitudes in Table 2 have on the enhanced contrast reported in this work have been analyzed by adding the associated thermal noise forces, also shown in Table 2, to the equation of motion in Equation 1. The discussion below focuses on the values obtained for $\Delta f = 2$ kHz in Table 2 since this is a detection bandwidth of practical relevance in standard AFM experiments [50].

The sensitivity of the phase shift to noise and signal can be defined here, and for the purpose of phase shifts in AM AFM, as follows. First assume that noise is allowed according to Table 2 ($\Delta f = 2$ kHz) for a given value of the Hamaker constant, H. Here both $H_1 = 1.4 \times 10^{-19}$ J and $H_2 = 1.4 \times 10^{-19}$ J have been used in the simulations. According to this, thermal noise alone should lead to a difference in phase shift $\Delta\phi_n(H) = \phi_n(A_{\mathrm{TN}} > 0) - \phi_n(A_{\mathrm{TN}} = 0)$ for a given value of H since there is an effective driving force F_{TNn} due to thermal fluctuations (Table 2). The average of $\Delta\phi_n$ for the two Hamaker values can be taken as the noise in the phase signal as follows

$$\Delta\phi_n(\mathrm{TN}) = \frac{\Delta\phi_n(H_2 + \mathrm{TN}) + \Delta\phi_n(H_1 + \mathrm{TN})}{2}, \qquad (18)$$

where TN stands for thermal noise as usual and $\Delta\phi_n(\mathrm{TN})$ stands for the difference in phase shift at harmonic n that induced by thermal noise alone. Next the signal is defined as the phase shift induced by variations in Hamaker alone

$$\Delta\varphi_n = \varphi_n(H_2) - \varphi_n(H_1). \qquad (19)$$

Finally, a parameter that quantifies the sensitivity of the phase shift to noise and signal, the phase ratio $\mathrm{PR}(\phi_n)$ can be defined from the ratio between Equation 19 and Equation 18:

$$\mathrm{PR}(\phi_n) = \frac{\Delta\phi_n}{\Delta\phi_n(\mathrm{TN})}. \qquad (20)$$

Large values of PR result in a high sensitivity of the phase shift to the signal, whereas low values of PR indicate a sensitivity of the phase shift to noise only. Three cases are discussed, which, for simplicity, focus on harmonics 2, 3 and 6 only and on A_{0n} = 0, 1 and 10 pm.

Case 1: First, no higher harmonic external drives are allowed, which implies that $A_{0n} = 0$ in Equation 2 for $n > 1$. This is the standard operational mode in dynamic AFM, in which a single external drive is employed. In this case we have PR = 0 throughout (Table 3).

Case 2: Higher harmonic external drives are allowed. In particular, $A_{0n} = 1$ pm in Equation 2 for $n > 1$. This is the proposed mode of operation in this work. In this case we have PR > 1 throughout but the exact value depends on harmonic number (Table 3).

Case 3: Higher harmonic external drives are allowed. In particular, $A_{0n} = 10$ pm in Equation 2 for $n > 1$. This is the proposed mode of operation in this work. When compared to case 2, however, the magnitudes of the external drives have been increased. In this case we also have PR > 1 throughout (Table 3).

Table 3: The phase ratio for a given harmonic phase shift n, $\mathrm{PR}(\phi_n)$, as defined by Equation 20 when 1) no higher harmonic external drives are allowed ($A_{0n} = 0$) and when external drives lead to 2) $A_{0n} = 1$ pm and 3) $A_{0n} = 10$ pm.

	PR (ϕ_2)	PR (ϕ_3)	PR (ϕ_6)
case 1: A_{0n} =0	0.00	0.00	0.00
case 2: A_{0n} =1 pm	1.90	22.09	7.29
case 3: A_{0n} =10 pm	5.20	2.01	195.85

When looking at Table 3, one should recall that these are the upper-boundary values for noise since the phase of the thermal noise drives was set to be in quadrature. In summary, Table 3 shows that the phase ratio PR increases when external drives are applied at a given exact harmonic frequency, i.e., when $A_{0n} > 0$. This is consistent with standard multifrequency operation, for which impressive results have already been obtained by exciting frequencies close to the resonant frequency of the second flexural mode [17,25,26]. In standard monomodal dynamic AFM, in which a single external drive is employed, the higher harmonics are excited by the tip–sample interaction according to Equation 9. That is, energy needs to flow into the higher harmonic frequencies in order to increase the amplitude signal. It is reasonable to assume that the increase in the sensitivity of the phase shift to the signal, i.e., the force, when external drives are applied is a consequence of energy both entering and leaving the given harmonic frequency of choice. That is, the fact that energy is supplied by the external drive at a given harmonic n implies that both positive and negative energy transfer might also occur at that frequency. Furthermore, when external drives are employed, this transfer occurs for a given phase shift that is now measured relative to the angle of the driving force. This is in agreement with the presence of the phase shift in Equation 8 and the absence of the phase shift in Equation 9 and might be related to the increase in the sensitivity of the phase shift to the tip–sample force as predicted here.

Conclusion

In summary, we have introduced a method that makes readily accessible an arbitrary number of exact higher harmonics by externally driving them with amplitudes above the noise level. Driving with exact higher harmonics does not introduce subharmonic frequencies to the motion and the amplitudes do not significantly decay when the interaction is gentle. Once higher harmonic amplitudes are accessible, one can also detect variations in higher harmonic phase shifts. In this work, variations in sample composition, or chemistry, here modelled through the Hamaker constant, have been shown to lead to variations in higher harmonic phase shifts and amplitudes. In particular, variations in the Hamaker constant of the order of 10^{20} J can induce higher harmonic phase shifts in the order of 10°. This is provided the higher harmonic amplitudes are small enough, i.e., about 1–10 pm. These small variations in phase shift would suffice to distinguish between metals such as gold, silver or copper [40]. Higher harmonic phase shifts also provide the means to decouple the true topography from an apparent topography, which is induced by compositional variations. Furthermore this outcome should still be valid in standard bimodal imaging. Overall, the proposed approach, and variations, might ultimately fulfil the promise of rapid chemical identification with multiple contrast channels while simultaneously exerting only gentle forces on samples. Still it has to be acknowledged that, experimentally, it is expected that technical issues might arise from the multiple excitation of exact frequencies and from the set-up required to detect variations in higher harmonic phase. In particular, the set-up would require the generation of exact harmonic external drives to bring the harmonic amplitudes above the noise level while keeping them small enough to provide enough phase contrast. This last point is relevant since it has been shown that higher harmonic amplitudes should remain in the sub-100-pm range for the higher harmonic phase shifts to be significantly large, i.e., above 0.2°, in response to variations in the tip–sample force. On the other hand, an analysis of thermal fluctuation that exploits the equipartition theorem has also indicated that thermal noise should be of the order of 0.1–1.0 pm close to the higher harmonics modes. The implication is that the working amplitudes should lie in the range of 1 to 100 pm. The noise analysis has also shown that there is an increase in sensitivity of the phase shift to the tip–sample force when frequencies are externally excited. Nevertheless, ultimately, only experimental practice, implementation, ingenuity and further theoretical advances in the field are to establish what the limits of this approach are.

Acknowledgements

This project was funded by Ministerio de Economía y Competitividad (MAT2012-38319). The artistic figure was designed by Maritsa Kissamitaki.

References

1. Stark, R. W.; Heckl, W. M. *Surf. Sci.* **2000,** *457,* 219–228. doi:10.1016/S0039-6028(00)00378-2
2. Stark, M.; Stark, R. W.; Heckl, W. M.; Guckenberger, R. *Proc. Natl. Acad. Sci. U. S. A.* **2002,** *99,* 8473–8478. doi:10.1073/pnas.122040599
3. Sahin, O.; Quate, C.; Solgaard, O.; Atalar, A. *Phys. Rev. B* **2004,** *69,* 165416. doi:10.1103/PhysRevB.69.165416
4. Dürig, U. *New J. Phys.* **2000,** *2,* 1–12. doi:10.1088/1367-2630/2/1/005
5. Sahin, O.; Quate, C.; Solgaard, O.; Giessibl, F. J. Higher-Harmonic Force Detection in Dynamic Force Microscopy. In *Springer Handbook of Nanotechnology;* Bhushan, B., Ed.; Springer Verlag: Berlin, Germany, 2010; pp 711–729. doi:10.1007/978-3-642-02525-9_25
6. Payam, A. F.; Ramos, J. R.; Garcia, R. *ACS Nano* **2012,** *6,* 4663–4670. doi:10.1021/nn2048558
7. Garcia, R.; Herruzo, E. T. *Nat. Nanotechnol.* **2012,** *7,* 217–226. doi:10.1038/nnano.2012.38
8. Garcia, R.; Proksch, R. *Eur. Polym. J.* **2013,** *49,* 1897–1906. doi:10.1016/j.eurpolymj.2013.03.037
9. Fukuma, T.; Kobayashi, K.; Matsushige, K.; Yamada, H. *Appl. Phys. Lett.* **2005,** *86,* 193108–193110. doi:10.1063/1.1925780
10. Gotsmann, B.; Schmidt, C. F.; Seidel, C.; Fuchs, H. *Eur. Phys. J. B* **1998,** *4,* 267–268. doi:10.1007/s100510050378
11. Gross, L.; Mohn, F.; Moll, N.; Liljeroth, P.; Meyer, G. *Science* **2009,** *325,* 1110–1114. doi:10.1126/science.1176210
12. Wastl, D. S.; Weymouth, A. J.; Giessibl, F. J. *Phys. Rev. B* **2013,** *87,* 245415–245424. doi:10.1103/PhysRevB.87.245415
13. Giessibl, F. J. *Science* **1995,** *267,* 68–71. doi:10.1126/science.267.5194.68
14. Kawai, S.; Hafizovic, S.; Glatzel, T.; Baratoff, A.; Meyer, E. *Phys. Rev. B* **2012,** *85,* 165426–165431. doi:10.1103/PhysRevB.85.165426
15. Stark, R. W. *Nanotechnology* **2004,** *15,* 347–351. doi:10.1088/0957-4484/15/3/020
16. Hutter, C.; Platz, D.; Tholén, E. A.; Hansson, T. H.; Haviland, D. B. *Phys. Rev. Lett.* **2010,** *104,* 050801–050804. doi:10.1103/PhysRevLett.104.050801

17. Kawai, S.; Glatzel, T.; Koch, S.; Such, B.; Baratoff, A.; Meyer, E. *Phys. Rev. Lett.* **2009,** *103,* 220801–220804. doi:10.1103/PhysRevLett.103.220801
18. Hembacher, S.; Giessibl, F. J.; Mannhart, J. *Science* **2004,** *305,* 380–383. doi:10.1126/science.1099730
19. Basak, S.; Raman, A. *Appl. Phys. Lett.* **2007,** *91,* 064107–064109. doi:10.1063/1.2760175
20. Xu, X.; Melcher, J.; Basak, S.; Reifenberger, R.; Raman, A. *Phys. Rev. Lett.* **2009,** *102,* 060801–060804. doi:10.1103/PhysRevLett.102.060801
21. Sahin, O.; Magonov, S.; Su, C.; Quate, C. F.; Solgaard, O. *Nat. Nanotechnol.* **2007,** *2,* 507–514. doi:10.1038/nnano.2007.226
22. Gadelrab, K.; Santos, S.; Font, J.; Chiesa, M. *Nanoscale* **2013,** *5,* 10776–10793. doi:10.1039/c3nr03338d
23. Rodríguez, T. R.; García, R. *Appl. Phys. Lett.* **2004,** *84,* 449–551. doi:10.1063/1.1642273
24. Lozano, J. R.; Garcia, R. *Phys. Rev. Lett.* **2008,** *100,* 076102–076105. doi:10.1103/PhysRevLett.100.076102
25. Patil, S.; Martinez, N. F.; Lozano, J. R.; Garcia, R. *J. Mol. Recognit.* **2007,** *20,* 516–523. doi:10.1002/jmr.848
26. Martinez-Martin, D.; Herruzo, E. T.; Dietz, C.; Gomez-Herrero, J.; Garcia, R. *Phys. Rev. Lett.* **2011,** *106,* 198101–198104. doi:10.1103/PhysRevLett.106.198101
27. Solares, S. D.; Chawla, G. *Meas. Sci. Technol.* **2010,** *21,* 125502. doi:10.1088/0957-0233/21/12/125502
28. Kawai, S.; Glatzel, T.; Koch, S.; Such, B.; Baratoff, A.; Meyer, E. *Phys. Rev. B* **2010,** *81,* 085420–085426. doi:10.1103/PhysRevB.81.085420
29. Proksch, R. *Appl. Phys. Lett.* **2006,** *89,* 113121–113123. doi:10.1063/1.2345593
30. Herruzo, E. T.; Perrino, A. P.; Garcia, R. *Nat. Commun.* **2014,** *5,* No. 3126. doi:10.1038/ncomms4126
31. Kiracofe, D.; Raman, A.; Yablon, D. *Beilstein J. Nanotechnol.* **2013,** *4,* 385–393. doi:10.3762/bjnano.4.45
32. Stark, R. W. *Appl. Phys. Lett.* **2009,** *94,* 063109–063111. doi:10.1063/1.3080209
33. Chakraborty, I.; Yablon, D. G. *Nanotechnology* **2013,** *24,* 475706. doi:10.1088/0957-4484/24/47/475706
34. Steidel, R. *An introduction to mechanical vibrations,* 3rd ed.; John Wiley & Sons: New York, NY, USA, 1999.
35. Tolstov, G. P.; Silverman, R. A. *Fourier Series;* Dover Publication: New York, NY, USA, 1976.
36. Herruzo, E. T.; Garcia, R. *Beilstein J. Nanotechnol.* **2012,** *3,* 198–206. doi:10.3762/bjnano.3.22
37. Aksoy, M. D.; Atalar, A. *Phys. Rev. B* **2011,** *83,* 075416–075421. doi:10.1103/PhysRevB.83.075416
38. Solares, S. D.; Chawla, G. *J. Appl. Phys.* **2010,** *108,* 054901. doi:10.1063/1.3475644
39. Engel, A.; Müller, D. J. *Nat. Struct. Mol. Biol.* **2000,** *7,* 715–718. doi:10.1038/78929
40. Israelachvili, J. *Intermolecular and Surface Forces;* Academic Press: Burlington, MA, USA, 1991.
41. Hamaker, H. C. *Physica (Amsterdam)* **1937,** *4,* 1058–1072. doi:10.1016/S0031-8914(37)80203-7
42. Stark, R. W.; Heckl, W. M. *Rev. Sci. Instrum.* **2003,** *74,* 5111–5114. doi:10.1063/1.1626008
43. Preiner, J.; Tang, J.; Pastushenko, V.; Hinterdorfer, P. *Phys. Rev. Lett.* **2007,** *99,* 046102–046105. doi:10.1103/PhysRevLett.99.046102
44. Dulebo, A.; Preiner, J.; Kienberger, F.; Kada, G.; Rankl, C.; Chtcheglova, L.; Lamprecht, C.; Kaftan, D.; Hinterdorfer, P. *Ultramicroscopy* **2009,** *109,* 1056–1060. doi:10.1016/j.ultramic.2009.03.020
45. Turner, R. D.; Kirkham, J.; Devine, D.; Thomson, N. H. *Appl. Phys. Lett.* **2009,** *94,* 043901. doi:10.1063/1.3073825
46. Raman, A.; Trigueros, S.; Cartagena, A.; Stevenson, A. P. Z.; Susilo, M.; Nauman, E.; Contera, S. A. *Nat. Nanotechnol.* **2011,** *6,* 809–814. doi:10.1038/nnano.2011.186
47. Butt, H.-J.; Jaschke, M. *Nanotechnology* **1995,** *6,* 1–7. doi:10.1088/0957-4484/6/1/001
48. Heim, L.-O.; Kappl, M.; Butt, H.-J. *Langmuir* **2004,** *20,* 2760–2764. doi:10.1021/la036128m
49. Hu, S.; Raman, A. *Nanotechnology* **2008,** *19,* 375704–375714. doi:10.1088/0957-4484/19/37/375704
50. Ramos, J. R. Desarrollos y applicaciones de la microscopía de fuerzas para el estudio de proteínas y de células cancerosas. Ph.D. Thesis, Universidad Autónoma de Madrid, Madrid, 2013.

License and Terms

Beilstein Journal
of Nanotechnology

Frequency, amplitude, and phase measurements in contact resonance atomic force microscopies

Gheorghe Stan*[1,2] and Santiago D. Solares[2]

Full Research Paper

Open Access

Address:
[1]Material Measurement Laboratory, National Institute of Standards and Technology, Gaithersburg, MD 20878, USA and [2]Department of Mechanical Engineering, University of Maryland, College Park, MD 20742, USA

Email:
Gheorghe Stan* - gheorghe.stan@nist.gov

* Corresponding author

Keywords:
contact-resonance AFM; dynamic AFM; frequency modulation; phase-locked loop; viscoelasticity

Beilstein J. Nanotechnol. **2014,** *5,* 278–288.
doi:10.3762/bjnano.5.30

Received: 26 November 2013
Accepted: 18 February 2014
Published: 12 March 2014

This article is part of the Thematic Series "Noncontact atomic force microscopy II".

Guest Editors: U. D. Schwarz and M. Z. Baykara

Abstract

The resonance frequency, amplitude, and phase response of the first two eigenmodes of two contact-resonance atomic force microscopy (CR-AFM) configurations, which differ in the method used to excite the system (cantilever base vs sample excitation), are analyzed in this work. Similarities and differences in the observables of the cantilever dynamics, as well as the different effect of the tip–sample contact properties on those observables in each configuration are discussed. Finally, the expected accuracy of CR-AFM using phase-locked loop detection is investigated and quantification of the typical errors incurred during measurements is provided.

Introduction

A number of atomic force microscopy (AFM) variants have emerged since the introduction of the original technique in 1986 [1]. Besides topographical acquisition and spectroscopy, an important application nowadays is the measurement of conservative and dissipative interactions across nanoscale surfaces, which is highly relevant for viscoelastic materials such as polymers and biological samples. These measurements can be carried out through a combination of contact and dynamic AFM modes. Within the force modulation method [2], the tip and the sample are brought into contact at a prescribed tip–sample force setpoint (cantilever deflection setpoint, as in contact mode imaging) and the sample is excited with a sinusoidal oscillation in the vertical direction (atomic force acoustic microscopy (AFAM) configuration [3]), such that the tip oscillation amplitude and its phase with respect to the excitation can be measured and converted into a loss and storage modulus. In contact resonance AFM (CR-AFM) [3-9] a similar setup is used, supplying the sinusoidal excitation either at the base of the cantilever (in the so-called ultrasonic atomic force microscopy (UAFM) configuration [4]) or to the sample stage (in the AFAM configuration [3]). In both cases, the effective resonance frequency, amplitude, and phase of various eigenmodes of the cantilever–tip system are generally measured through excitation frequency "sweeps" for quantitative determination of the same elastic and viscous responses of the material. More recently, other methods have been introduced to more rapidly infer the frequency response (amplitude vs frequency curves) of the tip–sample contact. In the band excitation (BE) method, a time-dependent signal containing a band of frequencies around the desired resonance is applied at each pixel of the scan, such that the frequency response at that location can be rapidly obtained through a Fourier transform of the cantilever tip response and a fit to a Lorentzian curve [10,11]. This calculation allows mapping of the resonance frequency and quality factor across the sample, from which viscoelastic properties can also be inferred. In contrast, in the dual-amplitude resonance tracking (DART) method, the frequency response curve is rapidly inferred from the phase and amplitude response at two frequencies around the resonance frequency during a real-time scan [12].

Intermittent-contact methods have also been used to characterize conservative and dissipative tip–sample interactions simultaneously with topographical acquisition. This was originally performed using the tapping-mode (amplitude modulation) technique [13], within which variations in the phase contrast can be directly related to changes in energy dissipation [14,15]. Conservative and dissipative interactions are generally expressed in terms of the virial (V_{ts}) and the dissipated power (P_{ts}), respectively [15-20]. In the last ten years, intermittent-contact measurements have been enhanced through multifrequency excitation methods [21-27]. In multifrequency AFM, the fundamental cantilever eigenmode is typically controlled in conventional AM- or FM-AFM mode for topographical measurement, while one or more higher eigenmodes are driven simultaneously in order to also map compositional (viscoelastic) contrast. Since the higher eigenmodes are not directly affected by the topographical acquisition controls, they can be tuned independently to map V_{ts} and P_{ts} with high sensitivity. However, with the exception of small-amplitude FM-AFM [28,29] in which the tip–sample force gradient can be measured directly, the mapping of V_{ts} and P_{ts} in intermittent-contact imaging generally only provides a qualitative map of surface viscoelasticity.

In this work the focus is on the CR-AFM technique. Specifically, we analyzed the response variables for the two configurations currently in use (UAFM and AFAM), and restricted our analysis to the first two cantilever eigenmodes. Similarities and notable differences were observed in the signals and calculated variables (frequency, amplitude and phase) for the two cases, which require careful analysis for proper experimental setup and interpretation. As an example, we analyzed the errors introduced during resonance frequency tracking through the use of a phase-locked loop (PLL), which leads to different results in both configurations. This is a highly relevant practical consideration, since PLL techniques offer versatility and speed of characterization when they can be implemented accurately.

Results and Discussion

Equation of motion for a cantilever beam in UAFM and AFAM configurations

In this work two CR-AFM configurations will be analyzed: UAFM [4], with the cantilever vibrated from its base (Figure 1a), and AFAM [3], with the sample vibrated from underneath (Figure 1b). In both configurations the vibration is in the form of a mechanical oscillation of variable frequency and the detection is performed at the end of the cantilever where the tip is located. The dynamics of the cantilever–tip–sample system in each of these configurations was discussed by Rabe in [30]. We limit ourselves to briefly reviewing the equations necessary for our analysis. For simplicity, the vertical

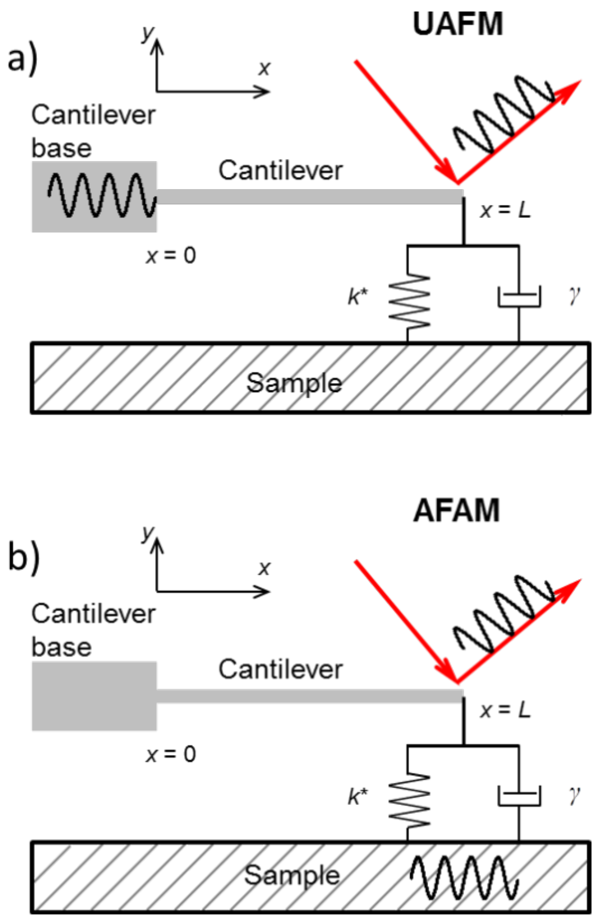

Figure 1: a) UAFM configuration with a mechanical vibration applied to the base of the cantilever and signal detection at the end of the cantilever. b) AFAM configuration with a mechanical vibration applied to the sample and signal detection at the end of the cantilever.

tip–sample coupling was modelled as a spring in parallel with a dashpot (Kelvin–Voigt model) and no lateral contact coupling was considered; vertical and lateral refer here to the normal and parallel directions to the sample surface, respectively.

The Euler–Bernoulli equation of motion for damped flexural vibrations of a cantilever beam in air is

$$EI\frac{\partial^4 y(x,t)}{\partial x^4}+\eta_{\mathrm{air}}\rho A\frac{\partial y(x,t)}{\partial t}+\rho A\frac{\partial^2 y(x,t)}{\partial t^2}=0 \qquad (1)$$

where the cantilever is described by its Young's modulus E, second moment of area of its cross section I, mass density ρ, and cross-sectional area A, and η_{air} characterizes the damping of the oscillations in air. The general solution of Equation 1 is in the form of $y(x,t) = y(x)e^{i\omega t}$, with

$$\begin{aligned} y(x) = {} & A_1(\cos\alpha x+\cosh\alpha x)\\ & +A_2(\cos\alpha x-\cosh\alpha x)\\ & +A_3(\sin\alpha x+\sinh\alpha x)\\ & +A_4(\sin\alpha x-\sinh\alpha x) \end{aligned} \qquad (2)$$

with A_1, A_2, A_3, and A_4 constants and α the complex wave number of a flexural oscillation, $\alpha=\sqrt[4]{\rho A\left(\omega^2-i\eta_{\mathrm{air}}\omega\right)/EI}$.

For the UAFM and AFAM configurations shown in Figure 1, the following boundary conditions are imposed to the general solution:

$$y(x)\big|_{x=0}=\begin{cases}A_{\mathrm{d}}, & \text{UAFM}\\ 0, & \text{AFAM}\end{cases}, \qquad (3)$$

$$\left.\frac{\partial y(x)}{\partial x}\right|_{x=0}=\begin{cases}0, & \text{UAFM}\\ 0, & \text{AFAM}\end{cases}, \qquad (4)$$

$$\left.\frac{\partial^2 y(x)}{\partial x^2}\right|_{x=L}=\begin{cases}0, & \text{UAFM}\\ 0, & \text{AFAM}\end{cases}, \qquad (5)$$

and

$$\left.\frac{\partial^3 y(x)}{\partial x^3}\right|_{x=L}=\begin{cases}\dfrac{\Theta(\alpha)}{L^3}\,y(x)\big|_{x=L}, & \text{UAFM}\\[2ex] \dfrac{\Theta(\alpha)}{L^3}\left[y(x)-A_{\mathrm{d}}\right]_{x=L}, & \text{AFAM}\end{cases}, \qquad (6)$$

where L is the length of the cantilever, A_{d} the driven amplitude, and $\Theta(\alpha)$ is given by

$$\begin{aligned}\Theta(\alpha) &= 3\frac{k^*}{k_{\mathrm{c}}}+i(\alpha L)^2\gamma^*\sqrt{\frac{1}{EI\rho A}}\\ &= 3\frac{k^*}{k_{\mathrm{c}}}+i(\alpha L)^2 p\end{aligned} \qquad (7)$$

Here $k_{\mathrm{c}} = 3EI/L^3$ is the cantilever spring constant, k^* the contact stiffness, γ^* the contact damping constant, and $p=\gamma L/\sqrt{EI\rho A}$ the dimensionless contact damping constant. With the above specified boundary conditions the solution further simplifies to

$$\begin{aligned} y(x) = {} & A_1(\cos\alpha x+\cosh\alpha x)\\ & +A_2(\cos\alpha x-\cosh\alpha x)\ ,\\ & +A_4(\sin\alpha x-\sinh\alpha x) \end{aligned} \qquad (8)$$

with the following constants for the two configurations:

$$A_1=\begin{cases}\dfrac{A_{\mathrm{d}}}{2}(\cos\alpha x+\cosh\alpha x), & \text{UAFM}\\ 0, & \text{AFAM}\end{cases}, \qquad (9)$$

$$A_2^{\mathrm{UAFM}}=\frac{A_{\mathrm{d}}\left[\Theta(\alpha)M^+-(\alpha L)^3\sin\alpha L\sinh\alpha L\right]}{2N(\alpha)}, \qquad (10)$$

$$A_4^{\mathrm{UAFM}}=\frac{A_{\mathrm{d}}\left[(\alpha L)^3M^+-2\Theta(\alpha)\cos\alpha L\cosh\alpha L\right]}{2N(\alpha)}, \qquad (11)$$

$$A_2^{\mathrm{AFAM}}=-\frac{A_{\mathrm{d}}\Theta(\alpha)(\sin\alpha L+\sinh\alpha L)}{2N(\alpha)}, \qquad (12)$$

and

$$A_4^{\mathrm{AFAM}}=\frac{A_{\mathrm{d}}\Theta(\alpha)(\cos\alpha L+\cosh\alpha L)}{2N(\alpha)}, \qquad (13)$$

with $M^{\pm} = \sin\alpha L\cosh\alpha L \pm \sinh\alpha L\cos\alpha L$, $N(\alpha) = (\alpha L)^3(1 + \cos\alpha L\cosh\alpha L) + \Theta(\alpha)M^-$, and $\Theta(\alpha)$ given by Equation 7. In particular, the deflection of the end of the cantilever reduces to

$$y(L)=\begin{cases} A_\mathrm{d}(\alpha L)^3\dfrac{\cos\alpha L+\cosh\alpha L}{N(\alpha)}, & \text{UAFM}\\[2ex] A_\mathrm{d}\Theta(\alpha)\dfrac{M^-}{N(\alpha)}, & \text{AFAM.}\end{cases} \tag{14}$$

The magnitude of the deflection and phase are given by:

$$|y(x)|=\sqrt{\left|\mathrm{Re}\left[y(x)\right]\right|^2+\left|\mathrm{Im}\left[y(x)\right]\right|^2} \tag{15}$$

and

$$\Phi(x)=-\tan^{-1}\left(\frac{\mathrm{Im}\left[y(x)\right]}{\mathrm{Re}\left[y(x)\right]}\right), \tag{16}$$

respectively.

We illustrate our analysis with a rectangular Si cantilever of length L = 225.03 µm, width w = 30.00 µm, and thickness T = 4.89 µm. With mass density ρ_Si = 2329.00 kg/m^3 and Young's modulus E_Si = 130.00 GPa, the cantilever's spring constant was calculated as k_c = 10.00 N/m. Using these parameters and considering η_air = 2.50 s^{-1} in Equation 1, the first two eigenmodes are characterized by the dynamic parameters given in Table 1. The frequency dependences of the amplitude ratio and phase around resonance are shown in Figure 2 for the first two free eigenmodes of the cantilever. For calculations of the free-eigenmodes, the cantilever was vibrated in the UAFM configuration. In the following analysis we will characterize the contact damping by the dimensionless contact damping constant p rather than the actual contact damping constant γ^*. The discussion is focused on the dynamics of the cantilever in the two CR-AFM configurations only and further consideration of various contact geometries would be required to convert the measured dynamic parameters into the elastic and viscous properties of the materials and structures probed [8,9,31-33].

Table 1: Cantilever parameters.

	Mode 1	Mode 2
Resonance frequency (kHz)	116.54	730.37
Amplitude ratio[a]	458.69	1593.10
Phase (degree)	90.05	270.01
Quality factor *Q*	292.90	1835.64

[a] The amplitude ratio refers to the amplitude at resonance, *A*, normalized to the driven amplitude, A_d.

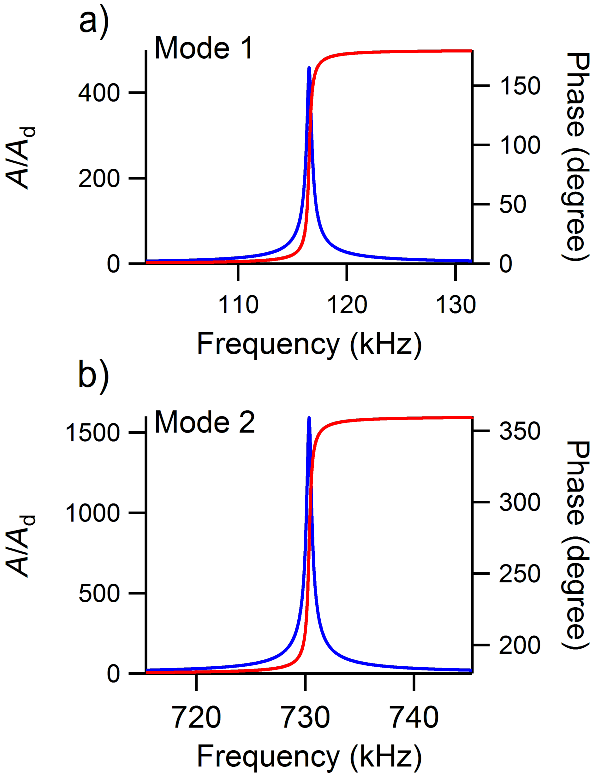

Figure 2: Amplitude ratio and phase of the a) first and b) second free eigenmodes of a cantilever vibrated in the UAFM configuration, measured at the tip.

Amplitude and phase along the cantilever

In Figure 3 are shown the amplitude ratio and phase of the first eigenmode along the cantilever for the UAFM (Figure 3a) and AFAM (Figure 3c) configurations for the same contact stiffness, k^* = 20 N/m, and three different contact damping values: mild (p = 0.10), medium (p = 0.25), and strong (p = 0.50) contact damping. In both configurations, the calculated displacement along the cantilever shows the deformed shape of the first eigenmode with a node at the base of the cantilever (x = 0) and an antinode at the end of the cantilever ($x = L$), with smaller and smaller displacement values as the contact damping increases. In contrast to the displacements, the phase response is quite different in magnitude and shape. Thus, in the UAFM configuration, the phase of the first eigenmode (refer to Figure 3a) goes from 0 at the base of the cantilever to around 90 degrees at the end of the cantilever. The resonance state at the end of the cantilever for the UAFM configuration is detailed in Figure 3b in terms of amplitude and phase. From this, little change in the phase can be observed for the range of considered contact damping, from 91.1 degrees for p = 0.10 to 95.5 degrees for p = 0.50. Interestingly, as can be seen in Figure 3a, the phase is about 90 degrees at 87% of the length of cantilever, independent of the contact damping values. The key observation here is that the phase at the end of the cantilever in the UAFM configuration varies by a few degrees around 90 degrees depending on the magnitude of the contact damping. However, a completely different response in phase is shown in Figure 3c and 3d for the AFAM configuration. First, the phase of the first AFAM eigenmode is essentially constant (very small variation) along the cantilever. Second, its magnitude changes significantly with the considered contact damping. It decreases from essentially 90 degrees when no contact damping is present to 82.6 for p = 0.10, to 72.1 degrees for p = 0.25, and to 57.1 degrees for p = 0.50.

An analogous analysis can be carried out for the amplitude and phase of the second eigenmode shown in Figure 4. The shape of the second eigenmode of the cantilever exhibits two nodes (at the base of the cantilever and at 77% of the length of the cantilever) and two antinodes (at 46% of the length of the cantilever and at the end of the cantilever). Both the UAFM and AFAM configurations impose the same shape for the second eigenmode but the amplitude is about one order of magnitude larger in UAFM than in AFAM. As in the case of the first eigenmode discussed above, the phase of the second eigenmode differs substantially between the two configurations. In the UAFM configuration, the phase is 0 at the cantilever base, shows a 90 degrees plateau around the first antinode, goes through 180 degrees at the second node, and shows another plateau of 270 degrees at the end of the cantilever; 270 degrees is equivalent here to a resonance at −90 degrees. As observed in Figure 4a at the end of the cantilever and also in Figure 4b from the frequency dependences around the resonance, the phase of the second eigenmode at the end of the cantilever experiences small variations as a function of contact damping: 269.1 degrees for p = 0.10 to 265.4 degrees for p = 0.50. In the AFAM configuration, the phase resembles the shape of a two-step function with a sharp transition at the second node. At the end of the cantilever, the phase of the second AFAM eigenmode shown in Figure 4c and 4d varies substantially with the contact damping considered: From 72.6 degrees for p = 0.10, to 52.0 degrees for p = 0.25, and to 32.6 degrees for p = 0.50.

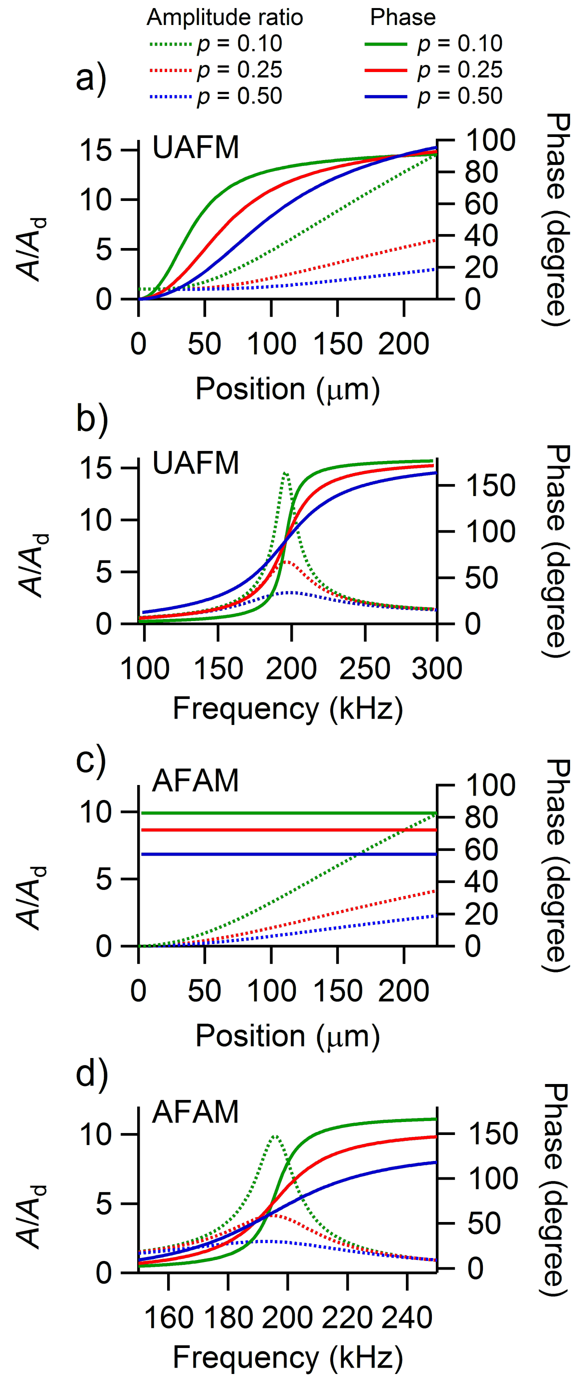

Figure 3: Amplitude ratio and phase of the first eigenmode along the cantilever in a) the UAFM and c) AFAM configurations, respectively. Frequency dependence of the amplitude ratio and phase of the first eigenmode at the end of the cantilever in b) the UAFM and d) AFAM configurations, respectively.

From the above discussion of the amplitude and phase of the first and second eigenmodes of the cantilever, we can conclude that for a given contact stiffness, the amplitude changes significantly with the contact damping and this change is qualitatively and quantitatively similar in UAFM and AFAM. However, the phases of the two configurations differ significantly from each other. In the UAFM configuration the phase experiences small variations as a function of contact damping, with values around 90 degrees (first eigenmode) or −90 degrees (second eigenmode). On the other hand, in the AFAM configuration, the phase is very sensitive to changes in contact damping and exhibits large variations. This analysis indicates that both the UAFM and AFAM amplitudes but only the AFAM phase are good measurable quantities for determining the contact damping of the tip–sample coupling. On the other hand, the UAFM phase is quite insensitive to the contact damping and it

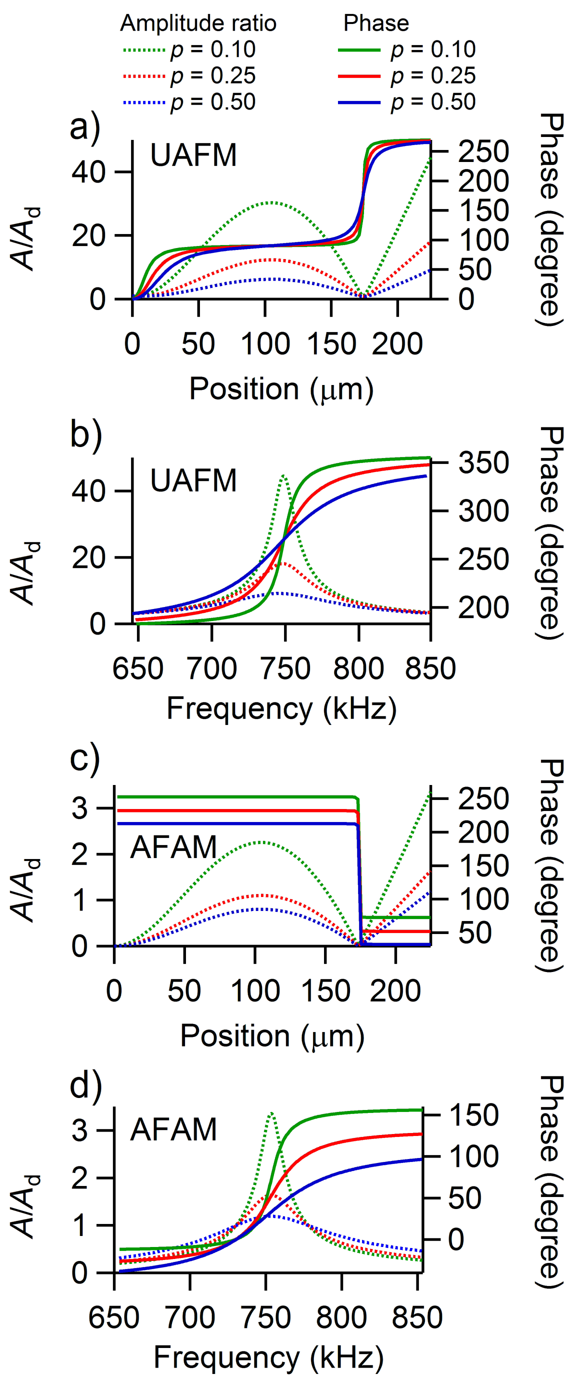

Figure 4: Amplitude ratio and phase of the second eigenmode along the cantilever in a) the UAFM and c) AFAM configurations, respectively. Frequency dependence of the amplitude ratio and phase of the second eigenmode at the end of the cantilever in b) the UAFM and d) AFAM configurations, respectively.

would not be a good measurement for it. However, as discussed later, the invariance of the UAFM phase to contact damping can be used to track the resonance state by phase-control techniques (i.e., PLLs) [34,35].

Contact resonance frequency, amplitude, and phase

To retrieve the contact stiffness and contact damping responses of a material, measurements are made in terms of resonance frequency, amplitude, and phase in any of the CR-AFM configurations. In the following we will analyze these various signals at the end of the cantilever as a function of contact stiffness and contact damping in UAFM and AFAM configurations and examine the differences between these two configurations.

The amplitude ratio, resonance frequency, and phase of the first eigenmode are shown as a function of the contact stiffness in Figure 5 for a small $p = 0.05$ contact damping and in Figure 6 for a medium $p = 0.25$ contact damping, respectively. All the cantilever parameters were taken to be the same as above, with $k_c = 10.00$ N/m. As can be seen in Figure 5 and Figure 6, for each of the contact damping values considered, there is no significant difference between the UAFM and AFAM resonance frequencies (red and grey continuous lines) over the investigated contact stiffness range. This shows that in terms of contact stiffness measurements based on the shift in the resonance frequency the UAFM and AFAM configurations provide the same result. The differences between the two configurations are notable in terms of amplitude and phase. In the UAFM configuration, the amplitude (green continuous line in Figure 5 and Figure 6) slowly increases with the increase in contact stiffness. For the two contact damping values considered in Figure 5 and Figure 6, the overall increase in UAFM amplitude was about 40% between the initial value at $k^* = 0$ N/m and end value at $k^* = 50$ N/m. A more abrupt increase can be observed for the AFAM amplitude (green dotted lines in Figure 5 and Figure 6). In the AFAM configuration the amplitude is zero at $k^* = 0$ N/m when the tip and the sample are basically uncoupled. In practice, however, small oscillations are induced in the cantilever when it is brought close to but still not in contact with the vibrated sample. So, in this case of very small contact stiffnesses, the theoretical AFAM configuration might not be reproduced in experiments. It is interesting to observe that the UAFM and AFAM amplitudes become comparable towards large contact stiffness couplings in both cases of small and medium contact damping. The phase variation as a function of contact stiffness is similar to the amplitude variation in each configuration. Thus, over the considered contact stiffness range, the UAFM phase (blue continuous line in Figure 5 and Figure 6) changes within one degree from its free value (90 degrees) in the case of a small $p = 0.05$ contact damping and within 4 degrees in the case of a medium $p = 0.25$ contact damping. However, a much larger variation is experienced by the AFAM phase (dotted blue line in Figure 5 and Figure 6) with the increase in the contact stiffness. From essentially zero degrees, in the absence of tip–sample coupling, the AFAM phase increases sharply in the range of small contact stiffnesses and has an asymptotical increase for contact stiffnesses comparable or larger than the cantilever stiffness. These asymptotic values of the AFAM phase however depend strongly on the actual contact damping. For the examples shown in Figure 5 and Figure 6, the AFAM phase approaches 87 degrees for a contact stiffness of $p = 0.05$ and 80 degrees for a contact stiff-

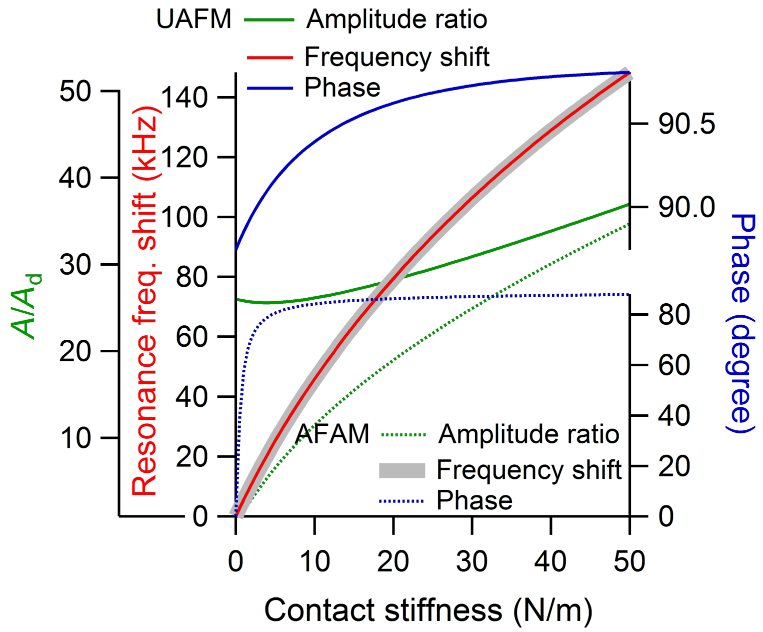

Figure 5: Amplitude ratio, frequency shift, and phase of the first eigenmode versus contact stiffness in UAFM and AFAM configurations when a small contact damping of $p = 0.05$ was considered.

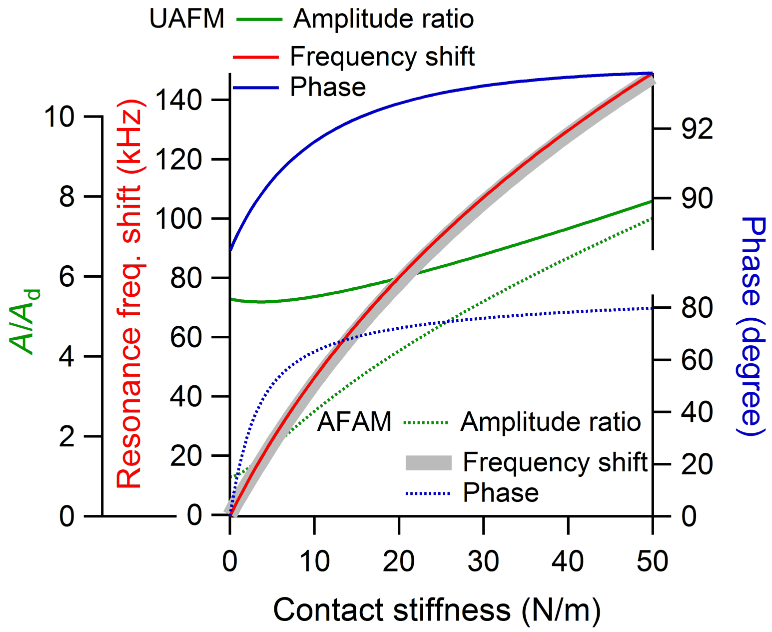

Figure 6: Amplitude ratio, frequency shift, and phase of the first eigenmode versus contact stiffness in UAFM and AFAM configurations when a medium contact damping of $p = 0.25$ was considered.

ness of $p = 0.25$. This reiterates the above observation that the AFAM phase is sensitive to contact damping and could be used as a measure of the tip–sample contact damping.

The variations of the contact resonance frequency, amplitude, and phase as a function of both contact stiffness and contact damping were fully analyzed in the maps shown in Figure 7 for the first eigenmode and in Figure 8 for the second eigenmode of UAFM and AFAM, respectively. In terms of contact resonance frequency, large shifts were observed over the range of considered contact stiffness and damping: about 130 kHz for the first eigenmode (Figure 7a and 7e) and about 50 kHz for the second

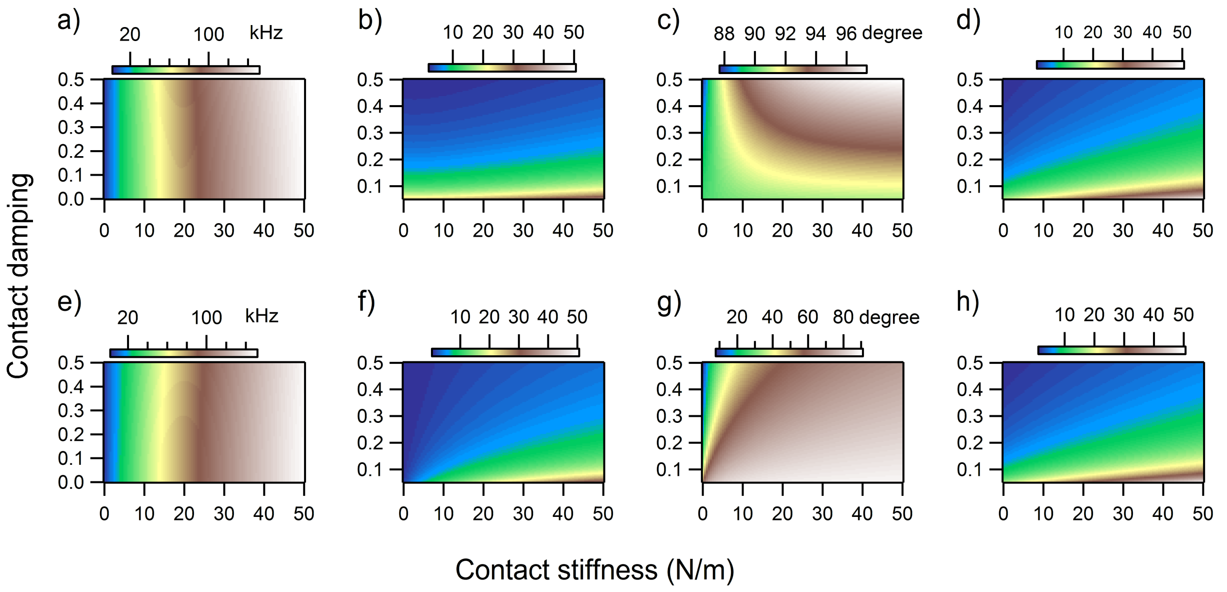

Figure 7: a) Frequency shift, b) normalized amplitude, c) phase, and d) quality factor *Q* of the first eigenmode in the UAFM configuration as a function of contact stiffness and contact damping. e) Frequency shift, f) normalized amplitude, g) phase, and h) quality factor *Q* of the first eigenmode in the AFAM configuration as a function of contact stiffness and contact damping.

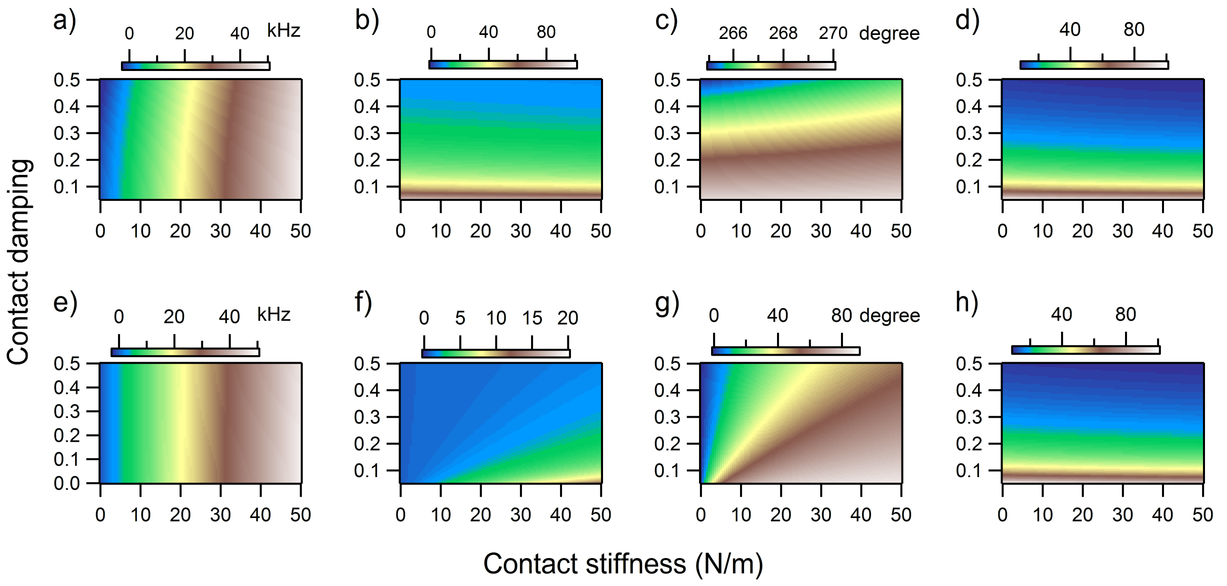

Figure 8: a) Frequency shift, b) normalized amplitude, c) phase, and d) quality factor *Q* of the second eigenmode in the UAFM configuration as a function of contact stiffness and contact damping. e) Frequency shift, f) normalized amplitude, g) phase, and h) quality factor *Q* of the second eigenmode in the AFAM configuration as a function of contact stiffness and contact damping.

eigenmode (Figure 8a and 8e). As can be seen, the frequency shifts are almost insensitive to contact damping and mainly responsive to contact stiffness variations only. On the other hand, a pronounced contact damping dependence and moderate contact stiffness dependence can be observed in the amplitude maps (Figure 7b and 7f for the first eigenmode and Figure 8b and 8f for the second eigenmode), especially for the UAFM configuration. With the exception of the small contact stiffness range, the UAFM and AFAM amplitude values are comparable for the first eigenmode (Figure 7b and 7f). In the case of the second eigenmode, the UAFM amplitudes are consistently larger than the AFAM amplitudes, exhibiting a better amplitude detection of the second UAFM eigenmode than its counterpart in the AFAM configuration. A concurrent dependence on contact stiffness and contact damping can be observed in the maps of the phase at resonance (Figure 7c and 7g for the first eigenmode and Figure 8c and 8g for the second eigenmode). The UAFM phase response to the considered contact stiffness and contact damping variations is of order of a few degrees around 90 degrees for the first eigenmode and few degrees below 270 degrees (−90 degrees) for the second eigenmode. Thus, the UAFM phase of the first eigenmode (Figure 7c) is less than 90 degrees for compliant materials with either low or high contact damping and stiff materials with low contact damping. The phase goes above 90 degrees in the less realistic case of stiff materials with high damping. An even smaller variation of only 5 degrees below the free resonance phase was observed for the second UAFM eigenmode (Figure 8c). As inferred from the above discussion, the AFAM phase, either for the first eigenmode (Figure 7g) or second eigenmode (Figure 8g) exhibits large variation as a function of contact stiffness and contact damping. Thus, the AFAM phase is around zero degrees at small contact stiffnesses and goes asymptotically towards 90 degrees as the contact stiffness increases. This asymptotic trend is progressively delayed with the increase in contact damping. An interesting behaviour is observed also in the maps of quality factor Q (Figure 7d and 7e for the first eigenmode and Figure 8d and 8e for the second eigenmode), calculated as the ratio of the resonance frequency to the width of the resonance peak, $\omega_n/\Delta\omega$. In general, the quality factor is directly associated with the damping response of the system. However, as it can be seen in Figure 7d and 7h, it depends on both the contact stiffness and contact damping. The Q-factor is almost independent of contact stiffness for the second UAFM and AFAM eigenmodes, in which case it can be used as a direct measurement of the tip–sample contact damping. Explicit relationships between the Q-factors of various contact eigenmodes and contact damping were intuitively proposed [36] and rigorously derived [37] previously for the AFAM configuration. The results shown in Figure 7h and Figure 8h are in agreement, within the common range of contact stiffness, with the Q-factor versus contact damping dependences shown in Figure 2 of [37] for the first two eigenmodes.

Phase-locked loop detection

By considering their specific dependences in either UAFM or AFAM configurations, the measured contact resonance frequency, amplitude, and phase can be converted into the stiffness and damping of the tip–sample contact coupling. One way of observing the fast change in the dynamics of a cantilever used in CR-AFM point measurements or scanning is to track the resonance state by PLL detection, similar with what is used in non-contact frequency modulation AFM. In non-contact AFM, PLL tracking has been implemented in either constant-excitation frequency modulation [17,18] or constant-amplitude frequency-modulation [19,20]. In the following we will refer only to the constant-excitation PLL setup in which the driving amplitude is constant and the frequency is adjusted continuously to maintain a constant phase difference between drive and response, φ_{PLL}. In the case of an AFM cantilever brought into contact from air, the PLL reference phase would be the phase of the free oscillation of the selected eigenmode. However, as we discussed above, the phase of a vibrated cantilever that is in contact with a sample, even when it is driven at the resonance, is not constant but varies in accordance with the magnitudes of the contact stiffness and contact damping. This means that in PLL detection the true resonance condition will not be retrieved. Instead one would obtain the state having the predefined PLL phase, φ_{PLL}. The error introduced by the PLL in measuring the resonance frequency will then by $\Delta f = f_{\text{resonance}} - f_{\text{PLL}}$, where $f_{\text{resonance}}$ is the dynamic resonance frequency and f_{PLL} is the frequency at which the phase of the detected signal is φ_{PLL}.

Based on its weak dependence on contact stiffness and contact damping, the UAFM phase can be used in a PLL detection [35,38] to maintain the cantilever–tip–sample system at the resonance and track the changes in the resonance frequency and amplitude. Figure 9 shows the errors introduced by the PLL in measuring the resonance frequency of the first and second eigenmodes when the locked phase was that of the free resonance of the respective eigenmode. As can be seen in Figure 9, the errors introduced by the PLL in determining the true resonance frequencies of the first two UAFM eigenmodes are within 1 kHz for low and medium contact damping ($p < 0.25$) over the contact stiffness range considered. In the case of very large contact damping, these errors extend to about 2 kHz or 3 kHz for some particular values of contact stiffness. Considering that these errors are for shifts of about 150 kHz for the resonance frequency of the eigenmode (refer to Figure 7a) and 50 kHz for the resonance frequency of the second mode (refer to Figure 8a), respectively, they result in negligible errors in the

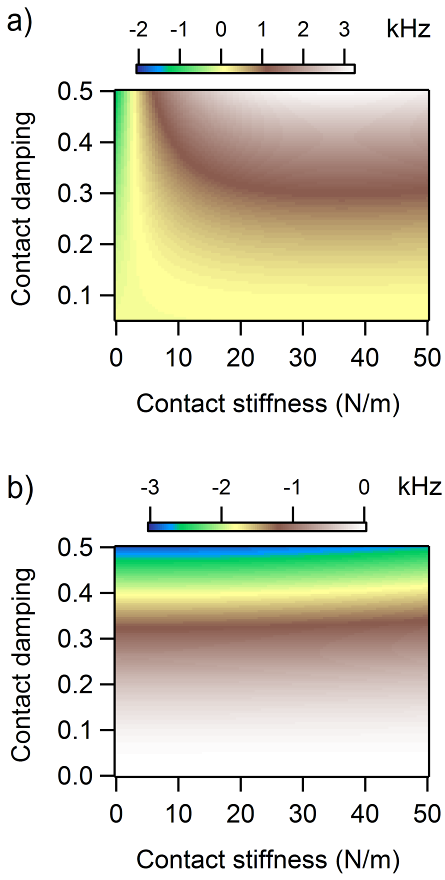

Figure 9: The frequency error introduced by a PLL in measuring the shift of the contact resonance frequency of (a) the first and (b) second eigenmodes in the UAFM configuration as a function of contact stiffness and contact damping. The corresponding frequency shifts over the investigated contact stiffness and contact damping ranges are shown in Figure 7a and Figure 8a for the two eigenmodes, respectively.

conversion of measured contact resonance frequencies into material elastic moduli.

A particular situation arises in the case of using PLL detection in the AFAM configuration. As was discussed above, large variations are experienced by the AFAM phase from out of contact to contact states. In the AFAM configuration the phase was found to be very sensitive to the stiffness and damping of the tip–sample contact. This phase sensitivity could be used directly for contact damping measurements [8] but would make impractical the PLL detection of the contact resonance of an AFAM eigenmode with respect to its free resonance. However, a moderate variation is experienced by the AFAM phase for contact stiffness comparable or greater than the stiffness of the cantilever (e.g., contact stiffnesses about or greater than 10 N/m in the examples considered in Figure 5 and Figure 6). It is therefore possible to perform PLL tracking even in the AFAM configuration by choosing a reference contact resonance state with respect to which moderate phase variations are experienced during contact measurements or scanning. This type of measurement has been performed also in the UAFM configuration of CR-AFM on Cu-low-*k* dielectric materials, with the PLL locked on the phase of a contact resonance state, after the tip was brought into contact at the desired applied force [35]. From a practical point of view, it is worth mentioning here that in the case of UAFM, the detection is very sensitive to the transfer function of the cantilever used and in some cases, depending on the cantilever used and tip–sample couplings, spurious resonances can mask or distort the real tip–sample coupling resonances [39,40]. On the other hand, in AFAM configuration, the frequency spectra are heavily overwritten by the transfer function of the excitation actuator (underneath the sample), which can provide cleaner spectra at the expense of a more aggressive tip–sample coupling.

Conclusion

The resonance frequency, amplitude, and phase of the first two eigenmodes of two contact resonance AFM (CR-AFM) configurations, namely a setup with sample stage excitation (AFAM) and one with cantilever base excitation (UAFM), were analyzed in detail. This allowed observing similarities and differences among the dynamic parameters of each of the CR-AFM configurations as a function of the mechanical coupling on different materials. Thus, while the contact resonance frequency is mostly sensitive to contact stiffness and less sensitive to contact damping, the resonance amplitude and phase exhibit a concurrent dependence on both contact stiffness and contact damping. Also, it was found that the two CR-AFM configurations differ greatly through their phase response. Thus, while the UAFM phase shows a reduced variation over a large range of material parameters, the AFAM phase is very sensitive to both contact stiffness and contact damping. These results suggest that, from an experimental point of few, UAFM would be the preferred CR-AFM configuration in phase-control detection applications. However, with appropriate use of their specific frequency dependences, both amplitude and phase are theoretically available for elastic modulus and dissipation measurements in both UAFM and AFAM configurations.

References

1. Binnig, G.; Quate, C. F.; Gerber, C. *Phys. Rev. Lett.* **1986,** *56,* 930–933. doi:10.1103/PhysRevLett.56.930
2. Radmacher, M.; Tillman, R. W.; Gaub, H. E. *Biophys. J.* **1993,** *64,* 735–742. doi:10.1016/S0006-3495(93)81433-4
3. Rabe, U.; Janser, K.; Arnold, W. *Rev. Sci. Instrum.* **1996,** *67,* 3281–3293. doi:10.1063/1.1147409
4. Yamanaka, K.; Nakano, S. *Jpn. J. Appl. Phys.* **1996,** *35,* 3787–3792. doi:10.1143/JJAP.35.3787

5. Hurley, D. C.; Kopycinska-Müller, M.; Kos, A. B.; Geiss, R. H. *Meas. Sci. Technol.* **2005,** *16,* 2167–2172. doi:10.1088/0957-0233/16/11/006
6. Passeri, D.; Bettucci, A.; Germano, M.; Rossi, M.; Alippi, A.; Sessa, V.; Fiori, A.; Tamburri, E.; Terranova, M. L. *Appl. Phys. Lett.* **2006,** *88,* 121910. doi:10.1063/1.2188376
7. Stan, G.; Price, W. *Rev. Sci. Instrum.* **2006,** *77,* 103707. doi:10.1063/1.2360971
8. Yuya, P. A.; Hurley, D. C.; Turner, J. A. *J. Appl. Phys.* **2008,** *104,* 074916. doi:10.1063/1.2996259
9. Stan, G.; Cook, R. F. *Nanotechnology* **2008,** *19,* 235701. doi:10.1088/0957-4484/19/23/235701
10. Jesse, S.; Kalinin, S. V.; Proksch, R.; Baddorf, A. P.; Rodriguez, B. J. *Nanotechnology* **2007,** *18,* 435503. doi:10.1088/0957-4484/18/43/435503
11. Kareem, A. U.; Solares, S. D. *Nanotechnology* **2012,** *23,* 015706. doi:10.1088/0957-4484/23/1/015706
12. Rodriguez, B. J.; Callahan, C.; Kalinin, S. V.; Proksch, R. *Nanotechnology* **2007,** *18,* 475504. doi:10.1088/0957-4484/18/47/475504
13. García, R.; Pérez, R. *Surf. Sci. Rep.* **2002,** *47,* 197–301. doi:10.1016/S0167-5729(02)00077-8
14. Martínez, N. F.; García, R. *Nanotechnology* **2006,** *17,* S167–S172. doi:10.1088/0957-4484/17/7/S11
15. Cleveland, J. P.; Annczykowski, B.; Schmid, A. E.; Elings, V. B. *Appl. Phys. Lett.* **1998,** *72,* 2613–2615. doi:10.1063/1.121434
16. García, R.; Tamayo, J.; San Paulo, A. *Surf. Interface Anal.* **1999,** *27,* 312–316. doi:10.1002/(SICI)1096-9918(199905/06)27:5/6<312::AID-SIA496>3.0.CO;2-Y
17. Hölscher, H.; Gotsmann, B.; Allers, W.; Schwarz, U. D.; Fuchs, H.; Wiesendanger, R. *Phys. Rev. B* **2001,** *64,* 075402. doi:10.1103/PhysRevB.64.075402
18. Gotsmann, B.; Seidel, C.; Anczykowski, B.; Fuchs, H. *Phys. Rev. B* **1999,** *60,* 11051–11061. doi:10.1103/PhysRevB.60.11051
19. Hölscher, H.; Gotsmann, B.; Schirmeisen, A. *Phys. Rev. B* **2003,** *68,* 153401. doi:10.1103/PhysRevB.68.153401
20. Schirmeisen, A.; Hölscher, H.; Anczykowski, B.; Weiner, D.; Schäfer, M. M.; Fuchs, H. *Nanotechnology* **2005,** *16,* S13–S17. doi:10.1088/0957-4484/16/3/003
21. García, R.; Herruzo, E. T. *Nat. Nanotechnol.* **2012,** *4,* 217–226. doi:10.1038/nnano.2012.38
22. Rodríguez, T. R.; García, R. *Appl. Phys. Lett.* **2004,** *84,* 449–451. doi:10.1063/1.1642273
23. Martinez, N. F.; Patil, S.; Lozano, J. R.; Garcia, R. *Appl. Phys. Lett.* **2006,** *89,* 153115. doi:10.1063/1.2360894
24. Solares, S. D.; Chawla, G. *J. Appl. Phys.* **2010,** *108,* 054901. doi:10.1063/1.3475644
25. Chawla, G.; Solares, S. D. *Appl. Phys. Lett.* **2011,** *99,* 074103. doi:10.1063/1.3626847
26. Lozano, J. R.; Garcia, R. *Phys. Rev. Lett.* **2008,** *100,* 076102. doi:10.1103/PhysRevLett.100.076102
27. Lozano, J.; Garcia, R. *Phys. Rev. B* **2009,** *79,* 014110. doi:10.1103/PhysRevB.79.014110
28. Kawai, S.; Glatzel, T.; Koch, S.; Such, B.; Baratoff, A.; Meyer, E. *Phys. Rev. Lett.* **2009,** *103,* 220801. doi:10.1103/PhysRevLett.103.220801
29. Naitoh, Y.; Ma, Z. M.; Li, Y. J.; Kageshima, M.; Sugawara, Y. *J. Vac. Sci. Technol., B: Nanotechnol. Microelectron.: Mater., Process., Meas., Phenom.* **2010,** *28,* 1210–1214. doi:10.1116/1.3503611
30. Rabe, U. In *Applied Scanning Probe Microscopy;* Bhushan, B.; Fuchs, H., Eds.; Springer: Berlin, 2006; Vol. II, p 3790.
31. Stan, G.; Ciobanu, C. V.; Thayer, T. P.; Wang, G. T.; Creighton, J. R.; Purushotham, K. P.; Bendersky, L. A.; Cook, R. F. *Nanotechnology* **2009,** *20,* 035706. doi:10.1088/0957-4484/20/3/035706
32. Stan, G.; Krylyuk, S.; Davydov, A. V.; Cook, R. F. *Nano Lett.* **2010,** *10,* 2031–2037. doi:10.1021/nl100062n
33. Hurley, D. C.; Campbell, S. E.; Killgore, J. P.; Cox, L. M.; Ding, Y. *Macromolecules* **2013,** *46,* 9396–9402. doi:10.1021/ma401988h
34. Kobayashi, K.; Yamada, H.; Matsushige, K. *Surf. Interface Anal.* **2002,** *33,* 89–91. doi:10.1002/sia.1168
35. Stan, G.; King, S. W.; Cook, R. F. *Nanotechnology* **2012,** *23,* 215703. doi:10.1088/0957-4484/23/21/215703
36. Caron, A.; Arnold, W. *Acta Mater.* **2009,** *57,* 4353–4363. doi:10.1016/j.actamat.2009.05.030
37. Yuya, P. A.; Hurley, D. C.; Turner, J. A. *J. Appl. Phys.* **2011,** *109,* 113528. doi:10.1063/1.3592966
38. Stan, G.; Solares, S. D.; Pittenger, B.; Erina, N.; Su, C. *Nanoscale* **2014,** *6,* 962–969. doi:10.1039/c3nr04981g
39. Hurley, D. C. Chapter 5. In *Applied Scanning Probe Methods;* Bhushan, B.; Fuchs, H., Eds.; Springer-Verlag: Berlin Heidelberg New York, 2009; Vol. XI, pp 27 ff.
40. Xu, X.; Koslowski, M.; Raman, A. *J. Appl. Phys.* **2012,** *111,* 054303. doi:10.1063/1.3689815

License and Terms

Beilstein Journal
of Nanotechnology

Effect of contaminations and surface preparation on the work function of single layer MoS_2

Oliver Ochedowski[1], Kolyo Marinov[1], Nils Scheuschner[2], Artur Poloczek[3], Benedict Kleine Bussmann[1], Janina Maultzsch[2] and Marika Schleberger*[1]

Full Research Paper

Address:
[1]Fakultät für Physik and CeNIDE, Universität Duisburg-Essen, Lotharstr. 1, 47057 Duisburg, Germany, [2]Institut für Festkörperphysik, Technische Universität Berlin, Hardenbergstr. 36, 10623 Berlin, Germany and [3]Solid State Electronics Department and CeNIDE, University of Duisburg-Essen, Lotharstr. 55, 47058 Duisburg, Germany

Email:
Marika Schleberger* - marika.schleberger@uni-due.de

* Corresponding author

Keywords:
KPFM; MoS_2; NC-AFM; surface potential; work function

Beilstein J. Nanotechnol. **2014,** *5,* 291–297.
doi:10.3762/bjnano.5.32

Received: 31 October 2013
Accepted: 11 February 2014
Published: 13 March 2014

This article is part of the Thematic Series "Noncontact atomic force microscopy II".

Guest Editors: U. D. Schwarz and M. Z. Baykara

Abstract

Thinning out MoS_2 crystals to atomically thin layers results in the transition from an indirect to a direct bandgap material. This makes single layer MoS_2 an exciting new material for electronic devices. In MoS_2 devices it has been observed that the choice of materials, in particular for contact and gate, is crucial for their performance. This makes it very important to study the interaction between ultrathin MoS_2 layers and materials employed in electronic devices in order to optimize their performance. In this work we used NC-AFM in combination with quantitative KPFM to study the influence of the substrate material and the processing on single layer MoS_2 during device fabrication. We find a strong influence of contaminations caused by the processing on the surface potential of MoS_2. It is shown that the charge transfer from the substrate is able to change the work function of MoS_2 by about 40 meV. Our findings suggest two things. First, the necessity to properly clean devices after processing as contaminations have a great impact on the surface potential. Second, that by choosing appropriate materials the work function can be modified to reduce contact resistance.

Introduction

Due to their unique properties which can differ a lot compared to bulk materials, two-dimensional materials are being targeted in a variety of research areas like surface physics, electrical engineering, chemistry and biomedical applications [1-4]. The 2D-material getting the most attention besides graphene are single layers of molybdenum disulfide (SLM) which consist of a plane of molybdenum atoms that are sandwiched between sulfur atoms. The main reason for this is the transition from an indirect (bulk MoS_2) to a direct (single layer MoS_2) band gap semi-conductor [5]. Single layer MoS_2 has a strong photoluminescence signal [5-9] and other interesting properties like a mechanical stiffness of $180 \pm 60\ \mathrm{N{\cdot}m^{-1}}$, which is comparable to steel [10,11], charge carrier mobilities that are comparable to Si [12,13], and it is possible to grow these ultrathin layers using

CVD [14-16]. The main advantage SLM has to offer compared to the model 2D-material graphene is its direct band gap. It allows the facile integration of SLM in electronic devices, which has been demonstrated for highly flexible transistors, optoelectronic devices, small-signal amplifiers, MoS_2 integrated circuits and chemical vapor sensors [12,17-21]. It has been reported that the performance of these devices can greatly vary due to the choice of the material of the contacts, the cleanliness of the SLM surface and a top gated structure with a high κ dielectric [22-27]. By choosing appropriate materials in 2D-devices the work function can be tuned to, e.g., lower the contact resistance and improve their performance. First experiments adressing this issue for MoS_2 by using Kelvin probe force microscopy (KPFM) have already been reported [28,29]. However, these measurements were not done on SLM but bilayer MoS_2 (BLM) and higher layer numbers and the measurements were performed under ambient conditions using amplitude modulated KPFM, both having a great impact on the results. In this work we study the work function of SLM on a standard SiO_2/Si substrate using non-contact atomic force microscopy (NC-AFM) and Kelvin probe force microscopy in situ. In our measurements we use a gold contact patterned on SLM in order to calibrate the work function of our AFM tip which allows us to determine quantitative work function values for SLM, BLM and few layer MoS_2 (FLM). Additionaly, we use reactive ion etching to pattern holes into the SiO_2 substrate. By comparing the work function of SLM on etched and pristine SiO_2 substrates, we show that a significant change in the work function can be achieved by substrate effects.

Experimental

For our studies we exfoliated MoS_2 (HQgraphene, Netherlands) on a patterned Si sample that has been covered by 90 nm SiO_2 layer (graphene supermarket, Calverton, NY, USA). The SiO_2 was patterned by using an inductive coupled plasma reactive ion etching (ICP-RIE) with Cl_2/N_2 chemistry. The etching mask used was a standard photoresist patterned by optical lithography. The etching was performed at 35 °C using 300 W of ICP and 150 W table power. The chamber pressure was adjusted to $8\cdot10^{-3}$ mbar during this procedure. Reactive ion etching was employed to locally alter the surface roughness and introduce defects in the SiO_2 substrate [30,31]. The resulting structures on the SiO_2 surface consist of etched holes with a depth of about 40 nm measured using AFM. Immediately after etching, the MoS_2 was exfoliated by mechanical cleavage [32]. Single layer MoS_2 flakes were located by using their optical contrast and verified using Raman spectroscopy [33,34]. For Raman point measurements and mappings, a Renishaw InVia Raman spectrometer (λ = 532 nm, $P < 0.4$ mW, spectral resolution ≈ 1 cm^{-1}) has been employed. Because SLM is highly flexibel, it is not covering the etched hole. Instead the SLM touches the etched SiO_2 surface at the bottom and follows the morphology like a membrane (Figure 1). While this leaves the SLM heavily strained on the edge of the hole, it allows to experimentally compare the effect of two differently treated subtrates (SiO_2 and RIE SiO_2) on the same MoS_2 flake. After identification of SLM areas, a Ti/Au (5 nm/15 nm) contact was patterned on the MoS_2 flake by photolithography. We used the Photoresist ARP-5350 (Allresist GmbH, Strausberg, Germany) with the developer AR 300-35 (Allresist GmbH, Strausberg, Germany). Acetone was used for the lift-off and finally the samples were boiled in isopropyl alcohole. The contact served two purposes. On the one hand, the sample was electrically connected to ground potential, on the other hand, the gold surface was used for calibrating the work function of the AFM tip during KPFM measurements.

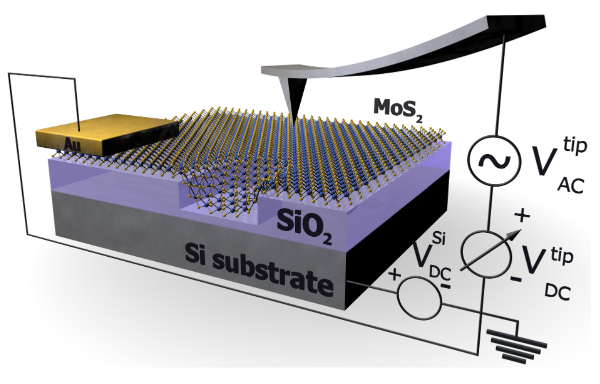

Figure 1: Schematic representation of the KPFM setup and the MoS_2 sample with the RIE SiO_2.

The contacted SLM sample is introduced into an ultra high vacuum system with a base pressure of about $2\cdot10^{-10}$ mbar. Non-contact AFM measurements were performed using a RHK UHV 7500 system with the PLL Pro 2 controller. Simultaneously to NC-AFM, frequency-modulated KPFM measurements were conducted to probe the local contact potential difference (CPD) between the tip and the surface [35-41]. As force sensors, highly conductive Si cantilevers with a typical resonance frequency of f = 300 kHz (Vistaprobe T300) were utilized. During KPFM measurements an AC voltage is applied to the tip (U_{AC} = 1 V and f_{AC} = 1 kHz) and the built in lock-in amplifier of the PLL Pro 2 is used to apply a DC voltage which minimizes the resulting electrostatic forces between tip and sample surface. This DC voltage corresponds to the local CPD.

Results and Discussion

Raman spectroscopy characterization

In Figure 2 we present an optical image of a sample prepared by the procedure described above together with additional Raman spectroscopy data. The SLM flake can be identified in the

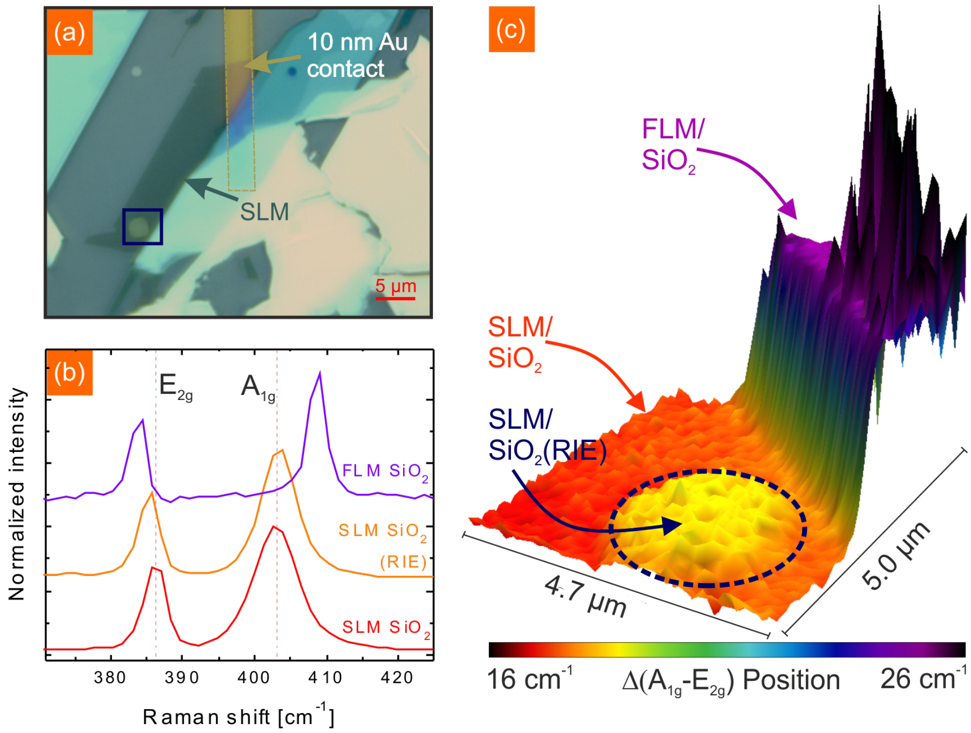

Figure 2: (a) Optical microscope image of an exfoliated MoS_2 flake on a prepatterned (RIE) SiO_2 substrate. A gold contact was attached to the MoS_2 in order to ground the flake for KPFM measurements. (b) Raman spectroscopy spectra of SL and FL MoS_2 on SiO_2 and SL MoS_2 on RIE SiO_2. For higher layer numbers the E_{2g} is shifted to lower wave number while the A_{1g} mode is shifted to higher wave numbers. (c) Raman mapping data of the area marked in (a) with the blue box. The difference between A_{1g} and E_{2g} mode is plotted revealing a shift of the Raman modes for SLM on the RIE SiO_2 substrate.

optical image in Figure 2a by its contrast, which is a transparent green tone. While the majority of the SLM flake is located on pristine SiO_2, a small part of the SLM flake is at the bottom of a hole which was patterned by RIE. To unambiguously identify SLM we used Raman spectroscopy and compared the results to data obtained by literature [34]. In Figure 2b the Raman spectra of SLM on SiO_2 and on SiO_2 (RIE) as well as FLM on SiO_2 is shown. The two prominent peaks, the E_{2g} and A_{1g} peak, correspond to the opposite vibration of the two S atoms with respect to the Mo atom and the out-of-plane vibration of only S atoms in opposite directions, respectively [42,43]. For SLM on SiO_2 the Raman shifts obtained for the E_{2g}, $\nu = 386.1$ cm^{-1}, and A_{1g}, $\nu = 403.0$ cm^{-1}, are consistent with values reported by other groups. For higher layer numbers the E_{2g} has been reported to shift to lower wave numbers while the A_{1g} shifts to larger wave numbers which is again in good agreement with our data. However, the SLM on RIE SiO_2 shows a different behaviour compared to SLM on pristine SiO_2. The E_{2g} is slightly downshifted to $\nu = 385.2$ cm^{-1} and the A_{1g} shows a minor shift to $\nu = 403.4$ cm^{-1}. Shifts of the E_{2g} and A_{1g} modes of SLM can have multiple reasons. Uniaxial tensial strain has been observed to cause a splitting in the E_{2g} mode and a shift to lower wave numbers for the resulting E^{-} and E^{+} modes by 4.5 and 1 cm^{-1}/% [44,45]. While the A_{1g} mode shows no distinct sensitivity to uniaxial strain, a charge carrier dependency has been observed [46]. Electron doping of $1.8{\cdot}10^{13}$ cm^{-2} leads to a linewidth broadening of 6 cm^{-1} and the phonon frequency decreases by 4 cm^{-1}. As our data shows a shift in both Raman active modes we suggest that the RIE SiO_2 surface causes a slight strain and maybe local doping by charge transfer in the MoS_2 flake. The Raman mapping shown in Figure 2c corresponds to the evaluation of point spectra performed in the green box marked in Figure 2a. Plotted is the difference of the E_{2g} an A_{1g} mode positions. While the difference between SLM and FLM on SiO_2 is significant with $\Delta = 8.2$ cm^{-1}, the difference between SLM on SiO_2 and on RIE SiO_2 is relatively small with $\Delta = 1.3$ cm^{-1}. As can be seen in the Raman mapping, the difference in the SLM induced by the substrate is constant over the whole flake and not just present in single point meaurements.

In-situ KPFM on single layers of MoS_2

For the NC-AFM and KPFM measurements the sample was introduced to the UHV system. Before the data collection the sample was heated in situ to 200 °C for 30 min to remove any adsorbates from ambience. In Figure 3a and Figure 3c the NC-AFM topography and the corresponding surface potential map are shown, respectively. On the right side the Ti/Au contact can be seen which is about 20 nm high and shows a distinct contrast in the surface potential in comparison to the MoS_2 layers. In Figure 3d a surface potential histogram of SLM, FLM and the gold surface of the Ti/Au contact is given. We find a surface potential of 4.27 V for SLM, 4.37 V for FLM and 4.89 V for gold. The surface potential itself is always a relative value based on the local CPD between the AFM tip and the sample surface. To obtain quantitative work function values, we calibrated the tip on the gold surface by using the known work function of gold Φ_{Au} = 5.10 eV [47,48]. With the relation $\Phi = 5.10\text{eV} - e\cdot(\text{CPD}_{\text{Au}} - \text{CPD}_{\text{nMoS2}})$ the work function of SLM $\Phi_{SLM} = 4.49 \pm 0.03$ eV and FLM $\Phi_{FLM} = 4.59 \pm 0.03$ eV can be assigned. The given errorbar consists of the experimental error of our system. Not included in this error is band bending, which occurs when doing KPFM measurements on a semi-conductor surface and a false estimation of the work function of the patterned gold contact. Besides graphite [49], gold is a common material to calibrate the work function of the AFM tip [48], but while the work function Φ_{Au} = 5.10 eV is often used, other work function values in the range from 4.74 eV to 5.54 eV have been reported as well [50,51]. Surface roughness, homogeneity and humidity can have an effect on the measured work function of metal surfaces as Guo et al. recently demonstrated [52]. The presented data is measured in situ after annealing and we are therefore confident that humidity can be neglected. We want to point out that an error in the work function calibration does not affect the work function values of SLM, BLM and FLM with respect to each other. While the surface potential on the Au contact in Figure 3 appears uniform, strong local variations can be observed on the MoS_2 flake. We attribute these features, marked in Figure 3a with green circles, to contaminations due to the patterning process. The height of these contaminations varies between 1 nm and 20 nm. These contaminations have a noticeable effect on the work function of SLM, as Φ_{SLM} can be lowered by up to 0.15 eV. As the work function of these contaminations is clearly different than that of the Au contact, the contaminations are most likely resist residues which have not been completely removed. Such contaminations may act as scattering centers or charge puddles which are likely to be detrimental to the performance of SLM devices [53]. For graphene and MoS_2 it has been shown, that adsorbates due to ambient exposure can have a strong impact on the work function of these materials, like inducing an additional charge transfer or even redox reactions with water [29,54].

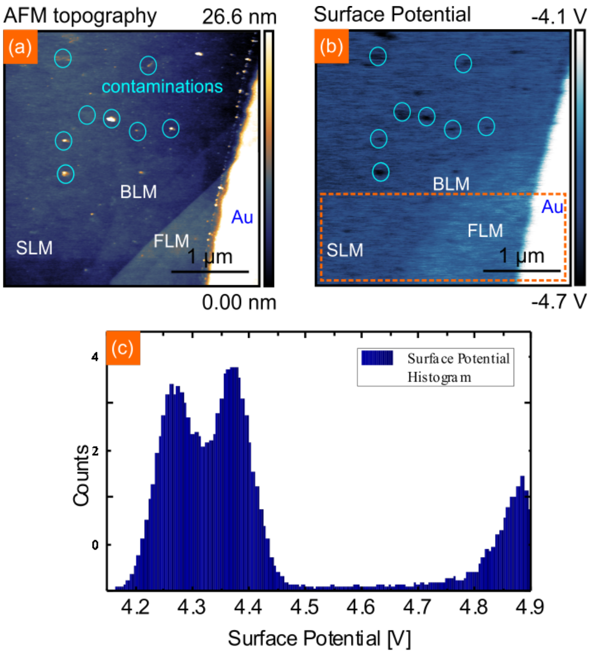

Figure 3: (a) NC-AFM image of MoS_2 flake on SiO_2 with a gold contact (height = 20 nm). Topography shows areas with contaminations due to processing. (b) Corresponding surface potential image to (a). The surface potential of MoS_2 is increasing with increasing layer thickness, contaminations can be clearly distinguished in the surface potential image. (c) Surface potential histogram of the box marked in (b).

In situ screening length of MoS_2

In the next step, we determine the work function of BLM and the screening length of MoS_2. For this the SLM/BLM/FLM section of Figure 3 has been measured again in more detail and the work function is analyzed by line profiles. Shown in Figure 4a–c are the NC-AFM topography, work function map and the corresponding line profiles, respectively. The measured height for BLM is 0.92 ± 0.10 nm, which is slightly higher than the interlayer spacing of a bulk MoS_2 crystal [55]. For FLM we get two different heights, one is 2.96 nm (≈5 layers) and 7.89 nm (≈12–13 layers). In the work function map in Figure 4b, three contrasts can be observed – SLM, BLM and FLM. As the work function for FLM 2.96 nm and the other FLM with 7.89 nm is not changing, we conclude from our data that the screening length of MoS_2 is at least 2.96 nm, which is in good agreement with previous findings for annealed MoS_2 [29]. Li et al. compared the screening length of pristine MoS_2 flakes on SiO_2 with annealed MoS_2 flakes and found a decrease from approximately 5 nm down to 2.5 nm for annealed MoS_2. Our measurements here yield a screening length between 1.6 and 2.96 nm, which is much lower than the value for pristine MoS_2. We therefore conclude that the investigated MoS_2 is not affected by ambient adsorbates. In Figure 4c we used the line profile to quantify the work function of SLM and BLM. The work function of SLM is determined to be the same as using the histogram analysis in Figure 3 with $\Phi_{SLM} = 4.49 \pm 0.03$ eV.

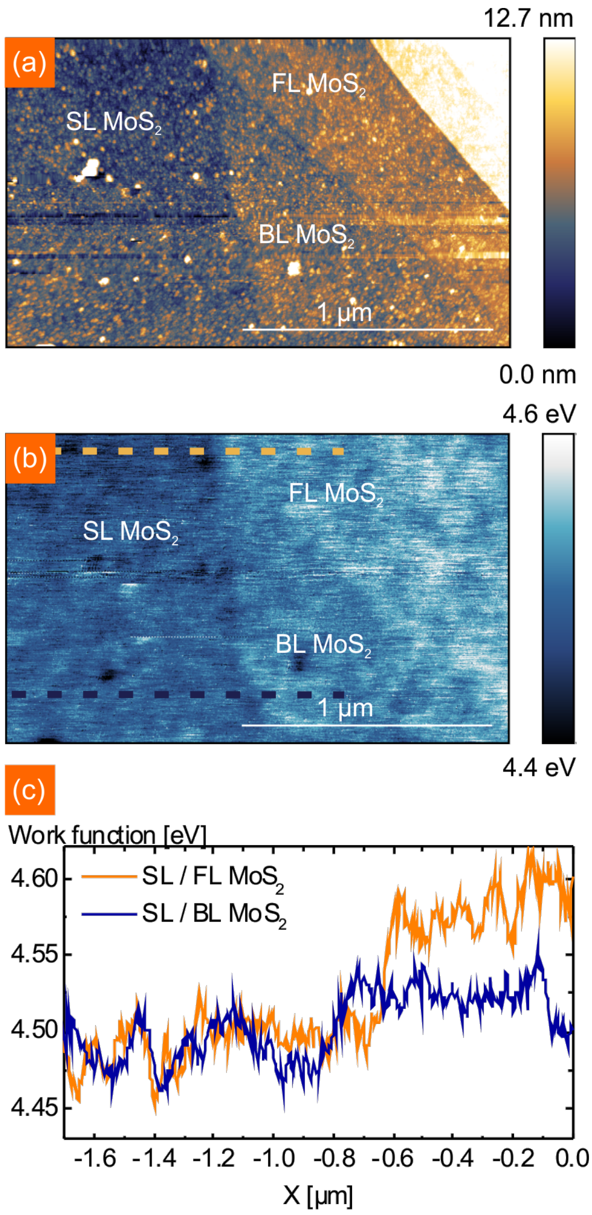

Figure 4: (a) NC-AFM zoom-in of an area consisting of 1L, 2L and FL MoS_2. (b) Corresponding KPFM image, calibration of the tip on the gold contact allows assignment of work functions to surface potential values. Plotted is the work function. (c) Line profiles of the work function corresponding to the lines marked in (b).

The work function of BLM is increased with respect to SLM by about 0.05 eV to $\Phi_{BLM} = 4.54 \pm 0.03$ eV. Again, contaminations on BLM appear to decrease the work function as can be seen in Figure 4b.

Substrate effects on the work function of single layer MoS_2

To study the effect of the substrate on the work function of SLM, we compare the work function of SLM on SiO_2 with SLM in the RIE SiO_2 holes in Figure 5. The work function map in Figure 5b shows an increased work function over the etched hole of about $\Delta\Phi = 0.04$ eV. This shift is caused by the charge transfer from the etched substrate which leads to an effective doping that has been proven to have a large impact on the optical properties of SLM [56]. The etched SiO_2 substrate has an effect on the surface potential distribution as well. By comparing histogram data of SLM on SiO_2 and RIE SiO_2 (see inset in Figure 5c) we find a decreased surface potential fluctuation by 0.02 eV for SLM on the etched SiO_2. The potential fluctuation is related to charge impurities which are detrimental for the performance of 2D-devices and KPFM is an efficient way to probe it [57]. Further, a lower potential fluctuation indicates a higher charge homogeneity. Charge inhomogeneity has been shown to play a crucial role in the oxidative reactivity of graphene [58]. At the edge of the etched hole, where SLM is heavily bent, a strong increase in the work function by another $\Delta\Phi = 0.05$ eV compared to SLM on the RIE SiO_2 substrate caused by stress can be observed. It has been shown by Castellanos-Gomez et al. that heavy strain in SLM has a large impact on the band gap of SLM [59]. However, KPFM only measures the contact potential difference (from which we derive the work function). For insulating materials there is no straightforward relation between the contact potential difference and the band-gap. Therefore, our results are not directly comparable. The plot in Figure 5c sums up our findings with respect to the work function of MoS_2. The work function of FLM in ambient has been determined previously by amplitude modulated KPFM. The reported values of $\Phi = 5.25$ eV [28] are significantly higher than the values found here. This difference is clearly due to the contaminations which are absent in our measurements. Our data should instead be compared to the values determined by other means like ultraviolet photoelectron spectrosocopy [60-63]. The excellent agreement again underlines the importance of UHV measurements if intrinsic properties are to be probed.

Conclusion

In conclusion we have performed the first in situ Kelvin probe force microscopy measurements on single layers of MoS_2 on a SiO_2 substrate. We find work functions of $\Phi_{SLM} = 4.49$ eV, $\Phi_{BLM} = 4.54$ eV and $\Phi_{FLM} = 4.59$ eV for SLM, BLM and FLM respectively. We observe a screening length between 1.6 and 3.5 nm which indicates a clean MoS_2 flake. We have further investigated the effect of the substrate on the work function of MoS_2 by partly etching the SiO_2 substrate. Raman spectroscopy measurements suggests substrate effects like strain which increase the work function of SLM of $\Delta\Phi = 0.04$ eV on etched SiO_2. The next step is to investigate completely free standing MoS_2 flakes without a substrate in order to probe the intrinsic charge homogeneity and work function of SLM.

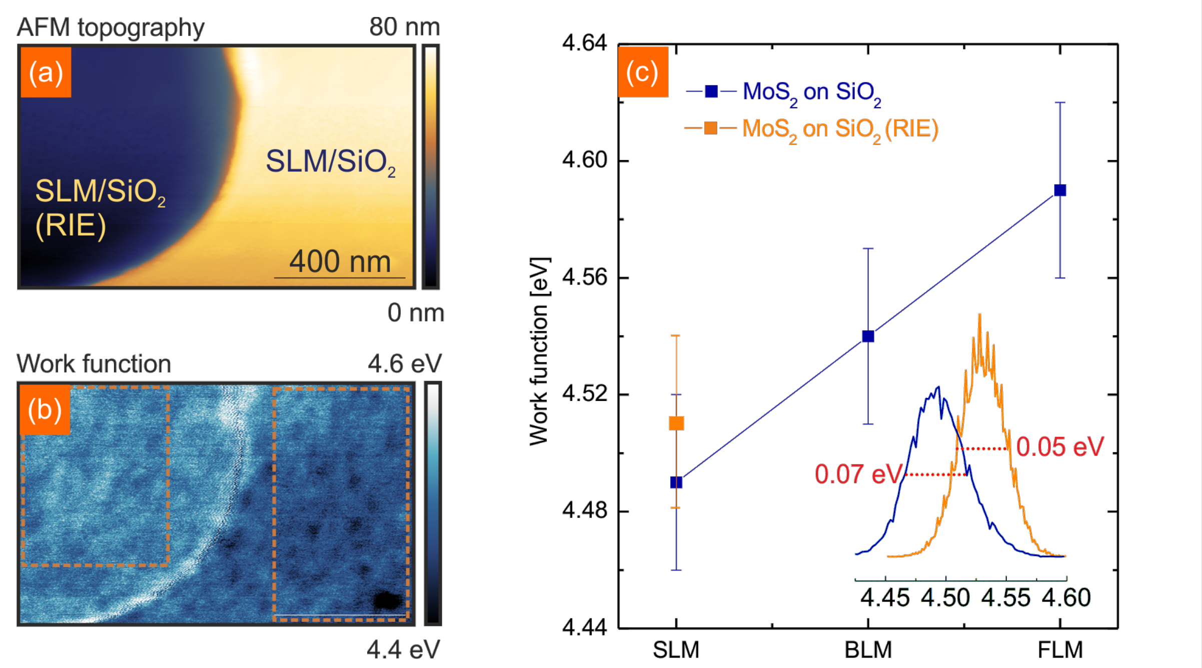

Figure 5: (a) NC-AFM topography of SLM on SiO_2 and holes etched in SiO_2 using RIE. (b) Work function map corresponding to the topography shown in (a). The work function of SLM on etched SiO_2 is increased compared to pristine SiO_2. (c) Layer dependent work function of MoS_2. The inset shows the work function histogram evaluation of the areas marked in (b). The FWHM of SLM on RIE SiO_2 is decreased by 0.02 eV.

Acknowledgements

We acknowledge financial support from the DFG in the framework of the Priority Program 1459 Graphene (O.O., N.S.), the SFB 616 Energy dissipation on surfaces (K.M., B.K.B.), and from the ERC under Grant No. 259286 (J.M.). We thank M. Freudenberg for graphics support.

References

1. Geim, A. K. *Science* **2009,** *324,* 1530–1534. doi:10.1126/science.1158877
2. Novoselov, K. S.; Fal'ko, V. I.; Colombo, L.; Gellert, P. R.; Schwab, M. G.; Kim, K. *Nature* **2012,** *490,* 192. doi:10.1038/nature11458
3. Xu, M.; Liang, T.; Shi, M.; Chen, H. *Chem. Rev.* **2013,** *113,* 3766. doi:10.1021/cr300263a
4. Shen, H.; Zhang, L.; Liu, M.; Zhang, Z. *Theranostics* **2012,** *2,* 283. doi:10.7150/thno.3642
5. Mak, K. F.; Lee, C.; Hone, J.; Shan, J.; Heinz, T. F. *Phys. Rev. Lett.* **2010,** *105,* 136805. doi:10.1103/PhysRevLett.105.136805
6. Scheuschner, N.; Ochedowski, O.; Schleberger, M.; Maultzsch, J. *Phys. Status Solidi B* **2012,** *1249,* 2644. doi:10.1002/pssb.201200389
7. Plechinger, G.; Schrettenbrunner, F.-X.; Eroms, J.; Weiss, D.; Schüller, C.; Korn, T. *Phys. Status Solidi RRL* **2012,** *6,* 126. doi:10.1002/pssr.201105589
8. Tonndorf, P.; Schmidt, R.; Böttger, P.; Zhang, X.; Börner, J.; Liebig, A.; Albrecht, M.; Kloc, C.; Gordan, O.; Zahn, D. R. T.; Michaelis de Vasconcellos, S.; Bratschlitsch, R. *Opt. Express* **2013,** *21,* 4908. doi:10.1364/OE.21.004908
9. Cappelluti, E.; Roldan, R.; Silva-Guillén, J. A.; Ordejón, P.; Guinea, F. *Phys. Rev. B* **2013,** *88,* 075409. doi:10.1103/PhysRevB.88.075409
10. Castellanos-Gomez, A.; Poot, M.; Steele, G. A.; van der Zant, H. S. J.; Agrait, N.; Rubio-Bollinger, G. *Adv. Mater.* **2012,** *24,* 772. doi:10.1002/adma.201103965
11. Bertolazzi, S.; Brivio, J.; Kis, A. *ACS Nano* **2011,** *5,* 9703. doi:10.1021/nn203879f
12. Radisavljevic, B.; Radenovic, A.; Brivio, J.; Giacometti, V.; Kis, A. *Nat. Nanotechnol.* **2011,** *6,* 147. doi:10.1038/nnano.2010.279
13. Lembke, D.; Kis, A. *ACS Nano* **2012,** *6,* 10070. doi:10.1021/nn303772b
14. Yu, Y.; Li, C.; Liu, Y.; Su, L.; Zhang, Y.; Cao, L. *Sci. Rep.* **2013,** *3,* No. 1866. doi:10.1038/srep01866
15. Zhan, Y.; Liu, Z.; Najmaei, S.; Ajayan, P. M.; Lou, J. *Small* **2012,** *8,* 966. doi:10.1002/smll.201102654
16. van der Zande, A. M.; Huang, P. Y.; Chenet, D. A.; Berkelbach, T. C.; You, Y.; Lee, G.-H.; Heinz, T. F.; Reichman, D. R.; Muller, D. A.; Hone, J. C. *Nat. Mater.* **2013,** *12,* 554. doi:10.1038/nmat3633
17. Wang, H.; Yu, L.; Lee, Y.-H.; Shi, Y.; Hsu, A.; Chin, M. L.; Li, L.-J.; Dubey, J.; Kong, M.; Palacios, T. *Nano Lett.* **2012,** *12,* 4674. doi:10.1021/nl302015v
18. Buscema, M.; Barkelid, M.; Zwiller, V.; van der Zant, H. S. J.; Steele, G. A.; Castellanos-Gomez, A. *Nano Lett.* **2013,** *13,* 358. doi:10.1021/nl303321g
19. Pu, J.; Yomogida, Y.; Liu, K.-K.; Li, L.-J.; Iwasa, Y.; Takenobu, T. *ACS Nano* **2012,** *12,* 4013. doi:10.1021/nl301335q
20. Radisavljevic, B.; Whitwick, M. B.; Kis, A. *Appl. Phys. Lett.* **2012,** *101,* 043103. doi:10.1063/1.4738986
21. Perkins, F. K.; Friedman, A. L.; Cobas, E.; Campbell, P. M.; Jernigan, G. G.; Jonker, B. T. *Nano Lett.* **2013,** *13,* 668. doi:10.1021/nl3043079
22. Late, F. J.; Liu, B.; Ramakrishna Matte, H. S. S.; David, V. P.; Rao, C. N. R. *ACS Nano* **2012,** *6,* 5635. doi:10.1021/nn301572c
23. Das, S.; Chen, H.-Y.; Penumatcha, A. V.; Appenzeller, J. *Nano Lett.* **2013,** *13,* 100. doi:10.1021/nl303583v

24. Li, S.-L.; Wakabayashi, K.; Xu, Y.; Nakaharai, S.; Komatsu, K.; Li, W.-W.; Lin, A.; Aparecido-Ferreira, Y.-L.; Tsukagoshi, K. *Nano Lett.* **2013,** *13,* 3546. doi:10.1021/nl4010783
25. Fontana, M.; Deppe, T.; Boyd, A. K.; Rinzan, M.; Liu, A. Y.; Paranjape, M.; Barbara, P. *Sci. Rep.* **2013,** *3,* No. 1634. doi:10.1038/srep01634
26. Chen, W.; Santos, E. J. G.; Zhu, W.; Kaxiras, E.; Zhang, Z. *Nano Lett.* **2013,** *13,* 509. doi:10.1021/nl303909f
27. Bao, W.; Cai, X.; Kim, D.; Sridhara, K.; Fuhrer, M. S. *Appl. Phys. Lett.* **2013,** *102,* 042104. doi:10.1063/1.4789365
28. Hao, G.; Huang, Z.; Liu, Y.; Qi, X.; Ren, L.; Peng, X.; Yang, L.; Wei, X.; Zhong, J. *AIP Adv.* **2013,** *3,* 042125. doi:10.1063/1.4802921
29. Li, Y.; Xu, C.-Y.; Zhen, L. *Appl. Phys. Lett.* **2013,** *102,* 143110. doi:10.1063/1.4801844
30. Rad, M. A.; Ibrahim, K.; Mohamed, K. *Superlattices Microstruct.* **2012,** *51,* 597. doi:10.1016/j.spmi.2012.03.002
31. Gatzert, C.; Blakers, A. W.; Deenapanray, N. K.; Macdonald, D.; Auret, F. D. *J. Vac. Sci. Technol., A* **2006,** *24,* 1857. doi:10.1116/1.2333571
32. Novoselov, K. S.; Jiang, G.; Schedin, F.; Booth, T. J.; Khotkevich, V. V.; Morozov, S. V.; Geim, A. K. *Proc. Natl. Acad. Sci. U. S. A.* **2005,** *102,* 10451. doi:10.1073/pnas.0502848102
33. Castellanos-Gomez, A.; Agraït, N.; Rubio-Bollinger, G. *Appl. Phys. Lett.* **2010,** *96,* 213116. doi:10.1063/1.3442495
34. Lee, C.; Yan, H.; Brus, L. E.; Heinz, T. F.; Hone, J.; Ryu, S. *ACS Nano* **2010,** *4,* 2695. doi:10.1021/nn1003937
35. Nonnenmacher, M.; O'Boyle, M. P.; Wickramasinghe, H. K. *Appl. Phys. Lett.* **1991,** *58,* 2921. doi:10.1063/1.105227
36. Kitamura, S.; Iwatsuki, M. *Appl. Phys. Lett.* **1998,** *72,* 3154. doi:10.1063/1.121577
37. Glatzel, T.; Sadewasser, S.; Lux-Steiner, M. Ch. *Appl. Surf. Sci.* **2003,** *210,* 84. doi:10.1016/S0169-4332(02)01484-8
38. Sadewasser, S.; Glatzel, T.; Shikler, R.; Rosenwaks, Y.; Lux-Steiner, M. Ch. *Appl. Surf. Sci.* **2003,** *210,* 32. doi:10.1016/S0169-4332(02)01475-7
39. Rosenwaks, Y.; Shikler, R.; Glatzel, T.; Sadewasser, S. *Phys. Rev. B* **2004,** *70,* 085320. doi:10.1103/PhysRevB.70.085320
40. Zerweck, U.; Loppacher, C.; Otto, T.; Grafström, S.; Eng, L. M. *Phys. Rev. B* **2005,** *71,* 125424. doi:10.1103/PhysRevB.71.125424
41. Elias, G.; Glatzel, T.; Meyer, E.; Schwarzman, A.; Boag, A.; Rosenwaks, Y. *Beilstein J. Nanotechnol.* **2011,** *2,* 252. doi:10.3762/bjnano.2.29
42. Bertrand, P. A. *Phys. Rev. B* **1991,** *44,* 5745. doi:10.1103/PhysRevB.44.5745
43. Li, H.; Zhang, Q.; Yap, C. C. R.; Tay, B. K.; Edwin, T. H. T.; Olivier, A.; Baillargeat, D. *Adv. Funct. Mater.* **2012,** *22,* 1385. doi:10.1002/adfm.201102111
44. Conley, H. J.; Wang, B.; Ziegler, J. I.; Haglund, R. F., Jr..; Pantelides, S. T.; Pantelides, T.; Bolotin, K. I. *Nano Lett.* **2013,** *13,* 3626. doi:10.1021/nl4014748
45. Zhu, C. R.; Wang, G.; Lui, B. L.; Marie, X.; Quiao, X. F.; Zhang, X.; Wu, X. X.; Fan, H.; Tan, P. H.; Amand, T.; Urbaszek, B. *Phys. Rev. B* **2013,** *88,* 121301(R). doi:10.1103/PhysRevB.88.121301
46. Chakraborty, B.; Bera, A.; Muthu, D. V. S.; Bhowmick, S.; Waghmare, U. V.; Sood, A. K. *Phys. Rev. B* **2012,** *85,* 161403(R). doi:10.1103/PhysRevB.85.161403
47. Michaelson, H. B. *J. Appl. Phys.* **1977,** *48,* 4729. doi:10.1063/1.323539
48. Orf, N. D.; Baikie, I. D.; Shapira, O.; Fink, Y. *Appl. Phys. Lett.* **2009,** *94,* 113504. doi:10.1063/1.3089677
49. Ochedowski, O.; Kleine Bussmann, B.; Ban d'Etat, B.; Lebius, H.; Schleberger, M. *Appl. Phys. Lett.* **2013,** *102,* 153103. doi:10.1063/1.4801973
50. Giovannetti, G.; Khmyakov, P. A.; Brocks, G.; Karpan, V. M.; van den Brink, J.; Kelly, P. J. *Phys. Rev. Lett.* **2008,** *101,* 026803. doi:10.1103/PhysRevLett.101.026803
51. Domanski, A. L.; Sengupta, E.; Bley, K.; Untch, M. B.; Weber, S. A. L.; Landfester, K.; Weiss, C. K.; Butt, H.-J.; Berger, R. *Langmuir* **2012,** *28,* 13892. doi:10.1021/la302451h
52. Guo, L. Q.; Zhao, X. M.; Bai, Y.; Qiao, L. J. *Appl. Surf. Sci.* **2012,** *258,* 9087. doi:10.1016/j.apsusc.2012.06.003
53. Chen, J.-H.; Jang, C.; Adam, S.; Fuhrer, M. S.; Williams, E. D.; Ishigami, M. *Nat. Phys.* **2008,** *4,* 377. doi:10.1038/nphys935
54. Ryu, S.; Liu, L.; Berciaud, S.; Yu, Y.-J.; Liu, H.; Kim, P.; Flynn, G. W.; Brus, L. E. *Nano Lett.* **2010,** *10,* 4944. doi:10.1021/nl1029607
55. Molina-Sánchez, A.; Wirtz, L. *Phys. Rev. B* **2011,** *84,* 155413. doi:10.1103/PhysRevB.84.155413
56. Scheuschner, N.; Ochedowski, O.; Kaulitz, A.-M.; Gillen, R.; Schleberger, M.; Maultzsch, J. *arXiv.org* **2013,** No. arXiv:1311.5824. [cond-mat.mtrl-sci].
57. Burson, K. M.; Cullen, W. G.; Adam, S.; Dean, C. R.; Watanabe, K.; Taniguchi, T.; Kim, P.; Fuhrer, M. S. *Nano Lett.* **2013,** *13,* 3576. doi:10.1021/nl4012529
58. Yamamato, M.; Einstein, T. L.; Fuhrer, M. S.; Cullen, W. G. *ACS Nano* **2012,** *6,* 8335. doi:10.1021/nn303082a
59. Castellanos-Gomez, A.; Roldán, R.; Cappelluti, E.; Buscema, M.; Guinea, F.; van der Zant, H. S. J.; Steele, G. A. *Nano Lett.* **2013,** *13,* 5361. doi:10.1021/nl402875m
60. McGovern, I. T.; Williams, R. H. *Surf. Sci.* **1974,** *46,* 427. doi:10.1016/0039-6028(74)90318-5
61. McMenamin, J. C.; Spicer, W. E. *Phys. Rev. B* **1977,** *16,* 5474. doi:10.1103/PhysRevB.16.5474
62. Kamaratos, M.; Papageorgopoulos, C. A. *Surf. Sci.* **1986,** *178,* 865. doi:10.1016/0039-6028(86)90362-6
63. Yun, J.-M.; Noh, Y.-J.; Yeo, J.-S.; Go, Y.-J.; Na, S.-I.; Jeong, H.-G.; Kim, J.; Lee, S.; Kim, S.-S.; Koo, H.-Y.; Kim, T.-W.; Kim, D.-Y. *J. Mater. Chem. C* **2013,** *1,* 3777. doi:10.1039/c3tc30504j

License and Terms

Beilstein Journal
of Nanotechnology

Challenges and complexities of multifrequency atomic force microscopy in liquid environments

Santiago D. Solares[§]

Full Research Paper

Open Access

Address:
Department of Mechanical Engineering, University of Maryland,
College Park, MD 20742, USA

Email:
Santiago D. Solares - ssolares@umd.edu

§ Phone: +1 (301) 405-5035, Fax: +1 (301) 314-9477

Keywords:
amplitude-modulation; bimodal; frequency-modulation; liquids;
multifrequency atomic force microscopy

Beilstein J. Nanotechnol. **2014,** *5,* 298–307.
doi:10.3762/bjnano.5.33

Received: 02 December 2013
Accepted: 18 February 2014
Published: 14 March 2014

This article is part of the Thematic Series "Noncontact atomic force microscopy II".

Guest Editors: U. D. Schwarz and M. Z. Baykara

Abstract

This paper illustrates through numerical simulation the complexities encountered in high-damping AFM imaging, as in liquid enviroments, within the specific context of multifrequency atomic force microscopy (AFM). The focus is primarily on (i) the amplitude and phase relaxation of driven higher eigenmodes between successive tip–sample impacts, (ii) the momentary excitation of non-driven higher eigenmodes and (iii) base excitation artifacts. The results and discussion are mostly applicable to the cases where higher eigenmodes are driven in open loop and frequency modulation within bimodal schemes, but some concepts are also applicable to other types of multifrequency operations and to single-eigenmode amplitude and frequency modulation methods.

Introduction

Multifrequency atomic force microscopy (AFM) refers to a family of techniques that involve simultaneous excitation of the microcantilever probe at more than one frequency [1]. The first of these methods was proposed by García and coworkers in 2004 to carry out simultaneous non-contact amplitude-modulation imaging and open-loop (phase contrast) compositional mapping of surfaces in air by exciting and controlling the first two eigenmodes of the cantilever [2]. This approach has since been extended to intermittent contact characterization using open loop and frequency modulation [3,4], imaging in liquid and vacuum environments [5-8], and to trimodal operation [9-11]. There also exist a number of other multifrequency and multiharmonic AFM techniques which have been developed for different purposes [1,12-18].

Previous researchers have shown that the dynamics of the AFM cantilever become extremely complex for low-Q environments, such as liquids [19-28] (see Figure 1), and have identified phenomena such as the momentary excitation of higher eigenmodes and multiple-impact regimes [21,26], mass loading and fluid-borne cantilever excitation [19,23,24], discrepancies between the photodetector signal and the actual tip position for base-excited cantilever systems [24,28] and non-ideal spectroscopy curves (for example, curved amplitude–distance curves where multiple regimes are observed as kinks [19]). Although the focus of these studies has not been on techniques designed for driving the cantilever at different frequencies simultaneously, it is not surprising that all of the above phenomena are also present in multifrequency operations and that the various issues compound with the added complexity of multifrequency AFM [9,29-32], such that more and more experience and knowledge is required from the user to carry out meaningful measurements. With multifrequency methods it can be more difficult to achieve suitable imaging conditions and to properly interpret the results, and no single recipe works in all cases. This paper explores through simulation the implications of the low-*Q* cantilever dynamics within the specific context of bimodal AFM imaging. The primary focus is on (i) the amplitude and phase "relaxation" (equilibration) for driven higher eigenmodes between successive taps of the fundamental eigenmode regardless of the point of application of the excitation (base or tip), (ii) momentary excitation of non-driven eigenmodes, and (iii) additional artifacts introduced by the use of base excitation. The discussion is most directly applicable to bimodal techniques where the higher eigenmode is driven in open loop [5,8] or frequency modulation [4], but the principles are general enough that they are also relevant to other multifrequency methods and in some cases also to single-mode frequency and amplitude modulation techniques. Finally, it is noted that some of the challenges discussed here, namely those caused by sharp variations in the tip–sample forces can be mitigated through the use of small-amplitude operation [7,8], although this may not always be feasible, depending on the type of sample and the type of instrument that is available.

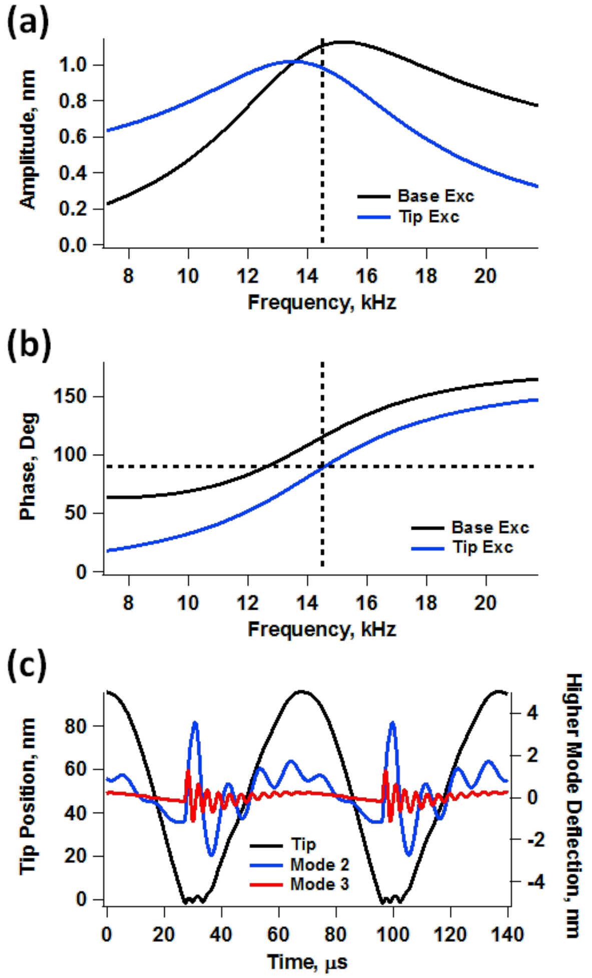

Figure 1: Example of measurement artifacts previously observed in single-mode AFM operation in liquids: distortion of the frequency response (a) and phase response (b) curves with base excitation (the "Tip Exc" traces provide the true response); momentary excitation of higher eigenmodes and multiple tip–sample impacts for every cycle of the fundamental eigenmode (c). The simulation parameters are v_1 = 14.5 kHz, k_1 = 0.03 N/m, Q_1 = 2, Q_2 = 6, A_{free} = 75 nm, A_{setpoint} = 55% and sample modulus of elasticity of 2 GPa (Hertzian contact).

Results and Discussion

Amplitude and phase relaxation of driven eigenmodes

Previous work by Raman and coworkers [22] demonstrated that in high-damping environments the phase contrast derives primarily from an "energy flow channel" that opens up when higher modes of the cantilever are momentarily excited through the tip–sample impact (see Figure 1c), which is more prevalent for softer cantilevers than for harder ones. When this happens, the phase contrast does not map dissipation, but instead short-range conservative interaction variations. The phenomenon is called momentary excitation because the oscillation of the higher eigenmodes begins with the tip–sample impact, governed by the frequency and amplitude of the fundamental eigenmode, and decays in between successive taps of the cantilever. This fast decay occurs because the quality factor of the higher eigenmodes is generally smaller than the ratio of eigenfrequencies [21,26]. In the case of bimodal AFM, a similar phenonmenon takes place, where the driven higher eigenmode is perturbed every tip–sample impact and the perturbation relaxes in between successive taps. However, the situation is slightly different since the eigenmode is also being actively driven with a sinusoidal excitation. Here the perturbation appears to the user as a momentary variation in the phase and amplitude of the higher mode (see Figure 2a and 2b), which relaxes until the phase and amplitude reach the values they would have in the absence of the sample, just before the next impact occurs. This rich behavior is not captured in the phase and amplitude signals (see Figure 2c), which are obtained through averaging over

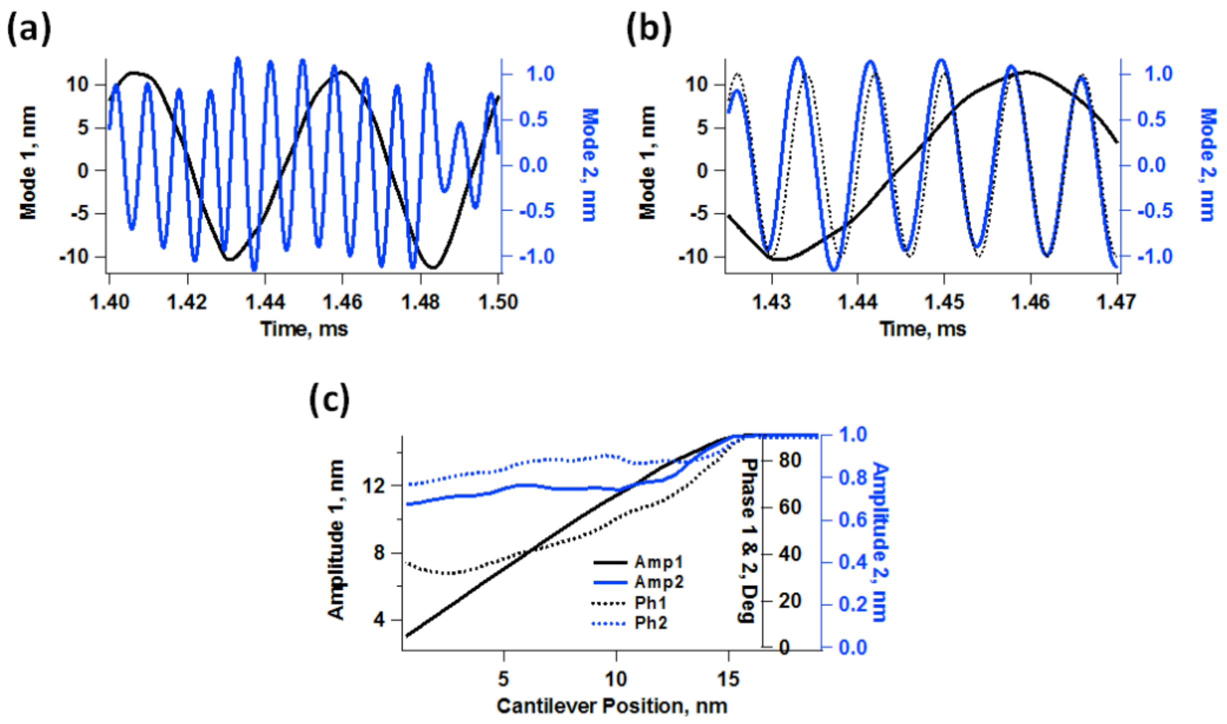

Figure 2: Bimodal AFM simulation illustrating the phase and amplitude relaxation of the second eigenmode: (a) different response of the first and second eigenmode over successive tip–sample impacts (successive tip–sample impacts are different because the v_2/v_1 ratio is generally not an integer); (b) phase relaxation of the second eigenmode (the dotted line shows the fully relaxed response – notice how this eigenmode's response gets ahead with respect to the dotted line and undergoes a change in amplitude after the impact but then recovers before the next tap); (c) seemingly normal amplitude and phase spectroscopy curves. The cantilever parameters are v_1 = 20 kHz, k_1 = 0.25 N/m, Q_1 = 3, Q_2 = 6, A_{free} = 15 nm, and A_{setpoint} = 70% (a and b only). The sample was modeled as a standard linear solid (see methods section) with K_o = 3.5 N/m, K_{inf} = 3.5 N/m and $C_d = 1 \times 10^{-5}$ Ns/m.

multiple oscillation cycles. However, such behavior can preclude the application of the phase spectroscopy theories that have been developed for operation in air environments, which assume a nearly-equilibrated eigenmode oscillation where all cycles are sinusoidal and similar in phase and amplitude [33,34].

Due to the short equilibration times in liquids, in bimodal operation the response of the cantilever eigenmodes exhibits a distinct transient and a relaxed contribution. The relaxed contribution is equal to the eigenmode's response in the absence of the sample. The transient contribution is a result of the forces that take place during each impact. The ability of these forces to modify the response of each individual eigenmode is strongly dependent on the imaging conditions. This is illustrated in Figure 3 for two cases involving different quality factor and higher mode amplitudes. In general, higher modes are more likely to be perturbed when their free amplitude is small (discussions on this topic can be found in references [8,11]). However, the oscillation of the fundamental eigenmode is more likely to be perturbed with larger amplitudes of the higher eigenmode due to a more irregular impact. This is also illustrated in Figure 3, which includes real-time trajectories and frequency space representations of the first two eigenmode responses. The two cases analyzed correspond to slightly different values of the quality factors, but their effect was not significant in the range considered. Figure 4 shows a more direct comparison of the second eigenmode response under similar conditions for different free amplitudes, providing also an example for a 'harder' sample. As it is well known, stiffer samples are more likely to perturb the oscillation of a given cantilever. This is extremely important, as samples with inhomogeneous stiffness can give rise to different types of perturbations across the surface, such that quantitative interpretations of the contrast across the entire sample may become meaningless. Furthermore, the level of cantilever perturbation is also highly sensitive to the amplitude setpoint, as illustrated in Figure 5 for three different cantilever positions above the sample. Clearly, the oscillation changes significantly as the cantilever is lowered towards the sample (Figure 5a), even though the average phase and amplitude response do not exhibit drastic variations (Figure 5b). This is highly relevant when carrying out quantitative comparisons for different types of samples, which may require individual optimization of the imaging conditions.

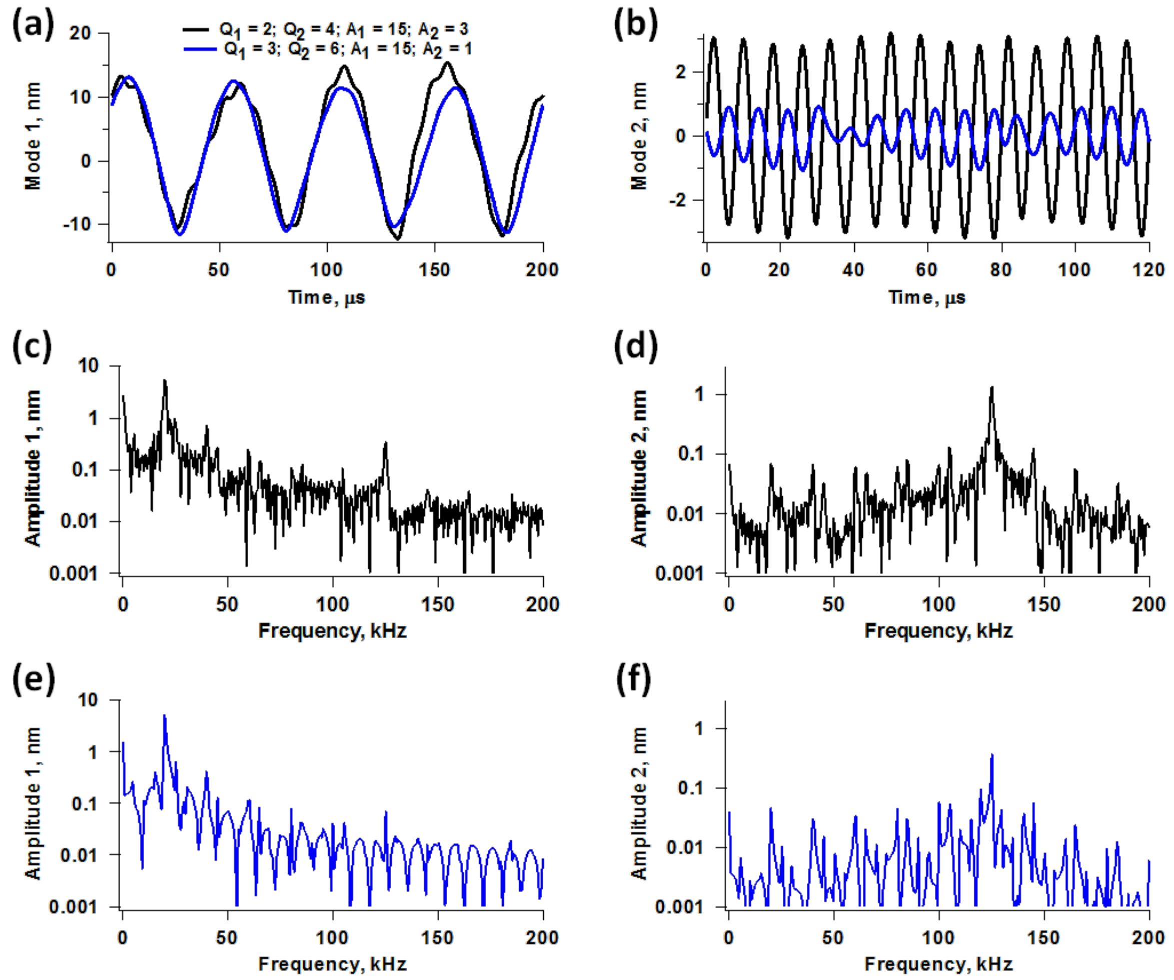

Figure 3: Illustration of eigenmode perturbation for two different cases. The results are color coded for the two cases considered, $Q_1 = 2$, $Q_2 = 4$, $A_1 = 15$ nm and $A_2 = 3$ nm for case 1 (black traces), and $Q_1 = 3$, $Q_2 = 6$, $A_1 = 15$ nm and $A_2 = 1$ nm for case 2 (blue traces). (a) mode 1 responses in time space; (b) mode 2 responses in time space; (c) and (d) mode 1 and mode 2 spectra, respectively, for case 1; (e) and (f) mode 1 and mode 2 spectra, respectively, for case 2. The amplitude setpoint is approximately 70% and the sample parameters are the same as for Figure 2. Notice how the use of a smaller value of A_2 results in a sharper spectrum for the first mode but a less sharp spectrum for the second mode, and vice-versa.

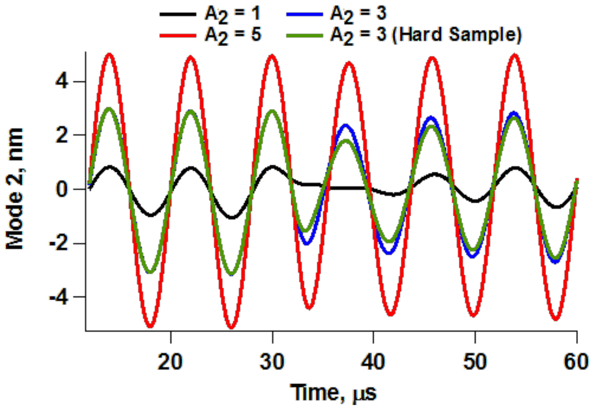

Figure 4: Second eigenmode response for different second mode free amplitude values for the same conditions as the simulations in Figure 3, and for a stiffer sample with $K_o = 7$ N/m and $K_{inf} = 7$ N/m (green trace), which causes greater perturbation for a given amplitude.

The phenomena introduced by the higher eigenmode phase and amplitude relaxation within an oscillation cycle of the fundamental eigenmode bring about obvious challenges in the interpretation of phase contrast images. However, the difficulties become even more significant if one wishes to implement bimodal operations involving frequency modulation (FM) control of the higher eigenmode [4]. While the phase contrast results may become less and less meaningful as momentary perturbations become more and more severe, one is still generally able to obtain an image with open loop drive of the higher mode. However, the implementation of FM requires either a phase-locked loop (PLL) or time delay (phase shifting), both of which are more complex and highly sensitive to perturbations. The time delay version of FM is even more susceptible to instabilities because the excitation of the cantilever is created from the real-time response of the cantilever, one cycle at a time.

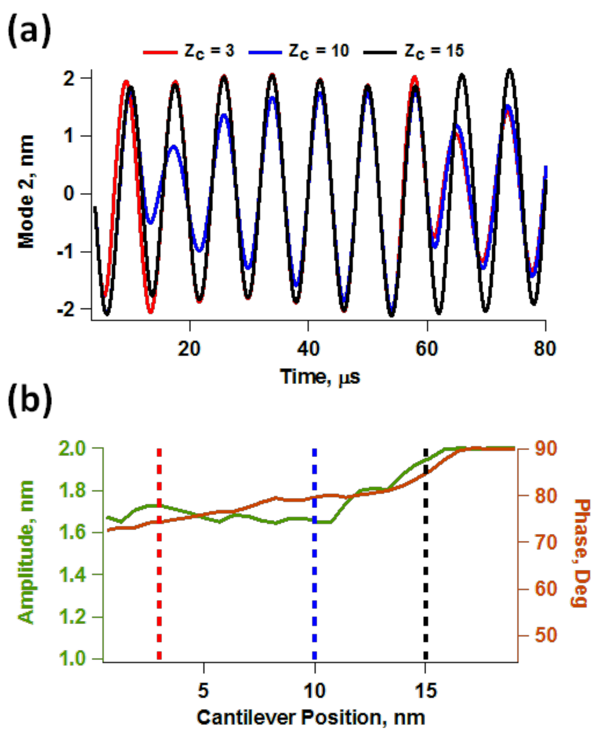

Figure 5: (a) Illustration of the drastically varying response of the higher eigenmode as the cantilever is brought closer to the sample (Z_c denotes the cantilever position above the sample); (b) second phase response for the three responses shown in (a).

Figure 6 shows frequency and time domain second eigenmode responses obtained by sweeping the excitation frequency from low to high using chirp functions [35] while keeping the cantilever at a fixed height above the sample within bimodal operation. The trace for a cantilever height Z_c = 20 nm is the free (unperturbed) response away from the sample. As the cantilever is lowered (Z_c = 16 nm and Z_c = 12 nm), the response becomes noisier, although it still retains its general Lorentzian behavior, suggesting that FM control may still be possible if sufficient signal averaging is performed. While the time delay version of FM may be impractical due to the cycle-to-cycle variations in the phase and amplitude, PLL operation may still be feasible, since the latter is based on the calculation of the average instantaneous phase which the system attempts to gradually lock to a specific value according to user-defined gains. However, even in this case the results may or may not be meaningful and characterization may be undesirably slow, depending on the severity of the perturbations induced by the tip–sample forces. The situation becomes more favorable as the higher mode quality factor increases such that the phase and amplitude relaxation becomes slower and intermixing of transients from different cycles occurs, similar to what happens in air environments. Specifically, for the *i*-th higher eigenmode it would be necessary that its quality factor be significantly greater than the ratio ν_i/ν_1 such that the transients extend appreciably beyond one cycle of the fundamental frequency (here ν_1 is the fundamental eigenfrequency and ν_i is the higher mode eigenfrequency). For some applications, there may exist cantilevers that meet these requirements and in other cases it may be possible to utilize high-Q techniques designed for characterization in liquids, such as the recently proposed trolling mode method [36]. For comparison purposes Figure 7 shows typical second eigenmode responses for bimodal and trimodal operation in air. Even for the trimodal case, which corresponds to a very drastic situation in which the second eigenmode amplitude is very small compared to the fundamental amplitude and four times smaller than the third mode amplitude, the response is much more regular than for the results discussed above for liquid imaging.

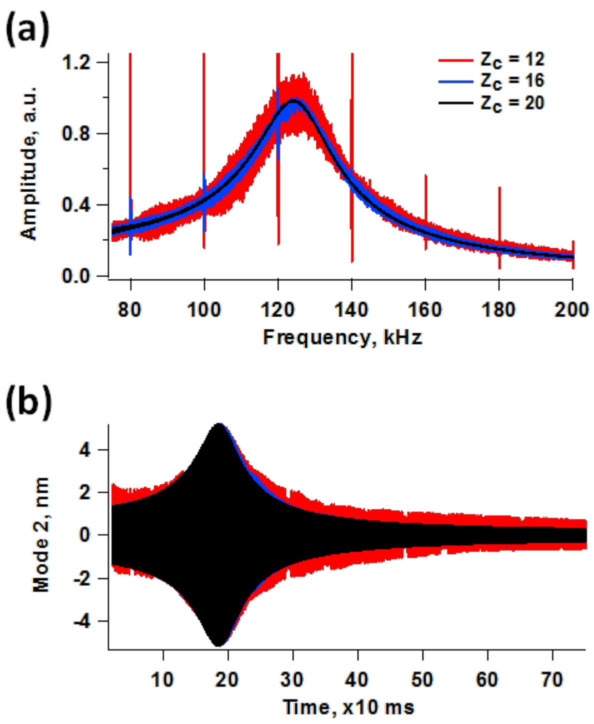

Figure 6: Frequency space (a) and time space (b) responses of the system of Figure 5 for three different cantilever positions above the sample, obtained by sweeping the frequency from low to high using a chirp function while keeping the cantilever at the fixed height indicated. Z_c = 20 nm corresponds to the free response. The results shown in (a) were obtained through application of the fast Fourier transform to the results shown in (b).

Momentary excitation of non-driven eigenmodes

While the previous section focuses on the momentary perturbation of the driven higher eigenmodes, one must still be mindful of the momentary excitation of non-driven eigenmodes, since both phenomena have the same underlying cause. As exten-

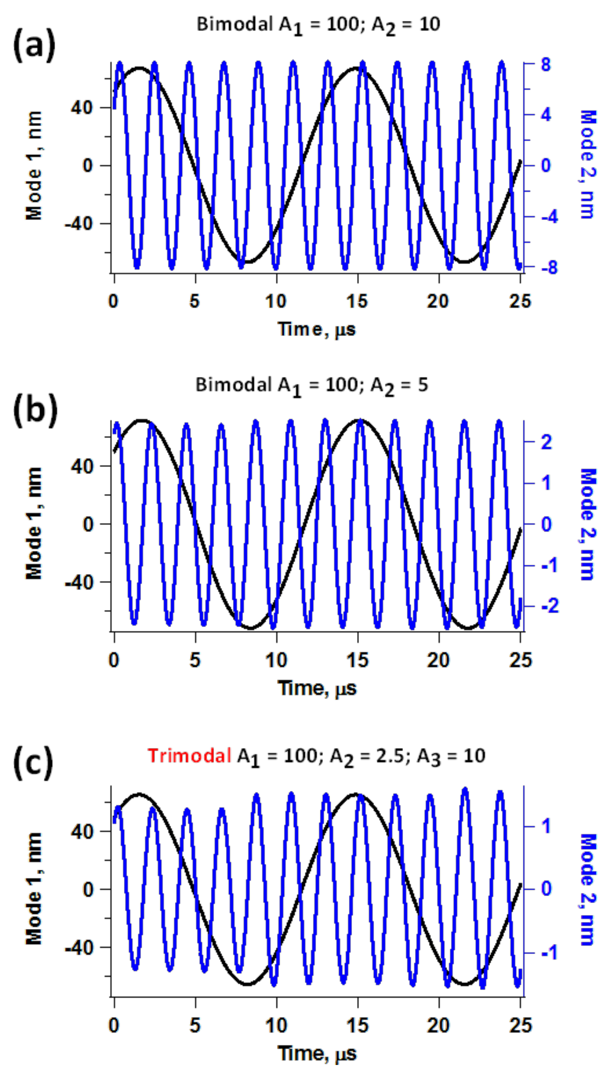

Figure 7: Typical eigenmode responses for bimodal and trimodal AFM operation in air with Q_1 = 150, Q_2 = 450, Q_3 = 750, ν_1 = 70 kHz, ν_2 = 437.5 kHz, ν_3 = 1.25 MHz and k_1 = 2 N/m: (a) bimodal operation with A_1 = 100 nm and A_2 = 10 nm (A_1/A_2 = 10); (b) bimodal operation with A_1 = 100 nm and A_2 = 5 nm (A_1/A_2 = 20); (c) trimodal operation with A_1 = 100 nm and A_2 = 2.5 nm (A_1/A_2 = 40 and A_3/A_2 = 4). The sample parameters were K_o = 10 N/m, K_{inf} = 10 N/m and C_d = 1 × 10^{-5} Ns/m.

sively studied through simulation and experiment by Raman and coworkers, momentary excitation occurs when the spectrum of the tip–sample forces overlaps with the frequency response (transfer) function of the higher eigenmodes, which is more likely to occur in low-Q environments for which the eigenmode bandwidth is greater [21,26]. This phenomenon also occurs in multifrequency AFM with the added complexity that the tip–sample forces depend strongly on the parameters chosen to drive the higher eigenmodes, as well as on their nonlinear interaction with the fundamental eigenmode oscillation. As a result, the observed momentary excitation of non-driven eigenmodes will also depend strongly on the driven higher eigenmode parameters. Figure 8a shows five successive force trajectories for bimodal operation using similar conditions and for a similar sample as for Figure 2, for three different second mode amplitudes. As expected, there is a significant change in tip–sample penetration as the second mode amplitude increases [11,37], leading to different force spectra (Figure 8b). Since all three spectra overlap at least with the third eigenmode frequency response, they all lead to its momentary excitation to different degrees, as shown in Figure 8c. Furthermore, in contrast to single-mode operation, the momentary excitation can differ significantly for successive fundamental eigenmode oscillations (not shown). This is because the ratio of the second to the first eigenfrequency is not an integer, which leads to different successive impacts. Since the third eigenmode is an “energy channel” separate from the two driven eigenmodes [22], its momentary excitation leads to changes in the response of the other two modes in a manner which is not easily predictable a priori. Some generalization is possible, but since there is no single interpretation that applies in all cases, monitoring of the higher mode responses, as well as user experience and discretion are critical for studies that go beyond simple qualitative observations.

Base excitation and cantilever tuning artifacts

The differences between base- and tip-excited systems have also been previously discussed for single-mode operation [19,24,28], but as for the issues discussed in the two previous sections, they are worth revisiting here in the specific context of multifrequency AFM. These differences are not extremely relevant for simple imaging applications, but they are critical when a higher eigenmode is used to carry out compositional mapping while imaging. While most of the AFM systems in use only have base excitation capability, it is important to keep in mind the fact that unless the cantilever base motion is known with high accuracy (unfortunately this is not practical and only possible within highly controlled experiments) and the cantilever behaves in an ideal manner, it is not possible to determine the true tip trajectory from the photodetector reading. This is because the photodetector measures cantilever deflection (this can be approximated as tip position minus base position), not tip position. Figure 9 illustrates the photodetector readings that would be obtained for different values of the quality factor for a given second eigenmode tip oscillation (labeled as “Real”). Clearly spectroscopic measurements are not meaningful unless the true probe trajectory is known. This is a challenge that remains unsolved even in the most sophisticated base-excitation experiments, which is further compounded by the non-ideal behavior of piezo shaker systems, cantilevers and the surrounding fluid [19,23,24]. One obvious consequence of this difficulty is that tip–sample dissipative and conservative forces cannot be measured accurately with base-excited systems when

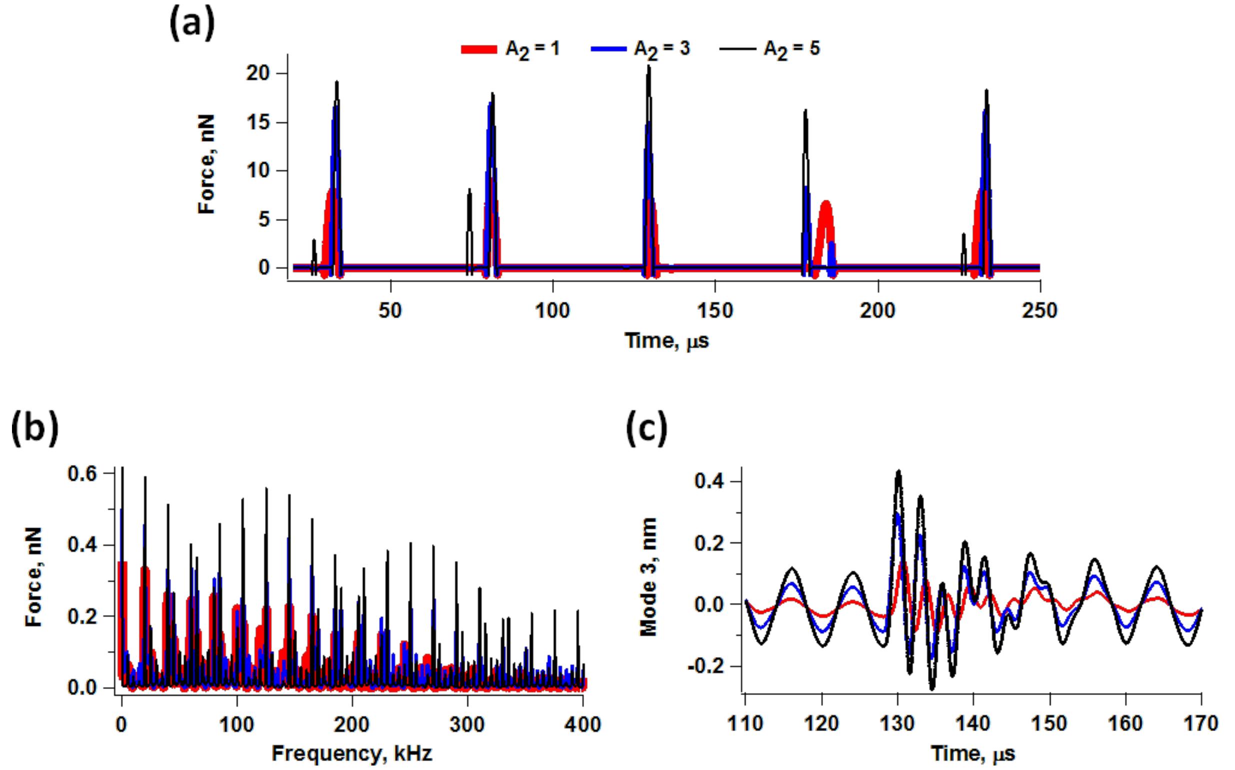

Figure 8: Illustration of the force trajectory of five successive tip–sample impacts for bimodal AFM conditions similar to those used to construct Figure 2, for three different second mode amplitudes ranging from 1 nm to 5 nm (a) along with the corresponding force spectra (b) and typical third eigenmode momentary excitation responses (c).

the effective quality factor of the cantilever changes throughout the measurement. In such cases, the phase of the oscillation would artificially change as tip–sample dissipation changes, leading to inaccurate readings. In frequency modulation operation this would cause the system to lock to a varying (non-constant) phase, which would render the results meaningless. Accurate measurements of this type with base-excited systems would only be possible if one carries out volume scanning above the surface, running a full frequency sweep curve at each grid point and fitting it to the appropriate base excitation response curve [28]. This practice is not the norm and would be time consuming, but is not necessarily out of reach since the transient times in liquid are short and the measurements can be carried out much more rapidly than in air or vacuum.

In the cases where frequency modulation operation can still be stably implemented with tip excitation whether for single- or multimode operation, it is important to note that the phase of the oscillation must be locked to 90 degrees during tuning even if this does not correspond to the amplitude peak (this is true for tip-driven systems and compounds itself with the previously discussed complexities of base excitation). This is because the peak frequency in low-Q environments shifts significantly to lower frequencies (see Figure 10), while the frequency at which the phase is 90 degrees remains at the natural frequency. The natural frequency is the only frequency at which all the phase curves intersect for a given (ideal) cantilever driven in environments with different levels of damping (see Figure 10). The type of errors introduced when locking the phase to that of the

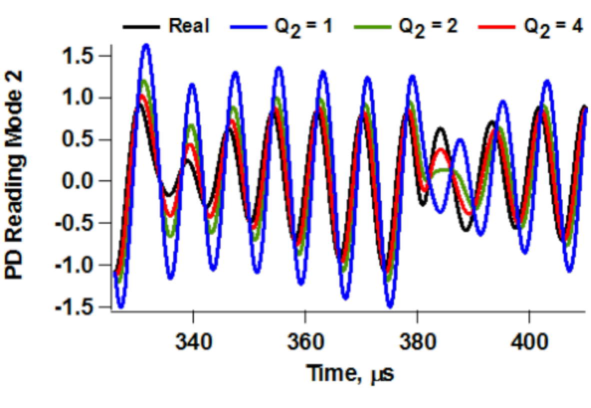

Figure 9: Illustration of the photodetector (PD) reading that would be obtained for a given second eigenmode trajectory (taken from a tip-excited bimodal simulation) for different values of the quality factor when the cantilever is driven using base excitation. There is a clear discrepancy between the photodetector reading and the real trajectory as Q drops.

peak frequency can also be understood using Figure 10. Consider the case when the phase is locked to the maximum response amplitude for a cantilever driven in an environment such that $Q = 3$ (blue traces). The frequency of the peak is indicated by a thick red arrow on the graph (notice that this frequency is to the left of the natural frequency), and the corresponding phase can be found by following the vertical green line downwards until it intersects the phase response for this value of the quality factor. Now, if the level of tip–sample dissipation changes due to tip–sample interactions, such that the effective quality factor drops to 1.5, the phase will remain locked at the same value, but now the phase response of the system will follow a different curve (red dotted line). If one now follows the horizontal green line towards the left until it intersects the new phase response and then draws a vertical line downwards to find the corresponding frequency (thick green arrow), it is clear that the eigenmode will now be driven at a different frequency, leading to the incorrect conclusion that there has been a change in the nature of the conservative forces (since only the dissipative forces have changed). The user will conclude that there has been a frequency shift, when this is clearly not the case. These issues also occur in amplitude modulation AFM and can lead to phase shift measurements that are not quantitatively meaningful.

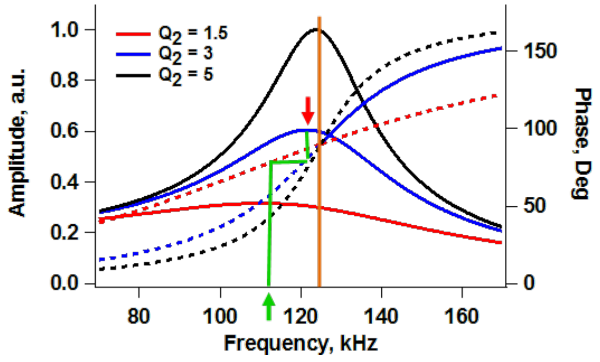

Figure 10: Cantilever amplitude and phase response for various levels of damping in low-*Q* environments. The thick red and green arrows and the green line illustrate the nature of the errors made in determining the resonance frequency when a frequency modulation operation is locked to the peak frequency instead of the natural frequency (see discussion in the text).

One final issue to consider for base excited AFM systems is the well-known "forest of peaks" observed during tuning of the cantilever, which makes the selection of the imaging eigenmode difficult. This is even more problematic in multifrequency operation, where one needs to select more than one eigenmode and where the ratio of their eigenfrequencies has important implications with regards to sensitivity. Furthermore, the observed peaks do not generally exhibit a "clean" Lorentzian response, which can render the assumption of harmonic oscillator dynamics questionable. Finally, this non-Lorentzian behavior may also complicate the calibration of the photodetector sensitivity (in V/nm), since there is no guarantee that the selected eigenmodes have the assumed shape. As with various other issues discussed in this document, there is no single answer that fits all situations. Instead, the operator must rely on careful observation and experience in assessing the appropriateness of the eigenmode selection, and must also carefully calibrate the system.

Conclusion

The key non-idealities observed in low-Q AFM have been discussed in the context of multifrequency operation, where additional complexities emerge due to the interaction of the driven and non-driven eigenmodes with one another. A number of challenges have been identified, which are mostly related to open loop and frequency modulation control of the higher eigenmode, and which users should be mindful of when carrying out characterization, especially in the cases where quantitative interpretation of the results is desired. While the focus has been on identifying nonidealities without providing simple or complete solutions, the objective is not to paint a bleak picture of the technique, but rather to raise awareness of open research questions that require further attention within multifrequency AFM.

Methods

For the numerical simulations three eigenmodes of the AFM cantilever were modeled using individual equations of motion for each, coupled through the tip–sample interaction forces as in previous studies [9,38]. Driven eigenmodes were excited through a sinusoidal tip force or base displacement of constant amplitude and frequency equal to the natural frequency. Chirp excitation functions [35,39] were used to construct the amplitude vs frequency curves, where applicable. Most of the simulations for liquid environment used quality factor values in the range $Q_1 = 1–7$, $Q_2 = 2Q_1–3Q_1$; $Q_3 = 3Q_1–5Q_1$. The equations of motion were integrated numerically and the amplitude and phase of each eigenmode were calculated using the customary in-phase (I) and quadrature (Q) terms:

$$I = \int_{N\tau} z(t)\cos(\omega t)dt \tag{1}$$

$$Q = \int_{N\tau} z(t)\sin(\omega t)dt \tag{2}$$

where $z(t)$ is the eigenmode response in the time domain, N is the number of periods over which the phase and amplitude were averaged, ω is the excitation frequency, and τ is the nominal period of one oscillation. The amplitude and phase can be calculated, respectively, as:

$$A = \frac{\omega}{\pi N}\sqrt{I^2 + Q^2} \tag{3}$$

$$\varphi = \tan^{-1}(Q / I) \tag{4}$$

The repulsive tip–sample forces were accounted in most simulations through a standard linear solid (SLS) model (Figure 11) [11,40], but Hertzian contacts [41] were also used in some cases. Long-range attractive interactions were included but for liquid environment simulations were assumed to be screened down to ≈10% of their typical value in air for a tip radius of curvature of 10 nm and a Hamaker constant of 2×10^{-19} J (no screening was considered for the simulations in air). Unless otherwise indicated, the trajectories shown indicate the true eigenmode or tip response, as opposed to the photodetector reading, which does not necessarily correspond to the true trajectory (as discussed in the text).

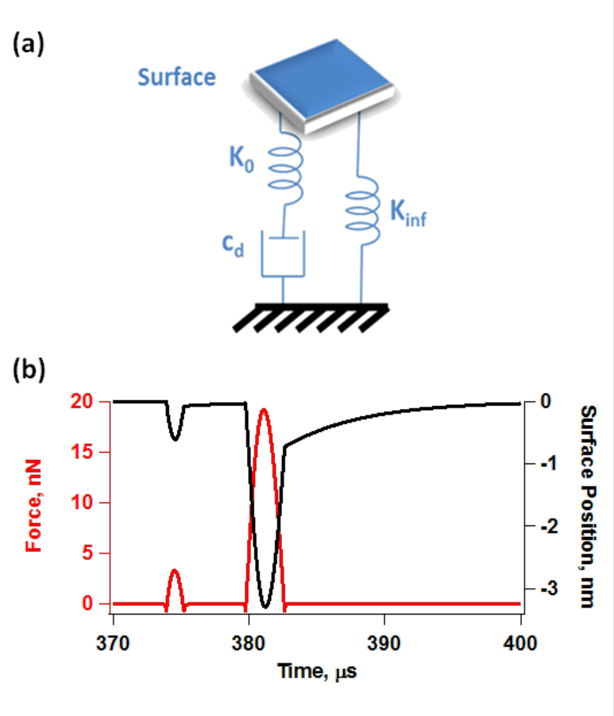

Figure 11: (a) Standard linear solid model; (b) illustration of tip–sample impact force trajectory and surface recovery for a bimodal imaging case.

Acknowledgements

The author gratefully acknowledges support from the U.S. Department of Energy, through award DESC0008115.

References

1. Garcia, R.; Herruzo, E. T. *Nat. Nanotechnol.* **2012,** *4,* 217–226. doi:10.1038/nnano.2012.38
2. Rodrı́guez, T. R.; Garcı́a, R. *Appl. Phys. Lett.* **2004,** *84,* 449–451. doi:10.1063/1.1642273
3. Proksch, R. *Appl. Phys. Lett.* **2006,** *89,* 113121. doi:10.1063/1.2345593
4. Chawla, G.; Solares, S. D. *Appl. Phys. Lett.* **2011,** *99,* 074103. doi:10.1063/1.3626847
5. Martínez, N. F.; Lozano, J. R.; Herruzo, E. T.; Garcia, F.; Richter, C.; Sulzbach, T.; Garcia, R. *Nanotechnology* **2008,** *19,* 384011. doi:10.1088/0957-4484/19/38/384011
6. Kawai, S.; Glatzel, T.; Koch, S.; Such, B.; Baratoff, A.; Meyer, E. *Phys. Rev. Lett.* **2009,** *103,* 220801. doi:10.1103/PhysRevLett.103.220801
7. Herruzo, E. T.; Asakawa, H.; Fukuma, T.; Garcia, R. *Nanoscale* **2013,** *5,* 2678–2685. doi:10.1039/c2nr33051b
8. Ebeling, D.; Solares, S. D. *Nanotechnology* **2013,** *24,* 135702. doi:10.1088/0957-4484/24/13/135702
9. Solares, S. D.; Chawla, G. *Meas. Sci. Technol.* **2010,** *21,* 125502. doi:10.1088/0957-0233/21/12/125502
10. Solares, S. D.; Chawla, G. *J. Appl. Phys.* **2010,** *108,* 054901. doi:10.1063/1.3475644
11. Ebeling, D.; Eslami, B.; Solares, S. D. *ACS Nano* **2013,** *7,* 10387–10396. doi:10.1021/nn404845q
12. Stark, M.; Stark, R. W.; Heckl, W. M.; Guckenberger, R. *Proc. Natl. Acad. Sci. U. S. A.* **2002,** *99,* 8473–8478. doi:10.1073/pnas.122040599
13. Sahin, O.; Magonov, S.; Su, C.; Quate, C. F.; Solgaard, O. *Nat. Nanotechnol.* **2007,** *2,* 507–514. doi:10.1038/nnano.2007.226
14. Platz, D.; Tholén, E. A.; Pesen, D.; Haviland, D. B. *Appl. Phys. Lett.* **2008,** *92,* 153106. doi:10.1063/1.2909569
15. Li, Y. J.; Takahashi, K.; Kobayashi, N.; Naitoh, Y.; Kageshima, M.; Sugawara, Y. *Ultramicroscopy* **2010,** *110,* 582–585. doi:10.1016/j.ultramic.2010.02.014
16. Jesse, S.; Kalinin, S. V.; Proksch, R.; Baddorf, A. P.; Rodriguez, B. J. *Nanotechnology* **2007,** *18,* 435503. doi:10.1088/0957-4484/18/43/435503
17. Guo, S.; Solares, S. D.; Mochalin, V.; Neitzel, I.; Gogotsi, Y.; Kalinin, S. V.; Jesse, S. *Small* **2012,** *8,* 1264–1269. doi:10.1002/smll.201101648
18. Rodriguez, B. J.; Callahan, C.; Kalinin, S. V.; Proksch, R. *Nanotechnology* **2007,** *18,* 475504. doi:10.1088/0957-4484/18/47/475504
19. Basak, S.; Raman, A. *Appl. Phys. Lett.* **2007,** *91,* 064107. doi:10.1063/1.2760175
20. Kiracofe, D.; Raman, A. *J. Appl. Phys.* **2010,** *108,* 034320. doi:10.1063/1.3457143
21. Melcher, J.; Xu, X.; Raman, A. *Appl. Phys. Lett.* **2008,** *93,* 093111. doi:10.1063/1.2976438
22. Melcher, J.; Carrasco, C.; Xu, X.; Carrascosa, J. L.; Gómez-Herrero, J.; de Pablo, P. J.; Raman, A. *Proc. Natl. Acad. Sci. U. S. A.* **2009,** *106,* 13655–13660. doi:10.1073/pnas.0902240106
23. Tung, R. C.; Jana, A.; Raman, A. *J. Appl. Phys.* **2008,** *104,* 114905. doi:10.1063/1.3033499
24. Xu, X.; Raman, A. *J. Appl. Phys.* **2007,** *102,* 034303. doi:10.1063/1.2767202
25. Xu, X.; Carrasco, C.; de Pablo, P. J.; Gomez-Herrero, J.; Raman, A. *Biophys. J.* **2008,** *95,* 2520–2528. doi:10.1529/biophysj.108.132829

26. Xu, X.; Melcher, J.; Basak, S.; Reifenberger, R.; Raman, A. *Phys. Rev. Lett.* **2009,** *102,* 060801. doi:10.1103/PhysRevLett.102.060801
27. Xu, X.; Melcher, J.; Raman, A. *Phys. Rev. B* **2010,** *81,* 035407. doi:10.1103/PhysRevB.81.035407
28. Herruzo, E. T.; Garcia, R. *Appl. Phys. Lett.* **2007,** *91,* 143113. doi:10.1063/1.2794426
29. Stark, R. W. *Appl. Phys. Lett.* **2009,** *94,* 063109. doi:10.1063/1.3080209
30. Stark, R. W. *Mater. Today* **2010,** *13,* 24–32. doi:10.1016/S1369-7021(10)70162-0
31. Chakraborty, I.; Yablon, D. G. *Nanotechnology* **2013,** *24,* 475706. doi:10.1088/0957-4484/24/47/475706
32. Kiracofe, D.; Raman, A.; Yablon, D. *Beilstein J. Nanotechnol.* **2013,** *4,* 385–393. doi:10.3762/bjnano.4.45
33. Lozano, J. R.; Garcia, R. *Phys. Rev. Lett.* **2008,** *100,* 076102. doi:10.1103/PhysRevLett.100.076102
34. Lozano, J. R.; Garcia, R. *Phys. Rev. B* **2009,** *79,* 014110. doi:10.1103/PhysRevB.79.014110
35. Kareem, A. U.; Solares, S. D. *Nanotechnology* **2012,** *23,* 015706. doi:10.1088/0957-4484/23/1/015706
36. Minary-Jolandan, M.; Tajik, A.; Wang, N.; Yu, M. F. *Nanotechnology* **2012,** *23,* 235704. doi:10.1088/0957-4484/23/23/235704
37. Ebeling, D.; Solares, S. D. *Beilstein J. Nanotechnol.* **2013,** *4,* 198–207. doi:10.3762/bjnano.4.20
38. Solares, S. D.; Chang, J.; Seog, J.; Kareem, A. U. *J. Appl. Phys.* **2011,** *110,* 094904. doi:10.1063/1.3657940
39. Solares, S. D. *J. Appl. Phys.* **2012,** *111,* 054909. doi:10.1063/1.3692393
40. Williams, J. C.; Solares, S. D. *Beilstein J. Nanotechnol.* **2013,** *4,* 87–93. doi:10.3762/bjnano.4.10
41. García, R.; Pérez, R. *Surf. Sci. Rep.* **2002,** *47,* 197–301. doi:10.1016/S0167-5729(02)00077-8

License and Terms

The definitive version of this article is the electronic one which can be found at:
doi:10.3762/bjnano.5.33

Beilstein Journal
of Nanotechnology

Exploring the complex mechanical properties of xanthan scaffolds by AFM-based force spectroscopy

Hao Liang‡1, Guanghong Zeng‡2, Yinli Li[1], Shuai Zhang[2], Huiling Zhao[1,2],
Lijun Guo[1], Bo Liu*1 and Mingdong Dong*2

Full Research Paper

Address:
[1]Institute of Photo-biophysics, School of Physics and Electronics, Henan University, Kaifeng, 475004 Henan, PR China and
[2]Interdisciplinary Nanoscience Center (iNANO), Aarhus University, DK-8000 Aarhus, Denmark

Email:
Bo Liu* - boliu@henu.edu.cn; Mingdong Dong* - dong@inano.au.dk

* Corresponding author ‡ Equal contributors

Keywords:
atomic force microscopy (AFM); force spectroscopy (FS); mechanical properties; xanthan scaffold

Beilstein J. Nanotechnol. **2014,** *5,* 365–373.
doi:10.3762/bjnano.5.42

Received: 22 November 2013
Accepted: 11 March 2014
Published: 27 March 2014

This article is part of the Thematic Series "Noncontact atomic force microscopy II".

Guest Editors: U. D. Schwarz and M. Z. Baykara

Abstract

The polysaccharide xanthan has been extensively studied owing to its potential application in tissue engineering. In this paper, xanthan scaffold structures were investigated by atomic force microscope (AFM) in liquid, and the mechanical properties of the complex xanthan structures were investigated by using AFM-based force spectroscopy (FS). In this work, three types of structures in the xanthan scaffold were identified based on three types of FS stretching events. The fact that the complex force responses are the combinations of different types of stretching events suggests complicated intermolecular interactions among xanthan fibrils. The results provide crucial information to understand the structures and mechanical properties of the xanthan scaffold.

Introduction

In general, a scaffold is composed of small units including sheet-like, cylinder-like, tube-like, sphere-like and sponge-like structures. Scaffold structures formed by various biopolymers have attracted more and more attention due to their potential applications in tissue engineering [1], such as cell incubation [2] and the repair of damaged tissue [3]. Xanthan, a polysaccharide which can self-associate into a scaffold structure [4,5], has been widely used in various fields, such as food additives [6] and drug delivery [7,8].

A number of tools, including NMR [9,10], circular dichroism (CD) [11], and atomic force microscopy (AFM) [12-14], has been used to explore the structures and properties of biopolymer scaffolds. Owing to its high resolution and versatility, AFM stands out of various tools and has been extensively employed in the study of biomaterials. For example, various morphologies of xanthan-based materials, such as fibrils, networks [4] and ring-like structures [5], have been revealed by AFM imaging. Furthermore, AFM is a powerful tool for studying the mechanical properties on the nanoscale. AFM-based force spectroscopy (FS) has been applied to investigate the fingerprint mechanical properties of single molecules [15,16]. FS was firstly used to study the polysaccharide dextran [17], and was later extended to other molecules such as DNA [18,19], proteins [20,21], other polysaccharides [22-24], and amyloid proteins [25,26]. Mechanical properties such as tensile strength, adhesive properties, and elastic modulus [27-29], have been investigated by FS. In the mechanical measurements of biomolecules, the unfolding of the regular secondary structure of proteins was characterized by periodical peaks on the force–distance curves, which allowed for the identification of the rupture force and the characteristic separation distance in the proteins [30]. In addition, the investigation of the mechanical properties of denatured and native polysaccharides such as xanthan fibrils has been carried out carefully [31]. Force plateaus were observed during the stretching of native xanthan, which could be attributed to the transition of helical secondary structures. In contrast, no plateaus were found during the stretching of denatured xanthan, which had no ordered secondary structures. Govedarica et al. [32] also concluded that the radius of gyration and the persistence length were responsible for the macroscopic polymer behavior. Therefore, it is very important to investigate the mechanical response of polymer complexes after manipulation.

In this study, the morphologies and mechanical properties of complex xanthan scaffolds, a new nanomaterial, were investigated by AFM and FS, respectively. The xanthan scaffold structures were obtained at both air/mica and isopropanol/mica interfaces, and three representative structures were probed by FS. We used a straightforward method to explain the complex force curve of the xanthan scaffold structure. The complex mechanical responses are actually the combinations of the force curves of three representative structures. Besides, the relative small persistence length in our study could indicate that xanthan is in its denatured form in isopropanol under our experimental conditions, which is of great importance in understanding the mechanical properties of xanthan scaffold material.

Experimental

Xanthan powder (Sigma-Aldrich Co.) was fully dissolved into deionized water by magnetic stirring of 24 h to prepare a 10 g/L stock solution, which then was annealed at 60 °C for 6 h and cooled to room temperature to obtain the xanthan scaffold solution [33]. The annealed 10 g/L xanthan stock solution was diluted to 0.01 g/L for further use. Two different surface adsorption methods were employed in our experiments. For AFM imaging under ambient conditions, 2 μL xanthan solution was dropped onto a freshly cleaved mica substrate (Ted Pella, Inc.) and air-dried for about 30–60 min. For AFM imaging in liquid and force spectroscopy measurements, 2 μL xanthan solution was deposited onto mica. After 60 s adsorption, an O-ring cell was equipped and a suitable amount of isopropanol (J&K Co) was injected as imaging buffer [5]. The AFM experiments were performed after 15 min of stabilization.

Atomic force microscopy

AFM imaging: AFM measurements were conducted on a commercial Agilent AFM/STM 5500 microscope (Agilent Technologies, USA) in contact mode. Nitride silicon cantilevers (OMCL-TR400PSA-1) with a spring constant of 0.02 N/m and a nominal tip radius of approximately 15 nm was used. The experiments were carried out under ultra-clean conditions at room temperature, and AFM imaging was performed both in air and isopropanol with a scanning frequency of 1 Hz and a vertical deflection of 0.5 V was applied. All the AFM images with 512 × 512 pixels were obtained at separate locations to ensure a high degree of reproducibility of experiment data. The images and force data were analyzed by the commercial software Scanning Probe Image Processor (SPIP^{TM}, by Image Metrology ApS, version 5.1.3, Lyngby, Denmark).

Force spectroscopy: Mechanical measurements of the xanthan scaffolds were performed by force measurement at a loading rate of 1 μm/s. The FS experiments were performed in isopropanol as buffer [5] in neutral environment with the diluted solution. The measurement started with the tip approaching the sample surface until a predefined deflection value was reached. The tip was then retracted from the surface and returned to its initial position. During the process, a force pulling curve was recorded. If the tip picked up xanthan fibrils on the surface, the fibrils would be stretched before they tear off from the tip. Depending on the number of attachment points, at which xanthan fibrils were attached to the tip, single or multiple rupture events may be observed in a single stretching.

Results and Discussion

The physical structure of xanthan molecules both in solid state and in solution is dominated by semi-flexible double helices, which resemble networks of rods linked by junction zones [34]. Multiple rods randomly wind and overlap with each other, forming complex scaffold structures. The contact mode AFM image (Figure 1A) obtained in air reveals the uniformly-spread xanthan scaffold. The AFM image (Figure 1B) in liquid shows a similar yet clearer network structure. Gaussian distributions were applied to fit the height distributions for the images in air and in liquid, respectively. Two populations were found for both samples (Figure 1C), which represent the measured heights of the substrate and the heights of the xanthan scaffold, respectively. The substrate peaks are normalized to 0 nm. Hence, the heights of fibrils in air and isopropanol are around 0.36 nm and

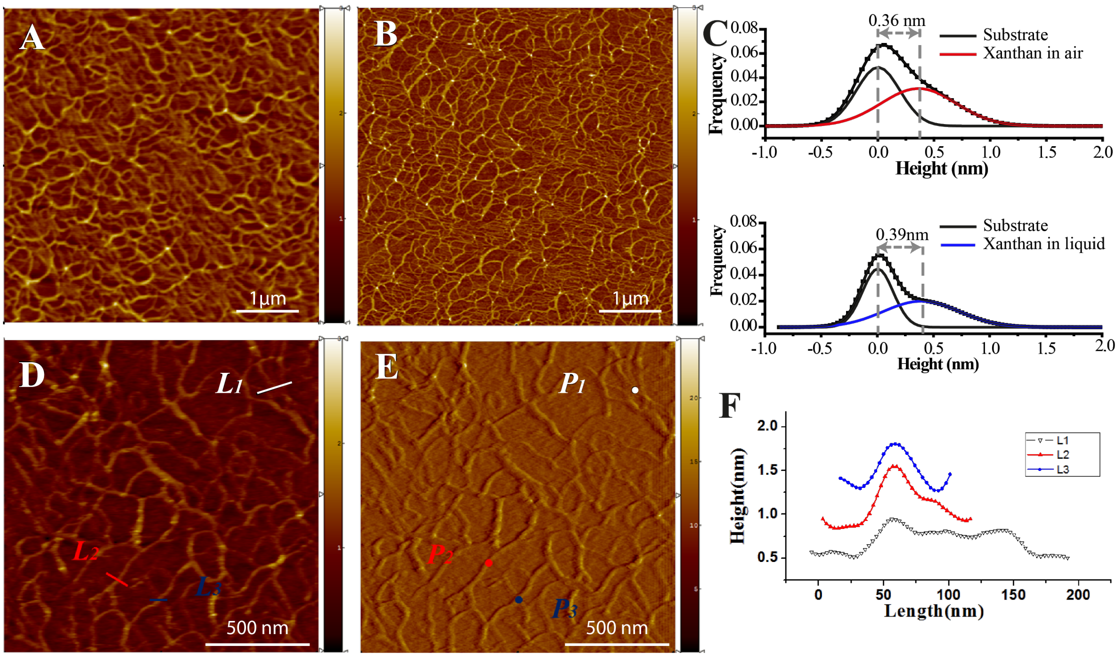

Figure 1: AFM images of xanthan scaffold A) in air, B) in isopropanol. C) Height histograms of xanthan scaffold in air and in isopropanol, respectively. D) Topography image in isopropanol. E) Corresponding deflection image in isopropanol. F) Line profiles that correspond to the marks L_1, L_2 and L_3 in Figure 1D.

0.39 nm, respectively (Figure 1C). The AFM topography and deflection images (Figure 1D,E) of the xanthan scaffolds were obtained in isopropanol buffer. Three representative structures (Figure 1E, P_1, P_2 and P_3) are identified to perform the mechanical measurements by FS. P_1 is characterized by multiple overlapping fibrils; P_2 is characterized by two overlapping fibrils; and P_3 is characterized by a single-fibril structure. Line profiles of the typical structures are showed in Figure 1F.

The above results confirmed our previous morphological studies on the temperature-enhanced re-organization of xanthan gels into 2D network of fibers. Based on this, we move forward to investigate the mechanical properties of the scaffolds by FS. FS was carried out on the xanthan scaffolds in isopropanol buffer, and four typical kinds of force curves with different numbers of rupture events were obtained (Figure 2). A single event curve (Figure 2A) is characterized by a single peak with a large rupture force, which indicates the stretching and rupture of a single xanthan fibril. Double and triple events curves (Figure 2B and Figure 2C) are characterized by two or three independent peaks, which indicate that the AFM tip fished two or three xanthan fibrils at the same time. Multiple events are usually observed during the manipulation at point P_1 (Figure 2D), indicating that more than three fibrils were attached, yielding sequential ruptures and intermolecular interactions.

Force curves with one peak could be obtained during manipulating all three typical structures. The peak corresponds to a single stretching event. For convenience, this kind of curve is defined as “type 1” (t_1), to distinguish it from the more complicated force curves, which will be discussed later. The schematic diagram in Figure 3A shows a superposition of 13 force curves with single events but with different rupture lengths, which range from tens to thousands of nanometers. Figure 3B shows a distribution of single events with different rupture forces and rupture lengths obtained by manipulating three different structures. The rupture force is the force needed to break the interaction between the xanthan fibrils and the AFM tip, and the rupture length represents the length of fibrils being stretched. Three domains exhibit distinctive trends of mechanical response. For clearer comparison, the distributions of rupture force and rupture length were separately illustrated in two histogram schematics (Figure 3C and Figure 3D). The distributions of rupture force that were obtained by pulling the three different structures show a similar trend, although the rupture length distributions are distinctive for each measurment. The rupture forces (Figure 3C) range from 50 to 400 pN, indicating the value of the nonspecific interaction force between the AFM tip and a single xanthan fibril. However, the rupture lengths of the force curves in manipulating three different structures are different. At P_1, the rupture length is small, ranging from 50 to 200 nm. In contrast, the rupture length at P_3 is much larger,

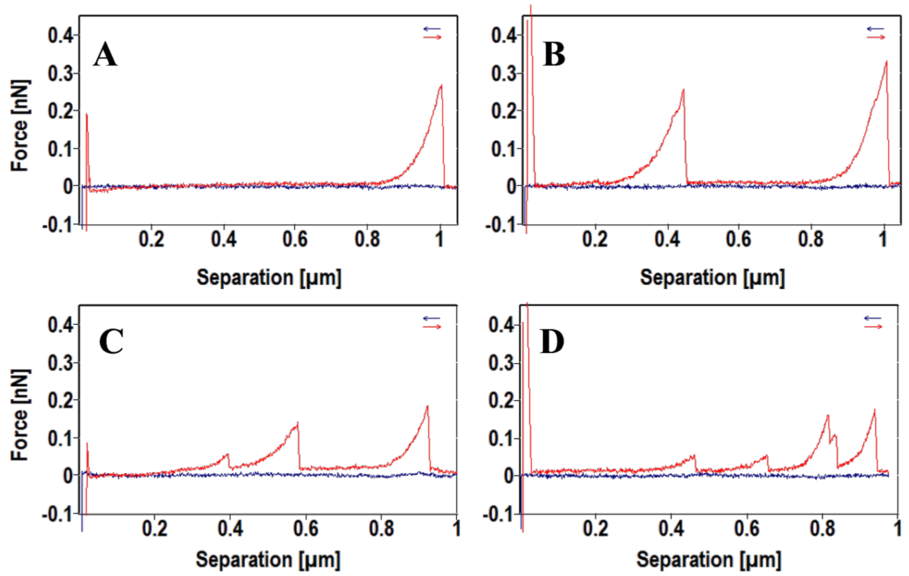

Figure 2: Typical force curves with different number of rupture events. A) Single event. B) Double events. C) Triple events. D) Multiple events.

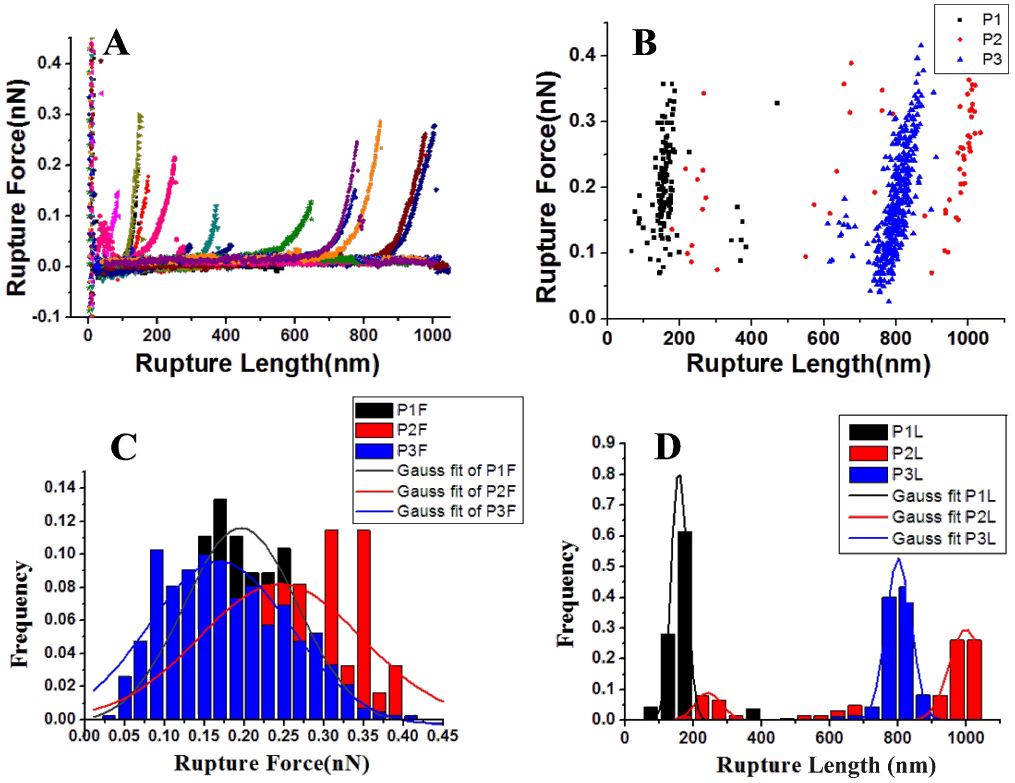

Figure 3: A) Schematic diagram of the superposition of force curves with single events. B) Distributions of rupture length and rupture force of various single events obtained by manipulating distinctive structures P_1, P_2 and P_3. C,D) The frequency distributions of rupture force and rupture length.

ranging from 750 to 900 nm. The huge difference of rupture length can be attributed to the different length of free xanthan fibrils between the junctions in the fibril network. At P_1, xanthan fibrils intensely wind and overlap with each other, which results in shorter free fibrils and thus much smaller rupture lengths than those of P_3, at which the single fibril is attached to two fibrils far away from each other. At P_2, the rupture length is similar to that at P_3. The distribution is slightly wider, which is possibly the result of the tip picking up the underlying fibril at P_2.

In addition to rupture force and rupture length, other information, such as the molecular elasticity, can be derived from the force curves by fitting the force pulling peaks with proper models. The worm-like chain (WLC) [35] model is usually applied to study the behavior of semi-flexible polymers. The equation is as follows:

$$F(x) = \frac{k_B T}{p}\left[\frac{x}{L} + \frac{1}{4\left(1-\frac{x'}{L}\right)^2} - \frac{1}{4}\right],$$

where the contour length, L, represents the length of the lifted fibrils and the persistence length, p, is a parameter for describing the flexibility of polymer coils, which is defined by the decay length of the directional correlation function along the polymer chain [26]. As showed in Figure 4A, the single stretching event observed at P_3 was well fitted by WLC model. The superposition of typical force curves after normalization of the separation length indicated that the force curves were measured from identical fibers. The persistence length is 0.35 ± 0.27 nm and contour length is 954 ± 157 nm (n = 92). It should be noted that the measured persistence length exhibits a much smaller value than that in the previous study [36,37]. Actually, the stiffness of a polymer depends on the specific experimental environment, e.g., ionic strength, salt concentration, and solution pH can largely influence the measured persistence length of xanthan [32,38-40]. In our study, we used isopropanol instead of water. Xanthan likely forms more hydrogen bonds in water than in isopropanol, and therefore the stiffness measured in isopropanol should be less than that in water. The discrepancy of measured persistence length between our study and the previous study could also suggest that the helical structure of xanthan may collapse and that the xanthan in the scaffold is denatured in isopropanol under our experimental conditions, which can weaken the stiffness of xanthan.

Apart from single large peaks, much smaller peaks were observed preceding the large peaks, as shown in Figure 5A and Figure 5B, which indicated that the pulled fibrils experienced one (arrow α in Figure 5A) or more tiny mechanical responses (arrow β and γ in Figure 5B) before the rupture from the AFM tip. These force curves are defined as “type 2” (t_2). Type 2 force curves frequently occurred during the stretching of the xanthan scaffold. The rupture force of a single kink is around 33 pN (arrow in Figure 5C), and the rupture length is mostly between 450 and 650 nm (arrow in Figure 5D). For force curves with two kinks, the rupture force distribution is similar to that of a single kink. However, a minority concentrates at 175 pN (data not shown), which can be contributed to the weight of fibrils attached on tip. The rupture length distribution agrees well with the dimension of the scaffold cavity.

The network structure is composed of randomly winding fibrils. Usually, more than two fibrils could be picked up at the same time during the manipulation. Figure 6A shows a typical double-event force curve composed of two independent single peaks. This kind of force curve was mainly obtained in manipulating the structures P_1 and P_2. The inset is a proposed model (in Figure 6A), in which two fibrils with different lengths were simultaneously pulled away from mica substrate. The shorter one ruptured from the tip first, followed by the longer one. Another type of double-event force curves (Figure 6B) was frequently observed, which is characterized by two continuous peaks, i.e. the second peak rises before the first peak falls back to zero. This type of force curves is defined as “type 3” (t_3)

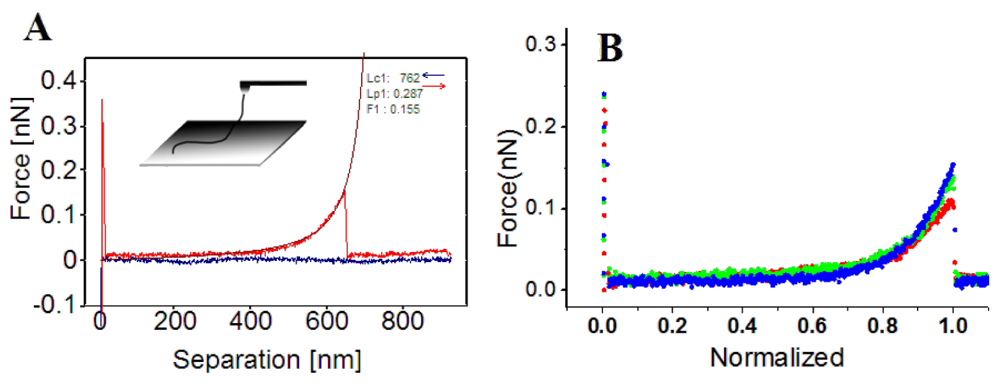

Figure 4: A) Typical “type 1” (t_1) force curve fitted with the WLC model. The inset is the model proposed to illustrate the single stretching events. B) The superposition of normalized single events (n = 3).

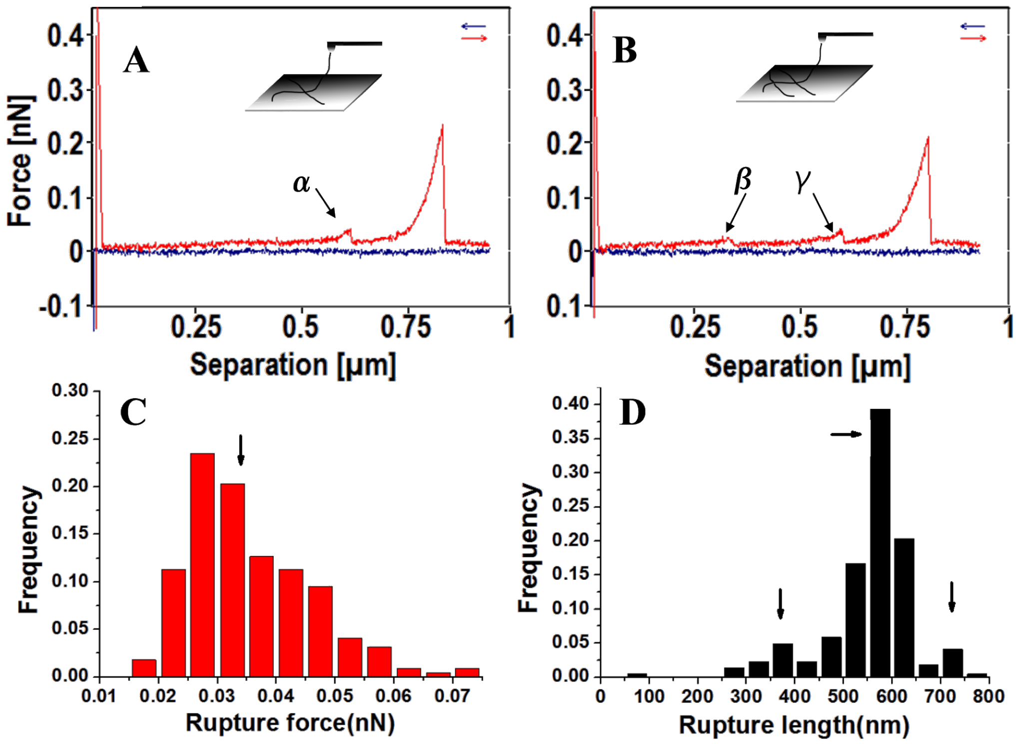

Figure 5: A,B) Typical single stretching event with one and two kinks (type 2), the insets are the proposed models. C,D) The frequency distributions of rupture force and rupture length of kinks in force curves with only one kink, respectively.

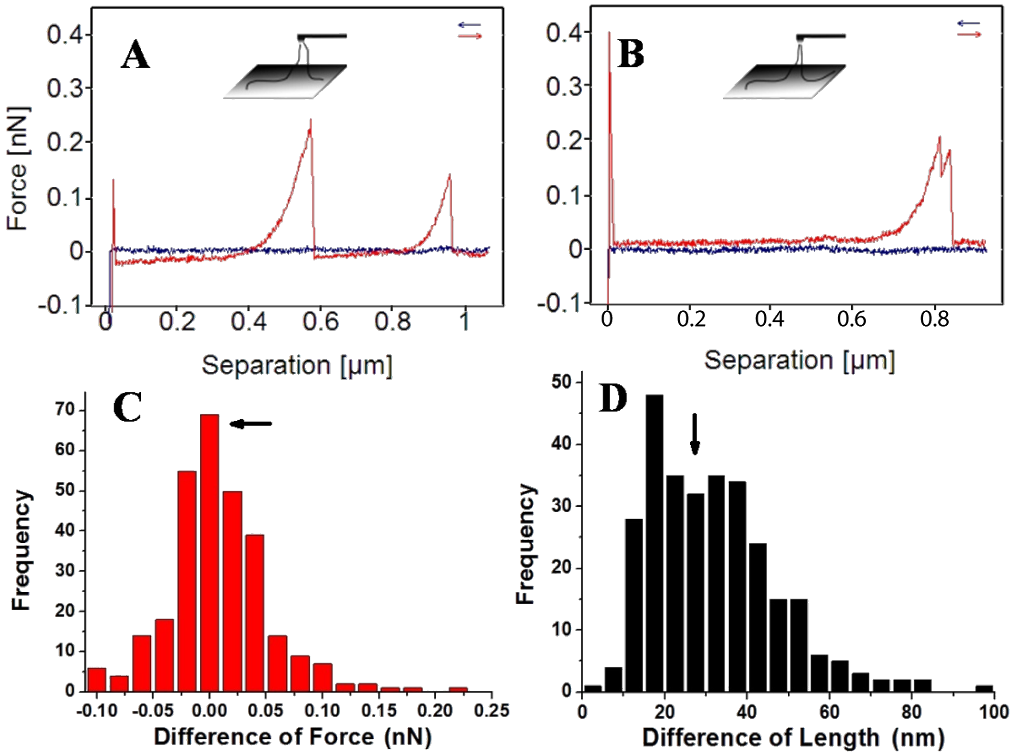

Figure 6: A) Typical double-peak force curve. B) “type 3” (t_3) force curve. C,D) histograms of the differences between the rupture forces and rupture lengths of the two continues peaks in t_3 force curves.

force curves. The corresponding mechanism might be explained in the way that two xanthan fibrils were pulled away from mica and ruptured from the AFM tip almost simultaneously. By further analysis of the FS data, it is found that the difference of the rupture forces of the two independent peaks (as in Figure 6A) is around 80 pN (not shown in the plot). One possible reason is that the weight of the detached fibrils contributes to larger rupture force of the second peak. In contrast, the difference between the rupture forces of the two continuous peaks (like Figure 6B) is around 0 nN (arrow in Figure 6C), as the two continuous peaks ruptured from the AFM tip almost at the same time. The rupture length difference between the two peaks is about 30 nm (arrow in Figure 6D), which is comparable with the dimension of the AFM tip, suggesting the two fibrils might be attached at both sides of the tip.

More complex mechanical responses were observed which can be deconvoluted into three typical force events. Figure 7A shows a combination of a t_2 and a t_1 force event, Figure 7B is composed of a t_2 and a t_3 force event, Figure 7C is composed of a t_3 and a t_1 event, and Figure 7D is composed of two t_2, one t_3 and one t_1 event. The insets are the models proposed to interpret the complex mechanical responses. As is shown in the inset of Figure 7A, the pulled fibril was detached from the underlying fibril before rupturing from the AFM tip. The tiny mechanical response is due to the adhesion force between the overlapping fibrils. As a more complex example, the inset of Figure 7B illustrates the case in which the tip fished two fibrils, one of which detached from a third underlying fibril before the two fibrils ruptured from the AFM tip. The force curve in Figure 7C is even more complex in that three fibrils were attached on the tip. Two of them ruptured first, followed by the longest third one. Whereas the most complex force curve is shown in Figure 7D. Similar but different from the one in 7C, the three fibrils experienced two fibril–fibril detachments before they ruptured from the tip sequentially. However, whether one of the fibrils experienced two detachments or two of the fibrils experienced one detachment independently cannot be distinguished from the force curve.

Conclusion

Scaffold structures of xanthan molecules were studied by AFM under ambient and liquid conditions. After AFM imaging in liquid, the mechanical properties of the xanthan scaffold were explored with force spectroscopy. Among various force responses observed, three basic types of force curve patterns were observed. Type 1 is characterized by a large peak indicating a single fibril was pulled away from mica substrate. Type 2 is characterized by a tiny peak corresponding to the separation of two overlapping fibrils. The rupture force of around 33 pN is the interaction force between two fibrils. Type 3 is characterized by two continuous peaks suggesting that two fibrils were attached on the AFM tip and ruptured almost at the same time. More complex force curves were explained by combined models. The investigation of the

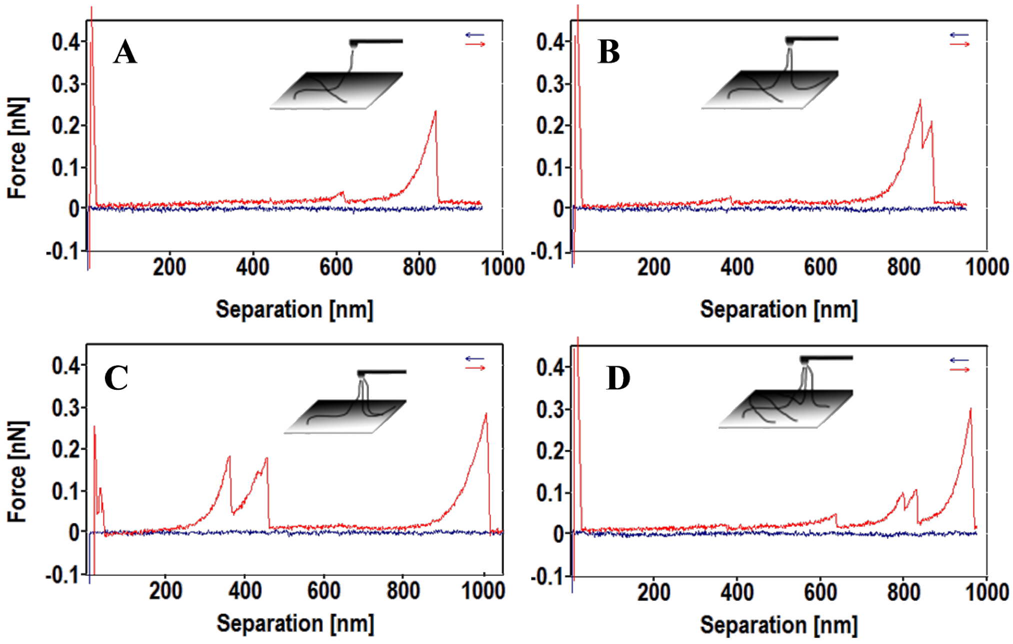

Figure 7: Mechanical responses composited by different type force curves. A) $t_1 + t_2$. B) $t_2 + t_3$. C) $t_1 + t_3$. D) $t_2 + t_2 + t_1 + t_3$.

mechanical properties of xanthan scaffold provides significant information toward understanding the self-assembled xanthan scaffold structure.

Acknowledgements

This work was supported by the National Natural Science Foundation of China (NO. 30900280), Henan Natural Science Research Office of Education project (NO. 2008A14003 and NO. 2010A140001), the Danish National Research Foundation (G. Z, S. Z., M. D.) and the Villum Foundation (M. D.).

References

1. Lee, K. Y.; Mooney, D. J. *Chem. Rev.* **2001,** *101,* 1869. doi:10.1021/cr000108x
2. Awad, H. A.; Butler, D. L.; Harris, M. T.; Ibrahim, R. E.; Wu, Y.; Young, R. G.; Kadiyala, S.; Boivin, G. P. *J. Biomed. Mater. Res.* **2000,** *51,* 233. doi:10.1002/(SICI)1097-4636(200008)51:2<233::AID-JBM12>3.0.CO;2-B
3. Perka, C.; Schultz, O.; Spitzer, R.-S.; Lindenhayn, K.; Burmester, G.-R.; Sittinger, M. *Biomaterials* **2000,** *21,* 1145. doi:10.1016/S0142-9612(99)00280-X
4. Iijima, M.; Shinozaki, M.; Hatakeyama, T.; Takahashi, M.; Hatakeyama, H. *Carbohydr. Polym.* **2007,** *68,* 701. doi:10.1016/j.carbpol.2006.08.004
5. Capron, I.; Alexandre, S.; Muller, G. *Polymer* **1998,** *39,* 5725. doi:10.1016/S0032-3861(97)10344-5
6. Davidson, R. L. *Handbook of water-soluble gums and resins;* McGraw-Hill: New York, NY, USA, 1980.
7. Shalviri, A.; Liu, Q.; Abdekhodaie, M. J.; Wu, X. Y. *Carbohydr. Polym.* **2010,** *79,* 898. doi:10.1016/j.carbpol.2009.10.016
8. Howard, K. A.; Dong, M.; Oupicky, D.; Bisht, H. S.; Buss, C.; Besenbacher, F.; Kjems, J. *Small* **2007,** *3,* 54. doi:10.1002/smll.200600328
9. Marcos, M.; Cano, P.; Fantazzini, P.; Garavaglia, C.; Gomez, S.; Garrido, L. *Magn. Reson. Imaging* **2006,** *24,* 89. doi:10.1016/j.mri.2005.10.008
10. Lee, H.-W.; Yang, W.; Ye, Y.; Liu, Z.-R.; Glushka, J.; Yang, J. J. *Biochim. Biophys. Acta, Proteins Proteomics* **2002,** *1598,* 80. doi:10.1016/S0167-4838(02)00338-2
11. Cai, W.; Wong, D.; Kinberger, G. A.; Kwok, S. W.; Taulane, J. P.; Goodman, M. *Bioorg. Chem.* **2007,** *35,* 327. doi:10.1016/j.bioorg.2007.01.003
12. Zhao, Y.; Tanaka, M.; Kinoshita, T.; Higuchi, M.; Tan, T. *J. Controlled Release* **2010,** *142,* 354. doi:10.1016/j.jconrel.2009.11.016
13. Verma, D.; Katti, K. S.; Katti, D. R. *Mater. Sci. Eng., C* **2009,** *29,* 2079. doi:10.1016/j.msec.2009.04.006
14. Rahbek, U. L.; Howard, K. A.; Oupicky, D.; Manickam, D. S.; Dong, M.; Nielsen, A. F.; Hansen, T. B.; Besenbacher, F.; Kjems, J. *J. Gene Med.* **2008,** *10,* 81. doi:10.1002/jgm.1120
15. Xu, S.; Dong, M.; Liu, X.; Howard, K. A.; Kjems, J.; Besenbacher, F. *Biophys. J.* **2007,** *93,* 952. doi:10.1529/biophysj.106.093229
16. Binnig, G.; Quate, C. F.; Gerber, C. *Phys. Rev. Lett.* **1986,** *56,* 930. doi:10.1103/PhysRevLett.56.930
17. Rief, M.; Oesterhelt, F.; Heymann, B.; Gaub, H. E. *Science* **1997,** *275,* 1295. doi:10.1126/science.275.5304.1295
18. Liu, N.; Bu, T.; Song, Y.; Zhang, W.; Li, J.; Zhang, W.; Shen, J.; Li, H. *Langmuir* **2010,** *26,* 9491. doi:10.1021/la100037z
19. Lee, G. U.; Chrisey, L. A.; Colton, R. J. *Science* **1994,** *266,* 771. doi:10.1126/science.7973628
20. Dong, M.; Sahin, O. *Nat. Commun.* **2011,** *2,* 247. doi:10.1038/ncomms1246
21. Rief, M.; Gautel, M.; Oesterhelt, F.; Fernandez, J. M.; Gaub, H. E. *Science* **1997,** *276,* 1109. doi:10.1126/science.276.5315.1109
22. Liu, C.; Wang, Z.; Zhang, X. *Macromolecules* **2006,** *39,* 3480. doi:10.1021/ma060054e
23. Xu, Q.; Zhang, W.; Zhang, X. *Macromolecules* **2001,** *35,* 871. doi:10.1021/ma011259k
24. Li, H.; Rief, M.; Oesterhelt, F.; Gaub, H. E.; Zhang, X.; Shen, J. *Chem. Phys. Lett.* **1999,** *305,* 197. doi:10.1016/S0009-2614(99)00389-9
25. Sandal, M.; Valle, F.; Tessari, I.; Mammi, S.; Bergantino, E.; Musiani, F.; Brucale, M.; Bubacco, L.; Samori, B. *PLoS Biol.* **2008,** *6,* 99. doi:10.1371/journal.pbio.0060006
26. Dong, M.; Hovgaard, M. B.; Mamdouh, W.; Xu, S.; Otzen, D. E.; Besenbacher, F. *Nanotechnology* **2008,** *19,* 384013. doi:10.1088/0957-4484/19/38/384013
27. Harder, A.; Walhorn, V.; Dierks, T.; Fernández-Busquets, X.; Anselmetti, D. *Biophys. J.* **2010,** *99,* 3498. doi:10.1016/j.bpj.2010.09.002
28. Guzmán, D. L.; Roland, J. T.; Keer, H.; Kong, Y. P.; Ritz, T.; Yee, A.; Guan, Z. *Polymer* **2008,** *49,* 3892. doi:10.1016/j.polymer.2008.06.047
29. Fisher, T. E.; Marszalek, P. E.; Fernandez, J. M. *Nat. Struct. Mol. Biol.* **2000,** *7,* 719. doi:10.1038/78936
30. Mostaert, A. S.; Jarvis, S. P. *Nanotechnology* **2007,** *18,* 044010. doi:10.1088/0957-4484/18/4/044010
31. Li, H.; Rief, M.; Oesterhelt, F.; Gaub, H. E. *Adv. Mater.* **1998,** *10,* 316. doi:10.1002/(SICI)1521-4095(199803)10:4<316::AID-ADMA316>3.0.CO;2-A
32. Govedarica, B.; Sovány, T.; Pintye-Hódi, K.; Škarabot, M.; Baumgartner, S.; Muševič, I.; Srčič, S. *Eur. J. Pharm. Biopharm.* **2012,** *80,* 217. doi:10.1016/j.ejpb.2011.09.008
33. Li, Y.; Li, Y.; Yao, Y.; Liu, B.; Chen, M.; Song, X.; Dong, M. *Colloids Surf., B* **2009,** *74,* 136. doi:10.1016/j.colsurfb.2009.07.007
34. Quinn, F. X.; Hatakeyama, T. *Polymer* **1994,** *35,* 1248. doi:10.1016/0032-3861(94)90019-1
35. Smith, S. B.; Finzi, L.; Bustamante, C. *Science* **1992,** *258,* 1122. doi:10.1126/science.1439819
36. Gamini, A.; Mandel, M. *Biopolymers* **1994,** *34,* 783. doi:10.1002/bip.360340610
37. Sato, T.; Norisuye, T.; Fujita, H. *Macromolecules* **1984,** *17,* 2696. doi:10.1021/ma00142a043
38. Camesano, T. A.; Wilkinson, K. J. *Biomacromolecules* **2001,** *2,* 1184. doi:10.1021/bm015555g
39. Li, H.; Rief, M.; Oesterhelt, F.; Gaub, H. E. *Appl. Phys. A* **1999,** *68,* 407. doi:10.1007/s003390050914
40. Milas, M.; Reed, W. F.; Printz, S. *Int. J. Biol. Macromol.* **1996,** *18,* 211. doi:10.1016/0141-8130(95)01080-7

License and Terms

Beilstein Journal
of Nanotechnology

Uncertainties in forces extracted from non-contact atomic force microscopy measurements by fitting of long-range background forces

Adam Sweetman*§ and Andrew Stannard§

Full Research Paper

Open Access

Address:
The School of Physics and Astronomy, The University of Nottingham, Nottingham, NG7 2RD, U.K.

Email:
Adam Sweetman* - adam.sweetman@nottingham.ac.uk

* Corresponding author
§ These authors contributed equally to this work.

Keywords:
background subtraction; DFM; F(z); force; atomic resolution; NC-AFM; Si(111); STM; van der Waals

Beilstein J. Nanotechnol. **2014,** *5,* 386–393.
doi:10.3762/bjnano.5.45

Received: 14 November 2013
Accepted: 03 February 2014
Published: 01 April 2014

This article is part of the Thematic Series "Noncontact atomic force microscopy II".

Guest Editors: U. D. Schwarz and M. Z. Baykara

Abstract

In principle, non-contact atomic force microscopy (NC-AFM) now readily allows for the measurement of forces with sub-nanonewton precision on the atomic scale. In practice, however, the extraction of the often desired 'short-range' force from the experimental observable (frequency shift) is often far from trivial. In most cases there is a significant contribution to the total tip–sample force due to non-site-specific van der Waals and electrostatic forces. Typically, the contribution from these forces must be removed before the results of the experiment can be successfully interpreted, often by comparison to density functional theory calculations. In this paper we compare the 'on-minus-off' method for extracting site-specific forces to a commonly used extrapolation method modelling the long-range forces using a simple power law. By examining the behaviour of the fitting method in the case of two radically different interaction potentials we show that significant uncertainties in the final extracted forces may result from use of the extrapolation method.

Introduction

Non-contact atomic force microscopy (NC-AFM) is now the tool of choice for surface scientists wishing to investigate interatomic and intermolecular forces on surfaces with sub-Angstrom precision. Although in principle it is relatively straightforward to extract the tip–sample force from the experimental observable (i.e., the shift in the resonant frequency of the oscillating cantilever Δf), in practice a significant amount of processing is usually required in order to obtain the desired quantity.

In this paper the focus primarily concerns the imaging and quantitative interpretation of atomic or molecular resolution

NC-AFM experiments conducted in ultrahigh vacuum (UHV). In these experiments, the quantity of interest is usually the site-specific/short-range force between the very apex of the tip and the surface. In any atomic resolution experiment using a scanning probe, atomic contrast must arise from an interaction that decays on a distance comparable to the interatomic spacing, otherwise atomic resolution would not be readily obtained. Consequently, the tip–sample interaction is usually modelled (for example using density functional theory (DFT) [1]) as the interaction between a small cluster of atoms (representing the tip) and a slab of surface atoms.

In order to extract the short-range force from the frequency shift measurement, however, the contribution from non-site-specific (i.e., long-range) forces must be removed. These are normally van der Waals and electrostatic in origin (here we ignore more complex cases such as magnetic systems).

The 'gold standard' for performing this subtraction is the so-called 'on-minus-off' method utilised by Lantz et al. [2], and Ternes et al. [3], amongst others. The principle behind this subtraction is quite simple: if there exists a region on the surface that is otherwise identical to the position at which the short-range force is to be measured, but is missing the atom or molecule that produces the short-range interaction, then performing the same measurement over that region will provide a measurement containing only the contribution of the long-range forces. A simple case is that of an adsorbed atom or molecule on a surface.

A measurement is first performed over the molecule, the tip is then moved some distance to the side and another measurement is performed over the same range of tip–sample separations. The contribution to the total force from the interaction between the macroscopic part of the tip and the bulk surface is the same, but the contribution from the molecule is removed. A similar procedure can be utilised for surface atoms if there is a large enough 'empty' region on a flat surface that does not exert any short-range force. A well-known example of this is the corner-hole on the Si(111)-(7 × 7) surface [2]. A cartoon of these two cases is shown in Figure 1B and Figure 1C.

Although the 'on-minus-off' technique provides a conceptually simple way of removing the long-range contribution, it has the

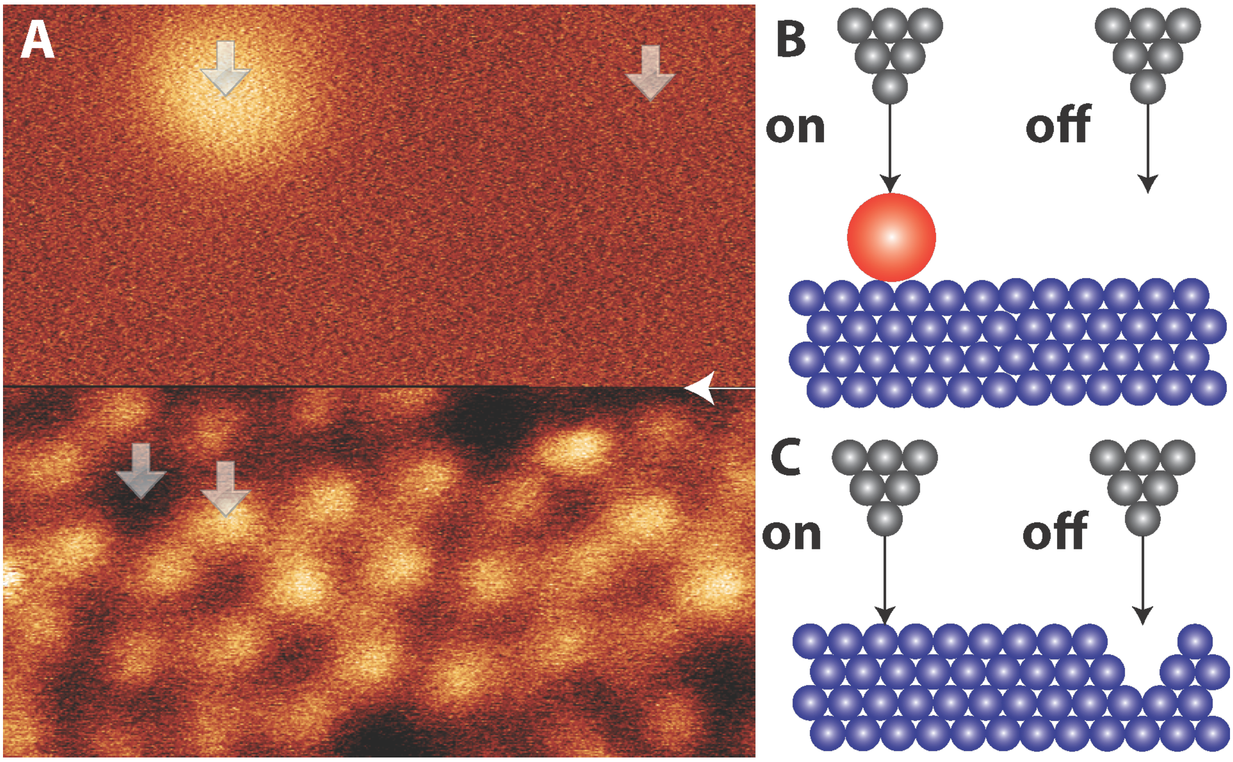

Figure 1: A) Constant Δf NC-AFM image of a C_{60} molecule adsorbed on the Si(111)-(7 × 7) surface showing atomic and molecular resolution. The position of the white arrow shows where the Δf setpoint was changed from $\Delta f = -53$ Hz (adatoms, lower half of image) to $\Delta f = -26.5$ Hz (C_{60}, upper half of image). Larger arrows show the $\Delta f(z)$ spectra positions. $V_{gap} = 0$ V. $A_0 = 0.11$ nm. $f_0 = 24866.3$ Hz. B) and C) Cartoon representations showing the principle behind 'on-minus-off' measurements on a molecule and surface adatom respectively.

limitation that it can only be applied on surfaces where such ‘null sites’ exist. In practice, on the vast majority of clean well-reconstructed surfaces, no such sites are available. In these instances attempts have been made to remove the long-range contribution by fitting the long-range background to a series of inverse power laws [4], and extrapolating the long-range force behaviour into the region where the short-range contributions are present. Although it is true that the long-range dispersion and electrostatic contributions might in principle be approximated by equations of this type, there has been surprisingly little discussion in the literature as to the uncertainties introduced using this technique. It is trivially true that any form of extrapolation must introduce a degree of uncertainty, but beyond this, there has been very little discussion regarding the uncertainties introduced during application of this technique to real experimental data, although some authors have provided estimates [5,6], or explicitly chosen not to utilise the technique [7]. A notable exception to this is the discussion that has surrounded Kelvin probe force microscopy (KPFM) where accurate modelling of this long-range regime is critical to interpreting results [8-10]. Nonetheless, long-range forces are readily subtracted in the literature using this method, often using simplistic models [1,6,11-14]. Results are then often compared to DFT modelling with subsequent interpretation of the data requiring accuracies on the order of a few 100’s [1,13], or sometimes even 10’s [12], of piconewtons. Interestingly, this technique has sometimes been applied in instances where ‘off’ measurements are, in principle, available [6,11].

In this paper we perform a simple set of force measurements using the same tip apex on two different surface locations where we are able to use the ‘on-minus-off’ method. This is done by depositing C_{60} molecules onto a clean Si(111)-(7 × 7) surface, and subsequently examining the both the tip–C_{60} and tip-silicon interactions. This method provides a useful way of checking the validity of the fitting method as we have access to two different interaction potentials (with ‘on’ and ‘off’ curves available in both cases), against which to test the long-range extrapolation method.

We find that although some fits do indeed recover similar force profiles to the ‘on-minus-off’ method, we show that there is no way of determining, *a priori*, which fit is correct without access to the ‘on-minus-off’ result. Consequently, we suggest that significant uncertainties may result from short-range forces extracted by this method on surfaces where no check is available.

Methods

The data in this paper were acquired using an Omicron Nanotechnology GmbH combined LT-STM/NC-AFM operating in UHV and at cryogenic temperatures (78 K at LN_2). Clean Si(111)-(7 × 7) samples were prepared by standard flash annealing to 1200 °C, rapid cooling to 900 °C, and then slow cooling to room temperature. A low coverage of C_{60} was prepared by depositing the molecules from a tantalum pocket onto the room temperature substrate. Following deposition the sample was immediately transferred into the scan head and left to cool before imaging.

Commercial qPlus sensors from Omicron with electrochemically etched tungsten wire glued to one tine of the tuning fork were introduced into the scan head without any further preparation. We typically recorded resonant frequencies of $f_0 \approx 25$ kHz, and, based on previous measurements of similar sensors [5,15], assume an effective stiffness of $k \approx 2000$ N/m. The sensors were first prepared on a clean silicon surface by standard STM techniques (pulsing and indentation) until good STM and NC-AFM resolution was achieved. Typically we used oscillation amplitudes (A_0) of between 0.1 and 0.3 nm during NC-AFM imaging. In order to eliminate any possible effect from either electronic crosstalk [16] or the so-called “Phantom Force” [17] all NC-AFM imaging was performed at 0 V (i.e., no detectable tunnel current). To stabilise the imaging conditions a custom-built atom tracking system developed at the University of Mainz [18] was used to apply feedforward correction to reduce the effect of thermal drift and piezo-electric creep.

To obtain the site-specific interaction force, single point $\Delta f(z)$ spectroscopy measurements were acquired on the adatoms, the cornerholes, the molecules, and ‘off’ the molecules, with all the spectra having identical parameters. In order to eliminate artefacts in the subtraction due to the shift in height due to the topographic feedback, the 'on' spectra were first aligned (on the z axis) to the 'off' spectra by a least mean squares fitting to the long-range part of the interaction [19] (this gave the same alignment within error as the method described by Sugimoto et al. [20]). The ‘off’ curve was then subtracted from the ‘on’ spectra and the resultant short-range $\Delta f(z)$ was inverted to force using the Sader–Jarvis formula [21]. Full technical details of the force extraction procedure, including the implementation of the force inversion algorithm and alignment procedure used for the ‘on-minus-off’ measurements, are presented in a forthcoming publication [19]. All data presented is the result of single $\Delta f(z)$ measurements and no averaging of curves has been performed to improve the signal-to-noise ratio.

In general, in order to perform long-range background subtraction, short-range curves are acquired and then aligned with a separate long-range curve before fitting, which can introduce additional uncertainties. In order to make a fairer comparison we performed high data density spectra out to long-range in all four positions. This ensured that the alignment of the ‘on’ and ‘off’ curves was identical for both the ‘on-minus-off’ method and the long-range extrapolation method.

We used a simple power law of form $a/(z + b)^c + d$ to fit the long-range part of the curve (using the standard curve fitting toolbox in MATLAB), assuming the tip–surface configuration can be modelled as a simple geometric shape positioned above a plane. Here a is related to the Hamaker constant of the material and size of the tip, b describes the divergence point of the long-range forces, c is the exponent governing the decay of the force, and d is an offset term taking into account any small deviation of the $\Delta f(z)$ tail from zero.

Although this form is almost certainly an oversimplification of the real interaction, it has been commonly applied [1,6,11-14] in these types of experiment. We note in passing that even for this simple function it was necessary to constrain the range and starting value of the fit parameters in order to ensure reliable convergence of the curve fitting algorithm (for example the parameter c was usually constrained to be between 1 and 3). All parameters were allowed to fully relax within the constraints that allowed for reliable convergence of the curve fitting algorithm, and we note that none of the fit parameter values were limited at the constraint boundaries for any of the fits presented here. In this work we did not investigate the effect on the fit due to the constraining or limiting of the free fit parameters, instead only analysing the fit that gave the best residuals for a given exclusion point (see below) for a full relaxation of all the fit parameters.

A key parameter in the curve fitting (not explicit in the equation itself) is how much of the curve to fit, as fitting part of the curve where short-range interactions are present will distort the form of the resultant fit, which should only approximate the long-range dispersion interactions. Although there is no definitive solution to determining where the short-range forces ‘turn on’, an estimate can be made by examining the Δf spectra taken over different sites. The point in z where the curves start to diverge can be taken as an estimate for the point where the measurement starts to become sensitive to site-specific interactions.

Results

Figure 1A shows a constant Δf image of a C_{60} molecule adsorbed on the Si(111)-(7 × 7) surface. In order to obtain atomic resolution on the substrate, and image the molecule without perturbing it [15,22], the setpoint was changed halfway up the image (see figure caption). In this instance the molecule is imaged at a low setpoint to reduce the chance of perturbing the tip state, and consequently no sub-molecular resolution is obtained. After obtaining the image, single point $\Delta f(z)$ spectra were taken on the silicon adatoms, the cornerholes, on top of the molecule, and ‘off’ the molecule.

Short-range forces were extracted by the two methods described in the experimental section. First by the ‘on-minus-off’ method, second by extrapolating a fit of the long-range force into the short-range regime. To test the consistency of the extrapolation method we produced fits using the same fitting method for both the ‘on’ and ‘off’ curves (noting that in an experiment requiring long-range extrapolation only the ‘on’ curve is available); i.e., fitting the long-range part of the curve using the power law described in the methods section, excluding different amounts of the short-range data and monitoring the subsequent effect on the extracted short-range forces. The resultant short-range forces, extracted by both methods, for the tip–sample interaction over both the silicon adatoms and the C_{60} molecule are shown in Figure 2.

Examining first the results on the C_{60} molecule, the ‘on-minus-off’ method shows a weak attractive force between tip and sample, suggesting either a molecular or weakly interacting silicon tip apex [23] which does not form a strong covalent bond with the molecule. Examining the short-range forces extracted by long-range extrapolation, fitting to the 'off' curve (Figure 2A), it is clear that the two fits excluding data below 0.5 and 0.3 nm systematically overestimate the short-range force, whereas the fit excluding ≤0.1 nm recovers a profile very close to the ‘on-minus-off’ method. Although the fit excluding ≤−0.1 nm obtains a more accurate minimum force value, we note the deviations in the tail show that the power law does not produce a good fit, and this is also clear in the residuals produced during curve fitting. Fitting to the ‘on’ curve produces similar results, except that the deviation in the fit when fitting down to −0.1 nm is much more pronounced, as we are clearly attempting to fit part of the short-range interaction, present in the on curve, using the power law.

With respect to the tip–silicon results (Figure 2C and Figure 2D), the force profiles from ‘on-minus-off’ are consistent with chemical bond formation between the tip apex and the reactive silicon adatom. Turning to the results obtained by long-range extrapolation, we observe a similar relative behaviour between the different fits as for the C_{60} results, with the notable exception that none of the curves accurately recover the correct short-range force profile, as all of the curves systematically overestimate the total short-range force, or show deviations due to failure of the power law fit.

An important subtlety here is the choice of the exclusion position, or rather, exactly how the exclusion position is deter-

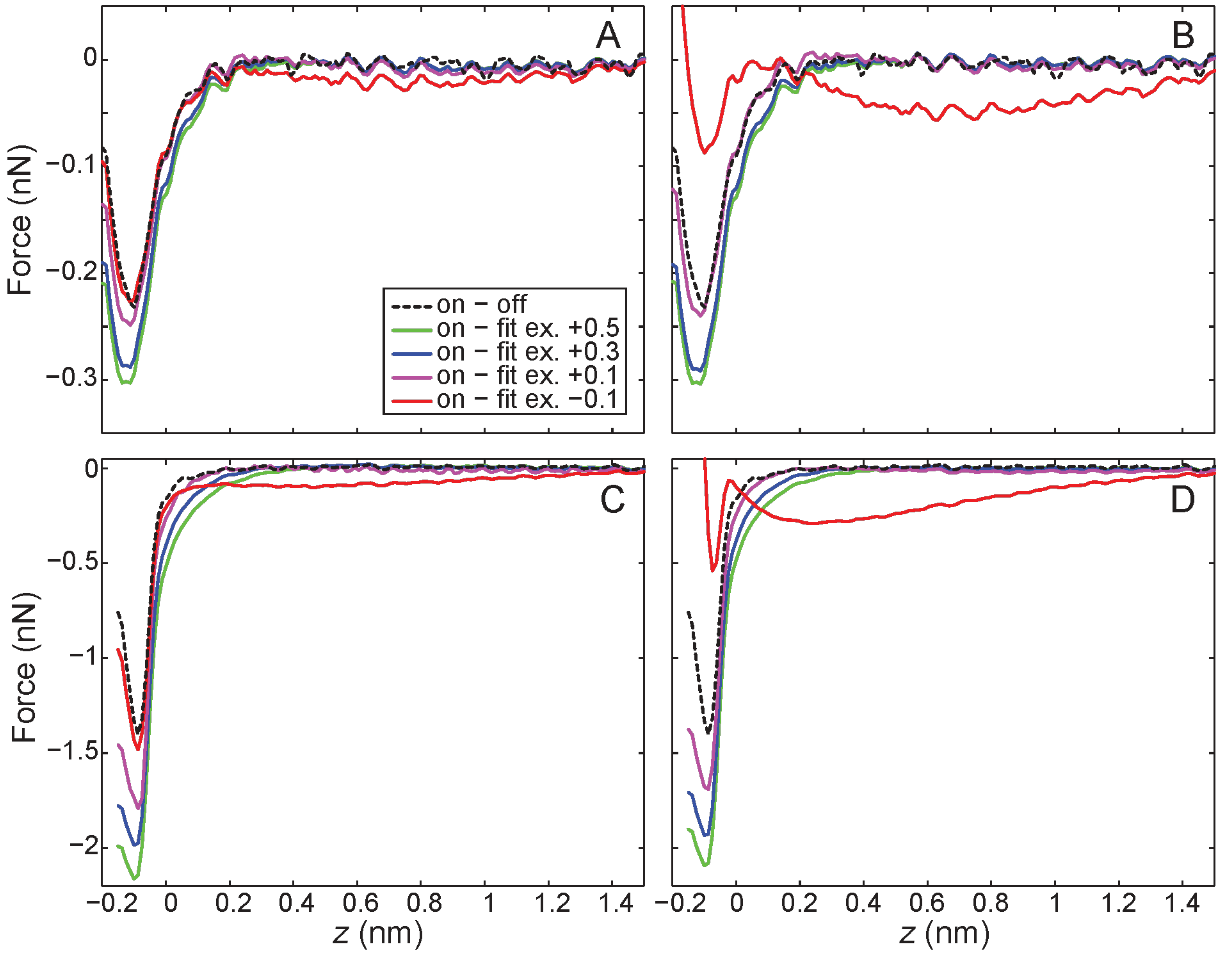

Figure 2: Extracted short-range force curves from ‘on-minus-off’ extraction, and comparison to long-range fitting for A) Tip–C_{60} interaction fitting to ‘off’ curve, B) Tip–C_{60} interaction fitting to ‘on’ curve, C) Tip–Si interaction fitting to ‘off’ curve, D) Tip–Si interaction fitting to ‘on’ curve. In the legend ‘ex’ indicates the point below which data was excluded from the fitting (e.g., ex = +0.1 indicates any data below +0.1 nm was excluded from the fit).

mined for a given dataset. Although on initial examination of the force curves it might be assumed that the fit excluding ≤0.1 nm provides a reasonable approximation to the ‘on-minus-off’ method, if we examine the raw Δf curves in detail (Figure 3A–C for the C_{60} data, D–F for Si data) it is interesting to note that if the ‘on-minus-off’ curve was not available for comparison we would have no reason to select this as the correct cut-off position. The divergence of the curves occurs somewhere between 0.2 nm and 0.3 nm, which should, in principle, strongly guide the choice of cut-off that determines which data to exclude from the fit. Therefore the fit excluding ≤0.1 nm actually fits part of the short-range interaction, and its agreement with the ‘on-minus-off’ method is purely fortuitous.

Consequently, in the absence of the ‘on-minus-off’ method as a check, the most rigorous position at which to start excluding data would be at approximately 0.3 nm. If this position were used, the overestimation of the short-range force would be approximately 20% in the case of the tip–C_{60} interaction, and approximately 40% in the case of the tip–silicon adatom interaction. Importantly, we note that these force values are all within the ‘sensible’ range of forces that might be expected for different tip structures common in this type of experiment. As such, if the forces were extracted using this method in an instance where no ‘on-minus-off’ check were possible, there would be no obvious reason to doubt their accuracy, especially if there was fortuitous agreement with results obtained from modelling calculations. In particular it is important to note that these uncertainties are larger than the systematic uncertainties usually present in NC-AFM experiments (usually dominated by the uncertainty in the oscillation amplitude of the cantilever), and critically, there is no reason to expect that the trend in the fit would to be systematic from tip to tip.

It is this uncertainty that lies at the crux of the matter regarding long-range background extrapolation methods. We wish to stress that it is not the case that the extraction of forces in this

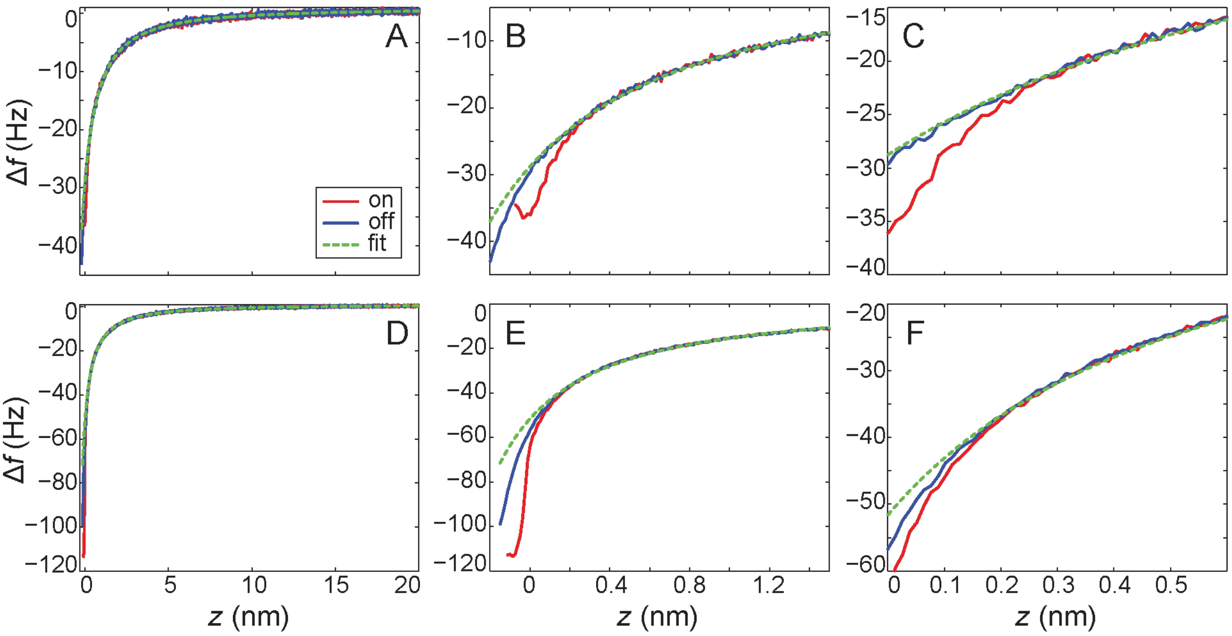

Figure 3: Close inspection of the divergence point between the ‘on’ and ‘off’ curves for A)–C) tip–C_{60} interaction, and D)–F) tip–Si interaction. Also plotted is the long-range fit for a cut-off of +0.1 nm which resulted in the short-range forces plotted in Figure 2. A)–C) shows the same data plotted on three different axis scale to show A) the long-range behaviour of the fit, B) the behaviour in the short-range regime, and C) the divergence point of the ‘on’ and ‘off’ curves. D)–E) shows the same progression for the tip–Si interaction.

manner necessarily produces incorrect, or unphysical, results, or even that the technique cannot in principle provide the ‘correct’ result. The issue is that in the absence of any independent check it is extremely difficult to quantify the uncertainty in the final extracted quantities. We again stress that the model used here to fit the long-range background is, although commonly used, an oversimplification, and a valid argument could be made that a more complex model, taking into account more details of the tip geometry, would be more robust.

In principle it is clear that more realistic models should better reflect the physical reality of the system, but an inherent issue is that these models introduce an even larger number of free parameters into the fit. Even if these parameters are weakly constrained to use ‘physical’ parameters, the range of possible fits (all producing ‘good’ fits to the long-range data) grows dramatically as the number of free parameters is increased. Most importantly, the fact that a given function produces a ‘good’ fit to the selected range of data does not, in itself, provide strong evidence that the extrapolation into the short-range force regime is accurate.

We note that the confidence in the fit to the long-range behaviour may be increased dramatically if a judicious knowledge of the tip structure is available, for example by use of *in situ* field ion microscopy (FIM), transmission electron microscopy (TEM), and/or scanning electron microscopy (SEM), on well-defined tips both before and after force spectroscopy experiments have been performed. If used on tips made from a single, well-characterised material, such methods might provide extremely strong bounds with which to constrain the free parameters of the fit, and the choice of tip model to be used. Consequently, we expect the uncertainties introduced from the fit could be reduced, and well-quantified, in such instances.

Although these techniques are sometimes used [24], in the vast majority of experimental setups these facilities are not available, and, even if available, drastically increase the time and difficulty in performing the measurements, as any indentation of the tip into the surface will require the tip structure checks to be repeated. This is likely to be even more important in the case of experiments using qPlus-type setups, where STM tip treatment methods are often used to prepare tips *in situ* on the surface. In these cases, significant transfer of material from tip to surface, and vice versa, can occur, and dramatically modify the long-range background profile.

Consequently, we suggest as a practical guide that ‘site-difference’ measurements, where the difference between two ‘on’ curves is taken [7,25], are used to make comparisons to calculated results on surfaces where ‘on-minus-off’ experiments are not feasible, or, if the absolute short-range force must be extracted by the extrapolation method, a discussion of the uncertainties should be presented. An estimate of the errors might be obtained practically by obtaining a number of fits with different models/parameters, and systematically varying the cutoff position of the fits. If the curve fitting algorithm is robust under different constraints and starting parameters, and different models return similar physical properties of the tip, then it seems that a robust estimate of the resultant uncertainties might be made.

Conclusion

In conclusion, we have presented a comparison of the results obtained from extracting site-specific forces in NC-AFM by 'on-minus-off' and extrapolation methods. Although extrapolation techniques can provide accurate force values, a significant uncertainty is introduced into the quantitative values of the resulting short-range forces. We recommend that the 'on-minus-off' technique is used where possible, and a judicious consideration of the uncertainties is presented when extrapolation techniques must be used, especially when comparing the results to calculated values. We also note that during the review process we became aware of a forthcoming publication by Kuhn et al. [26] which rigorously explores the uncertainties and consistency of the long-range background fitting method for a number of different tip–surface interaction models in the case where no 'off' curve is available, using a conventional silicon cantilever NC-AFM setup.

Acknowledgements

Adam Sweetman thanks the Engineering and Physical Sciences Research Council (EPSRC), and the Leverhulme Trust, respectively, for funding through Grants No. EP/G007837/1 and F00/114 BI. Andrew Stannard acknowledges the University of Nottingham for funding through a Nottingham Advance Research Fellowship. The authors are grateful to Philip Moriarty, Philipp Rahe and Samuel Jarvis for a number of stimulating discussions and comments on the manuscript.

References

1. Oyabu, N.; Pou, P.; Sugimoto, Y.; Jelínek, P.; Abe, M.; Morita, S.; Pérez, R.; Custance, Ó. *Phys. Rev. Lett.* **2006,** *96,* 106101. doi:10.1103/PhysRevLett.96.106101
2. Lantz, M. A.; Hoffmann, R.; Foster, A. S.; Baratoff, A.; Hug, H. J.; Hidber, H. R.; Güntherodt, H.-J. *Phys. Rev. B* **2006,** *74,* 245426. doi:10.1103/PhysRevB.74.245426
3. Ternes, M.; González, C.; Lutz, C. P.; Hapala, P.; Giessibl, F. J.; Jelínek, P.; Heinrich, A. J. *Phys. Rev. Lett.* **2011,** *106,* 016802. doi:10.1103/PhysRevLett.106.016802
4. Guggisberg, M.; Bammerlin, M.; Loppacher, C.; Pfeiffer, O.; Abdurixit, A.; Barwich, V.; Bennewitz, R.; Baratoff, A.; Meyer, E.; Güntherodt, H.-J. *Phys. Rev. B* **2000,** *61,* 11151–11155. doi:10.1103/PhysRevB.61.11151
5. Sweetman, A.; Jarvis, S.; Danza, R.; Bamidele, J.; Gangopadhyay, S.; Shaw, G. A.; Kantorovich, L.; Moriarty, P. *Phys. Rev. Lett.* **2011,** *106,* 136101. doi:10.1103/PhysRevLett.106.136101
6. Hauptmann, N.; Mohn, F.; Gross, L.; Meyer, G.; Frederiksen, T.; Berndt, R. *New J. Phys.* **2012,** *14,* 073032. doi:10.1088/1367-2630/14/7/073032
7. Such, B.; Glatzel, T.; Kawai, S.; Meyer, E.; Turanský, R.; Brndiar, J.; Štich, I. *Nanotechnology* **2012,** *23,* 045705. doi:10.1088/0957-4484/23/4/045705
8. Sadeghi, A.; Baratoff, A.; Ghasemi, S. A.; Goedecker, S.; Glatzel, T.; Kawai, S.; Meyer, E. *Phys. Rev. B* **2012,** *86,* 075407. doi:10.1103/PhysRevB.86.075407
9. Baier, R.; Leendertz, C.; Lux-Steiner, M. C.; Sadewasser, S. *Phys. Rev. B* **2012,** *85,* 165436. doi:10.1103/PhysRevB.85.165436
10. Bocquet, F.; Nony, L.; Loppacher, C. *Phys. Rev. B* **2011,** *83,* 035411. doi:10.1103/PhysRevB.83.035411
11. Morita, K.; Sugimoto, Y.; Sasagawa, Y.; Abe, M.; Morita, S. *Nanotechnology* **2010,** *21,* 305704. doi:10.1088/0957-4484/21/30/305704
12. Teobaldi, G.; Lämmle, K.; Trevethan, T.; Watkins, M.; Schwarz, A.; Wiesendanger, R.; Shluger, A. L. *Phys. Rev. Lett.* **2011,** *106,* 216102. doi:10.1103/PhysRevLett.106.216102
13. Yurtsever, A.; Fernández-Torre, D.; González, C.; Jelínek, P.; Pou, P.; Sugimoto, Y.; Abe, M.; Pérez, R.; Morita, S. *Phys. Rev. B* **2012,** *85,* 125416. doi:10.1103/PhysRevB.85.125416
14. Naitoh, Y.; Kamijo, T.; Li, Y. J.; Sugawara, Y. *Phys. Rev. Lett.* **2012,** *109,* 215501. doi:10.1103/PhysRevLett.109.215501
15. Chiutu, C.; Sweetman, A. M.; Lakin, A. J.; Stannard, A.; Jarvis, S.; Kantorovich, L.; Dunn, J. L.; Moriarty, P. *Phys. Rev. Lett.* **2012,** *108,* 268302. doi:10.1103/PhysRevLett.108.268302
16. Majzik, Z.; Setvín, M.; Bettac, A.; Feltz, A.; Cháb, V.; Jelínek, P. *Beilstein J. Nanotechnol.* **2012,** *3,* 249–259. doi:10.3762/bjnano.3.28
17. Weymouth, A. J.; Wutscher, T.; Welker, J.; Hofmann, T.; Giessibl, F. J. *Phys. Rev. Lett.* **2011,** *106,* 226801. doi:10.1103/PhysRevLett.106.226801
18. Rahe, P.; Schutte, J.; Schniederberend, W.; Reichling, M.; Abe, M.; Sugimoto, Y.; Kühnle, A. *Rev. Sci. Instrum.* **2011,** *82,* 063704. doi:10.1063/1.3600453
19. Stannard, A.; Sweetman, A. Imaging and Manipulation of Adsorbates using Dynamic Force Microscopy. *Advances in Atom and Single Molecule Machines;* Springer; Vol. 4, submitted.
20. Sugimoto, Y.; Pou, P.; Custance, Ó.; Jelínek, P.; Morita, S.; Pérez, R.; Abe, M. *Phys. Rev. B* **2006,** *73,* 205329. doi:10.1103/PhysRevB.73.205329
21. Sader, J. E.; Jarvis, S. P. *Appl. Phys. Lett.* **2004,** *84,* 1801. doi:10.1063/1.1667267
22. Simon, G. H.; Heyde, M.; Freund, H.-J. *J. Phys.: Condens. Matter* **2012,** *24,* 084007. doi:10.1088/0953-8984/24/8/084007
23. Ondráček, M.; Pou, P.; Rozsíval, V.; González, C.; Jelínek, P.; Pérez, R. *Phys. Rev. Lett.* **2011,** *106,* 176101. doi:10.1103/PhysRevLett.106.176101
24. Falter, J.; Langewisch, G.; Hölscher, H.; Fuchs, H.; Schirmeisen, A. *Phys. Rev. B* **2013,** *87,* 115412. doi:10.1103/PhysRevB.87.115412
25. Sharp, P.; Jarvis, S.; Woolley, R.; Sweetman, A.; Kantorovich, L.; Pakes, C.; Moriarty, P. *Appl. Phys. Lett.* **2012,** *100,* 233120. doi:10.1063/1.4726086
26. Kuhn, S.; Rahe, P. *Phys. Rev. B* **2014,** submitted.

License and Terms

Beilstein Journal
of Nanotechnology

Energy dissipation in multifrequency atomic force microscopy

Valentina Pukhova[1,2], Francesco Banfi[2] and Gabriele Ferrini[*2]

Full Research Paper

Address:
[1]Dipartimento di Fisica, Università degli Studi di Milano, I-20122 Milano, Italy and [2]Interdisciplinary Laboratories for Advanced Materials Physics (i-LAMP) and Dipartimento di Matematica e Fisica, Università Cattolica, I-25121 Brescia, Italy

Email:
Gabriele Ferrini[*] - gabriele.ferrini@unicatt.it

* Corresponding author

Keywords:
band excitation; multifrequency atomic force microscopy (AFM); phase reference; wavelet transforms

Beilstein J. Nanotechnol. **2014,** *5,* 494–500.
doi:10.3762/bjnano.5.57

Received: 22 October 2013
Accepted: 24 February 2014
Published: 17 April 2014

This article is part of the Thematic Series "Noncontact atomic force microscopy II".

Guest Editors: U. D. Schwarz and M. Z. Baykara

Abstract

The instantaneous displacement, velocity and acceleration of a cantilever tip impacting onto a graphite surface are reconstructed. The total dissipated energy and the dissipated energy per cycle of each excited flexural mode during the tip interaction is retrieved. The tip dynamics evolution is studied by wavelet analysis techniques that have general relevance for multi-mode atomic force microscopy, in a regime where few cantilever oscillation cycles characterize the tip–sample interaction.

Introduction

Multifrequency dynamic atomic force microscopy [1] is a powerful technique to retrieve quantitative information on materials properties such as the elastic constants and the sample chemical environment with a lateral resolution in the nanometer range. In this context the energy dissipation is a fundamental aspect of the tip–sample interaction, allowing to quantify compositional contrast variations at the nanoscale [2]. The applied forces and the energy delivered to the sample are relevant for the imaging and the manipulation of soft materials in a variety of environments [3]. The study of the nanomechanical properties of the cell, the development of sensitive nanomechanical devices, the characterization of mobile nanoparticles are all tasks that require a control of the force and energy involved in the tip–sample interactions [4].

Recently we introduced a wavelet cross-correlation (XWT) technique in atomic force spectroscopy to reconstruct complex force dynamics in the tip–sample impact regime, when higher cantilever modes are simultaneously excited [5]. The XWT analysis allows to retrieve the displacement, velocity and acceleration of the tip simultaneously for each flexural eigenmode upon impact. In the present work we build on that results to study in greater details the tip–sample force interactions separately for each mode and in particular the energy dissipation. Since the dissipative interactions are important in characterizing the compositional contrast of the sample at the nanometer scale [6], the possibility of measuring the interactions of each mode separately opens new channels to study the surface composition.

Results and Discussion

Wavelet analysis and experiments

This section is partially based on the time-frequency analysis outlined in our previous work [5]. Wavelet analysis allows to follow the spectral content of a signal $h(t)$ that evolves in time by projecting (convoluting) the signal over a set of oscillating functions with zero mean and a limited support (wavelets)

$$\Psi_{s,d}(t) = \frac{1}{\sqrt{a}}\Psi\left(\frac{t-d}{a}\right)$$

that are obtained by the translations (or delays, d) and dilations (or scaling, s) of a mother wavelet $\Psi(t)$ [7]. The temporal convolution of the signal with the wavelets at all possible scales and delays constitute the wavelet transform (WT) of the signal $W^h(s,d)$ [7]. Scaling is connected to frequency, delays to time. The signal spectrum $W^h(s,d)$ is a frequency–time representation that gives a measure of the local, i.e., at the point (s,d), resemblance of the signal and the wavelet. In wavelet analysis the basis can be chosen among an infinite set of functions that are mathematically admissible, in this work we use the complex Gabor wavelets [8,9].

To cross-correlate two time signals $h(t)$ and $g(t)$ in the frequency–time plane, we first take the wavelet spectrums of the signals $W^h(s,d)$ and $W^g(s,d)$, and then form the cross-wavelet (XWT) spectrum as $W^{hg}(s,d) = W^h(s,d)\, W^{g*}(s,d)$, where * denotes the complex conjugate. The wavelet coefficients can be represented in the polar picture as $W^h(s,d) = |W^h(s,d)|\exp(\Phi^h(s,d))$, where $|W^h(s,d)|$ is the wavelet amplitude, and $\Phi^h(s,d)$ is the absolute phase. Both power and phase pertain to the "point" (s,d) in the frequency–time plane. The important point in the XWT is that the relative phase difference between the two time series at the specified time–frequency point (s,d), can be retrieved as

$$\begin{aligned}\Phi^{hg}(s,d) &= \Phi^{h}(s,d) - \Phi^{g}(s,d)\\ &= \tan^{-1}\left(\frac{\Im\left(<s^{-1}W^{hg}(s,d)>\right)}{\Re\left(<s^{-1}W^{hg}(s,d)\right)}\right),\end{aligned}$$

where $\Phi^h(s,d)$ is the phase of h, $\Phi^g(s,d)$ is the phase of g, <> represents a smoothing operator, $\Re$ and $\Im$ are the real and imaginary parts, respectively.

Now we briefly recall the concept of phase carpet [5,10]. To analyze the phase evolution of the oscillating mode of a cantilever and, consequently, of the signal that is generated by the beam deflection method of choice, we need, as a reference, an oscillating function with a known phase at the same frequency of the mode under investigation. If the modes are more than one at the same time, we need a reference function for each one of them. A natural reference function for phase analysis is the *sinus cardinalis* function (sinc), defined as

$$A\,\mathrm{sinc}\left(\left(t-t_0\right)/a\right) = \frac{A\sin\left(\left(t-t_0\right)/a\right)}{\left(t-t_0\right)/a},$$

where a is a shape parameter that controls the width of the function centered at time t_0, and A is the peak amplitude. To understand the usefulness of the sinc function as a phase reference, consider the following identities:

$$\begin{aligned}\delta(t) &= \lim_{a\to 0}\frac{1}{a}\mathrm{sinc}\left(\frac{t}{a}\right)\\ &= \lim_{N\to\infty}\frac{1}{T}\left(1+2\cos(\omega t)+2\cos(2\omega t)+\ldots+2\cos(N\omega t)\right),\end{aligned} \tag{1}$$

where $\omega = 2\pi/T$. These identities show that as the shaping factor a tends to zero, the sinc function tends to a Dirac delta function that can be expressed as an infinite sum of cosines of increasing frequencies *all with phases equal to zero at time zero*. From Equation 1 an approximate relation can be derived to express the sinc as a sum of cosines:

$$\mathrm{sinc}\left(\frac{t}{a}\right) \approx \frac{1}{N+1}\left(1+2\cos(\omega t)+2\cos(2\omega t)+\ldots+2\cos(N\omega t)\right) \tag{2}$$

$$a = \frac{T}{2N+1} \tag{3}$$

where the approximation improves as N increases. The time width of the sinc function is related to the shaping parameter. Choosing the distance between the zero crossings on either side of the peak (Δt) as the time width gives $\Delta t = 2\pi\, a$. The Fourier transform is a rectangle function that extends from zero to a cut-off frequency $f_c = 1/a$ and that has phase nearly equal to zero at all frequencies. The cross-correlation of the wavelet transform of the signal with that of the sinc function allows to obtain a phase reference for every oscillation frequency that composes the signal in the neighborhood of the sinc peak. Note that the XWT rapidly tends to zero off the peak of the sinc function because its amplitude decreases rapidly. WT and XWT are particularly useful in assessing impact phenomena. As an example we will examine the jump-to-contact transition of a cantilever on a graphite substrate.

The deflection of a rectangular silicon cantilever is monitored through a beam-deflection system as the cantilever tip approaches a freshly cleaved surface of highly oriented pyrolytic graphite (HOPG) without any external excitation. The experiment is conducted in air, at room temperature (296 K) an a relative humidity of 55%. The temporal trace has been recorded with a digitizing oscilloscope with a vertical resolution of 8-bit, an analog bandwidth of 250 MHz, and a maximum sampling rate of 1 GSample/s. The average dimensions of the rectangular silicon cantilever are $40 \times 456 \times 2\ \mu\text{m}^3$ with a nominal tip radius of 10 nm. The elastic constant of the first free flexural mode was measured by the Sader method [11] to be $k_1 = 0.15 \pm 0.03$ N/m. A rms thermal amplitude of about 2 Å is measured at room temperature [12]. The cantilever approaches the graphite surface at constant velocity of 0.817 nm/ms. The inverse optical lever sensitivity (InvOLS) [13] has been measured as the inverse slope of the linear contact part of a standard force measurement [14] that was made on the graphite substrate.

The following steps, synthetised in Figure 1, allow to reconstruct the evolution of a multi-mode excitation of a cantilever, after a jump-to-contact transition [5]. 1) Single out the time period of interest, i.e., the neighborhood of the impact moment, Figure 1B. 2) Take a WT of the signal and individuate the excited modes that contribute to the dynamics, Figure 1C. 3) Each flexural mode is schematized as a damped harmonic oscillator (DHO), whose equation of motion is

$$\ddot{z}_i + \gamma_i \dot{z}_i + \omega_{0_i}^2 z_i = 0 \tag{4}$$

where i is the mode index, z_i is the oscillation amplitude, γ_i is the damping coefficient and $\gamma_i << \omega_{0_i}$ the resonance frequency [15]. Assuming as initial conditions $z_i(0) = z_{0_i}$, $\dot{z}_i(0) = 0$, and $\gamma_i << \omega_{0_i}$, the solution is well approximated by an exponentially decaying amplitude oscillating at the resonance frequency: $z_i = z_{0_i} e^{-\gamma_i t/2} \cos(\omega_{0_i} t) = z_{0_i} e^{-t/\tau_i} \cos(\omega_{0_i} t)$, where $\gamma_i = 2/\tau_i$. Each solution (z_i), is generally characterized by four parameters, the amplitude (z_{0_i}), the decay constant (τ_i), the frequency ($f_i = \omega_i/2\pi$) and phase (ϕ_i), $z_i = z_{0_i} e^{-t/\tau_i} \cos(\omega_{0_i} t + \phi_i)$. 4) Retrieve the parameters of each DHO through the WT and the XWT analysis, Figure 1C. 5) Reconstruct the cantilever signal as a sum of all DHO, Figure 1D. In particular, the WT allows to retrieve, for each mode, the amplitude, the decay constant and the frequency. Further, the XWT analysis retrieves the phase relative to the sinc function at a specific time, usually at the beginning of the time period of interest. With this infor-

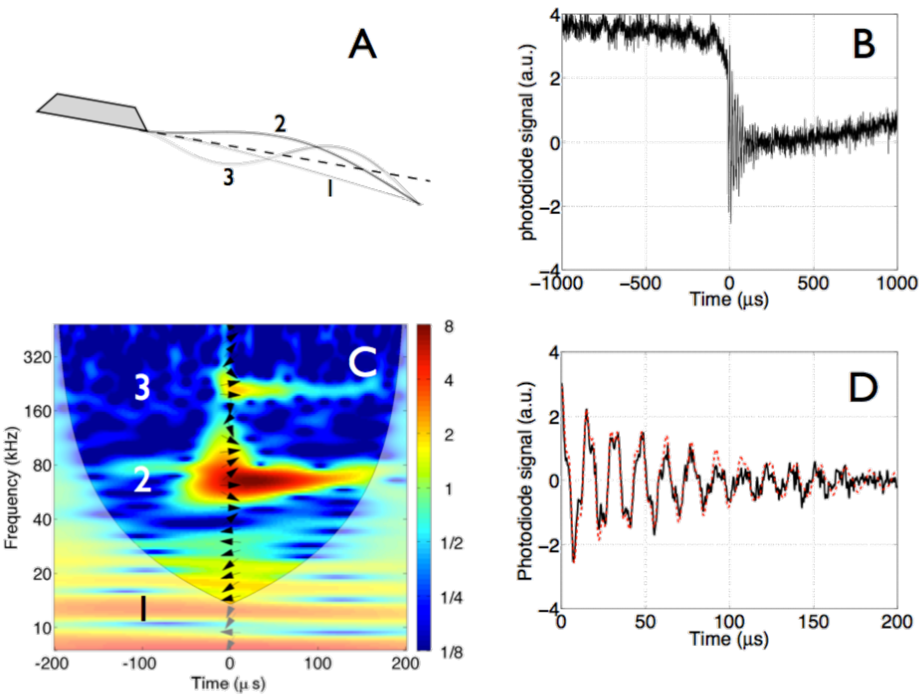

Figure 1: Synthesis of the wavelet retrieval method. (A) Schematic diagram of the modal shapes of the cantilever flexural modes. (B) The time evolution of the relaxation oscillations after the cantilever jump-to-contact transition. (C) The wavelet analysis of the relaxation oscillations. The numbers refer to the excited flexural modes of the cantilever, schematized in (A). Note that the fundamental mode does not oscillate because after the lever remains statically bent after the jump-to-contact. The slope of the arrows arranged in a vertical row superposed on the wavelet spectra measures the local phase difference between the signal and the reference sinc function at time zero. The phase difference has been calculated through wavelet cross-correlation, as explained in the text. Arrow pointing right: 0°; up: 90°; left: 180°; down: −90°. The areas, in which edge artifacts may distort the picture, are delimited by a lighter shade. (D) A reconstruction (red-dotted line) of the relaxation oscillations (continuous black line) obtained by the superposition of damped harmonic oscillators as detailed in the text. This figure is based on adapted versions of Figures 5a, 6, and the inset of Figure 2 in [5].

mation, following the superposition principle, it is possible to sum the contributions of the DHO and reconstruct the signal obtained from the beam deflection apparatus measuring the cantilever dynamics.

Note that the first free flexural mode does not contribute to the dynamics that we are analyzing, because it remains bent statically towards the surface after the jump-to-contact transition. The excited modes have frequencies that scale nearly as the second and third free flexural modes (see Table 1) and contribute to the relaxation oscillations that are seen in Figure 1. For these reasons the excited modes will be labeled as second and third mode. The reconstruction of the photodiode signal does not yet represent the effective displacement of the cantilever tip because of the characteristics of the beam-deflection apparatus, which is used in the experiments.

Table 1: Calculated free flexural frequencies [16] and experimental frequencies of the excited flexural modes given in units of the first free flexural frequency f_1 = 11.7 kHz. The theoretical scaling for the force constants (k_i) is reported for each flexural mode [1].

eigenmode *i*	f_i/f_1 (theo.)	f_i/f_1 (exp.)	k_i/k_1 (theo.)
1	1	1	1
2	6.27	5.58	39.3
3	17.55	17.73	308

Usually the deflection signal measured from the cantilever does not relate directly to the tip displacement, this is the case only when calibrated interferometers are used. Other techniques monitor the velocity through a Doppler velocimeter or the bending of the cantilever when using the popular beam-deflection method. The purpose is to relate the signal measured by the instrument (and reconstructed by the DHO) to the real tip deflection. In the beam-deflection method used in this experiment, the measured signal is proportional to the cantilever bending at the position of the laser spot, usually at the end of the cantilever. While the InvOLS of the first free flexural mode, which relates the bending of the cantilever to the deflection of the tip, is calibrated by using a static force curve, those of the higher modes are not. For the same tip deflection, the higher the mode the higher the bending of the cantilever end. This means that the InvOLS of the first free flexural mode must be corrected to relate the measured bending that is caused by higher modes to the corresponding tip deflections. This is done by means of the optical sensitivities σ_i reported in Table 2. This procedure allows to obtain the parameters of the DHO needed to reconstruct the cantilever deflection mode by mode. The parameters that are used to reconstruct the excited DHO mode dynamics, here labeled as the second and third mode, and hence the total tip deflection are reported in Table 2. Once the deflections of the second and third modes have been quantified, it is possible to access the velocity and acceleration of the tip caused by each flexural mode. We note that the description of the dynamics by using uncoupled DHO during the jump-to-contact is justified, because from experiment we do not have any hints of a non-linear coupling between the modes, and two uncoupled DHO are sufficient to reconstruct the detail of the experimental trace. In addition, and contrary to intuition, the second and third modes are not contact modes. This is proved by their frequency scaling, which is similar to that of free flexural modes and differs considerably from that of a pinned cantilever. For a discussion on this point we refer the reader to [5].

Table 2: Optical sensibilities σ_i and the damped harmonic oscillator parameters used for the reconstruction of the tip trajectory [5].

eigenmode *i*	σ_i (theo.)	z_{0_i} (nm)	τ_i (μs)	f_i (kHz)	ϕ_i (deg)
1	1	—	—	—	—
2	3.4731	0.66	70	65.3	−5.4
3	5.706	0.12	70	207.5	−19.7

Energy dissipation

The energy balance of each decaying mode obtained from Equation 4 in the time window $0 < t < \tau = 200$ μs (see Figure 1) can be written as

$$E_{b_i} = E_{\gamma_i} \tag{5}$$

where

$$\begin{aligned} E_{b_i} &= \Delta K_i + \Delta U_i E_{\gamma_i} \\ E_{\gamma_i} &= \int_0^\tau m_{\mathrm{eq}} \gamma_i v_i^2 dt \end{aligned}$$

i is the index of the mode, $\Delta K_i = 1/2\ m_{\mathrm{eq}}(v_i(0)^2 - v_i(\tau)^2)$ is the variation of kinetic energy, and $\Delta U_i = 1/2\ k_i(z_i(0)^2 - z_i(\tau)^2)$ is the variation of elastic potential energy. The energy balance described in Equation 5 has terms that depend on the balance of potential and kinetic energy on the left hand side (E_{b_i}) and on the time-integrated dissipative power on the right hand side (E_{γ_i}). We note that the elastic force of the cantilever is a conservative force that does not contribute to the dissipation. The dissipative constants γ_i are parameters that take into account the influence of the external environment, which is modeled as a viscous force. Dissipation is intrinsically difficult to explain microscopically in situations in which the ambient environment is complex (presence of gas molecules, water layers, etc.) but interesting since it potentially carries information on the tip–sample interactions.

Since the coefficients γ_i and k_i are measured/estimated independently, the energy balance described in Equation 5 is a test of the internal consistency of the model. In our previous work [5], we took the elastic constants of the higher modes equal to the values calculated by the scaling from beam theory, see Table 2. The equivalent mass (m_{eq}) of a rectangular cantilever is derived to be the same for all modes and equal to one quarter of the cantilever mass (m_{c}), as discussed in [17]. When the energy balance is calculated by using these parameters in Equation 5, a discrepancy in the energy balance of the second mode emerges. The variation of total energy (E_{b_2} = 7.8 eV) does not match the integrated dissipation (E_{γ_2} = 6 eV).

Another way to assess the consistency of the model is to use the total-force test, which means to compare the total forces acting on the tip calculated via the inertial mass $F_m = m_{\text{eq}}\ddot{z}$ with the total forces calculated via stiffness and dissipative forces $F_\gamma = -k_2z_2 - k_3z_3 - m\gamma v_2 - m\gamma v_3$. In this case a good match was obtained [5]. This means that even if the level of agreement in the total-force test appears to be satisfactory, the more stringent energy balance test singles out a discrepancy. The reason of the discrepancy in the energy balance is attributed to a different degree of interaction of the higher cantilever eigenmodes with the surface forces. It is well known that a force gradient at the sample surface modifies the equivalent stiffness of an interacting cantilever, by shifting the resonance frequency to lower values for attractive interactions [18]. In this case one must consider that the effective stiffness of the cantilever is not that of a free cantilever, as is implicitly assumed by using the stiffness scaling from beam theory.

The elastic constant of each mode is connected to the resonant frequency of the mode as $k_i = m_{\text{c}}/4\omega_{0_i}^2$, where i is the mode index. Since in this case the resonant frequency seen in the wavelet transform, see Figure 1, is that of the interacting cantilever, one would expect that the cantilever stiffness calculated by using the equivalent mass and the resonant frequency should incorporate the effects of the surface force gradients. In the present case, the scaling from beam theory of the elastic constant is respected with good approximation for the third mode but not for the second, as reported in Table 3. In order to obtain a good matching with the integrated dissipation, the equivalent stiffness of the second mode has to be taken equal to $m_{\text{c}}/4\omega_{0_2}^2$. The overall quality of the match of F_{m} vs F_γ improves and we obtain a very good agreement of the total variation of energy (E_{b_i}) and integrated dissipation (E_{γ_i}) for both modes, as reported in Table 3.

Having a general consistence regarding the energy conservation, we can correctly estimate the dissipated energy per cycle in each eigenmode, which is obtained as the difference between the maximum elastic energy stored in successive cycles, shown in Figure 2. As expected the energy dissipated per cycle in the two eigenmodes contributing to the cantilever dynamics decays exponentially. The quantification of the dissipation per mode evidenced a rather gentle interaction, with a total energy released from the tip of the order of 8 eV during the impact, considering that typical tapping mode interactions release energies per tap on the order of several tens of eV [19]. Moreover,

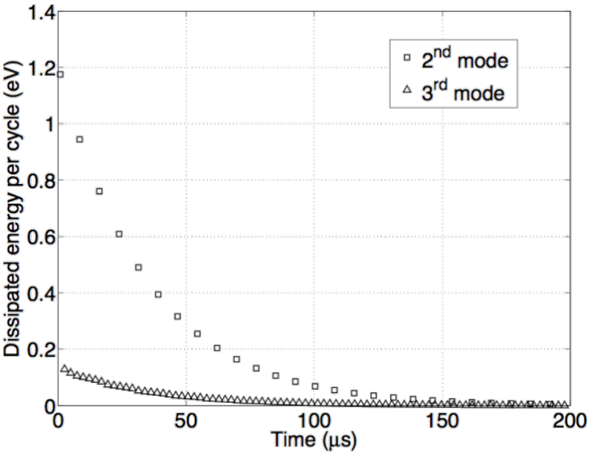

Figure 2: Dissipated energy per cycle vs time in each mode contributing to the dynamics described in Figure 3.

Table 3: Total dissipated energy calculated by a balance of potential and kinetic energy (E_{b_i}) and by integrating the dissipative forces (E_{γ_i}). Quality factors are derived as $Q_i = 2\pi f_i/\gamma_i$, where the damping coefficient $\gamma_i = 2/\tau_i$, see Table 2). Finally, the elastic constant derived from the theoretical scaling (k_i, see Table 1) and from the oscillator parameters ($m_{\text{c}}/4\omega_{0_i}^2$).

eigenmode i	E_{b_i} (eV)	E_{γ_i} (eV)	γ_i (10^4 s^{-1})	Q_i	k_i (N/m)	$m_{\text{c}}/4\omega_{0_i}^2$ (N/m)
2	5.97	5.97	2.85	14	5.9	4.4
3	2.00	1.98	2.85	45	46.2	44.5

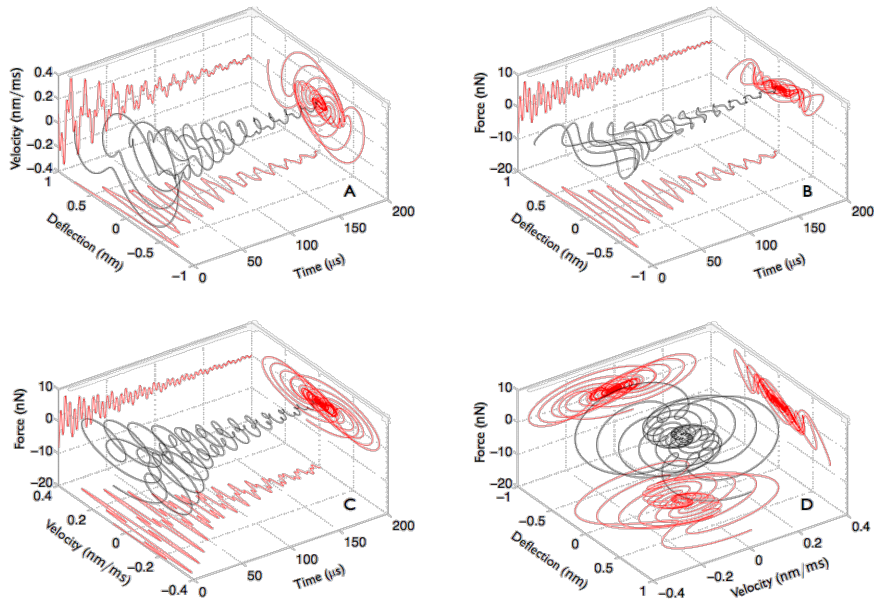

Figure 3: 3D-representation of the main observables describing the tip dynamics during the jump-to-contact transition. (A) deflection–velocity , (B) deflection–force and (C) velocity–force phase-spaces evolving in time. (D) Force vs velocity vs displacement phase-space representation.

the maximum energy released in a single cycle during the impact does not exceed 1.2 eV for the second mode and 130 meV for the third mode. The energy is released by eigenmodes characterized by different oscillations frequencies, thus opening the possibility to resonant energy transfer to samples or (nano)structures endowed with mechanical resonances at the eigenmode frequencies.

Finally, Figure 3 shows the evolution of the instantaneous deflection (z), force (F) and velocity (v) as a function of time in various 3D representations and a comprehensive representation of the phase-space of the motion. The spiraling trajectories are connected to and are a visual representation of the dissipated energy. Figure 3A is a representation of the displacement–velocity phase-space evolving in time. Figure 3B and Figure 3C are connected to the total instantaneous work ($F \cdot dz$) and power ($F \cdot v$), respectively, done on the tip during its displacement dz from time t to time $t + dt$. Figure 3D is a representation of the phase space parameters F, v, z.

Conclusion

The present work demonstrated the possibility to access the dissipated energy per cycle of each excited flexural mode excited during a jump-to-contact transition. The rationale is based on the reconstruction of the tip dynamics in the time–frequency space by a cross-correlation wavelet technique. Furthermore the instantaneous displacement, velocity and acceleration of a cantilever tip that impacts onto a graphite surface were reconstructed. The prospect of analyzing the dissipated energy of every single mode participating in a few cycle interaction during an impulsive tip–sample interaction will be of impact in many respects. An additional implementation of scanning probe imaging, which comprises the analysis presented here for every pixel, will add spatio-temporal imaging capabilities for each excited mode. Under a technical stand point, tip–sample interactions of only few cycles duration reduce the acquisition time and allow for a multiparameter analysis. The latter will increase the physical information gained by the tip–sample interaction. Nonlinear interactions are extremely sensitive to small changes in the tip–sample interactions. Their exploitation will therefore improve the sensitivity to compositional contrast and/or chemical environment. The methodology presented here will be beneficial to other fields that exploit impulsive force phenomena. Impulsive displacement fields in nanostructures, which are generated by ultrafast acoustic techniques, have recently been suggested in applications that range from mass-sensing [20] to nanometrology of thin films and embedded nanostructures. These applications are based on elastic multi-mode excitations that last few oscillations [21]. In this context the present analysis will enlarge the space of parameters to be exploited for the sensing action. Moreover, the techniques outlined in this work will find applications in a variety of fields of interest for nanotechnology. Few-cycle AFM will be useful to characterize the mechanical contact properties of nanostructures produced by femtosecond laser ablation [22], while wavelets techniques will be of relevance in inspecting the time dynamics of oscillatory modes and their phase relations in picosecond acoustic measurements.

Acknowledgements

This work has been partially supported by the Università Cattolica del Sacro Cuore through D.2.2 grants and the Fondazione Cariplo through grant ID 2011-0387 Controlled Nanostructures.

References

1. Garcia, R.; Herruzo, E. T. *Nat. Nanotechnol.* **2012,** *7,* 217. doi:10.1038/nnano.2012.38
2. Jesse, S.; Kalinin, S. V.; Proksch, R.; Baddorf, A. P.; Rodriguez, B. J. *Nanotechnology* **2007,** *18,* 435503. doi:10.1088/0957-4484/18/43/435503
3. Arlett, J. L.; Myers, E. B.; Roukes, M. L. *Nat. Nanotechnol.* **2011,** *6,* 203. doi:10.1038/nnano.2011.44
4. Bhushan, B., Ed. *Handbook of Nanotechnology;* Springer-Verlag: Berlin Heidelberg, 2010. doi:10.1007/978-3-642-02525-9
5. Pukhova, V.; Banfi, F.; Ferrini, G. *Nanotechnology* **2013,** *24,* 505716. doi:10.1088/0957-4484/24/50/505716
6. Garcia, R.; Gómez, C. J.; Martinez, N. F.; Patil, S.; Dietz, C.; Magerle, R. *Phys. Rev. Lett.* **2006,** *97,* 016103. doi:10.1103/PhysRevLett.97.016103
7. Mallat, S. G. *A Wavelet Tour of Signal Processing;* Academic Press, 1999.
8. Malegori, G.; Ferrini, G. *Beilstein J. Nanotechnol.* **2010,** *1,* 172. doi:10.3762/bjnano.1.21
9. Malegori, G.; Ferrini, G. *Nanotechnology* **2011,** *22,* 195702. doi:10.1088/0957-4484/22/19/195702
10. Banfi, F.; Ferrini, G. *Beilstein J. Nanotechnol.* **2012,** *3,* 294. doi:10.3762/bjnano.3.33
11. Sader, J. E.; Chon, J. W. M.; Mulvaney, P. *Rev. Sci. Instrum.* **1999,** *70,* 3967. doi:10.1063/1.1150021
12. Malegori, G.; Ferrini, G. *J. Vac. Sci. Technol., B* **2010,** *28,* C4B18. doi:10.1116/1.3305452
13. Higgins, M. J.; Proksch, R.; Sader, J. E.; Polcik, M.; Mc Endoo, S.; Cleveland, J. P.; Jarvis, S. P. *Rev. Sci. Instrum.* **2006,** *77,* 013701. doi:10.1063/1.2162455
14. Butt, H. J.; Cappella, B.; Kappl, M. *Surf. Sci. Rep.* **2005,** *59,* 1. doi:10.1016/j.surfrep.2005.08.003
15. Landau, L. D.; Lifshitz, E. M. *Mechanics,* 3rd ed.; Elsevier Butterworth-Heinemann: Oxford, 1976; p 75.
16. Butt, H.-J.; Jaschke, M. *Nanotechnology* **1995,** *6,* 1. doi:10.1088/0957-4484/6/1/001
17. Melcher, J.; Hu, S.; Raman, A. *Appl. Phys. Lett.* **2007,** *91,* 053101. doi:10.1063/1.2767173
18. Morita, S.; Wiesendanger, R.; Meyer, E., Eds. *Noncontact Atomic Force Microscopy;* Springer: Berlin, 2002. doi:10.1007/978-3-642-56019-4
19. Cleveland, J. P.; Anczykowski, B.; Schmid, A. E.; Elings, V. B. *Appl. Phys. Lett.* **1998,** *72,* 2613. doi:10.1063/1.121434
20. Nardi, D.; Zagato, E.; Ferrini, G.; Giannetti, C.; Banfi, F. *Appl. Phys. Lett.* **2012,** *100,* 253106. doi:10.1063/1.4729624
21. Nardi, D.; Travagliati, M.; Siemens, M. E.; Li, Q.; Murnane, M. M.; Kapteyn, H. C.; Ferrini, G.; Parmigiani, F.; Banfi, F. *Nano Lett.* **2011,** *11,* 4126. doi:10.1021/nl201863n
22. Cavaliere, E.; Ferrini, G.; Pingue, P.; Gavioli, L. *J. Phys. Chem. C* **2013,** *117,* 23305. doi:10.1021/jp406603q

License and Terms

Beilstein Journal
of Nanotechnology

Calibration of quartz tuning fork spring constants for non-contact atomic force microscopy: direct mechanical measurements and simulations

Jens Falter*[1,2], Marvin Stiefermann*[1,2], Gernot Langewisch[1],
Philipp Schurig[2], Hendrik Hölscher[3], Harald Fuchs[1,4]
and André Schirmeisen[2]

Full Research Paper

Open Access

Address:
[1]Center for Nanotechnology (CeNTech) and Institute of Physics, University of Münster (WWU), Heisenbergstrasse 1, 48149 Münster, Germany, [2]Institute of Applied Physics (IAP), Justus-Liebig-University Gießen, Germany, [3]Institute of Microstructure Technology (IMT), Karlsruhe Institute of Technology (KIT), Hermann-von-Helmholtz Platz 1, 76344 Eggenstein-Leopoldshafen, Germany and [4]Institute of Nanotechnology (INT), Karlsruhe Institute of Technology (KIT), Hermann-von-Helmholtz Platz 1, 76344 Eggenstein-Leopoldshafen, Germany

Email:
Jens Falter* - Jens.Falter@Uni-Muenster.de; Marvin Stiefermann* - Marvin.Stiefermann@ap.physik.uni-giessen.de

* Corresponding author

Keywords:
atomic force microscopy; calibration; instrumentation

Beilstein J. Nanotechnol. **2014,** *5,* 507–516.
doi:10.3762/bjnano.5.59

Received: 31 January 2014
Accepted: 26 March 2014
Published: 23 April 2014

This article is part of the Thematic Series "Noncontact atomic force microscopy II".

Guest Editors: U. D. Schwarz and M. Z. Baykara

Abstract

Quartz tuning forks are being increasingly employed as sensors in non-contact atomic force microscopy especially in the “qPlus” design. In this study a new and easily applicable setup has been used to determine the static spring constant at several positions along the prong of the tuning fork. The results show a significant deviation from values calculated with the beam formula. In order to understand this discrepancy the complete sensor set-up has been digitally rebuilt and analyzed by using finite element method simulations. These simulations provide a detailed view of the strain/stress distribution inside the tuning fork. The simulations show quantitative agreement with the beam formula if the beam origin is shifted to the position of zero stress onset inside the tuning fork base and torsional effects are also included. We further found significant discrepancies between experimental calibration values and predictions from the shifted beam formula, which are related to a large variance in tip misalignment during the tuning fork assembling process.

Introduction

Atomic force microscopy (AFM) allows the imaging of surfaces with true atomic resolution and the resolution of intra-molecular structures of molecules [1]. Furthermore, the non-contact AFM (nc-AFM) technique has the capability of quantifying the interaction forces acting between the probing tip and the sample site with atomic precision. Recent achievements of this force spectroscopy method manifest in the identification of the chemical identity of single atoms in an alloy [2] or the measurement of the force applied during the controlled manipulation of molecules or atoms on a surface [3,4]. nc-AFM experiments at the atomic scale usually demand well defined environments, such as ultrahigh vacuum (UHV) and low temperatures (LT). For these conditions, force sensors based on quartz tuning forks in the "qPlus" design [5] have been proven to routinely provide stable operation and sufficient sensitivity to achieve the highest resolution in nc-AFM experiments. Today, many commercially available AFMs for UHV and LT conditions are based on quartz sensors because of their impressive performance and easy technical implementation.

Common AFM sensors are microfabricated from silicon or silicon nitride with the tip already integrated. Their spread in geometric parameters is within a low range and the characterization of their geometric parameters has been presented extensively by theory and experiments [6-8]. Quartz tuning fork force sensors in contrast are usually hand-made and even though they are commercially available, they are far from mass production and therefore exhibit a large spread of geometric – and thus of elastic parameters. Especially the precise knowledge of the sensor stiffness k_{qPlus} is crucial for quantitative interpretation of force spectroscopy measurements. Early spectroscopy experiments compared relative forces with high accuracy, for which the absolute stiffness of the sensor was not critical. Latest measurements of the absolute interaction forces impress by their force resolution [3,4,9] but suffer from the large error and spread in the determination of the geometric factors of the "qPlus" sensors. The stiffness of the force sensor is necessary for the transformation of the experimental frequency shift data, Δf, to forces. Consequently, a force measurement can only be as precise as the determination of each factor in the equation that links the frequency shift to the tip–sample forces [8,10,11]. To calculate the force-vs-distance curve from measured frequency shift-vs-distance data, the inversion of the dependence of the frequency shift on the tip–sample forces has been derived [11-14] with high accuracy. All those formulas contain the stiffness of the sensor k_{qPlus} as prefactor and therefore directly suffer from an inaccurate determination of the spring constant.

Here we present an experimental procedure that allows for the direct measurement of the stiffness of a tuning fork sensor in the "qPlus" design with standard lab equipment. Our results reveal that a large spread of stiffness exists even in a series of commercially sold sensors. This finding underpins the urge of the individual characterization of each sensor. The standard equation [15] to calculate the stiffness from the geometric dimensions is the beam formula. Comparison of our experimental results with the formula show large discrepancies up to a factor of 5. In the next step we use extensive finite element method (FEM) modeling of the precise geometry of the tuning fork sensor in order to understand these deviations. The simulations show quantitative agreement with the beam formula if the beam origin is shifted to the position of zero stress onset inside the tuning fork base and torsional effects are included as well. Comparison with experimental spring constant data still show that the spring constant is overestimated by FEM and beam formula. This effect is attributed to a small but not negligible angle between the tip wire axis and the surface normal of the tuning fork prong.

Results and Discussion

Experiment

The quartz tuning fork, originally used as frequency normal in wrist watches constitutes the centerpiece of a force sensor in the "qPlus" design. Figure 1 shows micrographs from scanning electron microscopy (SEM) of a bare tuning fork (type DS26, Micro Crystal AG, Switzerland). These tuning forks are microfabricated from piezoelectric quartz, which is electrically contacted by gold electrodes placed onto the quartz substrate. The dimensions of the tuning fork can be easily measured by using SEM images as illustrated in Figure 1a and Figure 1b. The tuning fork has an overall length of l_{TF} = 3548 µm and a height of h_{TF} = 651.4 µm at the widest point while the substrate has a thickness giving the tuning forks width of w_{TF} = 120.8 µm and a prong thickness of t_{TF} = 207.3 µm. Figure 1c was taken from a derivative of the same type of tuning fork which differs only by the absence of notches at the basis compared to the tuning fork in panels a) and b) (compare arrows in panel a)). At this point it should be noted that all experiments and simulations presented here were carried out for both types (with and without notches). However, no differences were found in the stiffness of the sensors of the two types and therefore only one set (without notches) is presented here. In the "qPlus" design of nc-AFM force sensors, one prong and the end of the basis are fixed onto a carrier (usually from Macor) with epoxy glue. This type of fixation breaks the original quadrupole symmetry, in which both prongs oscillate around a forceless point that is found within the quartz body between the prongs. A very sharp tip etched from metal wire is attached to the end of the free prong, again with epoxy glue.

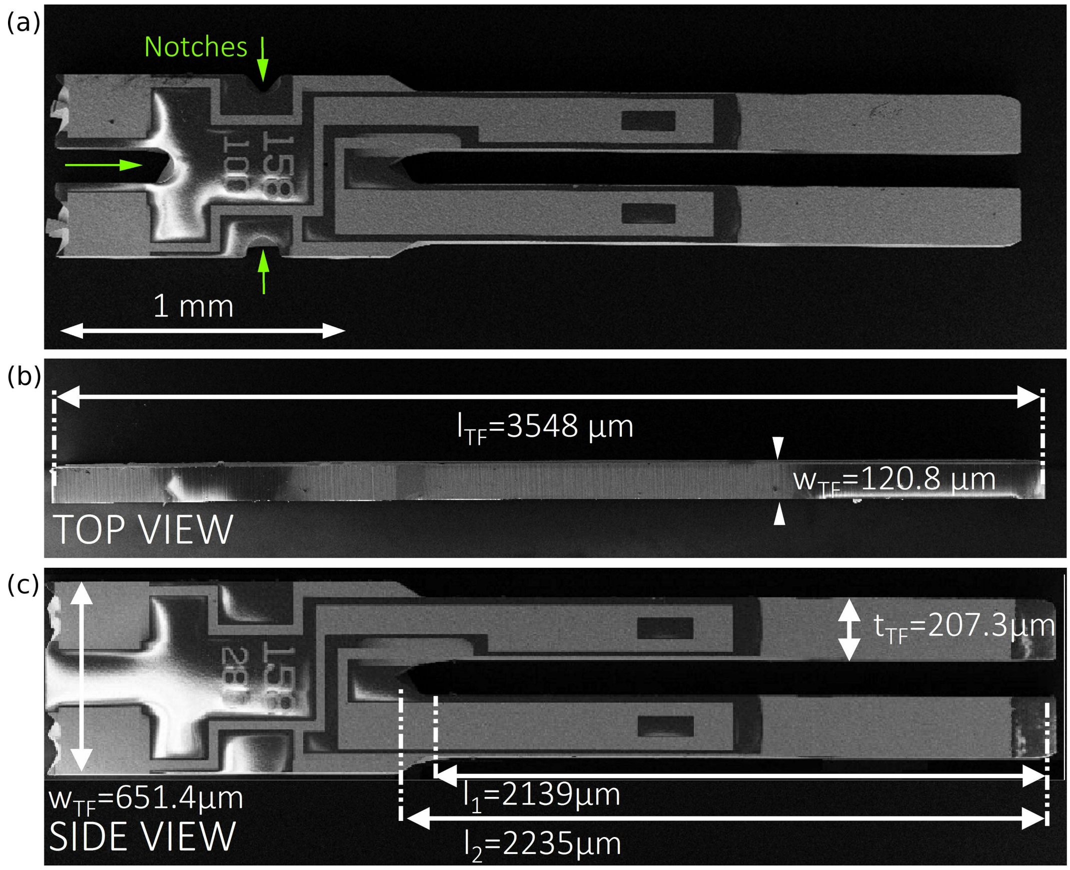

Figure 1: Determination of the geometric dimensions of a quarts tuning fork (Micro Crystal, type *DS*26 used for “qPlus”-force sensors from SEM images. (a) Sideview of tuning fork made from quartz with notches (cf. arrows) at the basis. (b) Topview of the tuning fork for measureing its width by the wafer thickness. (c) Sideview of an alternative geometric layout of DS26-type tuning fork without notches at the basis.

Commonly, spring constants of k_{qPlus} = 1800–2000 N/m are used for the force transformation. These values are estimated from the geometric dimensions of the free prong of the tuning fork and the Young’s modulus of quartz by using the beam formula according to Equation 1 [16].

$$k_{\text{beam}} = E_{\text{quartz}} \frac{w}{4} \left(\frac{t}{\Delta L} \right)^3 \qquad (1)$$

In this equation w and t are the width and thickness of the free prong, respectively and E_{quartz} is the Young’s modulus of quartz. The limitations for the validity of this formula are small deformations leading to only elastic stress/strain inside the uniform, rectangular cross section of the beam, which consists of isotropic material and is rigidly fixed at the end. These conditions are not necessarily fulfilled for a real tuning fork sensor. Since the tip wire is not necessarily placed at the very end of the prong, $\Delta L = L - L_0$ denotes the effective length of the free beam, i.e., the wire position L along the prong with respect to the beam origin L_0. The comparison with Figure 1a shows that a certain ambiguity exists in the position of this beam origin L_0. At the beam base the cross-section of the prong broadens before ending into the rigid basis. We here choose the point before the broadening as the zero point L_0 as it is commonly done in the nc-AFM literature in order to avoid inaccuracies in later discussions. Inserting our measured values of ΔL_1 = 2139 µm, w = 207.3 µm and t = 120.8 µm into Equation 1 together with the Young’s modulus of quartz of E_{quartz} = 78.7 GPa results in a stiffness of the free prong of k_{qPlus} = 1898 N/m. This is within the range of reported spring constant values k_{qPlus} = N/m [5] and k_{qPlus} = 2000 N/m [9], while the latter was calculated with a different Young’s modulus of E_{quartz} = 79.1 GPa to correct for the non-orthogonal crystallographic cut through the substrate of the tuning forks.

However, the underlying models of these calculations are barely in agreement with the actual geometry of real “qPlus” sensors, in which the force is applied through a metal wire glued onto the free prong. Therefore, the force application point is defined by the position of the glue point. Since these sensors are handmade it is obvious that the length ΔL cannot be regarded as constant for all sensors. The broadening of the beam towards the basis and the unknown Young's modulus of the material limit the usage of the beam formula for the description of the tuning fork stiffness. Even influences of the glue, which is used to fix the tuning fork onto its holder, and the resulting spread in the individual stiffness of these sensors have recently been reported [17]. Possible methods to determine the stiffness are adding some mass to the prong and analyze the change of the dynamic oscillation [15] or static deflection [17,18] of the cantilever. Alternatively, the stiffness can be estimated from thermal excitation [19]. Here we employed a very simple and easily implementable method to measure the stiffness of the tuning fork sensors by only using a micrometer screw and a scale. The setup for such a measurement is shown in Figure 2.

In order to validate this measurement method we assembled a test sensor similar to the "qPlus" sensor setup. In the same way as in a "qPlus" sensor, a quartz tuning fork was glued onto a Macor body, and a tungsten wire with a diameter of $d_{\text{W-wire}} = 50$ µm was glued onto the free prong. This sensor is mounted onto a traverse, which can be lowered by a micrometer screw (Mitutoyo, type 110-164) with an accuracy of $\Delta z = 5$ µm. Below the moveable traverse, a scale is placed (KERN & Sohn GmbH, type: KB 120-3) with a mass resolution of $\Delta m = 1$ mg. The force applied to the scale is then calculated by multiplying the weight with the gravitation constant $g = 9.81$ m/s^2 resulting in an accuracy of the force measurement of 9.81 µN. The stiffness of the sensor can now be measured by pushing the sensor onto the scale with the micrometer screw while simultaneously measuring the weight increase on the scale. By lowering the end of the wire into a fresh droplet of Torr Seal epoxy glue, it can be mechanically fixed onto a glass substrate resting on the scale (cf. Figure 2, inset). After the glue is cured out at room temperature, the stiff-

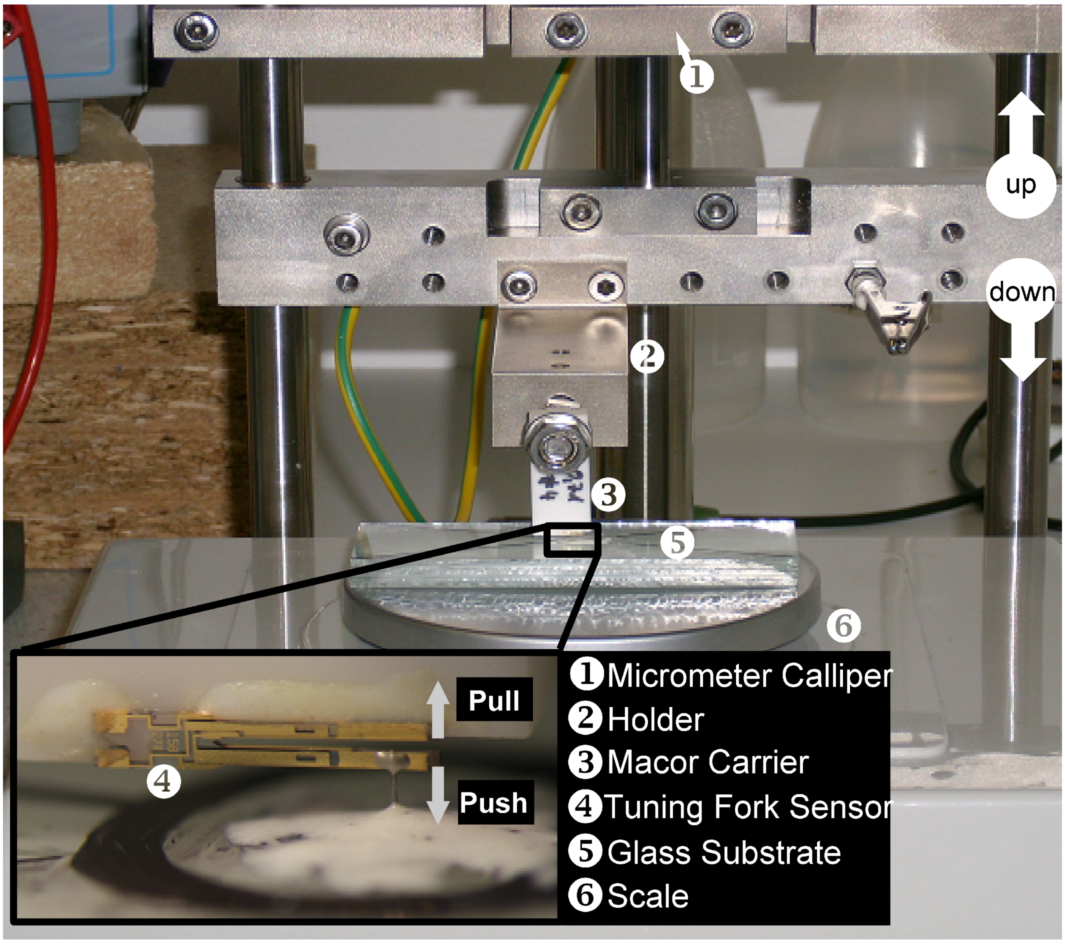

Figure 2: Photograph of the experimental setup. Not shown in the picture is the micrometer screw 1, which pushes or pulls the whole setup towards or from the scale. The Macor body 3, carrying the tuning fork sensor 4 is fixed to the holder 2. The inset shows a close-up of the tuning fork. The tuning fork is glued onto a Macor basis as in actual force sensors while the wire tip at the free prong is glued to a glass substrate. Latter transfers the force to the scale and delivers the mass for also pull the sensor away from the scale.

ness can be measured in both directions, pushing (increasing mass on scale) or pulling (decreasing mass on scale). Please note that during a pull-experiment under the present conditions the relative elongation of the tungsten wire remains lower than 0.1% and is therefore neglected in the further analysis. A reference experiment was performed with a bare Macor carrier (without tuning fork) to measure the stiffness of the experimental setup k_{setup} (mainly the compliance of the scale), which was in our case $k_{\text{setup}} = 5952$ N/m. The stiffness of the tuning fork can then be evaluated by Equation 2 representing a series of both stiffnesses.

$$k_{\text{tuningfork}} = \left(\frac{1}{k_{\text{measurement}}} - \frac{1}{k_{\text{scale}}}\right)^{-1} \qquad (2)$$

With the setup described above, the stiffness of the bare tuning fork was measured as a function of the position of the force application point, i.e., the tip wire. The diagram in Figure 3 shows data points recorded by pushing at different positions along the tuning fork prong. The deflection of the tuning fork rises with increasing the position of micrometer screw, starting from the point of contact at a position of 20 µm. The stiffness of the sensor can be evaluated by fitting these data by the solid lines within an error of less than 1%. The position was determined from photographs taken through a stereo microscope during the pushing experiment. The result of the position dependence is then compared with the values predicted by the beam formula (Equation 1) while using the effective beam length $\Delta L = L - L_0$ with respect to the force application point L. Table 1 lists the measured stiffness values as well as the values calculated from the beam formula. While for long prongs (large ΔL values), the measurement seems to be roughly within the range of the calculation, for shorter prongs (small ΔL) a drastic discrepancy between the measured stiffness and the calculated value is found (up to a factor of 5 or larger, cf. last column of Table 1).

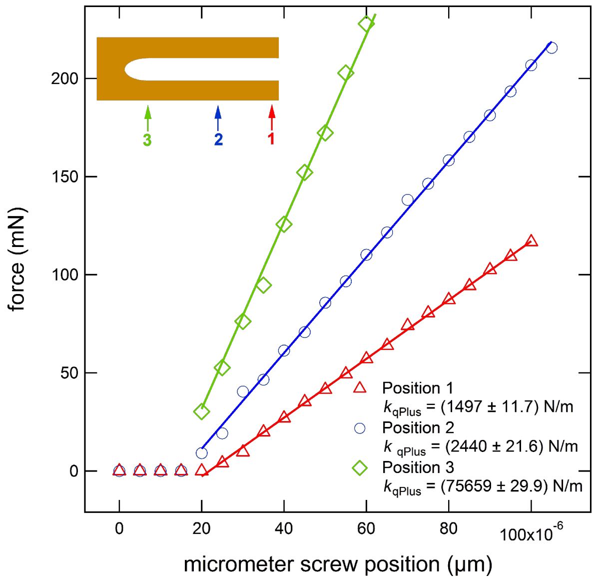

Figure 3: Diagram of a “push” experiment to measure the stiffness of the free prong of a “qPlus” sensor by the slope of the fit to the data points with an error of approx. 1%. The deflection of the prong starts at position 20 µm of the micrometer screw. The spring constant had been calculated in the range of increasing forces. The effective stiffness increases for decreasing effective prong length, i.e., for tip positions located further to the beginning of the prong. The stiffness was calculated from the slope.

In fact, a deviation between the experimental tuning fork stiffness and the beam formula is not unexpected. Previous simulations suggest that the zero point has to be chosen differently as it is commonly done when using the beam formula [20]. These findings motivated our detailed analysis of the mechanical tuning fork properties by FEM using the software Comsol Multiphysics (V 4.1a). In addition to the measurement of “custom-made qPlus” sensors, we also measured the spring constant of “qPlus” sensors from Omicron NanoScience GmbH, Taunusstein. The result is that even these sensors show a significantly high spread of k_{qPlus} = 1480–1708 N/m, which demonstrates the need to calibrate each individual sensor

Table 1: Comparison of the measurement of the stiffness with the calculation using the beam formula for the identical position at the prong.

position (µm)	measured spring constant (“push” experiment) (N/m)	calculated spring constant (beam formula) (N/m)	measured value/calculated value
408	65427	357386	0.18
604	33784	120717	0.27
1062	16150	17799	0.91
1085	6315	20576	0.31
1630	3088	4986	0.62
1653	4135	4719	0.88
1994	2000	2690	0.74
2052	2892	2460	1.18

that is used for quantitative nc-AFM force spectroscopy measurements.

FEM simulations

Special care was taken to make the geometric model of the "qPlus" sensor in the FEM software as realistic as possible, including gluing points as well as a metal tip. As for the tuning fork, an isotropic Young's modulus of E_{quartz} = 78.9 GPa was used. To obtain a realistic value of the Young's modulus of the glue for the FEM simulations, three samples made from "Torr Seal" were tested in a tensile test sample geometry accordant to DIN EN ISO 527 in a tensile test. Two of the Torr Seal samples were cured at a temperature of 100 °C resulting in E_{TorrSeal} = 6500 GPa and 6000 GPa, respectively. The third sample was cured at room temperature (RT) resulting in a Young's modulus $E_{\text{TorrSeal,RT}}$ = 4000 GPa. As our custom-build "qPlus" sensors are cured out in an oven, the value of E_{TorrSeal} = 6000 GPa was used in our FEM simulations for the epoxy glue. The geometry of the simulated model is depicted in Figure 4 in more detail. The sophisticated geometry of different sub-geometries, is meshed by tetrahedral elements, which allow a very fine mesh at the boundary lines as well as the boundary areas between the sub-geometries (in particular at the force application point from the wire through the glue droplet into the free prong).

In the next step a force was applied through the vertical axis of the wire and the displacement of the free prong was analyzed. Interestingly, a closer look at the stress distribution reveals that the stress is reaching several hundred microns into the basis of the tuning fork. Figure 5 shows the stress distribution within the tuning fork caused by a loading force of F_{load} = 1–100 mN, which results in a displacement of the very end of the free prong of x_{end} = 50 µm. Since the tip was attached to the side of the tuning fork, as it is also the case in commercial "qPlus" sensors, the different stress contributions of torsional and normal stress are color coded as the comparative von Mises stress (σ_{VMSmin}). The color code represents stress values from $\sigma_{\text{VMSmin}} = 0$ N/m^2 (red) to maximum values of $\sigma_{\text{VMSmax}} = 2.5 \cdot 10^8$ N/m^2 (violet). The area of onset of stress within the basis is marked by the dashed circle.

This finding suggests that the zero point L_0, as origin for the length of the cantilever, has to be adjusted when calculating the stiffness of a tuning fork by using the simple beam formula. To demonstrate this effect we first plot the stiffness of the tuning fork in Figure 6 using the zero point at the end of the narrow beam, i.e., $L_0 = 0$ as a reference curve. The logarithmic plot shows that the spring constant versus beam length curve (gray curves) does not follow a certain power law, e.g., ΔL^{-3} as expected from Equation 1. For direct comparison we also

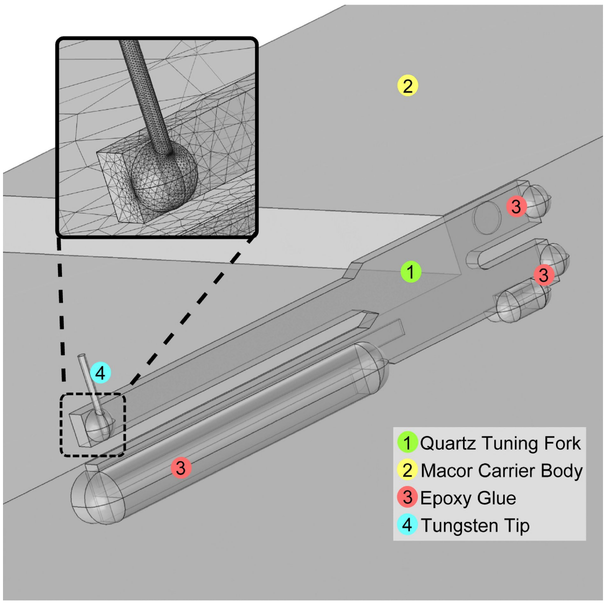

Figure 4: Image of the geometric model reflecting the geometry of an actual "qPlus" sensor. The model includes a tip (4) attached to the free prong with a droplet of epoxy glue, as well as the epoxy glue (3) at the rim and behind the tuning fork (1) fixing it to the Macor carrier (2). The sophisticated geometry is meshed with a tetrahedral elements (cf. inset) to better account for the transition between the individual geometry elements. The material properties were taken from literature, as for the Young's modulus of the epoxy glue, tensile experiments were carried out to determine a realistic value for the crucial connection of the force application point between the metal tip and the prong.

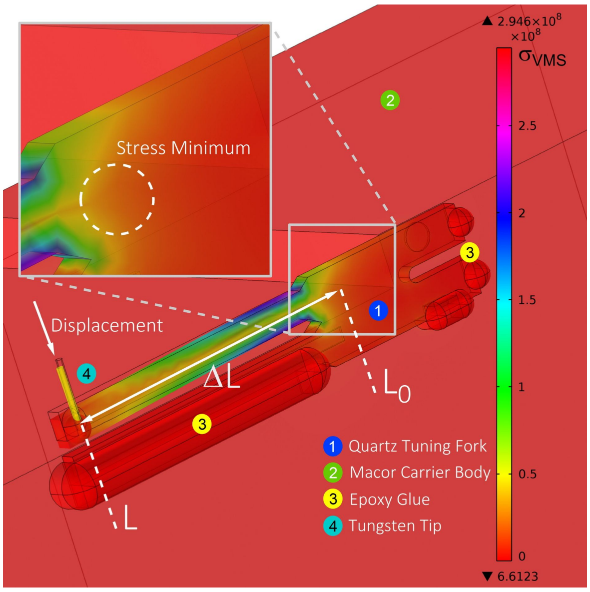

Figure 5: FEM simulation of von Mises stress. Analysis of the stress caused by the bending of the free prong. In contrast to the model for the beam formula, in which a cantilever is fixed at one end, the stress in the quartz tuning fork reaches beyond the end of the prong far into the basis of the tuning fork. The origin of the minimal Van Mises stress is indicated by the dashed circle (see inset).

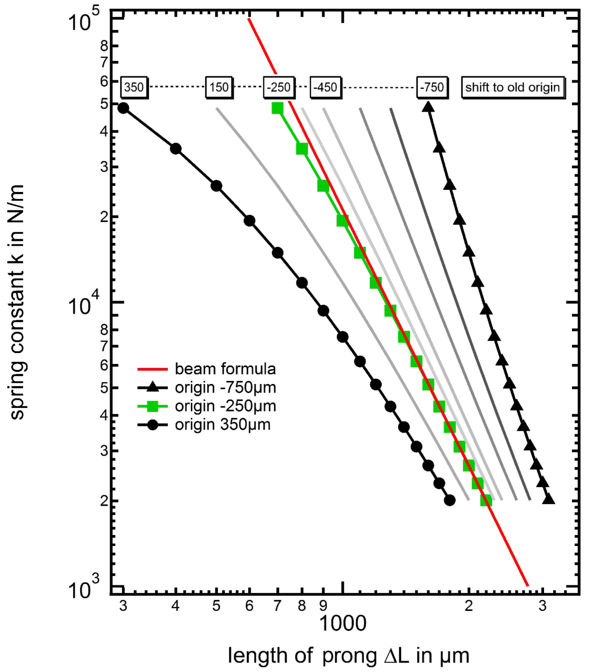

Figure 6: Diagram showing the results of the FEM simulation as a function of the shift of the origin. While for too large or too small chosen positions of the origin the curves show a non linear behavior, the a ΔL^{-3} behavior can be identified in the transition regime for a new effective origin position of approx. $L_0 = -250$ µm.

plotted the results from the beam formula of Equation 1 as a red solid line. Motivated by the non-negligible stress reaching into the tuning fork basis, the results of the FEM simulation are plotted for different beam origins $L_0 + \Delta L_0$ reaching into the base of the tuning fork. The resulting set of curves is plotted in the diagram of Figure 6, where the new effective origin L_0 was adjusted to a range from 350 µm to −750 µm. Here, in the transition regime between the two extreme L_0 positions, a linear behavior can be identified at an effective origin of $L_0 = -250$ µm, which is located “inside” the basis of the tuning fork with respect to the initial origin at $L_0 = 0$. For the new origin $L_0 = -250$ µm we find quantitative agreement between simulations and beam formula for larger tip wire positions $\Delta L > 1500$ µm, which is the case in conventional “qPlus” sensors but also indicates that additional care has to be taken when working with shorter prongs. Only if the tip wire is closer to the basis, some deviations occur, in which the beam formula is systematically overestimating the stiffness. Therefore we conclude that the beam formula can still be used to estimate the tuning fork prong spring constant, if the beam origin is set to the new effective position $L_0 = -250$ µm (for the tuning forks used here) and if the tip wire position is more than 1500 µm away from the origin.

In the following, the still existing deviation between the FEM results and the beam formula, is subject to further investigations. Therefore we simplify our experimental and FEM setup. To eliminate a possible influence caused by the tip, we carried out two separate measurement series to determine the spring constant directly by applying a force onto the top of a tuning fork sensor prong, together with an analogue FEM simulation. The experimental setup and the corresponding results are displayed by the graph and the photograph in Figure 7. The graph shows a high agreement between the FEM and experimental results with the beam formula, clearly identifying the tip as source for the discrepancy discovered in Table 1 and Figure 6. One reasonable explanation for the occurring discrepancy is the additional torsion induced into the prong by the wire attached at the side of the free prong.

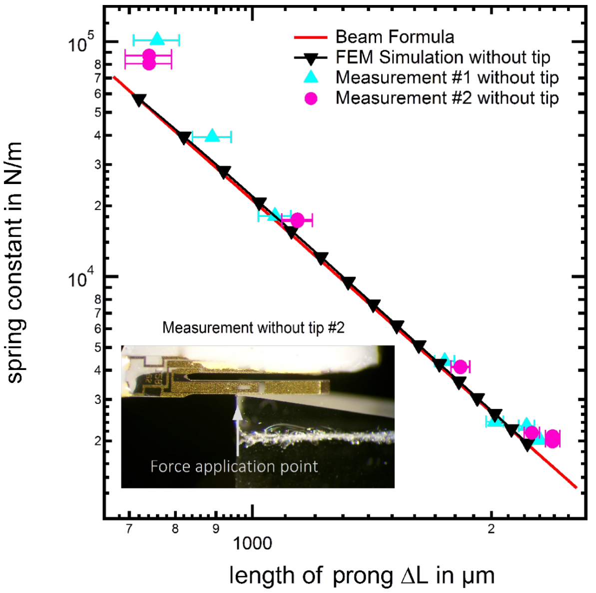

Figure 7: Comparison between the beam formula, experimental measurements and FEM simulation with the force directly applied to the tuning fork prong. The prior introduced origin shift has already been applied to the beam formula resulting in a higher compliance of the plot here.

Subsequently we investigate the influence of torsional motion of the tuning fork prong, which may also play an important role. While the beam formula only considers normal forces applied orthogonal to the axis of the prong, in the “qPlus” sensor configuration, the wire-tip is attached at the side causing a torque around the axis of the beam in addition to the bending of the prong. To evaluate the influence of the torsion, the simulation was repeated with the tip positioned at the center of the prong (indeed some experimentalists attach the wire-tip on the face side of the free prong to avoid torsion during the AFM-experiments). In our FEM simulations the position was chosen with the tip on the top of the prong (TOT), allowing us to vary the position of the force application point, for direct comparison to the results from the tip on side (TOS) configuration, which was discussed so far. Figure 8 shows the result of the FEM simulation in the two configurations, TOS (blue) and TOT (green). While for positions at large beam lengths, the deviation between the two configurations is negligible, in the regime of positions of short beam length values, a deviation can be noticed. The contribution caused by the torsion can be calculated analytically by the following relation [21]:

$$\Phi_t = \frac{TL}{GI_T}, \qquad (3)$$

in which T is the torsional momentum, Φ_t is the angle of twist in radians, L the length at which the force is applied, G the shear momentum and I_T the second momentum of area of the prong. To calculate the exact influence of the torsion to the overall spring constant, the tuning fork has to be seen as a system of two springs (deflection and torsion) connected in series. The red curve in the diagram shows the result from the simulated TOT-configuration where the effect of the torsion is corrected with the above equation. The torsion corrected curve coincides well with the curve simulated for the TOS configuration of the "qPlus" sensor. These results also demonstrate that torsion has a negligible influence at the free end of the prong, since the torsion spring constant is decreasing linearly whereas the deflection spring constant decreases with ΔL^{-3}. Only if the tip is mounted closer to the origin of the tuning fork body, the torsion has an increasing influence on the overall spring constant. This influence results in a smaller increase of the overall spring constant as the torsion spring constant is not increasing as fast as the deflection spring constant. This effect is obvious in the area of smaller ΔL-values, in which the TOS curve shows a recognizably lower spring constant, than the TOT-curve.

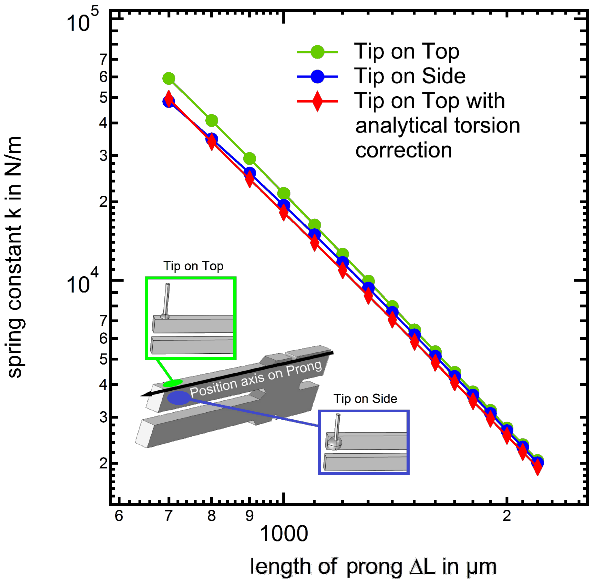

Figure 8: Comparison between tip on side (TOS) and tip on top (TOT) configurations as possible origin of the deviation between FEM Simulation and Experiment. The deviation was found to be larger in case of TOT than the contribution of torsion in the TOS configuration.

Before we proceed by finally comparing the results of the FEM calculations and the modified beam formula with the experimental spring constants, we consider one further important issue related to the hand-made "qPlus" sensor fabrication. Since the wire is glued on the prong, very often a small tilt of the wire long axis with respect to the prong surface normal cannot be excluded. Unfortunately, the torsion caused by the non central fixation of the tungsten wire is increasing, when the wire is not perpendicular mounted to the tuning fork. Therefore we conducted further FEM simulations considering a possible wire axis tilt, with the results shown in Figure 9. This figure demonstrates clearly that even a small misalignment of the wire axis can lead to large deviations of the effective spring constant, in particular for wire fixation points close to the tuning fork base.

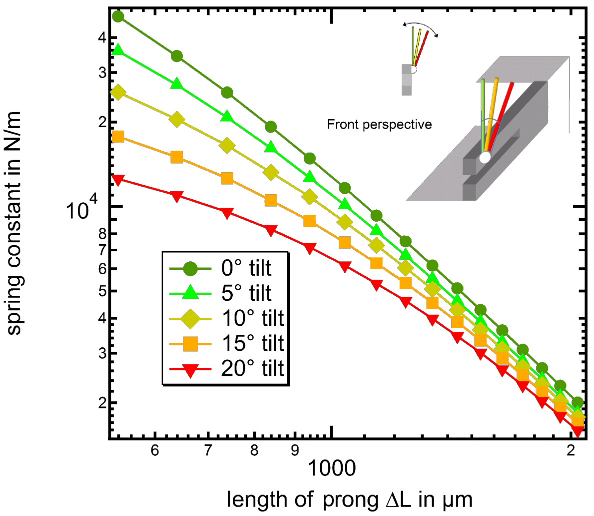

Figure 9: FEM simulation result displaying the influence of a tilted tungsten wire on the resulting spring constant versus a non tilted wire. It is obvious that a strongly tilted tip causes an increasing influence of torsion. Thus during the assembly one should also focus on the angle between tuning fork and wire trying to keep it as small as possible.

As the final step, Figure 10 now displays the comparison between the experimental results (black square markers), the FEM simulations including a small 5° tilt (green triangles) and the modified beam formula (red line). First we note that the experimental spring constant results show a considerable spread, in which almost identical tip positions may still result in differences of a factor of three in the most extreme cases, while differences of 50% are typically found. This spread in the indi-

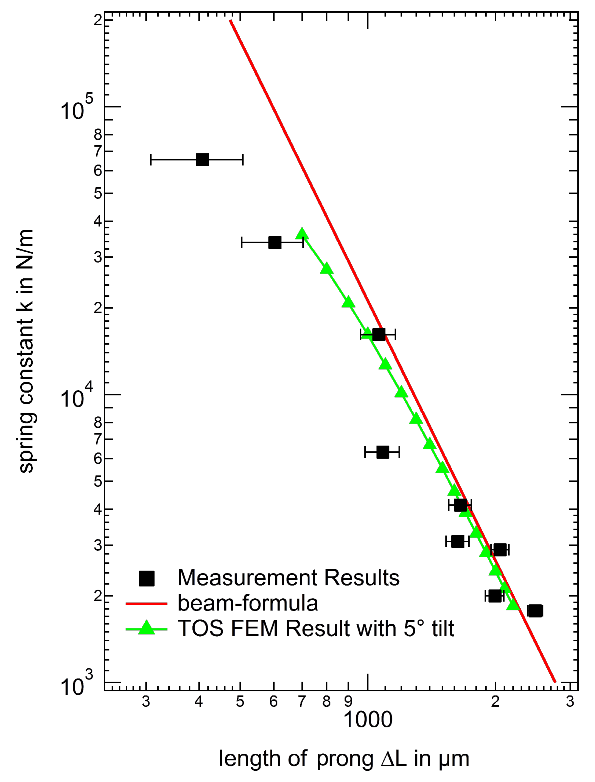

Figure 10: Comparison of the spring constants from experiment with FEM simulations and calculations using the beam formula (with the new origin L_0 = −250 µm for both). The experimental values still shows a deviation from the simulations and calculation respectively. This is possibly caused by some tilt of the sensor towards the force application axis where small angles cannot be completely avoided in the fabrication procedure.

vidual spring constants is most likely due to tip axis misalignment during the “qPlus” fabrication. Even when carefully assembling the tuning fork sensors under optical microscope inspection misalignment angles of up to 10° are common. In fact the spread in spring constants agrees with the range of misalignment angles considered in Figure 9. Despite this scatter in the individual data we find overall that there is a decent agreement between the measured spring constant values and the FEM results with a 5° tilt included, which is a realistic average value for careful manual tip fixation procedures. Furthermore, we can now directly compare how well the origin shifted beam formula agrees with FEM data and experimental values. Again, in the regime of large ΔL values ($\Delta L > 1500$ µm) the agreement between experiment and simulations/beam formula is acceptable, if the shifted origin method is applied. Please note that the scatter between the individual experimental data points is larger than the difference between beam formula and FEM data with 5° tilt angle.

From this section we conclude that using the conventional beam formula for the calculation of the spring constants of tuning forks results in a dramatic overestimation of the beam compliance. However, the origin shifted beam formula can be used to estimate the “qPlus” spring constant for $\Delta L > 1500$ µm. Still in this case a typical error of about 50% remains, which is mainly due to angular misalignment effects during the tip wire fixation to the free prong. For more precise spring constant determination, as required for quantitative force spectroscopy experiments, individual calibration of the used tuning fork sensors after the nc-AFM experiment is mandatory.

Conclusion

A simple method for measuring the spring constant of tuning fork sensors using a micrometer screw and a scale is presented. The experimental results are compared to the beam formula and FEM-simulations revealing the limits of the commonly used models for the determination of “qPlus” sensor stiffness. The combination of finite element method simulation with experimental measurements allows a comprehensive understanding of the spring constant behavior alongside the whole length of the free prong. This knowledge finally opens the opportunity to adapt the beam formula by shifting the origin of the beam formula and thus making it a reliable tool for the spring constant determination in the area around the last millimeter of the prong. Since the beam formula is calibrated by the present study, it can be used for the determination of spring constants of “qPlus” sensors by measuring the effective length between the force application point at the gluing droplet attaching the wire to the prong and the shifted coordinate for the zero point of $\Delta x_0 = -250$ µm into the basis. This length can either be measured from SEM images of tuning fork sensors or even simpler by microscopic photograph. However, the present study reveals that the stiffness of real sensors can differ from the simulations due to deviations between the real tuning fork tip alignment and the ideal FEM model geometry. Whenever a more precise value of the static spring constant is required, due to the significantly large spread of the experimental results, the presented method to measure the stiffness directly can be applied to the sensor after the AFM spectroscopy experiment.

Acknowledgements

It is a pleasure to thank Ingo Fenneker and Bernhard Falter (FH-Münster, Fachbereich Bauingenieurwesen) for the tension-test of the “Torr Seal” samples as well as Werner David and Stephan Diekmann (“Feinmechanische Werkstatt”, Physikalisches Institut, WWU Münster) for support and fruitful discussion. Financial support by the Deutsche Forschungsgemeinschaft (DFG) through the transregional collaborative research center “Multilevel Molecular Assemblies: Structure, Dynamics and Function” (TRR 061, project B7) is gratefully acknowledged.

References

1. Gross, L.; Mohn, F.; Moll, N.; Liljeroth, P.; Meyer, G. *Science* **2009,** *325,* 1110–1114. doi:10.1126/science.1176210
2. Sugimoto, Y.; Pou, P.; Abe, M.; Jelinek, P.; Pérez, R.; Morita, S.; Custance, Ó. *Nature* **2007,** *446,* 64–67. doi:10.1038/nature05530
3. Ternes, M.; Lutz, C. P.; Hirjibehedin, C. F.; Giessibl, F. J.; Heinrich, A. J. *Science* **2008,** *319,* 1066–1069. doi:10.1126/science.1150288
4. Langewisch, G.; Falter, J.; Fuchs, H.; Schirmeisen, A. *Phys. Rev. Lett.* **2013,** *110,* 036101. doi:10.1103/PhysRevLett.110.036101
5. Giessibl, F. J. *Appl. Phys. Lett.* **2000,** *76,* 1470–1472. doi:10.1063/1.126067
6. Senden, T.; Ducker, W. *Langmuir* **1994,** *10,* 1003–1004. doi:10.1021/la00016a600
7. Sader, J. E.; Larson, I.; Mulvaney, P.; White, L. R. *Rev. Sci. Instrum.* **1995,** *66,* 3789–3798. doi:10.1063/1.1145439
8. Sader, J. E.; Chon, J. W. M.; Mulvaney, P. *Rev. Sci. Instrum.* **1999,** *70,* 3967–3969. doi:10.1063/1.1150021
9. Albers, B. J.; Liebmann, M.; Schwendemann, T. C.; Baykara, M. Z.; Heyde, M.; Salmeron, M.; Altman, E. I.; Schwarz, U. D. *Rev. Sci. Instrum.* **2008,** *79,* 033704. doi:10.1063/1.2842631
10. Giessibl, F. J. *Appl. Phys. Lett.* **2001,** *78,* 123–125. doi:10.1063/1.1335546
11. Sader, J. E.; Jarvis, S. P. *Appl. Phys. Lett.* **2004,** *84,* 1801. doi:10.1063/1.1667267
12. Giessibl, F. J. *Phys. Rev. B* **1997,** *56,* 16010–16015. doi:10.1103/PhysRevB.56.16010
13. Dürig, U. *Appl. Phys. Lett.* **1999,** *75,* 433–435. doi:10.1063/1.124399
14. Hölscher, H.; Schwarz, U. D.; Wiesendanger, R. *Appl. Surf. Sci.* **1999,** *140,* 344–351. doi:10.1016/S0169-4332(98)00552-2
15. Cleveland, J. P.; Manne, S.; Bocek, D.; Hansma, P. K. *Rev. Sci. Instrum.* **1993,** *64,* 403. doi:10.1063/1.1144209
16. Chen, C. J. *Introduction to Scanning Tunneling Microscopy;* Oxford University Press: New York, 1993.
17. van Vörden, D.; Lange, M.; Schmuck, M.; Schmidt, N.; Möller, R. *Beilstein J. Nanotechnol.* **2012,** *3,* 809–816. doi:10.3762/bjnano.3.90
18. Sader, J. E.; Sanelli, J. A.; Adamson, B. D.; Monty, J. P.; Wei, X.; Crawford, S. A.; Friend, J. R.; Marusic, I.; Mulvaney, P.; Bieske, E. J. *Rev. Sci. Instrum.* **2012,** *83,* 103705. doi:10.1063/1.4757398
19. Berger, J.; Švec, M.; Müller, M.; Ledinský, M.; Fejfar, A.; Jelínek, P.; Majzik, Z. *Beilstein J. Nanotechnol.* **2013,** *4,* 1–9. doi:10.3762/bjnano.4.1
20. Simon, G. H.; Heyde, M.; Rust, H.-P. *Nanotechnology* **2007,** *18,* 255503. doi:10.1088/0957-4484/18/25/255503
21. Drake, B.; Prater, C. B.; Weisenhorn, A. L.; Gould, S. A.; Albrecht, T. R.; Quate, C. F.; Cannell, D. S.; Hansma, H. G.; Hansma, P. K. *Science* **1989,** *243,* 1586–1589. doi:10.1126/science.2928794

License and Terms

The definitive version of this article is the electronic one which can be found at:
doi:10.3762/bjnano.5.59